Effects Of Pulsation Frequency On Trailing Edge Plasma Actuators For Flight Control

HAMLIN, FREDERICK,WILLIAM

HAMLIN, FREDERICK,WILLIAM (2012) *Effects Of Pulsation Frequency On Trailing Edge Plasma Actuators For Flight Control*, Durham theses, Durham University. Available at Durham E-Theses Online: http://etheses.dur.ac.uk/5568/

Effects Of Pulsation Frequency On Trailing Edge Plasma Actuators For Flight Control

Abstract

This thesis details the aerodynamic testing of a dielectric barrier discharge (DBD) plasma actuator operating over a separation step created at the trailing edge of a modified NACA 0012 aerofoil. The work focuses specifically on the use of pulsed or interrupted plasma actuation as opposed to continuously driven actuation, to increase the change in the lift produced by activating the system.

The behaviour of the actuation system is characterised in a lamina flow regime at a Reynolds number of 1.33×10^5 using force balance measurements. At zero incidence the actuator produced a peak change in C_L of approximately 0.015. However, this result is sensitive to changes in the interruption frequency of the plasma, by changing the plasma drive waveform the system was able to produce both positive and negative changes in lift. A relationship was identified between the change in C_L produced and the ratio of the plasma interruption frequency to the natural vortex shedding frequency. This effect was investigated using both time averaged particle image velocimetry (PIV) and instantaneous phase locked PIV images captured in sequence throughout the plasma interruption cycle. The phase locked images showed how variation in the pulsation frequency was able to produce bi-directional actuation by either constructively or destructively interfering with the vortex formation from the back of the separation step. This interference in turn altered the level of separation which was occurring, altering the degree of upwash in the wake and therefore the lift generated by the aerofoil. PIV images were also gathered for device operation at a Reynolds number of 2.3×10^4; this produced a much higher ratio of DBD jet energy to that of the freestream. These conditions showed modified actuator behaviour due to the increased authority over the flow. However, the data still showed a strong interdependence on the reinforcement or destruction of the vortex street by the actuator interruption.

Furthermore, work was undertaken to develop an actuator topology based on thin metallised films along with a dielectric which was hardened against the chemical and electrical stresses present in a functioning DBD device. The failure mechanisms of metallised film actuators were investigated, and actuators with lifetimes exceeding 8 hours were demonstrated. A manufacture method for a silicon polymer (PDMS) – Kapton® laminate is detailed; this is shown to be highly resistant to both electrical breakdown and chemical attack by the oxygen plasma.

Effects Of Pulsation Frequency On Trailing Edge Plasma Actuators For Flight Control

Frederick William Hamlin, MEng.

School of Engineering and Computing Sciences

University of Durham

A thesis submitted to the University of Durham

For the degree of Doctor Of Philosophy

July 2012

Table Of Contents

Chapter 4 Wind Tunnel Results And Discussion 160

Chapter 5 Conclusions 255

List Of Figures

List Of Tables

List Of Abbreviations

AC	Alternating Current
CCD	Charge Coupled Device
CDF	Cumulative Distribution Function
CFD	Computational Fluid Dynamics
CI	Confidence Interval
CNC	Computer Numeric Control
DAQ	Data Acquisition [Device]
DBD	Dielectric Barrier Discharge
DC	Direct Current
DEHS	Di(2-EthylHexyl) Sebactate
EAP	Electroactive Polymer
EAP-IPMC	Electroactive Polymer - Ionic Polymer Metal Composites
EBPVD	Electron Beam Physical Vapour Deposition
FEP	Fluorinated Ethylene Polymer
FFT	Fast Fourier Transform
GRP	Glass Reinforced Plastic
HFP	Hexafluroproylene
HSE	Health and Safety Executive
HV	High Voltage
KiSa	Kibi Samples
LP	Low Pressure
MAV	Micro Aerial Vehicle
MCP	Master Control Program
MEMS	Micro Electro Mechanical Systems
MTBF	Mean Time Between Failure
NACA	National Advisory Committee for Aeronautics
NASA	National Aeronautics and Space Administration
NOTAR	No Tail Rotor
NPL	National Physical Laboratory
OADM	Optical Angle Distance Measurement
PDMS	Polydimethylsiloxane
PID	Proportional Integral Differential
PIV	Particle Image Velocimetry
PMMA	Poly(Methyl Methacrylate)
PMT	Photomultiplier Tube

PTFE	Polytetrafluoroethylene
PVC	Polyvinyl Chloride
Re	Reynolds Number
RIE	Reactive Ion Etch
RP	Rapid Prototype
SEM	Scanning Electron Microscope
SMA	Shape Memory Alloy
TFE	Tetrafluroethylene
UCAV	Unmanned Combat Air Vehicle
UV	Ultra-Violet [light]
VTOL	Vertical Take Off or Landing
YAG	Yttrium Aluminium Garnet

Nomenclature

CF	Carrier Frequency	Hz
C_L	Lift Coefficient	-
CpDyn	Coefficient Of Dynamic Pressure	-
CPitch	Pitch Coefficient	-
CpTot	Coefficient Of Total Pressure	-
CYaw	Yaw Coefficient	-
D_b	Drag During Backward Discharge	N
DC	Duty Cycle Ratio	%
D_f	Drag During Forward Discharge	N
DV	Drive Voltage	kV
F	Force	N
F^+	Nondimensional Actuator Frequency	-
f_{mod}	Plasma Modulation Frequency	Hz
F_{plasma}	Plasma Interruption Frequency	Hz
F_{shed}	Natural Shedding Frequency	Hz
g	Local Gravitational Acceleration	$m.s^{-2}$
H	Height Above Sea Level	m
IF	Interruption Frequency	Hz
Inc.	Incidence Angle	Deg
J	PIV Vertical Cell Index	-
L	Local Latitude	Deg
L_{sep}	Length Of Separation Zone	m
P	Momentum Per Linear Metre Of Actuator	$Kg.s^{-2}$
P_0	Pressure Of Hole 0 In 5 Hole Probe	Pa
P_{ave}	Average Of Outside Pressure Holes In 5 Hole Probe	Pa
P_{dyn}	Dynamic Pressure	Pa
P_{tot}	Total Pressure	Pa
R	Blade Radius	m
R_{leads}	Resistance Of Leads To Hotwire Probe	Ω
$R_{probe@20}$	Resistance Of Probe At 20°C	Ω
R_{set}	Resistance To Assign To Set Point Resistor In Bridge	Ω
$T_{ambient}$	Ambient Temperature Of Fluid Flow	°C
T_b	Thrust During Backward Discharge	N
T_f	Thrust During Forward Discharge	N
T_{set}	Target Temperature For Hotwire Operation	°C

U	X-Axis Velocity Component	m.s^{-1}
U_∞	Freestream Velocity	m.s^{-1}
U_{normal}	Velocity Component Of Flow Normal To Wire	m.s^{-1}
V	Velocity	m.s^{-1}
V_0	Voltage On Load Cell 1	V
V_1	Voltage On Load Cell 2	V
V_2	Voltage On Load Cell 3	V
Vel.	Nominal Test Velocity	m.s^{-1}
V_{error}	Output Voltage Of Hotwire Bridge	V
V_{out}	Output Voltage Of Hotwire Anemometer	V
X	Streamwise Distance Along Tunnel Relative To Leading Edge Of Aerofoil At Zero Incidence	mm
Y	Perpendicular Distance From Wall Or Plate	mm
Y	Lateral Displacement Within Tunnel Along Prismatic Axis Of Aerofoil	mm
Z	Vertical Displacement In Tunnel Perpendicular to Chord Line Of Aerofoil At Zero Incidence	mm
α	Incidence Angle	Rad
α_{20}	Temperature Coefficient Of Resistance At 20°C	$^{o}C^{-1}$
ω	Angular Velocity	Rad.s^{-1}

Declaration

I certify that the materiel contained within this thesis is wholly my own work, furthermore no part of it has previously been submitted for any degree or qualification at this, or any other, institution.

Statement Of Copyright

Acknowledgements

I would Like to acknowledge the academic help and support of my supervisors Dr David Sims-Williams and Prof. David Wood. I would also like to thank Dr Mark Rosamond, Dr. Andrew Gallant, Mike Wilson and Adam Sprot for their help in keeping me as sane as is possible after so many years in the engineering department. Lastly I wish to recognise the support of my parents in getting me through the trauma of a doctoral degree.

Chapter 1 Literature Review

1.1 Introduction

The experimental work in this thesis centres on plasma based flow control, as such a large portion of this literature review is dedicated to plasma actuators, and these are covered in depth in section 1.4. However, the initial remit was much broader, allowing for investigation into any project classified as active flow control, section 1.2 covers a range of applications looked at as being suitable for the application of active flow control techniques. Section 1.3 details a selection of MEMS actuator technologies from the literature which either have been or could be applied to the creation of an active flow control system. The comparison and summary of these actuator technologies and applications, along with the rationale and motivation for taking the project in the direction of plasma flow control is contained in section 1.5.

1.2 Active Flow Control Applications

Active flow control can be defined as "requiring energy to be expended for the control to take place" [1]. MEMS and or plasma actuator technology could be applied to many different flow control areas. However, good examples of flow control produce a large effect from only a small input actuation effort or energy; they find something that is close to a tipping point and provide a small disturbance to the steady state situation to provoke the flow to favour one regime or another. By optimising the timing, location and direction of the applied actuation the favoured outcome can be selected. A wide range of examples of areas which are likely to produce a favourable application for MEMS and or plasma technology or which have already had research work done on the application of either of these to them are given in this section, many of these were considered before the final project direction was established, and are included to provide context to the wider area of active flow control.

1.2.1 Bluff Body Drag Reduction

Active flow control can reduce the drag coefficient of large bluff bodies like the transport aircraft shown in Figure 1.1, which have all been designed primarily for ease of loading rather than aerodynamic performance. Using a simplified wind tunnel model of a rear loading ramp it was demonstrated in [2] that by using piezoelectric synthetic jet actuators positioned around the edge that the drag could be reduced. Significant drag reductions of 3% – 11% were achieved by eliminating the separation bubble at the base of the loading ramp. Flow visualization and computational fluid dynamic studies showed that the wake and vortex system was more steady behind the model when the piezoelectric actuators were operational.

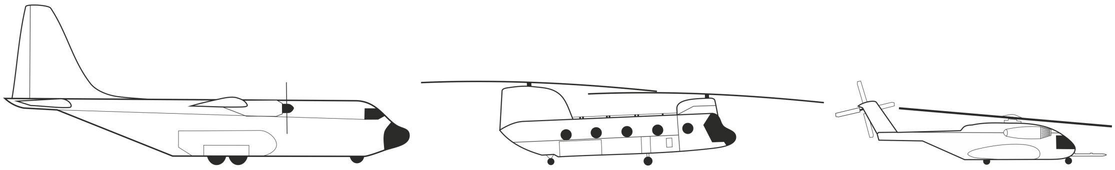

Figure 1.1 C130, CH47 And CH53 All Featuring Aft Loading Ramps

1.2.2 Aerofoil Flow Control

1.2.2.1 Plasma Flight Control

The three planes of rotation an aircraft can execute are roll, pitch and yaw. In conventional aircraft control all three are induced using moveable control surfaces to change the coefficient of lift of either the wings for roll, tail plane for pitch or vertical stabilisers for yaw as shown in Figure 1.2.

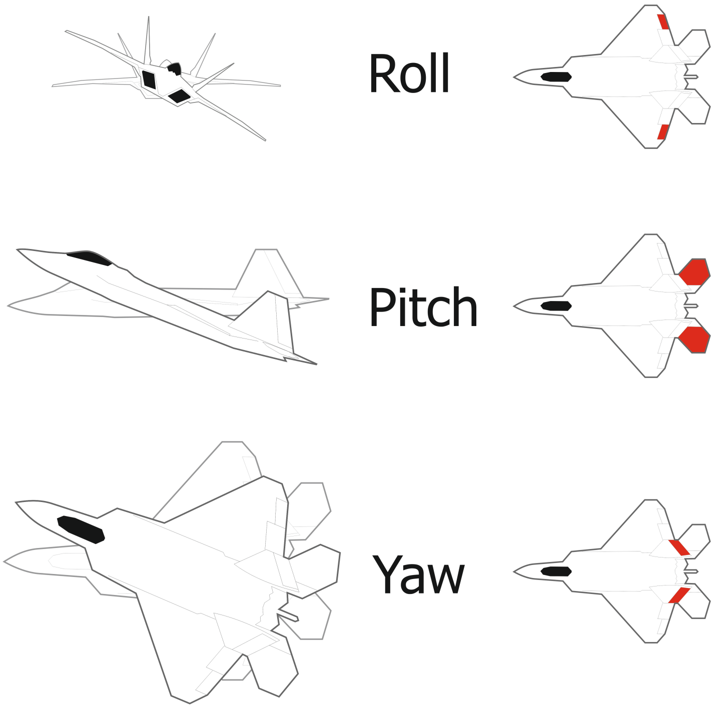

Figure 1.2 Conventional Flight Control Surfaces Of The F22 Raptor

In a plasma flight control setup, the conventional moving surfaces are either augmented with or replaced by plasma actuators which modify the flow over the aerofoil to replicate the change in lift which would have been accomplished by the movement of the conventional control surfaces. At low angles of incidence this effect can be achieved by modifying the back of the aerofoil so that it contains a separation step then, by activating the plasma, the flow over the wing can be altered as shown in Figure 1.3. When the flow is separated, although the drag is increased, the wing appears asymmetrical with significant camber [3], with a low upwash component to the flow over the bottom of the aerofoil; this gives the maximum lift from the wing. Conversely, when the flow is attached the wing appears far more symmetrical, the forces are more balanced and the lift is reduced. In this way a differential in lift between two wings can be created, and hence pitch and roll moments can be created. This can all be accomplished whilst reducing the complexity of the wing structure with an all solid state system and at a power consumption of only 2-4 W per linear metre of actuator [4].

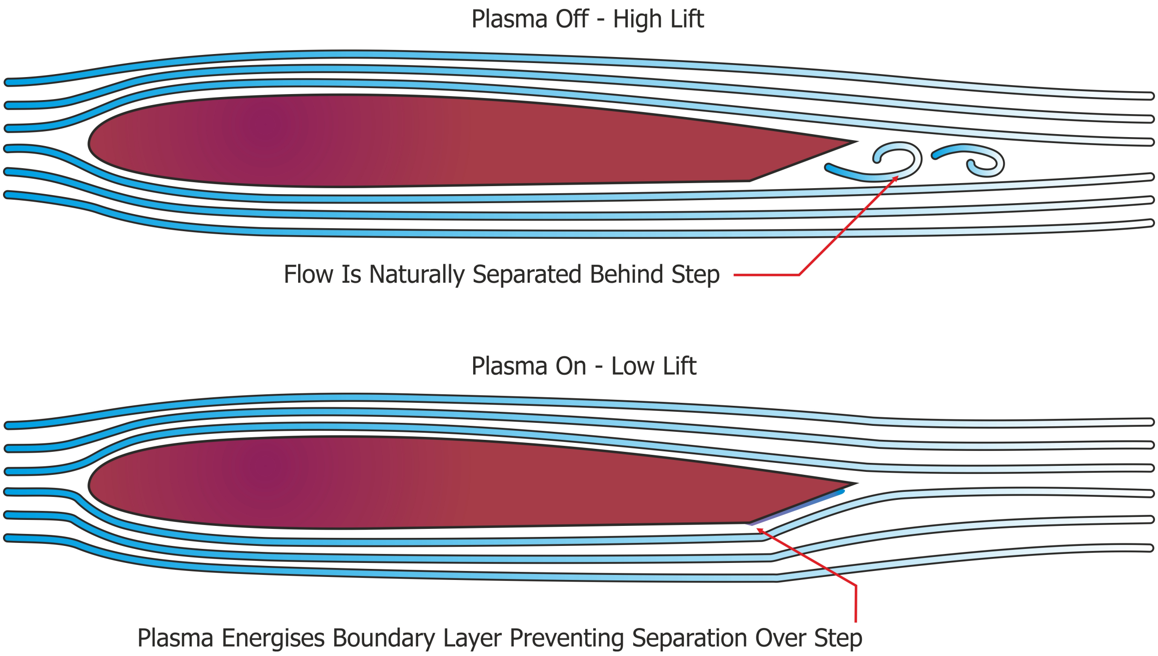

Figure 1.3 Effect Of Plasma Actuation On A Stepped Aerofoil

Patel et. al. in [3] tested a three dimensional half span model, shown in Figure 1.4, which utilised a trailing edge step to induce separation in the flow. As the model has a non-uniform cross-section to the wing along its span, the extent of the ramp varied; shown in yellow is the line demarcating the onset of the step, which then extends back to the training edge. Tests were conducted at a Reynolds number of $4.33x10^5$ (based on the mean aerodynamic chord). Two of their key results are shown in Figure 1.5. Firstly, that they were able to achieve significant levels of control actuation. Secondly the magnitude of change induced on C_L was much greater when the actuation was run in a unsteady manner at a 25% duty cycle (plasma active for 25% and off for 75% of the time) than when the plasma was run continuously (100% duty cycle); comparisons of delta C_L at maximum and zero degrees incidence are marked on the graphs for reference. The stated standard deviation for their tests was 0.00496 on C_L, this means that for the continuous actuation results the separation at each individual point is not considered statistically significant. However if all points on this graph are considered then the probability of them all randomly showing a negative C_L shift without an underlying aerodynamic effect produced by the actuator reduces to the point where the existence of some effect from continuous actuation can be considered significant. The effect seen with pulsed actuation is large enough to be considered significant at the individual points. The frequency at which they pulsed the plasma was determined by scaling a non-dimensional frequency based on Strouhal number to unity. They termed this F+ and it is given by the equation $F^+ = f_{mod} \times L_{sep} \times U_\infty^{-1} = 1$ where f_{mod} is the plasma modulation frequency, L_{sep} is the length of the separation zone and U_∞ is the freestream velocity.

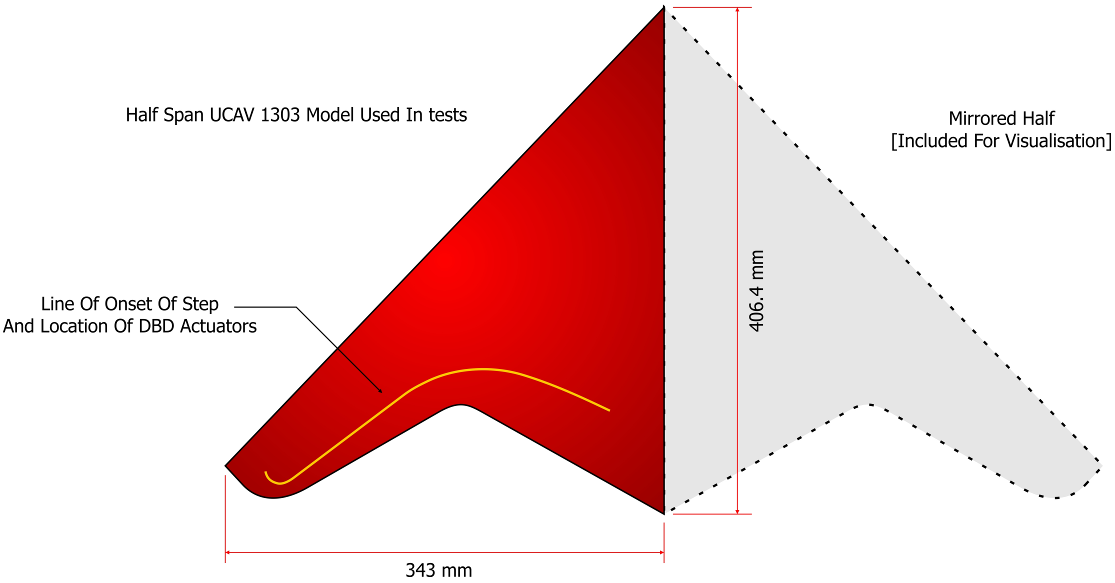

Figure 1.4 Plan Form Diagram Of Model Tested In [3]

In a 2D aerofoil test published in [4] a slightly modified topology containing both pressure side and suction side separation steps and plasma actuators (Figure 1.6) presented even larger changes in C_L by actuating either upper or lower DBD device; results are plotted in Figure 1.7. Again this test used unsteady forcing at the same non-dimensional $F^+ = 1$, and was conducted at a Reynolds number of 3.03×10^5.

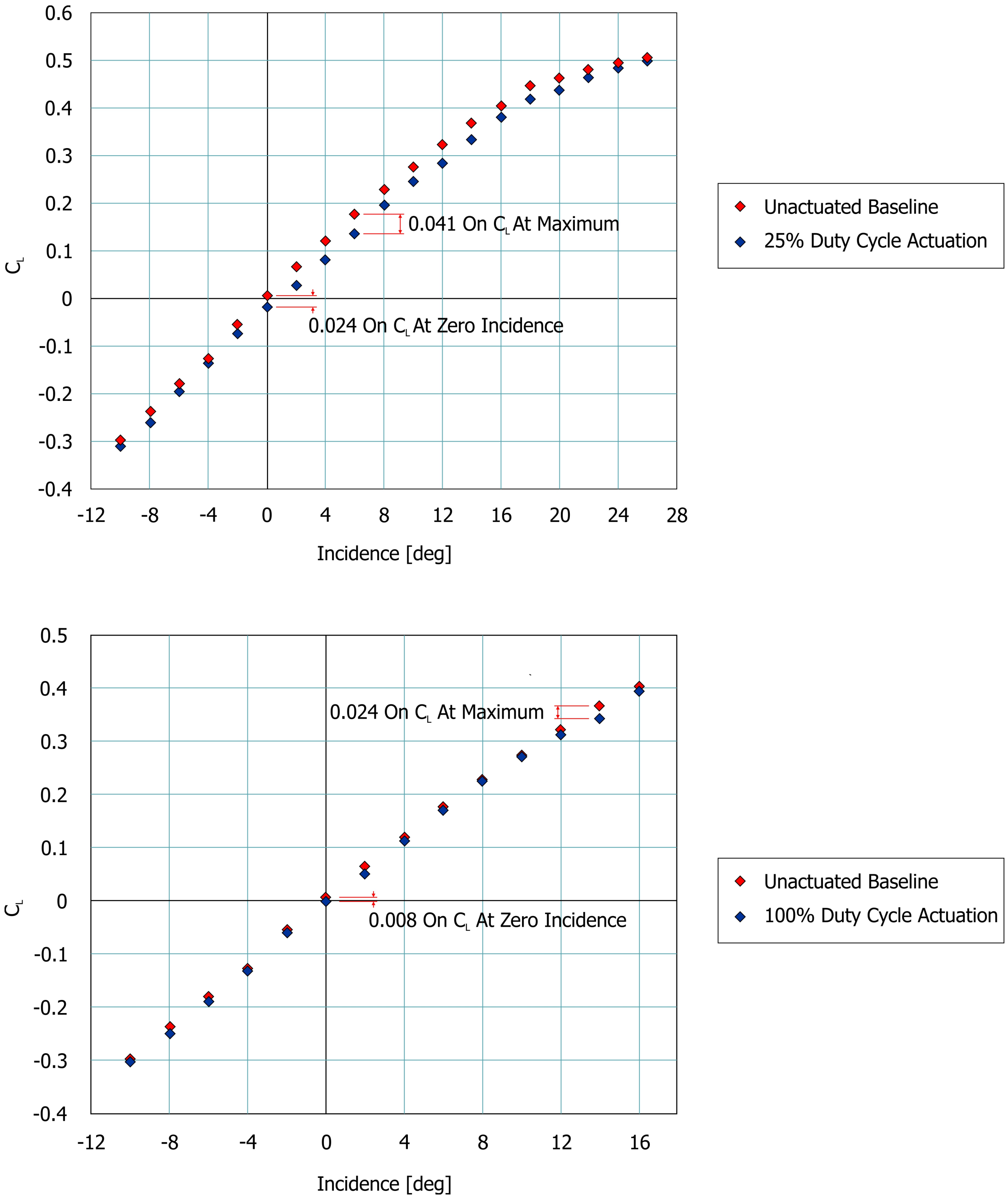

Figure 1.5 Effect Of Plasma Actuation (Replotted From [3])

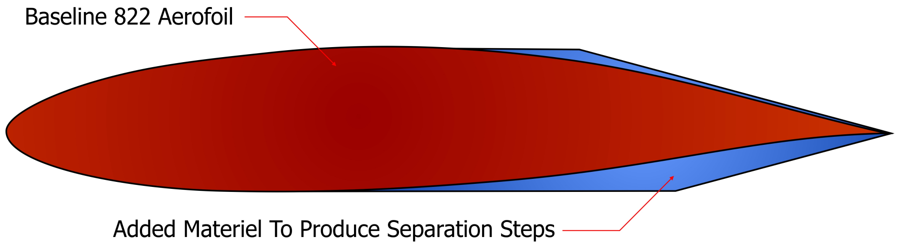

Figure 1.6 Dual Separation Step Profile Used By Patel et. al. In [4]

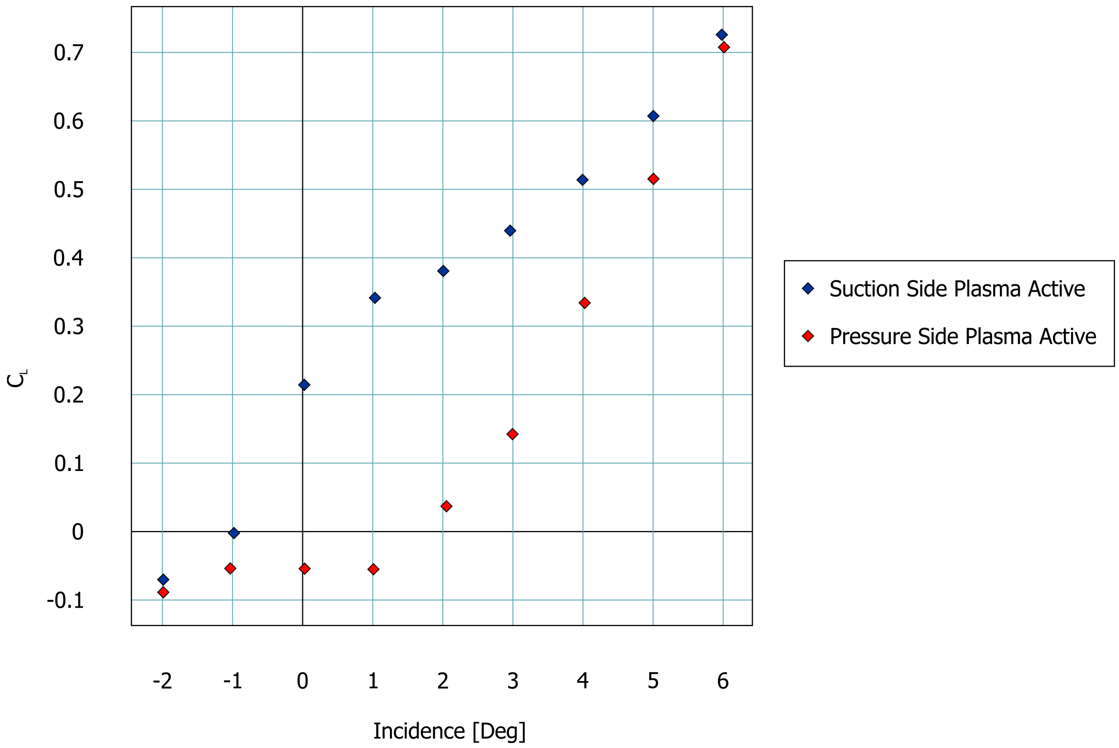

Figure 1.7 Effect On C_L With Dual Separation Steps (Replotted From [4])

A slightly different method of creating control forces was examined in [5]. Instead of using a separation step at the trailing edge of the aerofoil, at high angles of attack the leading edge vortex and subsequent vortex breakdown structure can be manipulated by DBD actuators to significantly affect the lift arising from the delta wing. Their experimental setup is outlined in Figure 1.8. Shown in Figure 1.9 is a key result from their work, where the leading edge actuators show very little control effect at low levels of incidence. However, above 10^o incidence significant actuation levels are shown. This is precisely where the conventional trailing edge control surfaces (flaps and ailerons) begin to suffer from the 3 dimensional separation and cross-flow forming over the training edge due to the leading edge vortex breakdown moving further forward on the suction side surface. Shown in Figure 1.10 is the data showing a favourable comparison of the leading edge plasma actuators to a 5^o flap deployment. This test was conducted at a Reynolds number of $4.12x10^5$.

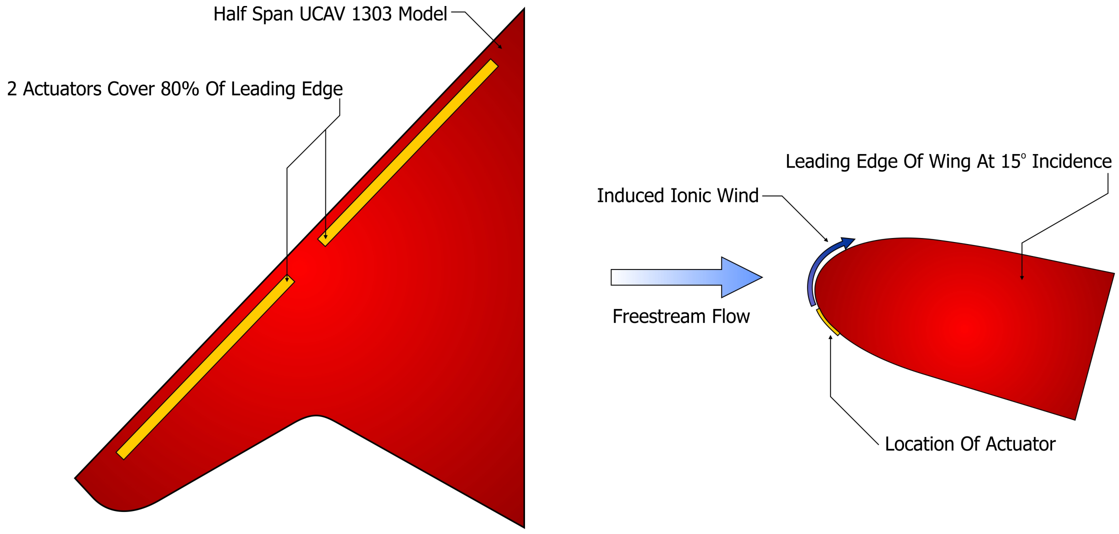

Figure 1.8 Location of leading Edge Plasma Actuators As Used In [5]

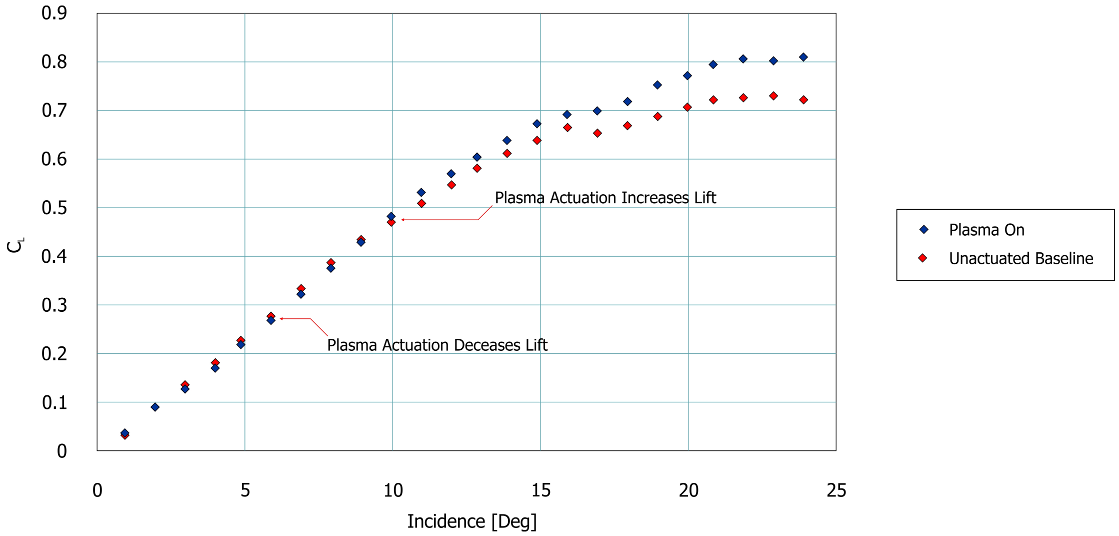

Figure 1.9 Effect Of Leading Edge Plasma Actuation (Replotted From [5])

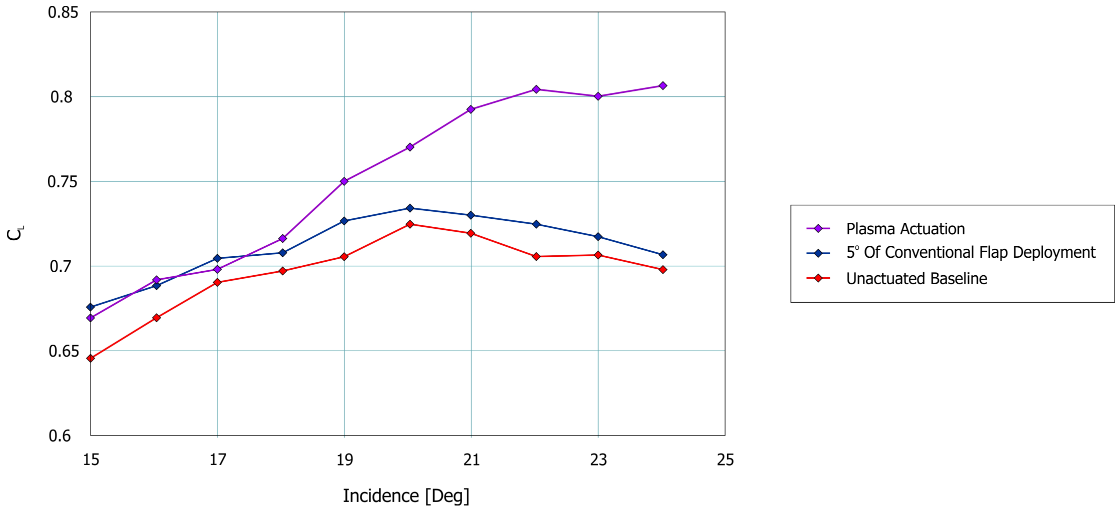

Figure 1.10 Comparison Of Leading Edge Plasma Actuators To Conventional Control Surfaces At High Angles Of Attack (Replotted From [5])

The principal of circulation control is shown in Figure 1.11. A blunt ended ellipsoid aerofoil is used, this means that there is no defined 2nd stagnation point as in a sharp edged aerofoil, by blowing air tangentially along the surface just before the trailing edge the Coandậ effect can be used to keep the flow attached further around the surface before it separates, this (in the configuration shown) increases the circulation around the aerofoil and therefore the lift, equally the opposite effect can be achieved by blowing along the pressure side of the aerofoil. The tangential blowing can be provided by compressed air as in [6], or possibly a plasma actuator as simulated in [7], the results of which are detailed in the figure.

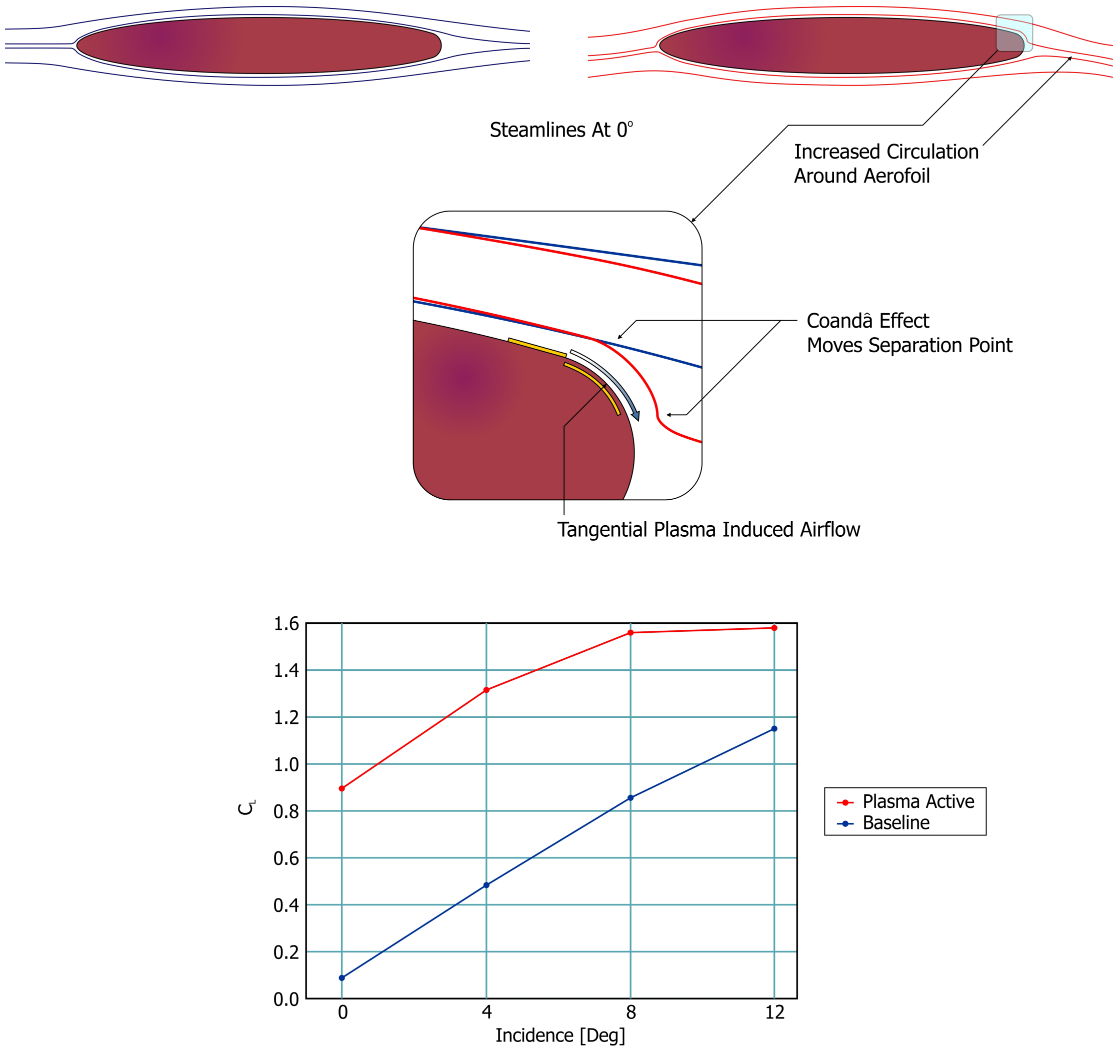

Figure 1.11 Circulation Control Aerofoil (Redrawn From [7])

1.2.2.2 High Lift Devices

Conventional slotted flaps are used to reduce the stall speed of an aircraft and increase lift available at take off. Slotted flaps increase the effective camber of the wing by deflecting downwards, but also air from the underside of the wing is ducted over the flap (Figure 1.12) , this airflow energises the boundary layer over the top of that section of the aerofoil allowing the wing to operate at higher maximum lift coefficients before separation occurs [8]. In some large commercial aircraft multiple slotted high lift devices at both the trailing edge (flaps) and leading edge (slats) are used to maximise lift coefficient. However this adds a lot of mass and complexity to the wing which it would be desirable to do without.

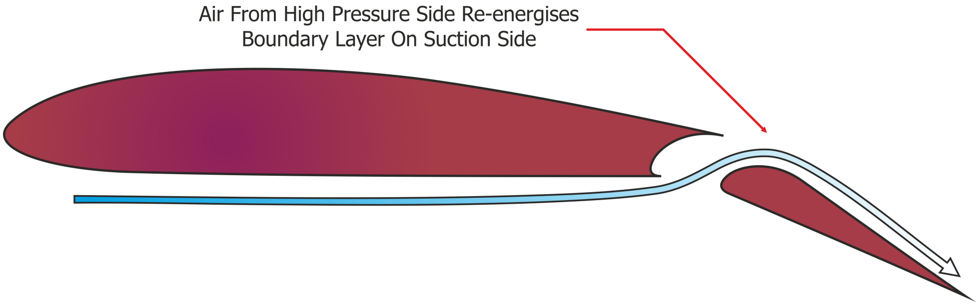

Figure 1.12 Conventional Slotted Flap

By using MEMS devices (covered in subsection 1.3) to increase the energy in the boundary layer of a non-flapped aerofoil, the aerofoil can be used at an increased angle of attack before the flow separates and the wing stalls. This has a similar effect to running a flap in a conventional wing in that it increases the maximum coefficient of lift available from the wing. Experiments have shown successful reattachment of separated flow to aerofoil profiles at angles up to 6° beyond the baseline stall condition in [9-10] (the results of smoke flow visualisations from [9] are illustrated in Figure 1.13 ($Re \approx 2.2x10^4$)), flow over inclined flat plates has also been demonstrated in [11].

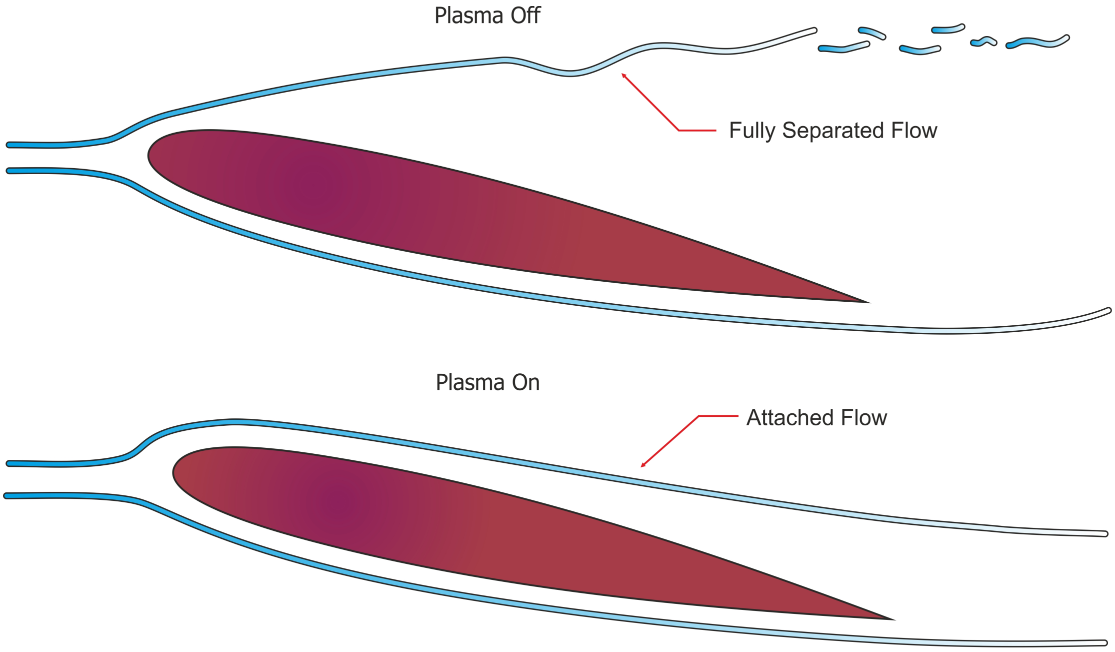

Figure 1.13 Plasma Actuators Reattach Normally Separated Flow

In these experiments separation is delayed by using the plasma discharge to accelerate the boundary layer next to the wall. The effect that accelerating the flow next to the wall has is shown in Figure 1.14, taking the case of the accelerated flow shown in purple and comparing it to the velocity profile of the un-accelerated case shown in blue. It can be seen it will not stop separation and, further downstream or in a higher pressure gradient, the accelerated flow will separate as well. Although [9-10] and [11] use plasma actuators in their studies it is also possible to use a synthetic jet actuator to achieve similar stall control qualities; by firing the synthetic jet into the boundary layer turbulent mixing is promoted and high energy fluid is brought into the wall from the free stream achieving a similar velocity profile to that of the plasma actuator. Good direct numerical simulation data for stall suppression over an aerofoil using synthetic jets is available in [12].

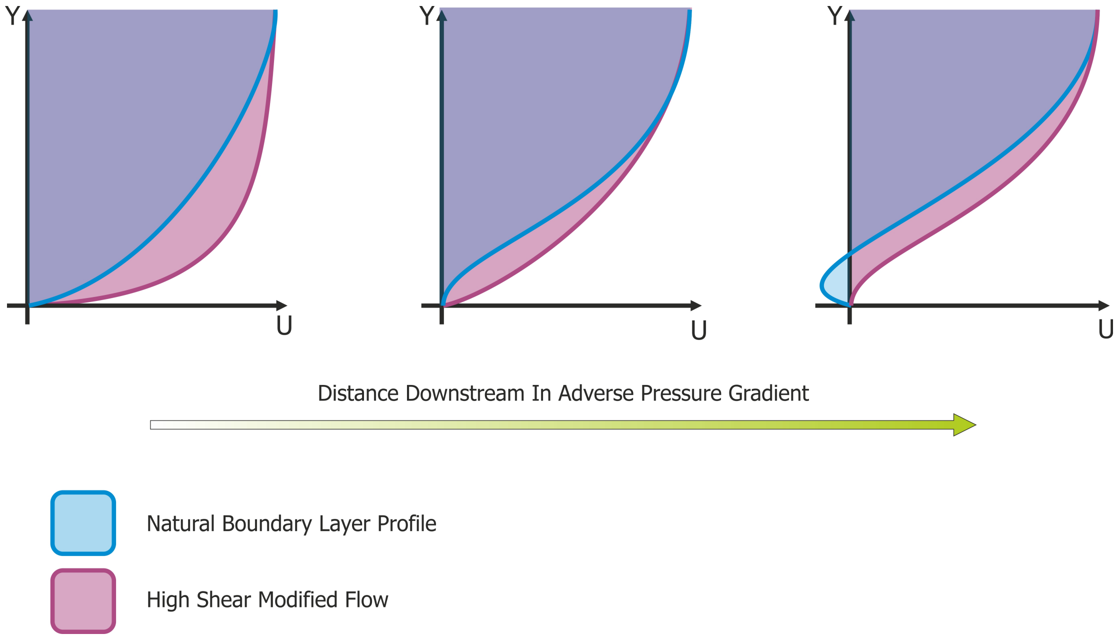

Figure 1.14 Separation Delay By Boundary Layer Modification

This approach of modifying the boundary layer at the leading edge of the wing can also be used to allow a wing profile which has been highly optimised for efficient operation at high Reynolds number where a turbulent boundary layer helps to prevent separation to function properly at a low Reynolds number where the laminar boundary layer is much more susceptible to separation. In CFD simulations in [13] it was shown that a likely source of the improvement in boundary layer profile was due instabilities being set up in the boundary layer by the actuation which are amplified by the flow field to create an effect larger than that purely due to the volume forcing which simulated the plasma.

Gurney flaps are another device used for producing high lift performance from a simple aerofoil. Originally invented for, and mostly used in, motorsport for increasing downforce to improve cornering performance [14]. They consist of a short flap set perpendicular to the pressure surface of the aerofoil at the trailing edge, extending a few % of the total chord length into the boundary layer. An interesting modification on this concept the use of a plasma actuator mounted on the gurney flap to modify the flow behaviour further increasing C_L (see Figure 1.15) . Using PIV to investigate the flow behaviour, Feng et. al. showed in [15] that activation of the plasma actuator pitched the average position of the centre of the wake down by up to 3.4°, enhancing the circulation around the aerofoil and increasing the lift generated. The results of this on the lift coefficient at a Reynolds number of 20,000 are shown in Figure 1.16, in this case the plasma was actuated at 9.8 kV, 17.8 kHz. It can be seen that the plasma actuation offers significant increase in lift when active, the authors concluded that the effect was approximately equal to an increase in the gurney flap height of 1% of chord length.

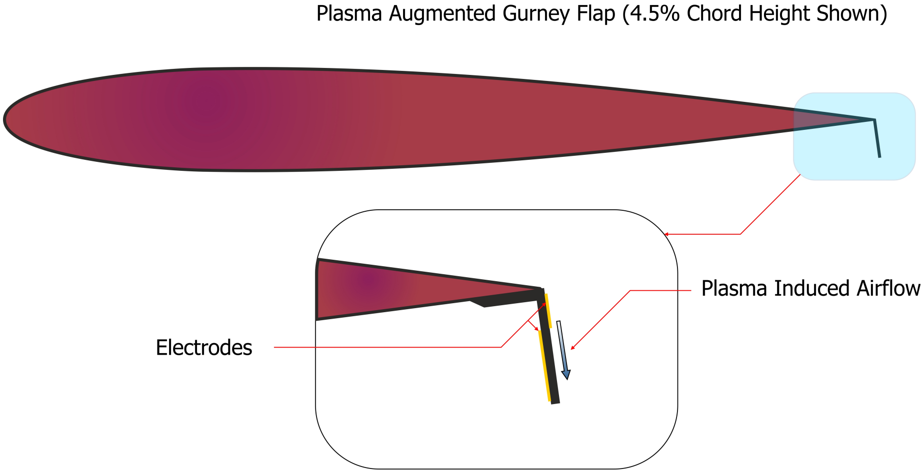

Figure 1.15 Plasma Gurney Flap

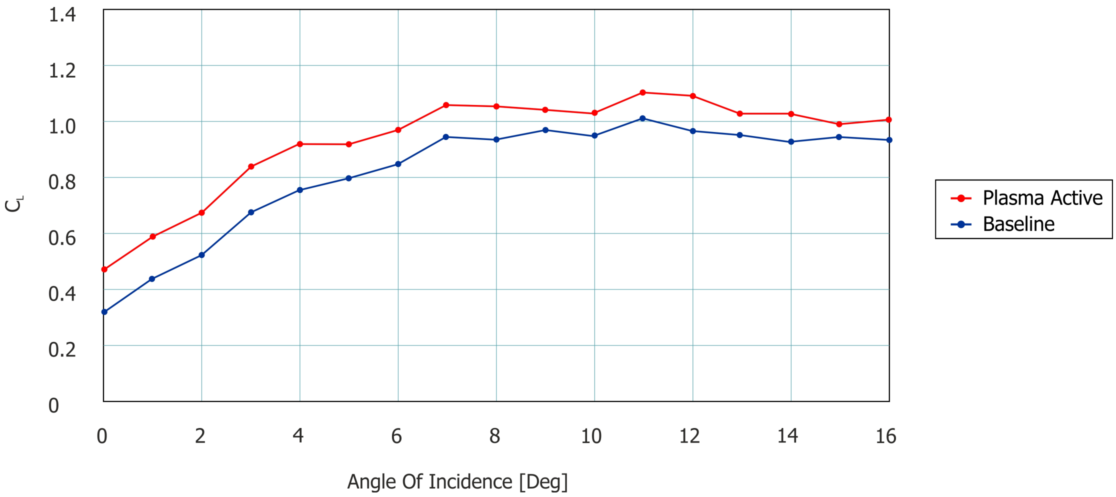

Figure 1.16 Effect OF Plasma Actuation On A Gurney Flap (Redrawn From [15])

Plasma actuators have also been used to improve the performance of plain moveable flaps. Shown in Figure 1.17 is a representation of the flow around a 25% chord length flap deflected by 30° as reported in [16]. The change in flow structure seen as created using a pulsed plasma modulated with a sine wave in a flow at a Reynolds number of 240K. The outcome of the reduction of the time averaged recirculation bubble is again to increase the circulation around the aerofoil and therefore increase the lift generated. The change in C_L demonstrated by actuating the plasma was on the order of 0.09. In results not duplicated here the paper showed how the frequency of the modulation relative to the flow was important, for the case illustrated the forcing was the same as the natural oscillation of the trailing edge flow field, with quaisi-steady forcing the separation could be increased, this is an important result which will has many similarities with the original work presented for this thesis.

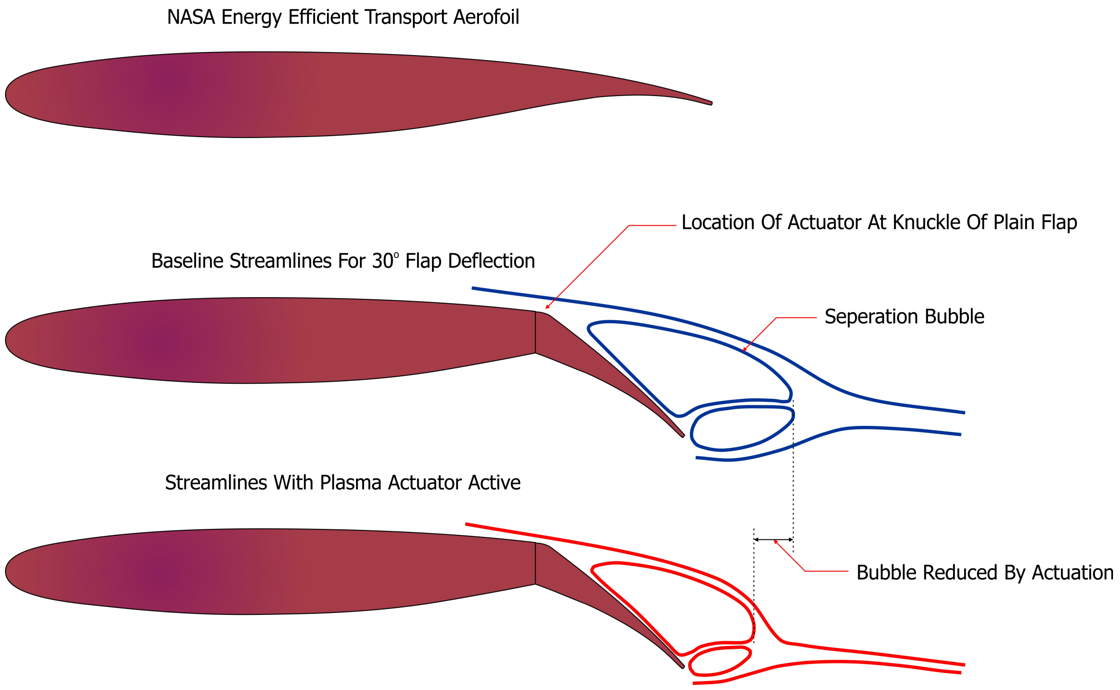

Figure 1.17 Improvement Of Flap Performance

Illustrated in Figure 1.18 is the concept of using plasma actuators to manipulate the tip effects of finite span wings to generate control forces as presented by Boesch et. al. in [17]. The pressure differential between the upper (suction) and lower (pressure) surfaces generates a flow around the end of the wing which sets up a strong vortex trailing off the wing tip, this vortex induces a downwash in the flow onto the wing, effectively reducing the angle of attack and with it the lift generated by that section of the wing and also increasing induced drag. For all non elliptical plan-forms this induced downwash velocity varies across the span of the aerofoil [18]. The active flow control element is introduced by using plasma actuators placed around the end of the semicircular wing tip to disrupt the formation of the vortex. The authors of [17] used CFD simulations to understand the effect on the flow field that placing plasma actuators around the wing tip to induce a flow against the pressure gradient would have. These simulations were validated by comparing the predicted lift change to experimental data. Their simulations showed that the plasma actuation was most effective when placed on the upper surface, here it created a small vortex which interacted with the flow coming round the wingtip (see Figure 1.18). Downstream of the trailing edge this resulted in a more diffuse weaker vortex, with a corresponding change in the induced downwash onto the leading edge, this change was on the order of 0.1^{o} and fairly uniform across the span. Figure 1.19 shows the experimental results and gain in lift achieved with the wing tip actuation.

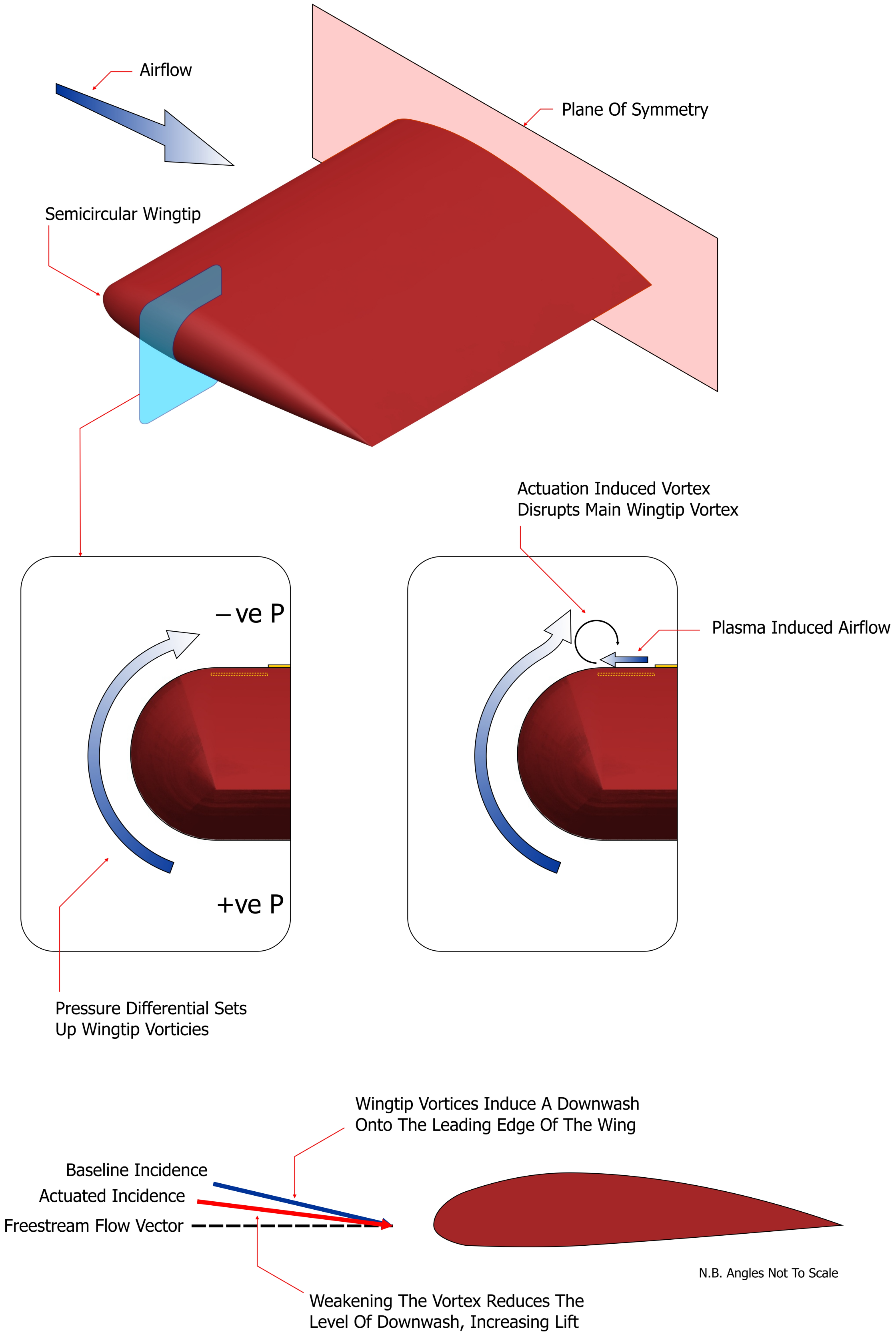

Figure 1.18 Wingtip Lift Control

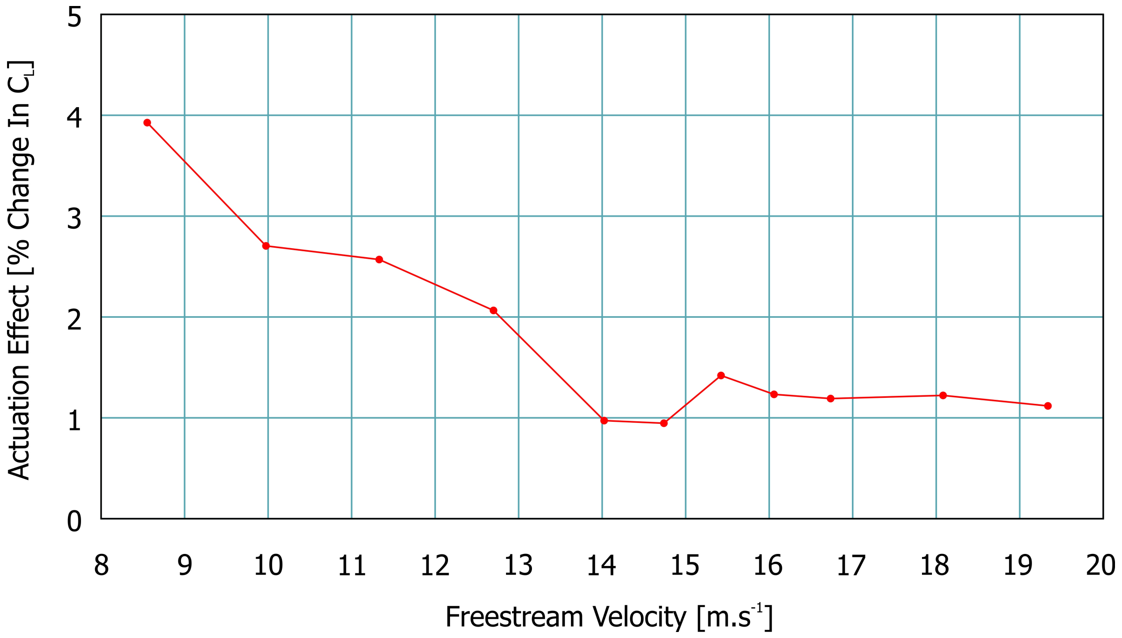

Figure 1.19 Experimental Results For Wingtip Plasma Control (redrawn from [17])

1.2.2.3 Low Pressure Turbine Stall Suppression

The latter stages in the turbines of aircraft turbofan engines can be subject to performance loss due to partial separation of the flow over the blade. By the time the fluid enters the last stages of a low pressure (LP) turbine it is still very hot and has been expanded most of the way to atmospheric pressure. At cruise altitude where atmospheric pressure is approximately ¼ of that at sea level a very low density flow field over the blades leads to a condition where the Reynolds number drops to the point where the laminar flow across the blade is insufficient to prevent flow separation of the boundary layer over the second half of the suction side of the blade. Huang et. al. showed in [19] that plasma actuators situated near to the separation point could drastically reduce the size of the separated bubble promoting reattachment and reducing separation losses. Measurements taken from pressure tapings in a wind tunnel cascade showed a performance similar to vortex generators in reducing losses but without the associated parasitic losses when they were not needed.

1.2.3 Skin Friction Reduction

MEMS technology can also be applied to skin friction reduction through the suppression of turbulent mixing in the boundary layer. Turbulent vortices increase the skin friction experienced by a surface by bringing high velocity fluid from the free stream towards the wall, increasing the velocity gradient of the boundary layer near the wall and therefore the shear stress (Figure 1.20). By using networks of shear stress sensors and actuators to detect an event which is moving fluid in towards the wall and then actuating in opposition to this, the effect of turbulent mixing on the shear stress could be reduced by 7% [20].

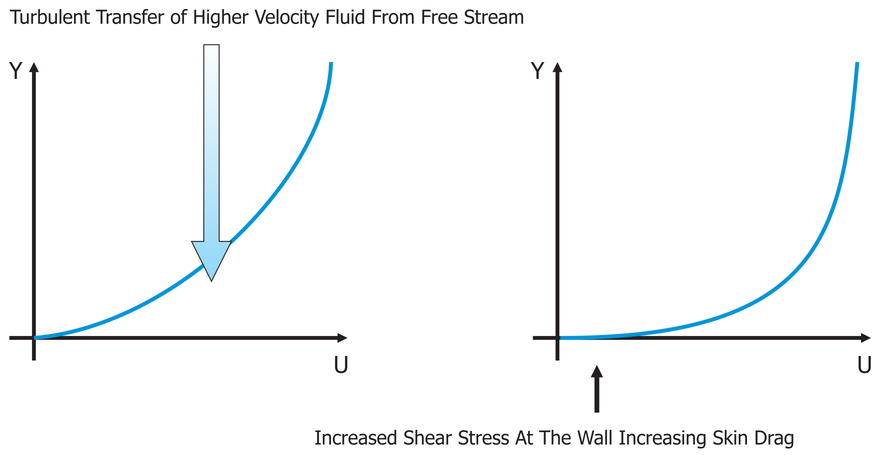

Figure 1.20 Skin Friction Increase Due to Turbulent Flow Conditions

Between vortex pairs present in the boundary layer there are two types of possible turbulent flow event; sweep events, which are those bringing fluid from the free stream towards the wall and ejection events which are those that move low velocity fluid away from the wall, these are formed by the interaction between the pairs of streamwise vortices [21] , illustrated in Figure 1.21. There are two methods for interacting with the turbulent events to oppose the mixing. The first and most common is a direct opposition jet, usually created by a synthetic jet actuator (see section 1.3). This is shown in Figure 1.22 where the jet pulse is used to push against the wall-bound fluid stopping the mixing. It is however unable to actuate against ejection events due to the nature of the synthetic jet actuator. Interesting examples of synthetic jet actuator skin friction reduction hardware and the differing feed forward / feedback control strategies used to determine actuation can be found in [20, 22-23] .

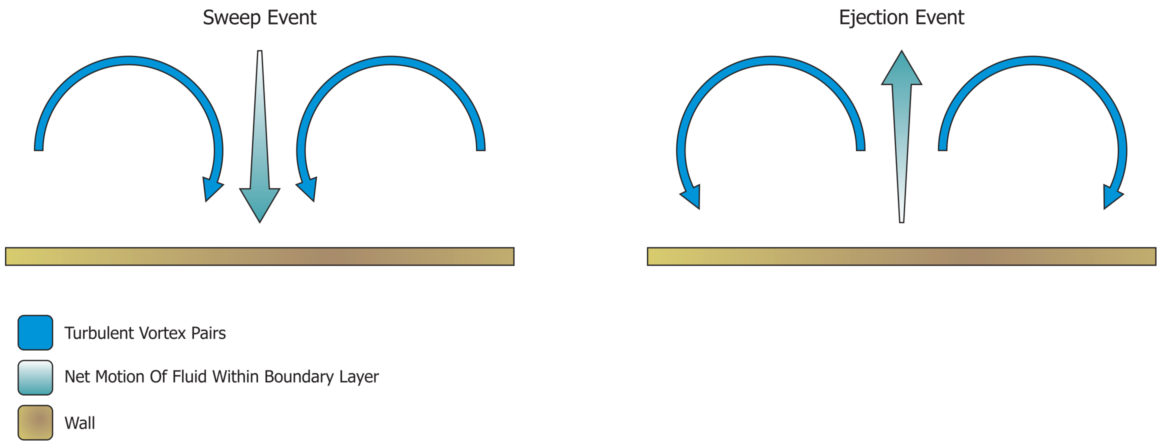

Figure 1.21 Sweep And Ejection Events

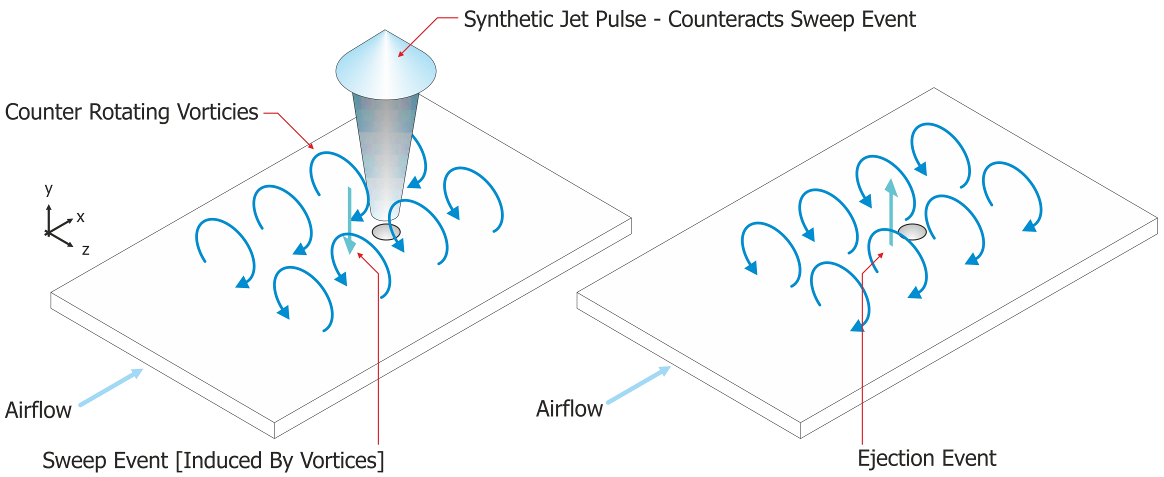

Figure 1.22 Turbulence Reduction By Direct Opposition

The second method of actuation that can be used to oppose the turbulent events bringing high velocity fluid in from the freestream is to deform the skin of the surface as the event passes over, again just as in the direct opposition jet, this reduces the shear stress at the wall and therefore the skin drag on the object. A direct numerical simulation of this was done in [21], and this is the actuation method shown in Figure 1.23. As the vortices passed over the actuation sites, the wall would push up against sweep events and move down in opposition to ejection events, and a total drag reduction of around 10% was achieved. The work of Suzuki et al [24] used physical actuators deforming a silicone membrane using rare earth magnets in an array; however much of their work was devoted to the development of the prediction techniques for identifying when a sweep event was occurring rather than on the actuation to reduce the effect of the event.

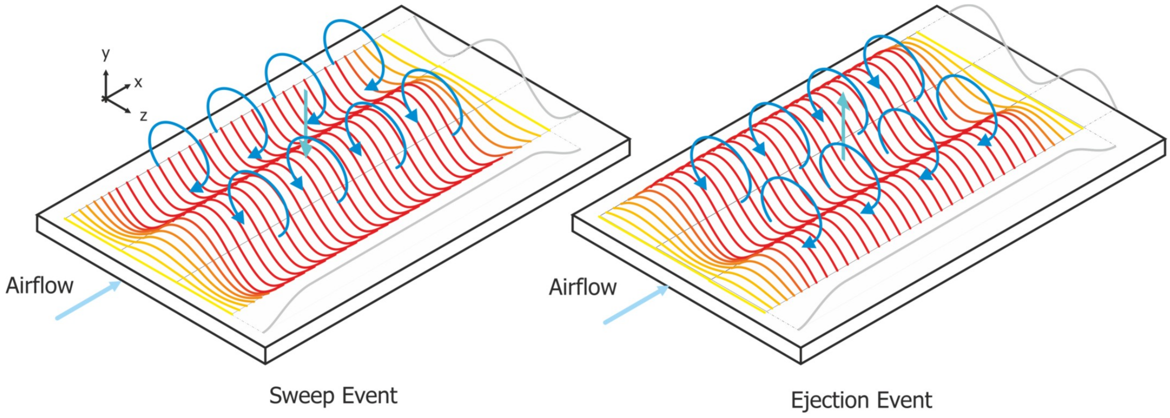

Figure 1.23 Turbulence Reduction By Wall Deformation

1.2.4 Flow Path Control

1.2.4.1 Thrust Vectoring

MEMS actuators have successfully been shown to be able to control the flow of jets in several studies by controlling separation around sectors of the perimeter of a diffuser, to encourage the flow to follow the line of the diffuser in the direction towards which it needs to be bent. Good examples of this application are shown in [25-27].

1.2.4.2 No Tail Rotor (NOTAR) Helicopters

NOTAR is a system developed by Hughes Helicopters & the McDonnell Douglas corporation in the 70’s and 80’s. Its purpose is to replace the tail rotor used by conventional helicopters to balance the torque reaction caused by the rotation of the main rotor blade with a torque reaction provided by directing the downwash over the tail boom using the Coandă effect (Figure 1.24). Full size NOTAR systems have been shown to offer several advantages, including reduced noise, due to the lack of the interaction between the tail rotor tip vortices with the main rotor [28]. NOTAR systems are also safer to operate at low level in wooded or urban environments due to the elimination of a tail rotor strike accident [29]

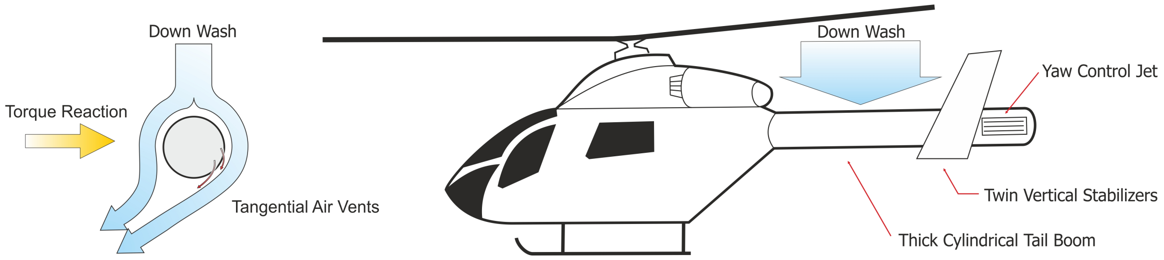

Figure 1.24 NOTAR Helicopter Operation

If the advantages of NOTAR could be applied to battlefield vertical takeoff or landing (VTOL) MAVs this would have obvious benefits to survivability and stealthiness. As has been shown in previous sections (1.2.2) MEMS technologies are ideally suited to flow attachment control applications and synthetic jet or plasma actuators could possibly be used to replace the tangential jets fed from the turbine compressors along the side of the tail boom in the full size rotorcraft. Experimental results showing synthetic jet flow diversion around a cylinder in a wind tunnel are show in [30].

1.2.4.3 Shockwave control

Most of the research presented so far is for subsonic and transonic flow conditions. However researchers are also looking at using mm scale structures to provide control forces in the high supersonic and hypersonic environment of guided artillery munitions [31]. By deploying structures into the airflow on one side of a small canard the resulting change in shock structure over the wing significantly changed the lift. This change was measured to be sufficient to create trajectory control in smart munitions.

1.2.4.4 Aerofoil Virtual Shaping

Virtual aerofoil shaping is a method of obtaining flight control forces by changing the apparent shape of the aerofoil by creating a separation bubble and using synthetic jet actuators to moderate its size. This effectively modifies the thickness of the aerofoil (Figure 1.25) [32], changing the pressure distribution over the upper surface of the wing. This change in pressure distribution alters the lift the wing is providing and can be used to provide pitch and roll moments.

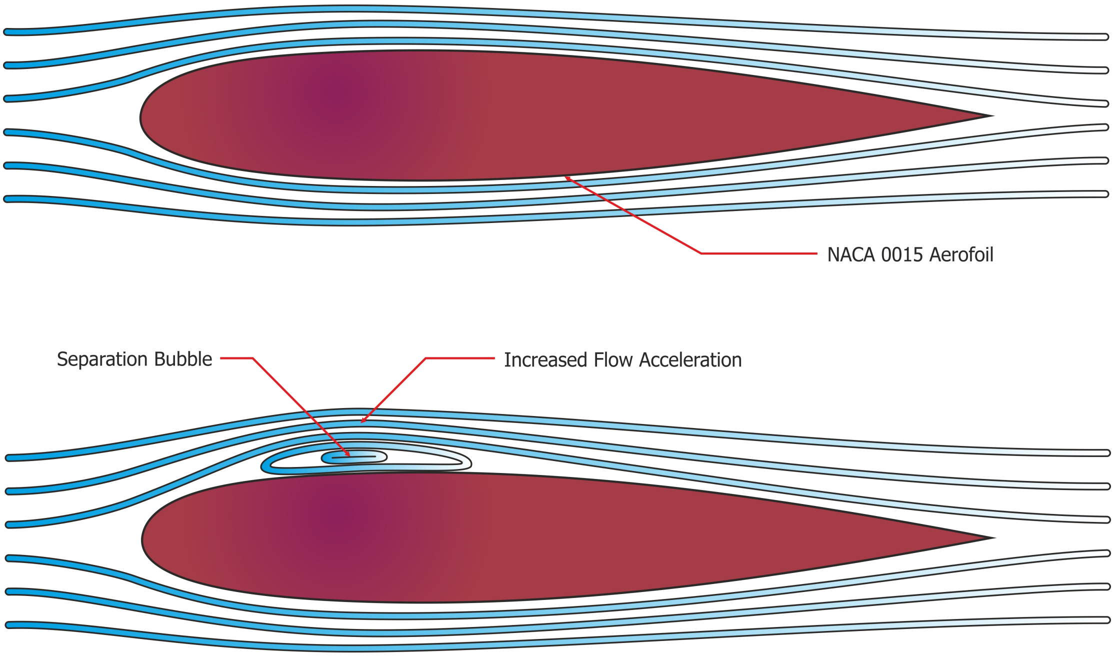

Figure 1.25 Aerofoil Virtual Shaping

1.2.5 Direct Thrust

Modern advances in electronic miniaturization have allowed the creation of nano-satellites. This classification is defined by a mass of between 1 and 10 kg [33], and as such the constraints on what control systems can be integrated are severe. In the survey conducted in

[33] only 1% of the satellites used a thruster system to stabilise themselves. However this is an area ideally suited to MEMS technology, to generate miniature space and weight efficient thrusters capable of producing the tiny forces required to stabilise such small satellites. Proper orbital stabilisation allows the satellite to maintain instrument and antenna alignment and allows for a larger range of mission objectives to be achieved with nano-satellites. Using a thruster system to achieve this rather than magnetic field or torque reaction methods allows the satellite to counteract orbital decay due to drag from the residual atmosphere still present in low earth orbit.

1.2.6 Active Vibration Control

1.2.6.1 Helicopter Vibration Suppression

Vibration active control uses arrays of actuators to damp out unwanted vibrations caused by aerodynamic transients and vortex shedding. Helicopters are susceptible to vibration not only from any imbalances in the rotating mass of the main rotor but also because the main rotor blades experience transient aeroelastic forces as they rotate [34]. The pressure distribution over the blade changes as it rotates and the local velocity along the blade varies due to the superposition of the forward velocity on the rotational velocity of the blade as discussed in [35] and illustrated in Figure 1.26. Flap hinges on the blades allow them to pitch up as they rotate. This reduces the severity of the pressure change by altering the incidence angle of the blade to compensate for the local velocity change and allows for stable flight [36]. However, it does not allow for the changes in the distribution of pressure along the length of the blade.

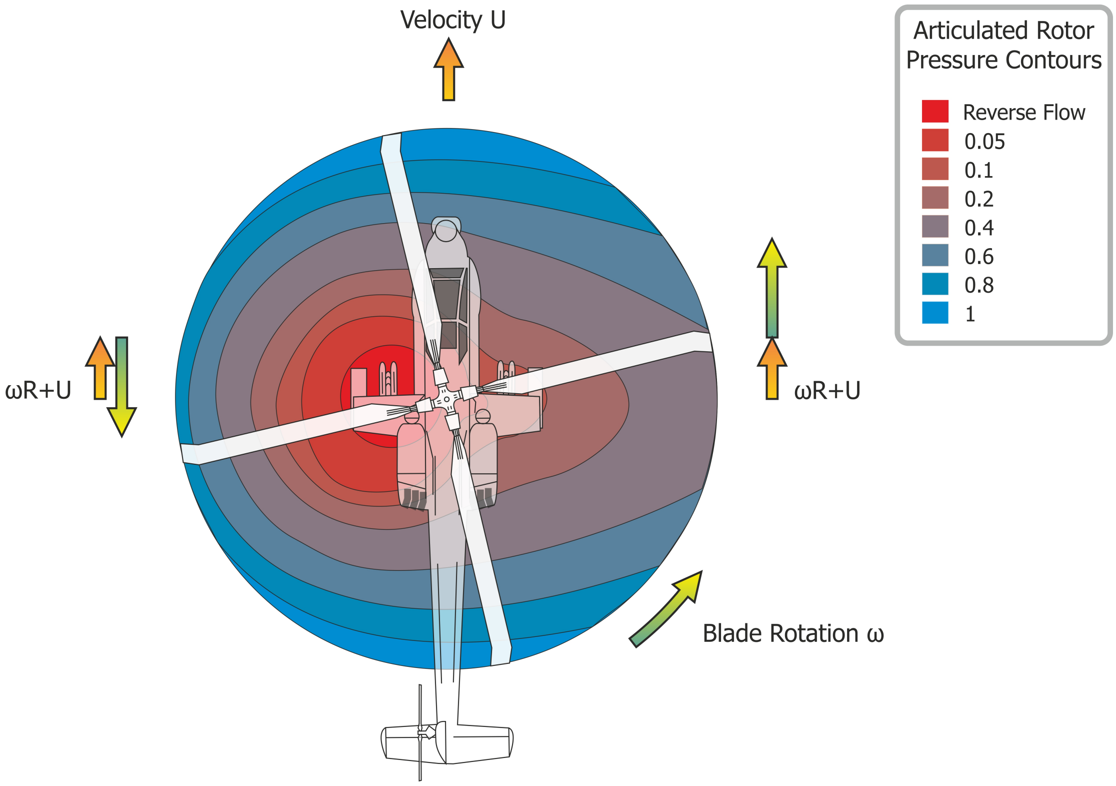

Figure 1.26 Pressure Contours On The Main Rotor Plane

The advance ratio for a helicopter is defined as $\frac{U}{\omega R}$ where U is the forward velocity of the helicopter in m.s^{-1}, ω is blade angular velocity in Rad.s^{-1} and R is blade length in m. As advance ratio increases, the transient deformation and loading changes on the rotor blades increases and this makes passive systems a poor solution as they cannot adapt to the changes in the loading conditions. To address this problem, [34] is a study of a 6 degree of freedom computer simulation of a helicopter with fully elastic and deformable rotors. This was used to optimize a system of 4 trailing edge flaps over the outer 20% of each rotor blade to reduce vibrational loading. In the report it is stated that the flap deflection angles required are achievable with directly acting piezoelectric actuators, and that at high advance ratios a vibration reduction of 72% is achievable.

1.2.6.2 Cavity Resonance Suppression

Vortex shedding and cavity resonance is important in a number of areas of both civilian and military applications. The most common example of where this impinges on everyday life is when a vehicle is driven with the sunroof open and an unpleasant buffeting sound can be generated at specific speeds. However, this also applies to other open cavities such as aircraft weapons bays [37] or landing gear wells where its effect can become quite destructive.

The problem is caused by the shedding of vortices from the leading edge of the cavity as the flow forms a shear layer between the stationary fluid inside the cavity and the high velocity fluid outside. The vortices are convected downstream, and when they impact the rear edge of the opening and break down an acoustic pressure wave is created (Figure 1.27) [38]. This sets up a positive feedback loop and is generally considered to form a Helmholtz resonator [39-42] from the car's interior volume. For a given geometry and ambient fluid the frequency of the vortex shedding is determined by fluid velocity. When the frequency of the vortex shedding and therefore acoustic excitation, hits the resonant frequency of the cavity air is driven in and out of the opening creating the buffeting [43].

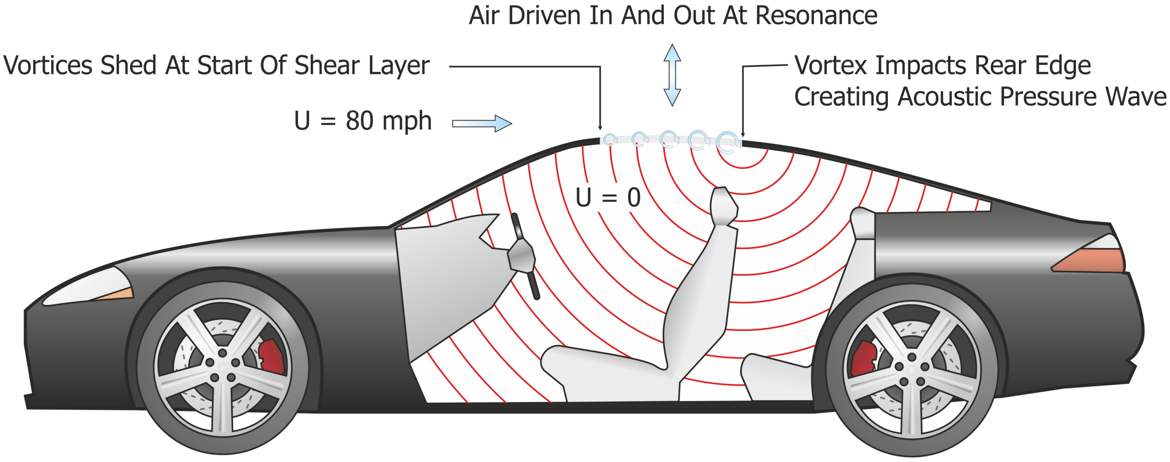

Figure 1.27 Sunroof Resonant Excitation

Work done at the NASA Glenn research centre [44] showed that the use of a fluidic oscillator at the upstream edge of a cavity exposed to various transonic and supersonic flows disrupted the vortex formation and successfully reduced the acoustic pressure in the cavity by an order of magnitude.

It is a possible that MEMS technology could be used to force the vortices to be shed at a much higher frequency than the resonant frequency of the system, thus avoiding the resonant response and subsequent buffeting that would normally occur.

1.2.7 Conclusions On Applications

Several possible applications for active flow control have been identified. These applications span military, civilian and scientific areas of interest. Many of them rely on controlling a flow separation either promoting or suppressing it, or on interfering with a system resonance, in this way they can provide a much larger global effect than the work that was done by the actuator. At the end of this chapter in section 1.5.2 the synergy between application and actuator will be discussed leading the way for the reasoning behind the eventual selection of the project scope from the applications discussed hereinbefore.

1.3 Active Flow Control Actuator Designs

This chapter details all the MEMS actuators considered at the start of the project, it should be noted that plasma actuators are discussed in depth in the next subsection (1.4), and as such comparisons and conclusions are left to the end of the chapter after all the data has been presented.

Micro electro-mechanical systems or MEMS actuators are devices which produce a movement or force as with any other actuator; however the features of their design and construction are on the µm–mm scale laterally and in the 10s of nm to 100s of µm range for their z axis dimensions. To do this, deposition and photolithographic patterning and etching techniques taken from integrated silicon chip manufacture are often required to overcome the difficulty of construction on such a small scale. Due to the small scale of MEMS actuators they are ideally suited for interacting with and modifying the boundary layers of flows.

Flow actuation using MEMS devices is achieved by one of three mechanisms; direct jet, synthetic jet or direct flow actuation. Each MEMS actuation technology has to be able to produce one of those to be effective in achieving flow control; by far the most common method used or to which existing technologies could be adapted to produce an actuation effect is the synthetic jet actuator (SJA). In a synthetic jet a net wall normal jet flow is synthesised from the ambient fluid rather than introducing new fluid into the flow domain as in a conventional jet. The formation of the jet has two phases; the ejection phase, where a diaphragm or piston which closes off a chamber below the jet orifice (Figure 1.28) is moved upwards, where the expulsion of fluid creates a strong stable vortex ring moving away from the orifice, and a fluid recovery phase, where the diaphragm moves down and refills the cavity with the ambient fluid, and where the fluid inflow is diffuse and slow compared to the expulsion, and leads to the net flow away from the wall [45] immediately above the orifice.

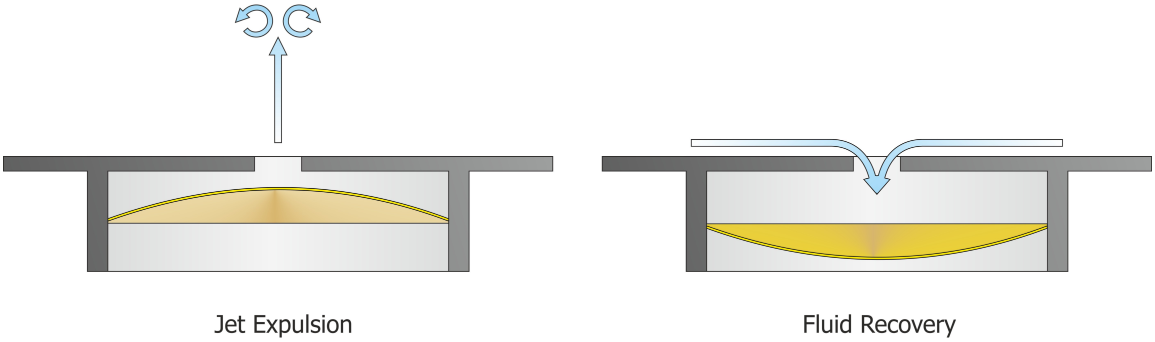

Figure 1.28 Generic Synthetic Jet Actuator

1.3.1 Electrostatic

Electrostatic actuators use a voltage differential to develop opposing charges between two surfaces. The coulomb force then moves one of the surfaces against the restraint of a flexible suspension towards the fixed surface.

Electrostatic actuators are one of the most technologically mature MEMS actuation methods, and are the basis for Texas Instruments digital micro mirror device or digital light processor (DLP) technology [46]. The electrostatically actuated mirror arrays were first invented in 1987, at which point they had a lifespan of 100 hours. Twenty five years of development and optimisation have resulted in a useful life in excess of 100,000 hours or 3 trillion mirror operations, exceeding the lifespan of competing non-MEMS based technologies [47].

Flat plate electrostatic actuators which offer piston like movement have also been developed. One of the more advanced designs is that developed by Qiao et. al. [48]. One of the fundamental disadvantages of the flat plate design is that, as the two plates approach, the force for a given applied voltage increases as: $F \propto Gap^{-2}$ [48]. This creates a point at which the increase in force from the closing of the gap can no longer be counter balanced by an increase in the force from the support structure deforming and the actuator ‘pulls in’ and will touch down on the base layer. The state of the art two beam support structure used in [48] is shown in Figure 1.29: it allows for the upper plate to move by up to 50% of its initial spacing before pull down occurs by increasing the stiffness of the suspension when part of the suspension arm touches down.

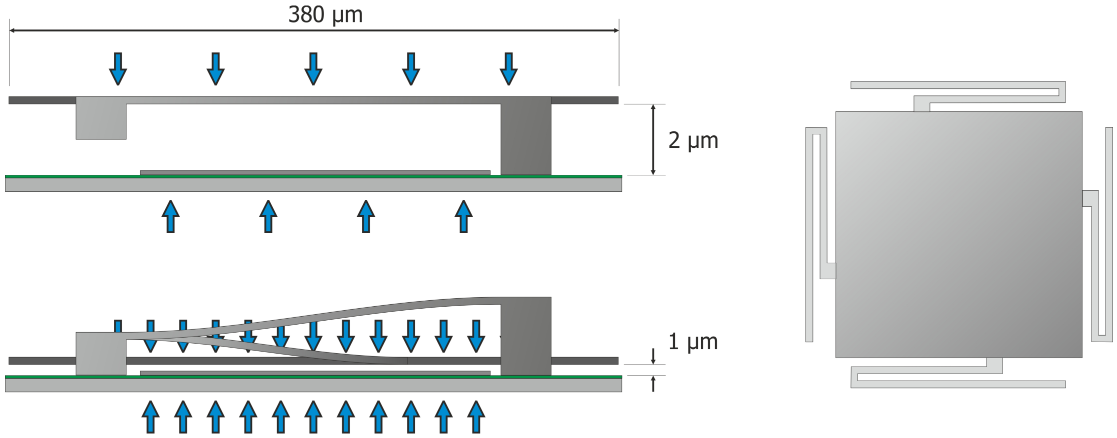

Figure 1.29 Electrostatic Actuator

Even with an advanced design like that shown in Figure 1.29 the actuation distance is only of the order of 1 µm with an actuation force of 40 µN (280 Pa over the surface area of the actuator). The primary design use for such actuators is in the optics industry to manipulate the phase of a light beam by moving mirrors through fractions of a wavelength, a task to which it is ideally suited with its rapid response time and dense packing structure. However the low force, displacement and the fragility of the structure render it less suitable for the creation of synthetic jets or direct flow actuation.

1.3.2 Electroactive Polymer (EAP) Actuators

1.3.2.1 Electrostrictive Patterned Electrode EAP

Electrostrictive polymer actuators use an electric field set up between two electrodes to compress a polymer membrane across its thickness. Due to the high Poisson’s ratio of the polymer used, this compression causes a significant radial expansion of the membrane. By pinning the membrane at its perimeter it is forced to buckle (Figure 1.30): the direction of buckling is determined by the relative stiffness of the two electrodes or any asymmetries in the system [49].

The key to improving the actuation characteristics of an EAP actuator is to improve the compliance of the electrodes as these, despite being only 170 nm thick, contribute most of the stiffness to the 35 µm skin [50]. To improve the compliance. the electrodes were etched in either a 4 armed spiral or as concentric rings each interconnected at a single point [49]. Through finite element analysis of the electrostatic fields and the stiffness of the membrane the design was optimised to give a deformation up to 10 times larger than that of an actuator with plain electrodes.

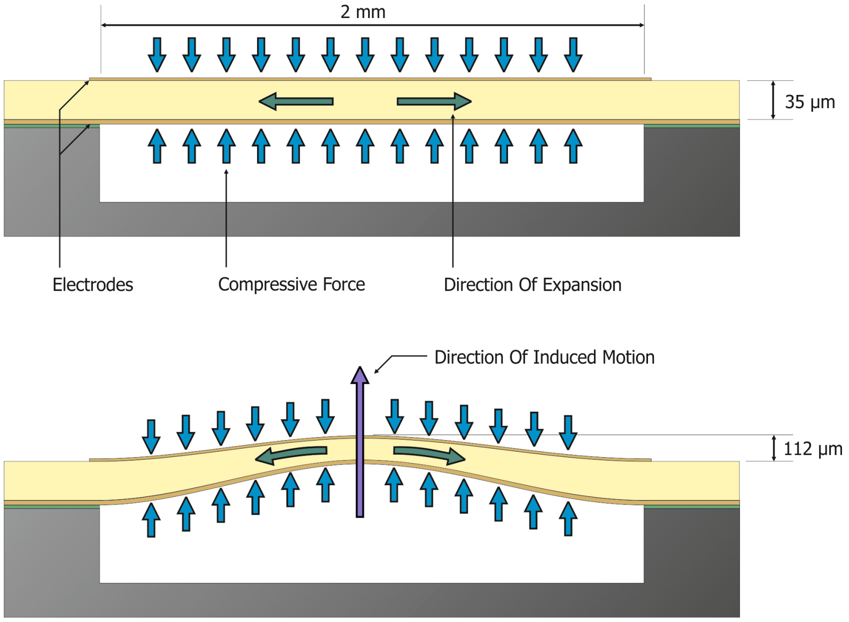

Figure 1.30 EAP Actuation

1.3.2.2 Electrostrictive Ion Implanted EAP

Dubois et. al. [50] worked on creating an electroactive polymer actuator which would overcome the difficulties in producing a sufficiently soft compliant electrode on the mm scale to allow deflections which were close to those seen in the macro scale EAP devices using conventional electrodes. By using metal ions implanted into the surface of the polymer skin to produce a conductive surface, they were able to replace the comparatively stiff patterned metal electrodes completely. Using these electrodes they were able to produce deflections of 13% of actuator diameter; this is of the same order of magnitude achieved in macro devices [50] and also significantly better than the 5.6% deformation ratio achieved by Pimpin et. al. [49] using a patterned electrode device.

1.3.2.3 Ionic Polymer Metal Composites (IPMC)

Ionic polymer metal composites use the motion of ions and solvent molecules within a gel to deform the gel membrane as shown in Figure 1.31 (based on [51]). The principal advantage of the IPMC actuator is its exceptionally low actuation voltage of around 1.5 – 4 volts. The disadvantage is the problem of solvent loss, e.g. Lee et. al. [52] were only able to achieve run times in air of 5-6 minutes despite trying various combinations of ions and solvents to maximise runtime, force and speed of actuation. Speed of actuation depends on ion mobility, with lighter ions like H^+ and Li^+ operating faster than heavier ions like Cu^{++}, but the range of operational speeds achieved spanned the range from 0.5 to 15 Hz, and as drive frequency increases the range of motion is decreased.

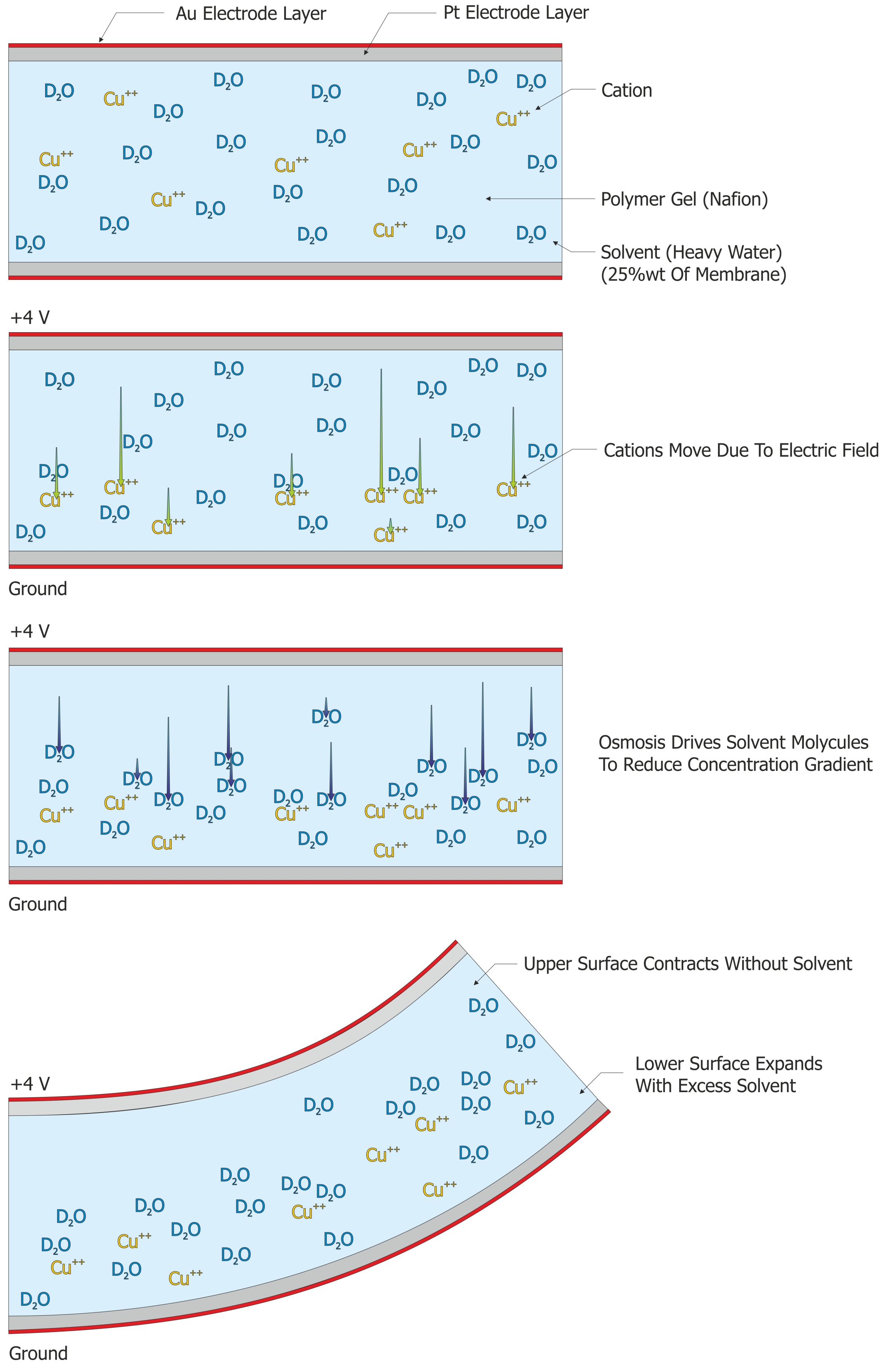

Figure 1.31 Ionic Polymer Metal Composite Actuator (Based On [51])

Shen & Tan [53] used MEMS patterning and dry etching techniques to produce an array of individual electrode pairs on a single gel membrane. In this way different parts of the membrane could be curved individually, and this allowed them to drive the compliant sheet as a biomimetic replica of a sunfish dorsal fin.

1.3.3 Piezoelectric

1.3.3.1 Piezoelectric Synthetic Jet

Lee at al [54] showed that piezoelecrically driven membranes could create synthetic jets of sufficient velocity to energise the boundary layer and delay separation under an adverse pressure gradient. Although their actuator was not manufactured using MEMS techniques (Figure 1.32), the overall dimensions would not preclude a MEMS based device on a similar scale. The advantages of this actuator are its relatively simple operation and low drive voltages of between 7.5 and 10 V.

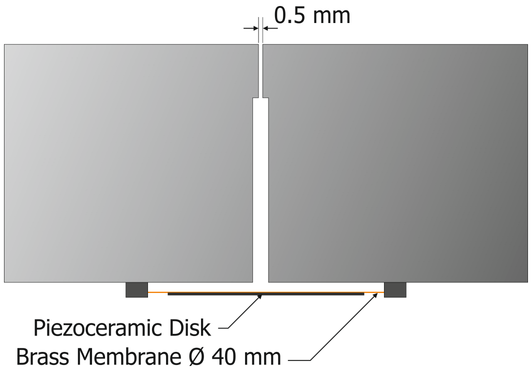

Figure 1.32 Resonant Disk Synthetic Jet

1.3.3.2 Resonant Beam Synthetic Jet

Another method which has been successfully demonstrated to produce fast controllable zero net mass flux jets of suitable magnitude for boundary layer control is the piezoelectric synthetic beam as used in [23] (Figure 1.33). By always driving the beam at its resonant frequency, a much larger deflection is obtained than would be achieved by driving the piezoceramic actuator in separate pulses in response to individual passing boundary layer events. Control is achieved by varying the amplitude of the drive voltage and therefore the amplitude of the resonant response. Although the device used in [23] was not manufactured using MEMS processes, it was pointed out in the conclusions that the topology of the device would lend itself to MEMS manufacture if the ruggedness of the process could be improved. Current MEMS piezoelectric cantilevers are commonly used as resonant mass balances, like those used in [55], but are much smaller than an aerodynamic device would need to be.

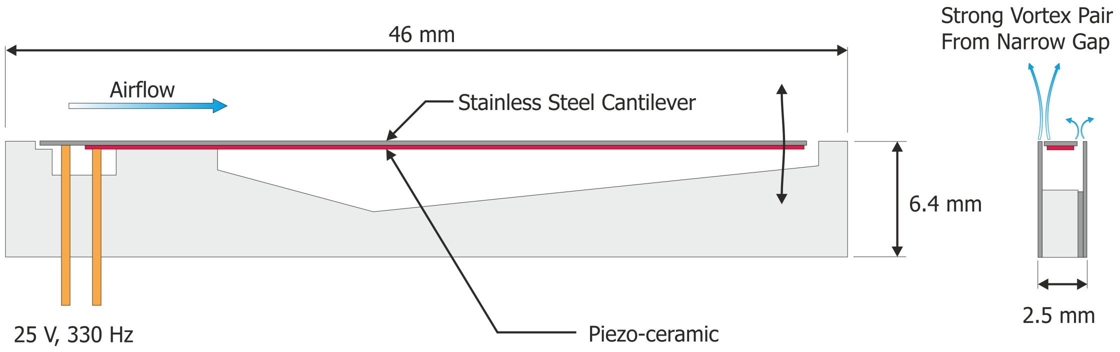

Figure 1.33 Macro Fabricated Resonant Beam [23]

1.3.3.3 Piezoelectric Valve

A piezoelectric bimorph valve utilises a piezoelectric cantilever structure to seal a micro-machined hole between a pressure cavity and the atmospheric airflow. Activation of the bimorph deflects the cantilever tip from the valve seat and an air jet is driven from the orifice in the device skin [56]. The structure of the device designed and tested at the BAE Systems Advanced Technology Centre and reported in [56] is shown in Figure 1.34.

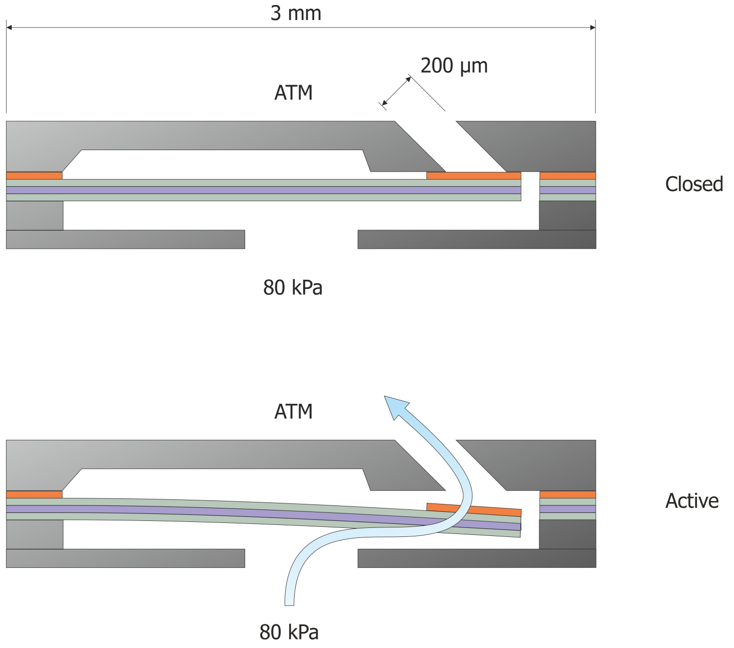

Figure 1.34 Piezoelectric Bimorph Valve

Because the device uses externally supplied pressurised air to create the jet, the velocity which is achievable is far greater than that from purely MEMS based systems, 300+ m/s for the device tested in [56] compared to 0.4 m/s for the MEMS based patterned electrode electroactive polymer device of a similar scale manufactured in [49]. This increased jet speed of the bimorph valve means that this technology can be used to influence higher speed flows.

1.3.3.4 Piezoelectric Vane

Rabinovitch & Vinson [57] numerically modelled and optimised a centimetre scale fin structure shown in Figure 1.35. The fins were actuated using the differential deflection of a pair of piezoelectric bimorphs, and were designed to provide sufficient torque and rotation to operate on a small scale aerial vehicle at flight speed.

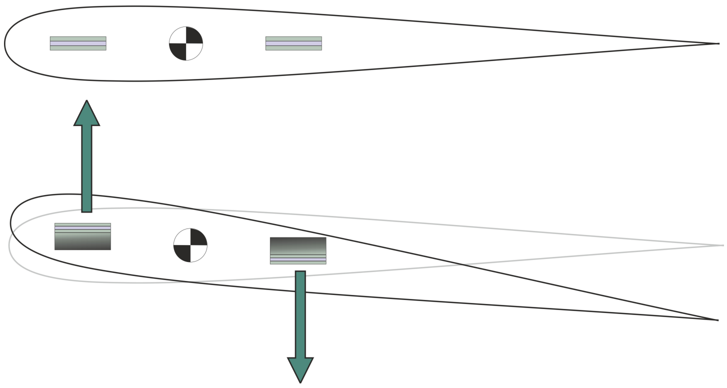

Figure 1.35 Fin Profile and Beams End On

Barrett & Vos [58] used a similar scheme but with a single longitudinally aligned piezoelectric bimorph strip positioned behind the fulcrum. They demonstrated a 4 fold improvement in the tip deflection of the cantilever by applying an elastic precompression force to the end (Figure 1.36). With this actuator they were able to achieve an aerofoil pitch control of ±22^{o} in speeds of up to 61.7 m.s^{-1}.

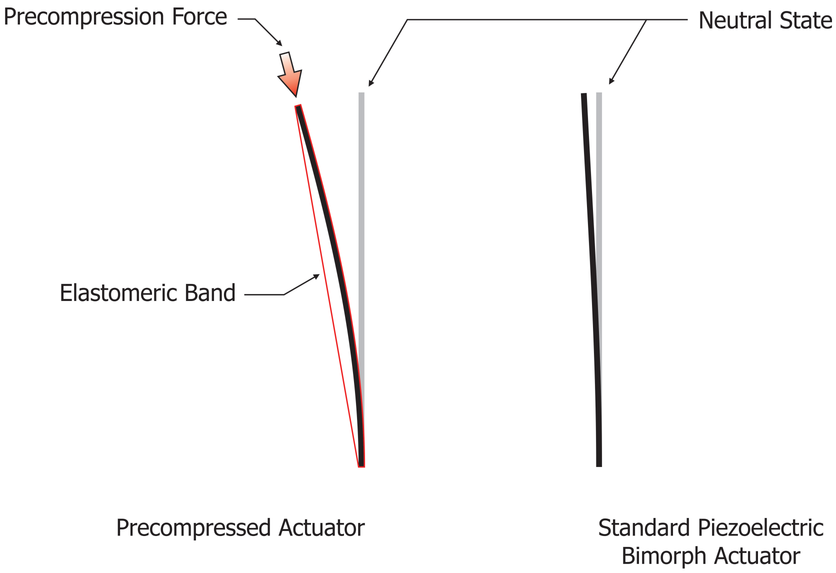

Figure 1.36 Precompressed Piezoelectric Bimoroph Actuator

1.3.4 Chemical MEMS Actuators

MEMS technology can be used in the construction of chemical micro-thruster arrays [59]. Small single shot solid propellant rocket assemblies can be manufactured as shown in Figure 1.37. The real benefit of manufacturing these using MEMS technology is the parallelisation of the process, where grid arrays of potentially hundreds of individual single use nozzle-ignitor-propellant assemblies can be manufactured with little more effort than a single unit. This implementation of 100's of individual units, enough to last the projected lifetime of the spacecraft, allows for the use of low complexity solid propellant technology where normally a much more complex hypergolic or monopropellant system able to start, stop and restart on demand would need to be used.

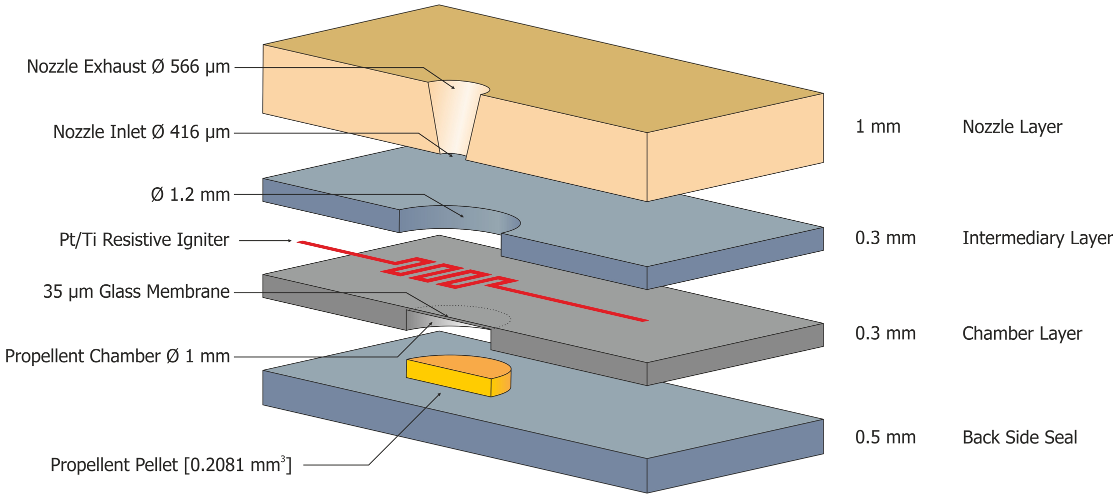

Figure 1.37 Solid Propellant Micro-thruster Cross-section

1.3.5 Passive MEMS Actuators

Cold gas satellite microthrusters detailed in [60] show innovative use of MEMS techniques to produce a heat exchanger and de Laval nozzle with structures on a scale that simply could not be manufactured through conventional machining (see Figure 1.38). The inclusion of the heat exchanger structure and platinum thin film resistor to pre heat the gas allows a more aggressive expansion ratio to be achieved in the nozzle. Increasing the expansion ratio whilst maintaining sonic conditions at the throat allows for higher exit velocities; this gives higher specific impulse values. The small scale of the micromachined nozzles allows for a set of 4 arranged to provide control in the X-Y plane to be produced within a 40 mm diameter silicon wafer.

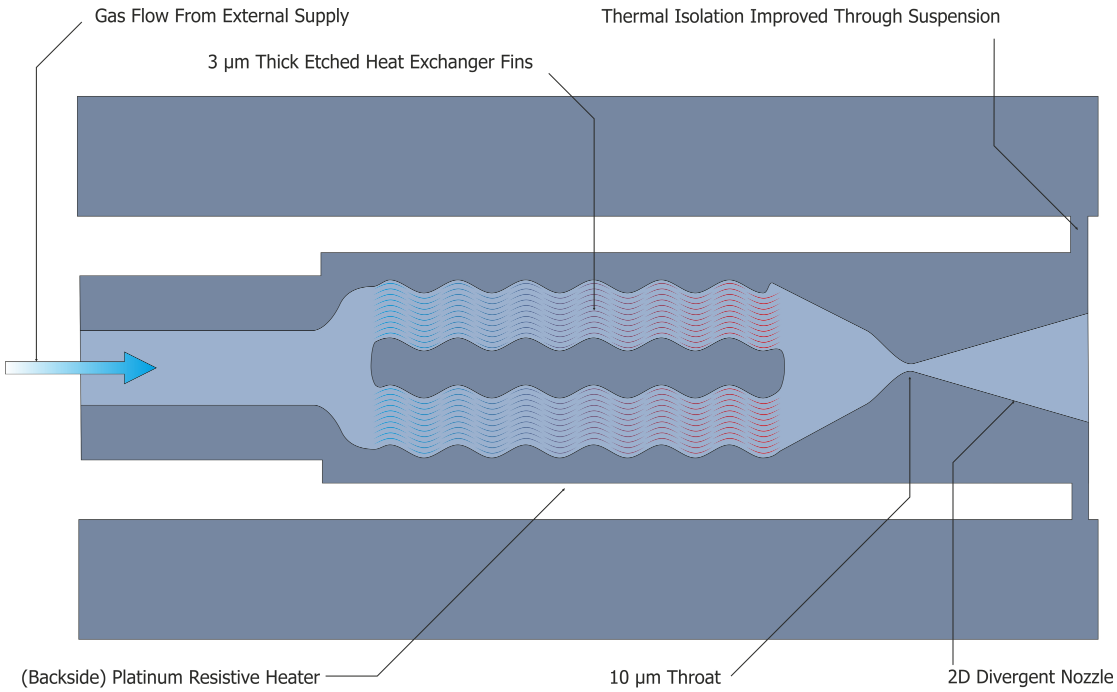

Figure 1.38 Micromachined Nozzle For Cold Gas Thruster

1.3.6 Thermal

1.3.6.1 Thermal Pneumatic Diaphragm

Thermal pneumatic actuators use a small heating element deposited onto a substrate which forms the bottom of a cavity. The top of the cavity is sealed using a flexible polymer membrane. Heating the air in the cavity causes it to expand and deform the flexible membrane. This type of actuator was used in [61] to produce micromirror arrays. Their results showed that the technology was capable of producing out of plane deformations an order of magnitude larger than electrostatic technologies, at 80 µm or 4% of its cavity diameter. However, the actuation frequency they achieved of 0.1 Hz precludes this technology in its current state from any active aerodynamic flow control applications. It may be possible to improve the response of the actuator by replacing the working fluid with an organic compound chosen to have its boiling point just above ambient, so that the actuator functions in a similar way to Expancel® thermally expandable microspheres [62].

1.3.6.2 Thermal Phase Change

Figure 1.39 details a MEMS valve system machined from silicon wafers using deep reactive ion etching (DRIE) and fusion bonded together [63]. The system works by using a resistive heater to melt the paraffin contained in a cavity which then expands. This expansion then distorts a corrugated diaphragm until it seals against a pair of valve seats. Because this system relies on heating and cooling of a non-trivial thermal mass the response time is in the order of a few seconds, insufficient for boundary layer control but is sufficient to provide a valve system for a satellite thruster system similar to that detailed in section 1.3.5.

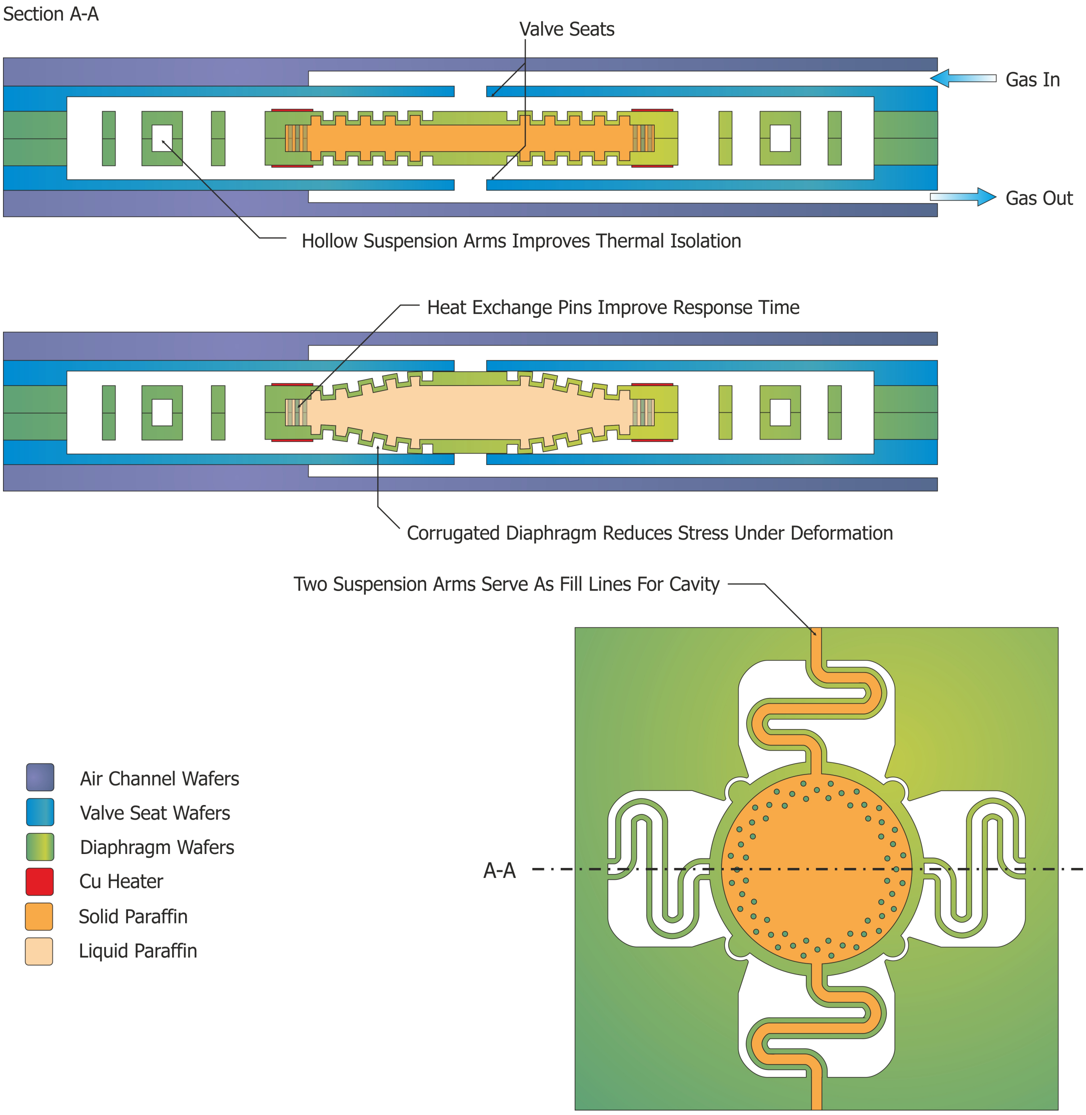

Figure 1.39 Phase Change Driven Gas Valve

1.3.6.3 Thermal Bimorph

Thermal bimorph actuators use the differential expansion of two beams, one of which is heated by a resistive element. Figure 1.40 shows a novel design used in [64] which eliminates the parasitic heating of the cold arm which is usually used as the return path for the current and thus experiences Joule heating reducing the differential expansion. With this actuator design they were able to achieve a linear deflection of 260 μm which corresponds to an angular deflection of 4.1°. One of the great advantages of this technology is that it provides actuation at a much lower voltage than electrostatic or piezoelectric based devices;

for example maximal deflection of the thermal beam was achieved at 2 V compared to 2 kV for electrostrictive EAP actuator designs [49]

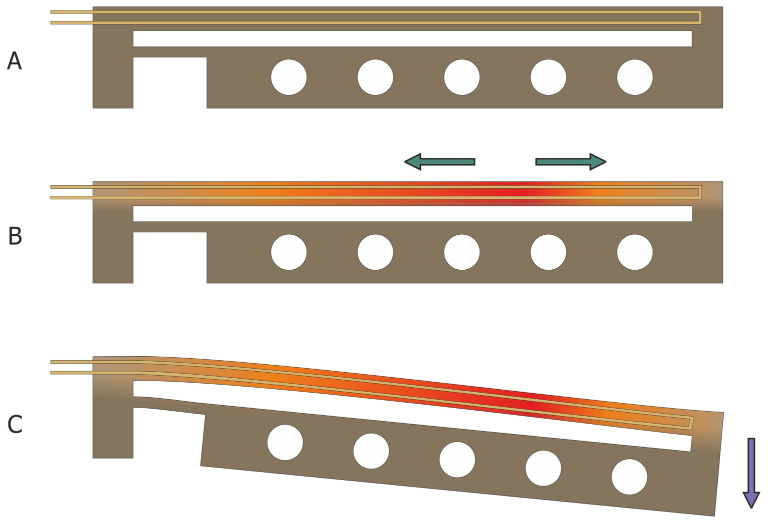

A) Thermal bimorph at rest

B) Heating element heats one arm of the beam,

C) Thermal expansion of top beam deflects the bimorph down.

Figure 1.40 Thermal Bimorph Stages Of Operation

1.3.6.4 Thermal Buckling Beam

Thermal beam actuators are activated by passing a current through a thin beam between two supports. This heats the beam causing it to expand significantly in the lengthwise direction and, as the beam is pinned at both ends, to buckle as shown in Figure 1.41. Vertical deflections for both metal and polysilicon beams are around 2% of their length [65]. Directionality of the buckle is determined by asymmetries in the beam design or stresses induced in manufacture.

The advantage of the thermal beam actuator is its high force output when compared to some actuation technologies; at 20 mN of actuation force the thermal beam actuators shown in [65] are 500 times more forceful than the electrostatic actuators in [48]. Due to the low thermal mass of actuators they are also not particularly hindered with regards to actuation frequency either, being able to operate at up to 4 kHz dependent on the length of the actuator beam. [65]

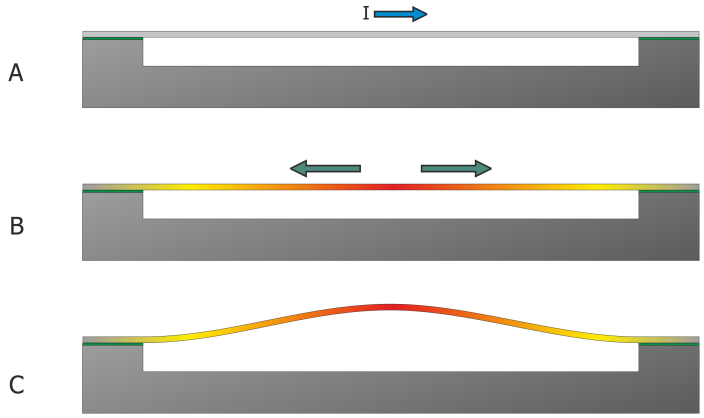

A) Current passed through beam,

B) Beam expands,

C) Beam buckles.

Figure 1.41 Thermal Bucking Beam Stages Of Operation

Cao et. al. [65] demonstrated a technique for establishing directional control of the buckling process. By creating a large magnetic field parallel to the direction of the beams deflection, a Lorentz force is applied to the beam when the heating current is being passed. By changing the direction the current was passed through the beam the direction of the force shown in Figure 1.42 could also be changed. Although the force is not parallel to the direction of displacement of the beam it is sufficient to cause a perturbation in the initial conditions which determined the direction of buckling when the beam expanded.

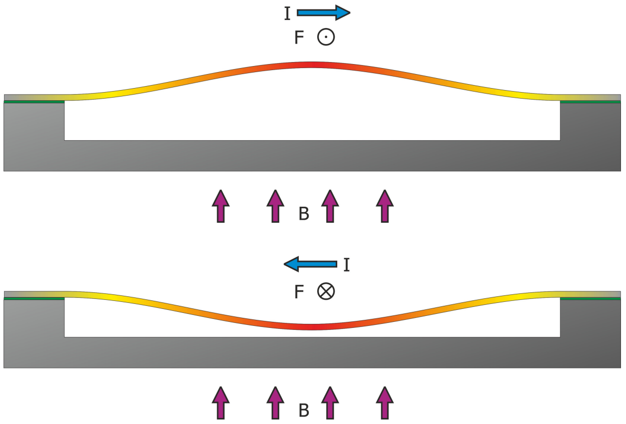

Figure 1.42 Directional Thermal Beam

1.3.6.5 Shape Memory Alloy (SMA) Vane

The shape memory alloy missile actuator described in [66] and shown in Figure 1.43, only displaced by 1 mm into the airflow: however it was able to produce "useful side forces" on the supersonic missile body test section they were using, by triggering vortices to grow more rapidly on one side than the other. It is possible that a similar control strategy could be implemented using MEMS technology if a sufficiently forceful actuator could be developed.

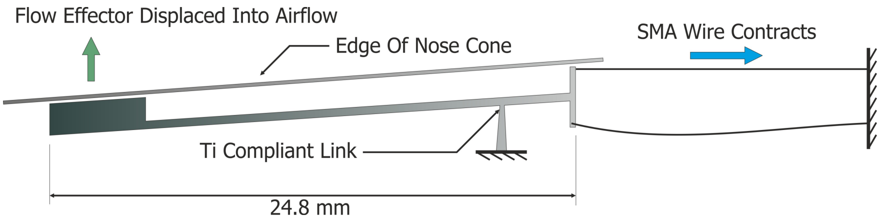

Figure 1.43 SMA Missile Vectoring System

1.3.7 Electromagnetic Actuators

1.3.7.1 Ferromagnetic Actuator

The use of an externally applied magnetic field to act upon a permanent magnet flap was used in [67] to create micromirrors for holographic storage. Shown in Figure 1.44 is a 'type 1' device; a variation in the angle of deflection of the mirrored flap was achieved by varying the external field strength. As the external field strength is changed the force exerted on the permanent magnet deposited on the back of the mirror is changed, altering the mirrors deflection.

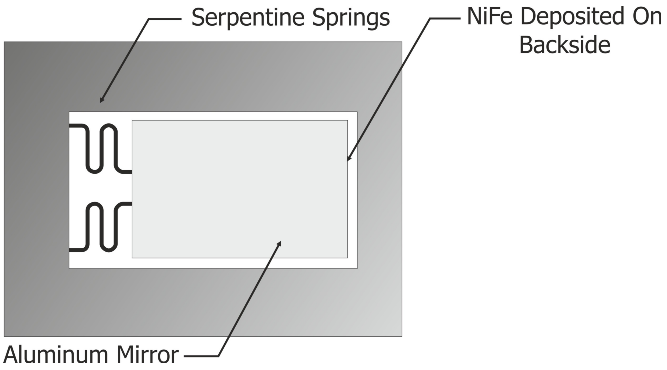

Figure 1.44 Permalloy Actuator

1.3.7.2 MEMS Electromagnetic Actuator

This is an adaptation of the ferromagnetic actuator shown previously, manufactured by the same team using etched silicon and a NiFe permalloy layer detailed again in [67]. However, it also contains a planar copper coil photolithographically etched onto the surface of the actuator (Figure 1.45). As with the plain permalloy actuator the coarse deflection adjustment is provided by varying the externally applied magnetic field. However, fine adjustments can be made by applying a current to the coil, which also allows the individual adjustment of different elements in an array of actuators which are subject to the same externally applied field.

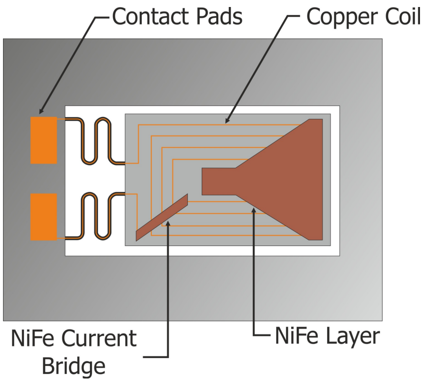

Figure 1.45 Permalloy and Electromagnetic Actuator

1.3.8 Pneumatic

1.3.8.1 Pneumatic Microvalve

By using externally applied control signals in the form of air pressure applied to a tapping point on their device, [68] showed a grid of synthetic jets which could each individually be turned on or off. The air pressure signal was used to deflect a polymer membrane to seal the synthetic jet orifice. This prevented pulsed air, driven by an audio speaker into a common cavity, from forming a synthetic jet at that location (Figure 1.46).

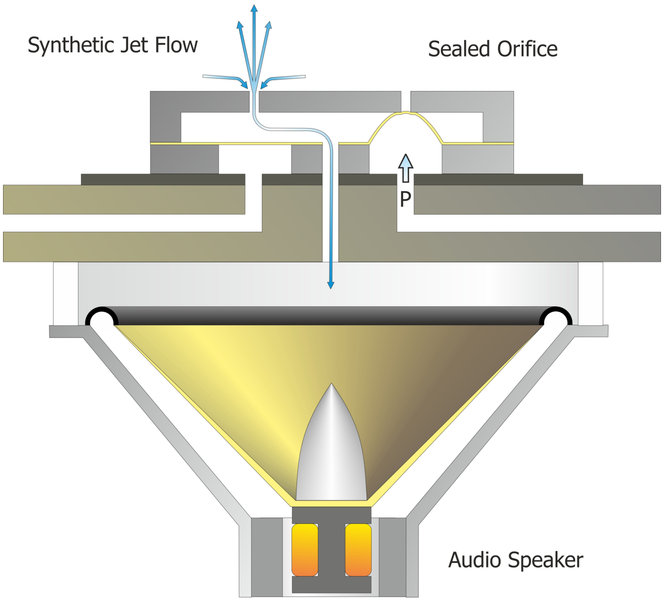

Figure 1.46 Pneumatic Microvalve

Unfortunately, although MEMS techniques were used in the manufacture of the orifice array and cavity, all the control was still supplied by externally operated pneumatic valves much larger than the actual array and driven using the loudspeaker cone. This defeats the object of using MEMS for flow control on any vehicle where the weight and space penalty would be excessive.

1.3.8.2 Pneumatic Micro balloon

Micro balloon actuators demonstrated in [69] were created using a variety of photolithographic patterning and etching techniques to produce robust actuators capable of producing a deflection of around 1 mm under the action of a low pressure pneumatic input signal driven from a central compressed air supply and conventional macro scale valves (Figure 1.47). The use of parallel construction techniques allows for the easy creation of arrays of potentially thousands of actuators: wind tunnel tests showed the suitability of the actuator for flight control and transonic flight tests on an F-16 showed the actuator was sufficiently rugged to survive the temperatures and forces associated with high speed flight.

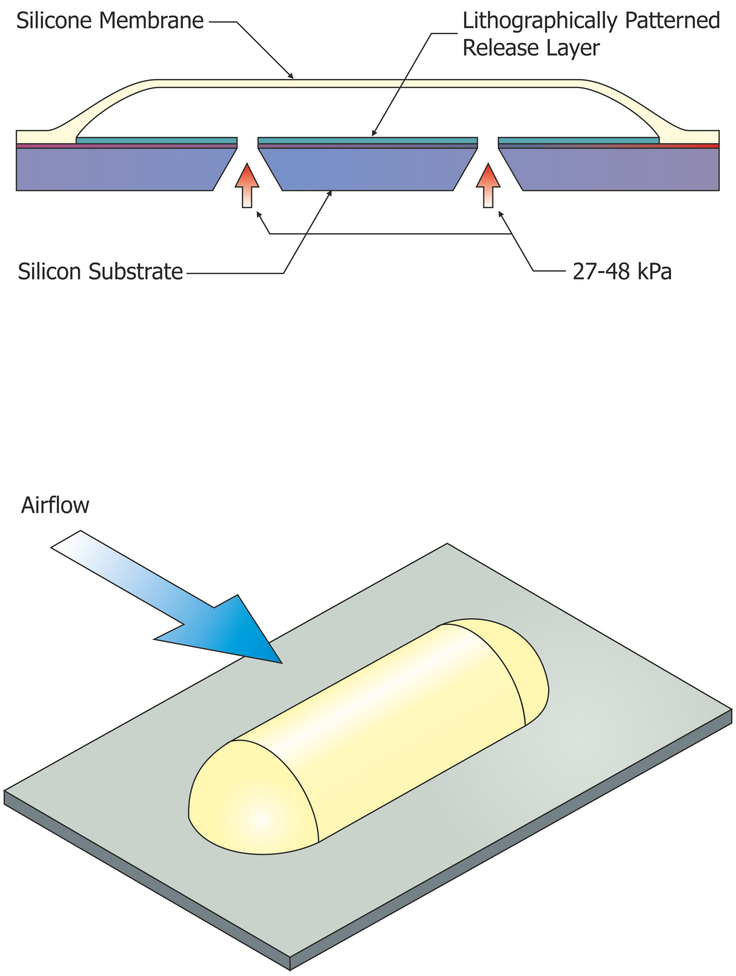

Figure 1.47 Micro Balloon Actuator

1.3.9 Summary Of MEMS Actuator Designs

The actuators that have been shown in this section can mostly be divided into three groups, synthetic jets, real jets (or more specifically micro machined valves to control real jets) and surface deformations to directly impinge on the flow. The majority of these designs are extremely complex to manufacture. All three modes of operation are well documented in their effect on boundary layers and flow control, even if the method of generating the jet or deformation differs the results and simulations are largely similar. An overview and comparison of the MEMS technologies shown here along with plasma actuators, which will be covered in the next section, is included at the end of this chapter.

1.4 Plasma Actuators

1.4.1 Operation Of The Single Dielectric Barrier Discharge

The most common form of electroaerodynamic plasma actuator is the single dielectric barrier discharge (DBD). Consisting of a pair of asymmetric electrodes separated by a dielectric and driven by an AC high voltage as shown in Figure 1.48, the DBD actuator has been under study since the late 1990's [70]. Actuators in the literature have been produced with a wide range of sizes and construction materials. Electrode widths vary from 1 mm and 2 mm for the upper and lower electrodes respectively [71] to widths of 50 mm [72]. The choice of dielectric is even more diverse, ranging from Kapton® polyimide film of 100 μm [73-74] to poly(methyl methacrylate) 36 mm thick [75] but more usually 2 – 5 mm thick [72, 76-77] . Other materials used in the construction of actuators include; GRP circuit board [71], Macor® machineable ceramic [78], poly(vinyl chloride) [77] and glass [79].

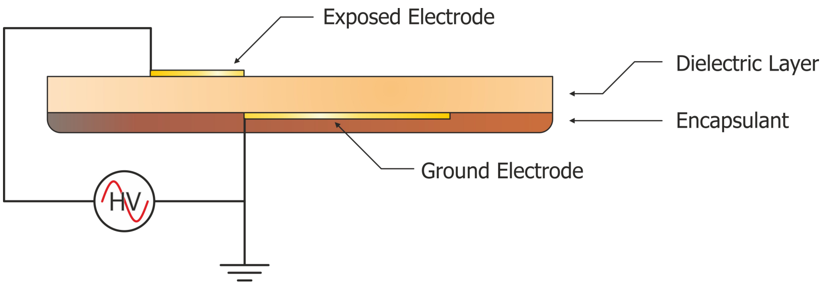

Figure 1.48 DBD Actuator Topology

When energised with a high voltage AC power supply, usually in the range 4-20 kV at around 1 kHz (see Figure 1.49), a DBD actuator produces an ionic wind streaming away from the edge of the exposed electrode in the direction of the ground electrode. PIV investigations in quiescent air such as [80] show that the air is drawn in from above the actuator and accelerated downstream as indicated by the blue arrow in Figure 1.50 [81]. Although some groups are looking at nanosecond pulses superimposed on a DC bias [73] or sawtooth [82] waveforms to maximise actuator output, the vast majority of DBD actuators are driven with a sinusoidal signal: all the following data refer to such devices.

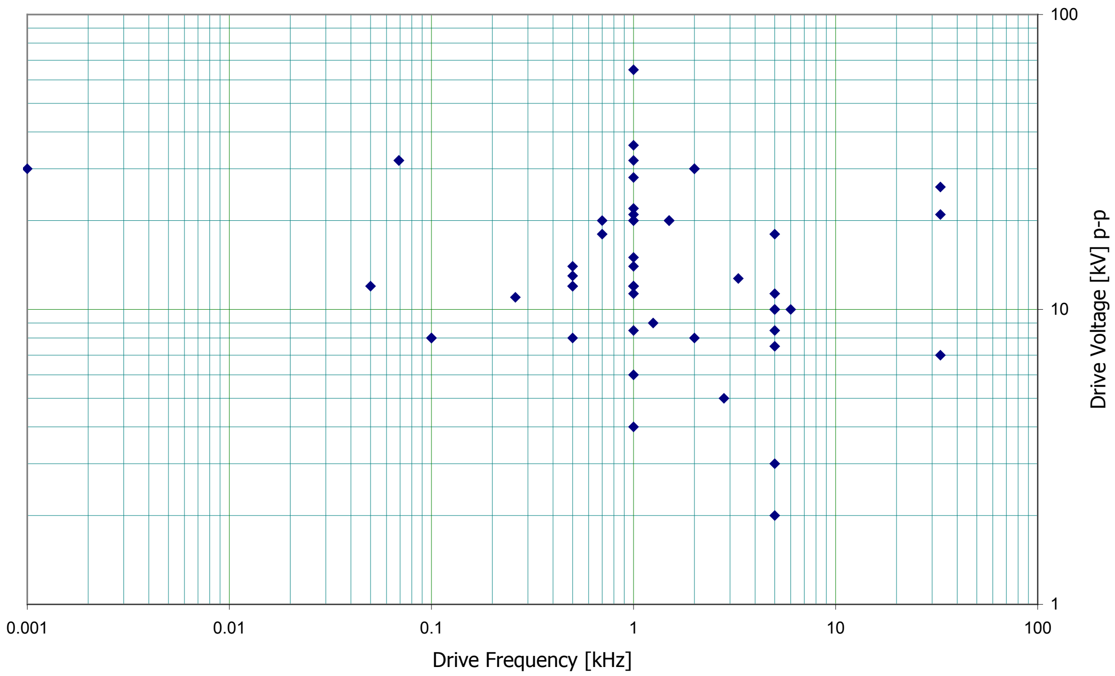

Figure 1.49 Drive Voltage And Frequency In Literature

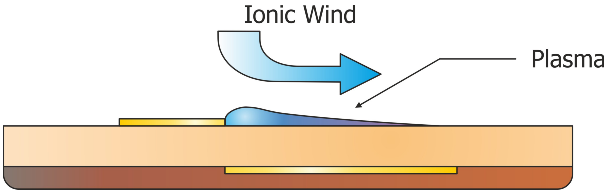

Figure 1.50 Ionic Wind Direction

It has been shown in the results of acoustic [83], current – voltage [84] and photomultiplier tube measurements [85] that the plasma ignites and quenches twice per voltage cycle. These two active periods are referred to as the forward and backward strokes, see Figure 1.51. In the forward stroke, when the voltage is negative going, electrons are emitted from the surface of the exposed electrode in a diffuse discharge and stored on the dielectric. In the backward stroke cathode directed streamer discharges return the stored charge to the exposed electrode. Figure 1.52 shows the electron motion: it is important to note electron flow is not the same as the plasma propagation during the cycle.

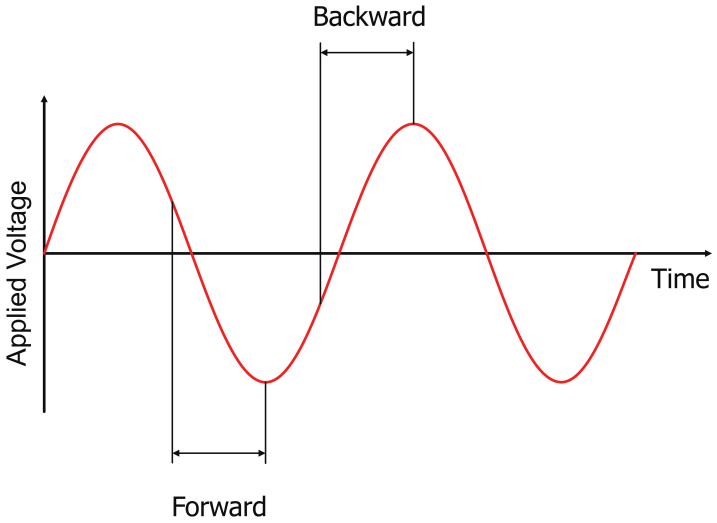

Figure 1.51 Plasma Ignition Points On AC Cycle

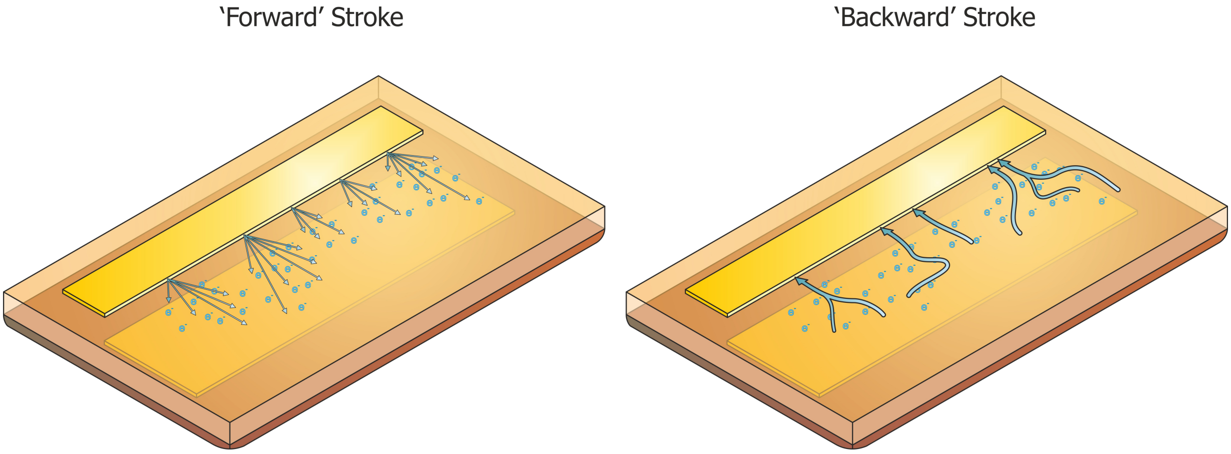

Figure 1.52 Comparison Of The Forward And Backward Stroke

The asymmetry between the forward and backwards strokes can be seen in Figure 1.53 which shows the voltage current traces of a DBD. The current trace has had the reactive component from charging and discharging the capacitive element of the actuator subtracted to highlight only the current spikes attributable to the microdischarge events. The spikes of the forward discharge are much smaller in magnitude than those of the backward discharge. This is consistent with a diffuse discharge on the forward stroke and streamer discharge mode of actuation on the reverse stroke as laid out in Figure 1.52.

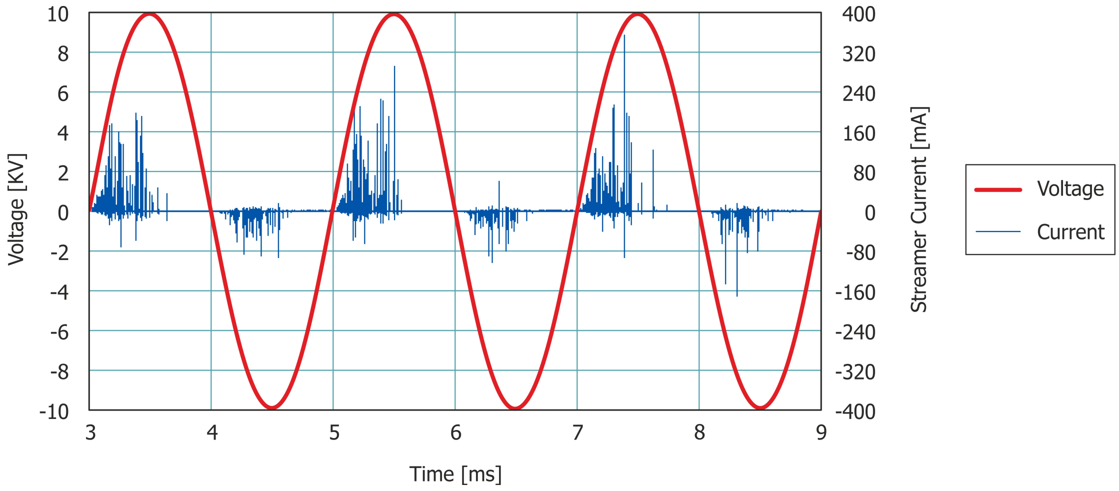

Figure 1.53 Voltage - Current Characteristic (Replotted Based On [84])

Data from a photomultiplier tube (PMT) synchronised with current measurements shown in Figure 1.54 again show the difference in the two half cycles, the large current spikes on the backward discharge (0.02 – 0.15 ms) can clearly be seen as individual events registered on the PMT output. However in contrast the forward stroke (0.22 – 0.35 ms) shows a much more uniform output, and individual discharge events can no longer be seen as they all amalgamate into one. Importantly this graph shows that although the current trace for the backwards stroke looks much more intense, the PMT data which is registering photons emitted during recombination and de-excitation of species in the plasma shows that there is no major disparity in ion generation.

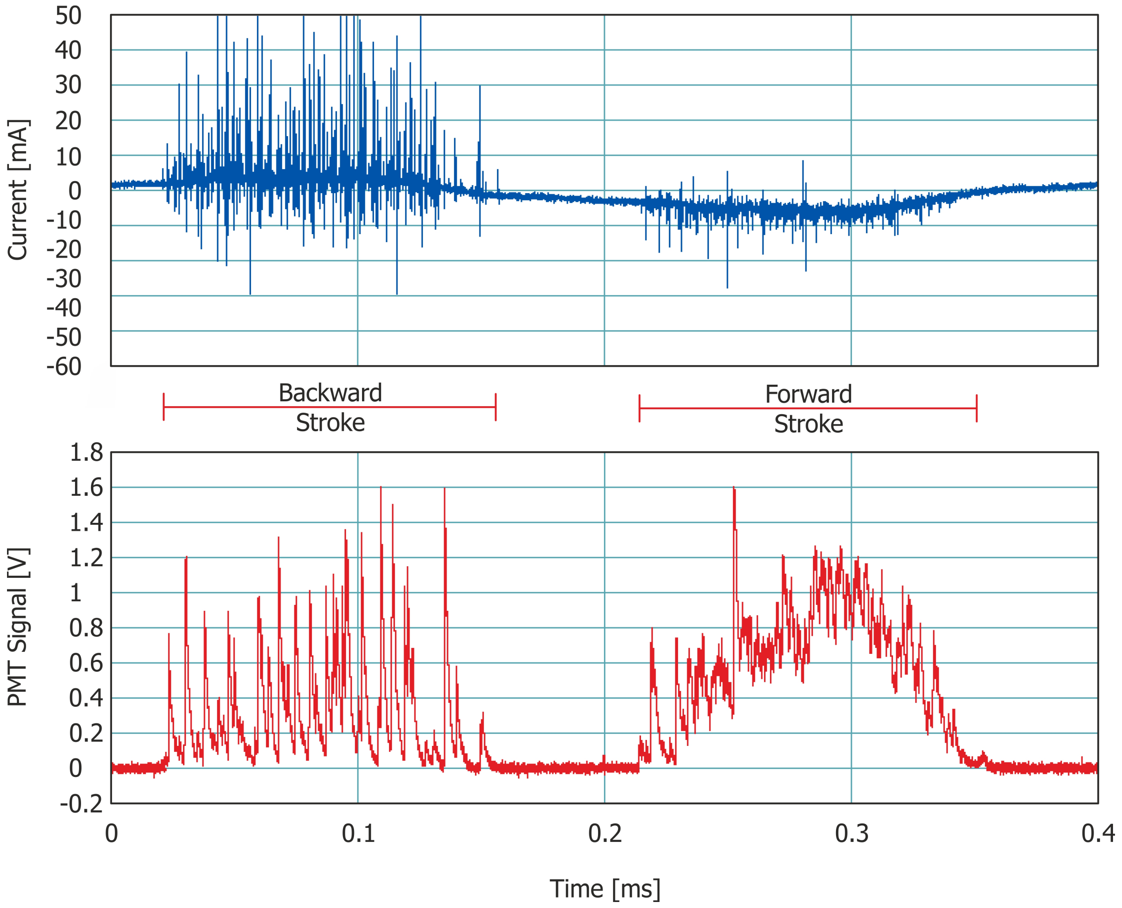

Figure 1.54 PMT - Current Data (Replotted Based On [86])

The following series of figures, Figure 1.55 through Figure 1.63 shows the stages of the plasma discharge in a DBD under sinusoidal excitation. This explanation was assembled by the author specifically for this review from various sources found in the literature. At the time of writing contradicting views on many aspects of the DBD formation are still to be found from academic sources, where this happened priority was given to those backed up by the clearest experimental observations. The Roman numeral tags in the image refer to the chronological sequence of events described in the text below. Starting from the end of the last backwards stroke just before the forward stroke cycle begins again.

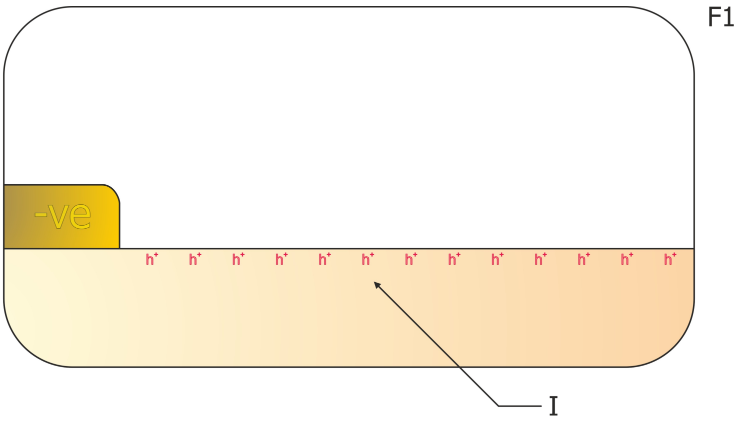

Figure 1.55 F1 – Forward stroke pre ignition condition

I It was shown in [87] through the use of v dot probe measurements of the surface charge on the dielectric that there was a significant positive DC bias on the surface of several kV over the operating cycle of the actuator. It has not been shown yet whether this is from ion implantation or electron holes on the dielectric surface, however they are arbitrarily shown here as electron holes.

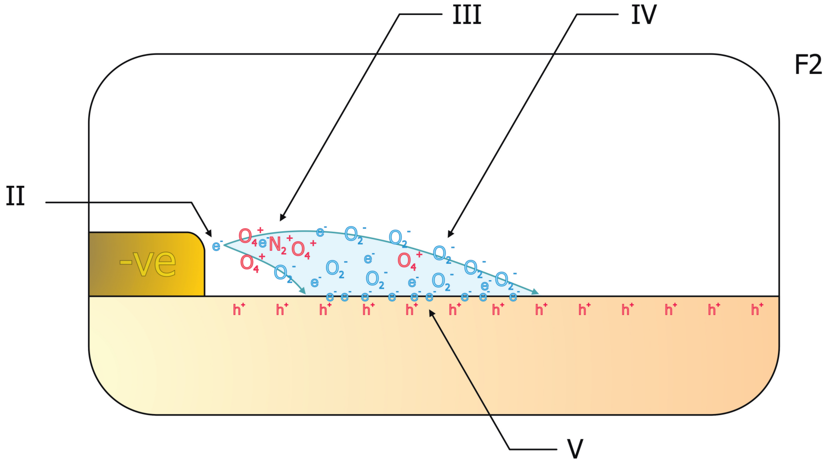

Figure 1.56 F2 – First forward micro discharge

II Free electrons generated by field emission from the electrode or background radiation are accelerated by the influence of the electric field away from the electrode edge towards the dielectric.

III High energy electrons generated in the intense electric field around the electrode tip impact neutral oxygen and nitrogen molecules, supplying sufficient energy to ionise the molecule and liberate further free electrons into an electron avalanche [88]. The diffuse discharge this creates has been shown experimentally through the use of short exposure images from intensified CCD cameras in [69, 79-80].

IV Further out from the electrode the electric field is weaker and therefore the probability of electron impact ionisation is reduced, where electrons drifting out of the ionisation zone towards the dielectric now undergo attachment to the oxygen [89-90] leading to the build up of a negative space charge.

V Electrons flow from the exposed electrode, and negative charge builds up on the dielectric surface until the voltage potential between the surface and the electrode is insufficient to support further ionisation at which point the micro discharge quenches.

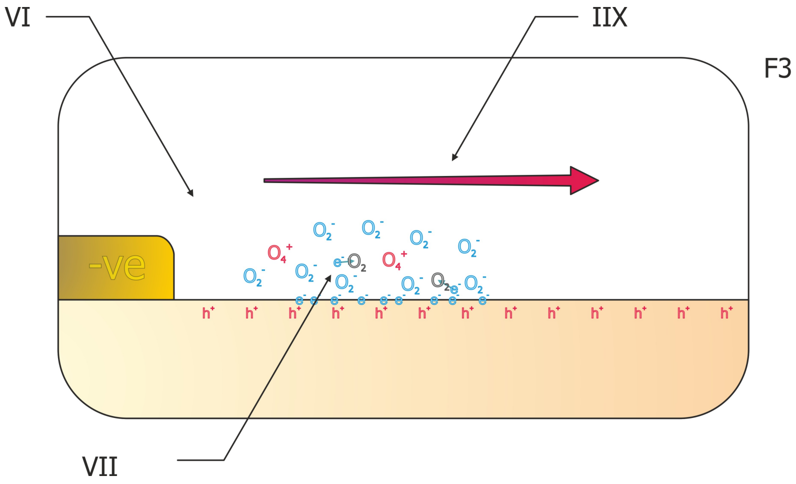

Figure 1.57 F3 – First micro discharge relaxation

VI Electrons and positive ions from the first micro discharge recombine almost instantly within a few nanoseconds, leaving a small amount of ion-ion plasma behind which persists for a couple of microseconds [73].

VII After the positive ion density drops by a factor of 10, free electrons couple to oxygen molecules to form further negative ions.

IIX Under the influence of the electric field the negative ions drift away from the surface electrode. Ionisation levels are so low (order 1ppm [91]) that it can be considered that all the momentum gained is coupled to the surrounding neutral species through ion-neutral collisions.

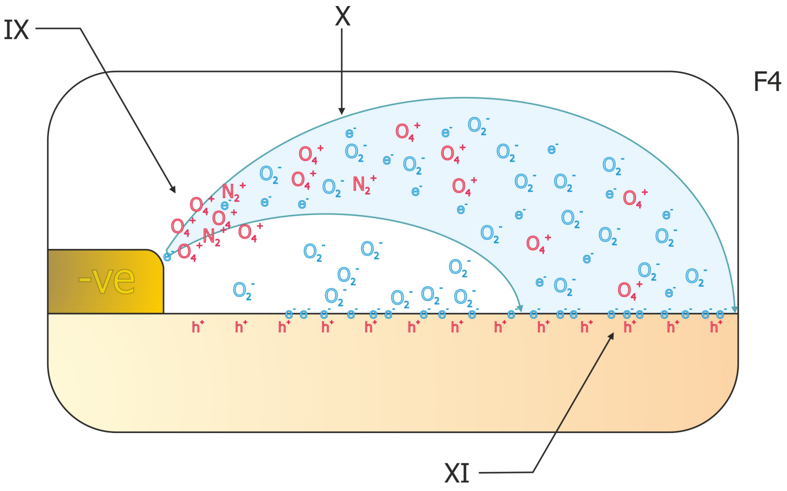

Figure 1.58 F4 – Second forward micro discharge

IX As the applied voltage continues to increase, eventually the electrode-surface electric field increases to the point at which a second micro discharge is initiated, again through an electron avalanche started at the tip of the exposed electrode. Unlike the streamer discharge present in the reverse half cycle (which is shown starting in the next figure (Figure 1.59)), ionisation always occurs in the area closest to the electrode tip as the plasma sheet moves downstream. This has been shown in simulations in [90, 92] and demonstrated experimentally in [88] by using cross correlation spectroscopy to plot the temporally resolved rate of photon emission by de-exciting nitrogen molecules in a single discharge.

X Surface charging from the first micro discharge changes the shape of the accelerating electric field, directing the plasma formation away form the surface of the dielectric. This leapfrogging nature is supported by the time resolved surface charge data from [87].

XI Again electrons flow onto the dielectric surface until the plasma self-extinguishes.

These micro-discharges repeat as the drive voltage continues to drop until the end of the forward stroke of the discharge cycle.

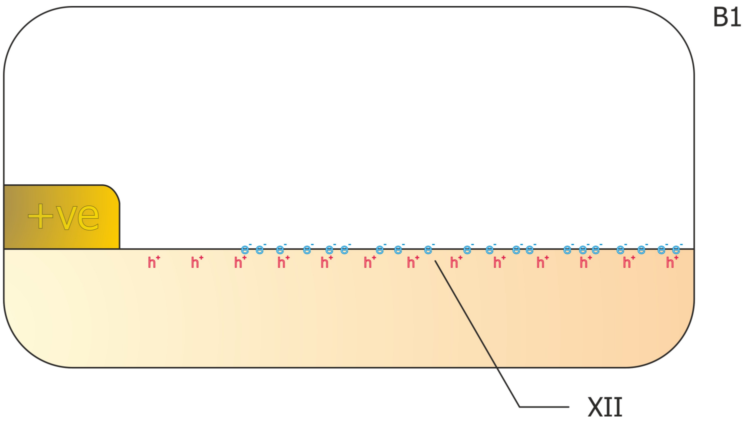

Figure 1.59 B1 – Backward stroke pre ignition condition

XII The number of electrons deposited on the surface during the forward discharge are just sufficient to produce a negative overall charge in the region near the electrode; further away (out of picture) the overall charge remains positive [85].

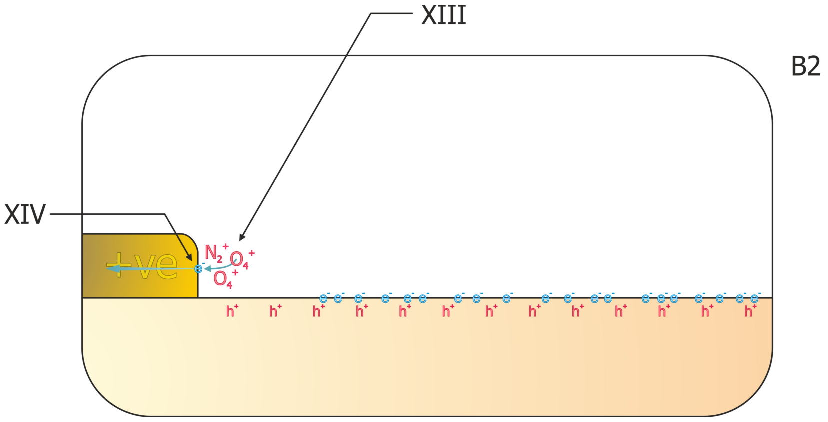

Figure 1.60 B2 – Corona like growth phase

XII As the exposed electrode goes positive in relation to the voltage plane created by the charge stored on the dielectric, the electric field becomes sufficient to produce a corona-like discharge around the edge of the electrode.

XIV Due to the difference in mobility and collision cross-section, electrons generated in the ionisation quickly find their way onto the exposed electrode while ions remain mostly fixed in place during this time. A strong electric field is generated due to the build up of charge.

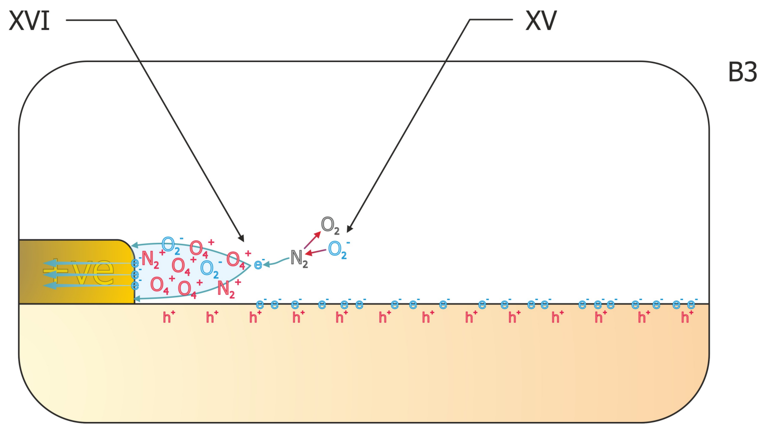

Figure 1.61 B3 – Streamer Initiation

XV Once the field is intense enough, the discharge needs seed electrons to propagate. These can be obtained from ionising background radiation or as Figure 1.61 the liberation of electrons from one of the last few negatively charged ions remaining from a previous discharge cycle through a high energy impact with a neutral species [93].

XVI Seed electrons gain sufficient energy to initiate electron avalanches in front of the charge cloud which starts to form into a cathode directed streamer.

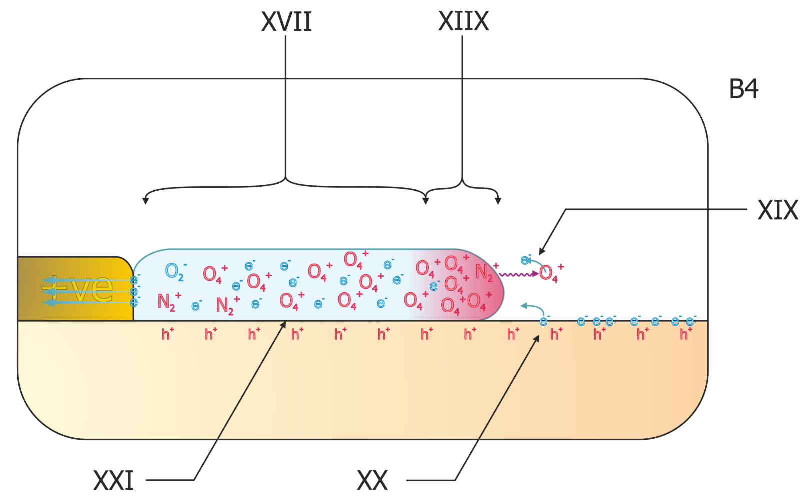

Figure 1.62 B4 – Streamer Propagation

XVII, XIIX A streamer discharge forms, consisting of two parts; a neutral body, marked XVII and a head containing a high ion density [94] (marked XIIX). Unlike the diffuse micro discharges all of the ionisation occurs in the head of the streamer [95] and propagates downstream [92]. This is corroborated experimentally by the data from by [88].

XIX, XX	The streamer propagates by producing a continuously advancing wave of seed electrons in front of the highly charged head and accelerating them under the electric field. The ions exhibit very little movement during the lifespan of the discharge.

XIX	This shows the photoionisation of an oxygen molecule by a UV photon emitted from a de-exciting nitrogen molecule. The presence of streamer-like discharges in computer simulations which do not take into account photoionisation, background radiation and remaining seed ions [92] supports the idea shown in XX that the seed electrons pulled from the surface could have a significant effect on the streamer discharge.

XXI	As the inactive tail section get longer and charge density decays, the resistance of the plasma increases; this reduces the electric potential transferred to the head from the electrode, and eventually the potential reduces to a point that can no longer sustain ionisation and the discharge quenches.

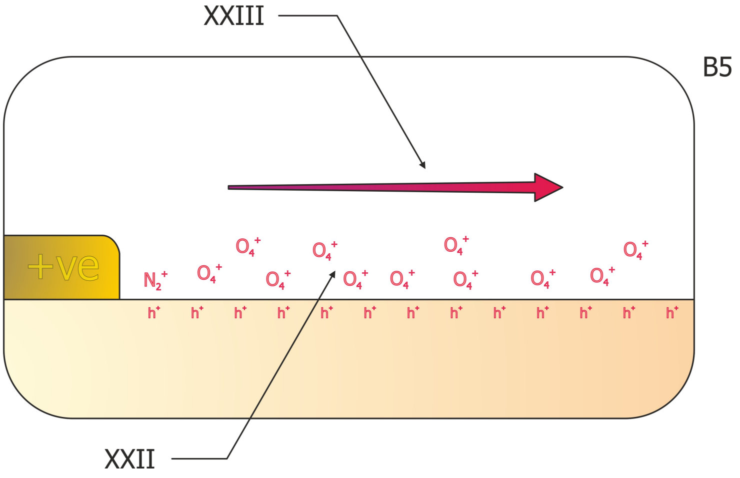

Figure 1.63 B5 – Streamer Relaxation

XXII	The electric field present in the streamer head is such that it favours O_4^+ ion production over electron capture to produce O_2^- ions. When the ionisation process ceases and current flow stops, after the resulting electron-ion recombination, significant levels of positive ions remain [90].

XXIII	During this period, the ions are accelerated under the electric field again away from the exposed electrode, coupling momentum to the surrounding fluid.

This explanation of the plasma cycle is in agreement with experimentally derived data, in that the cycle produces a Push-Push actuation effect, i.e. both halves of the actuation cycle produce a momentum contribution to the ionic wind away from exposed electrode edge. This is as distinct from a pull-PUSH or PUSH-pull actuation regime where the body forced from the two cycles is in opposition but an asymmetry in their magnitude provides a time averaged velocity away from the electrode edge. This was first shown experimentally in [79] and later by the same team in [96] with equipment capable of better time resolution. A diagram of their experimental setup is shown in Figure 1.64. The torsion pendulum they constructed contained two DBD actuators operating in opposition to each other to apply a rotational force around the axis. Using an interferometer monitored by a high speed camera allowed them to determine the position of the mirror to better than 20.4 nm. Differentiating the position measurement with respect to time and filtering to remove noise yielded the results given in Figure 1.65. The high temporal resolution of the data clearly shows the individual acceleration and deceleration phases associated with each cycle. Marked on the diagram are: forwards and backwards stroke thrust T_f, T_b respectively, forwards and backwards stroke drag D_f, D_b, and finally the net work input to the pendulum and therefore fluid during that half cycle W_f and W_b. Comparing T_f to T_b the magnitude is largely similar, the difference in work done between the two half cycles which has lead to some experimental studies to conclude that the 90+ percent of the momentum addition that comes from the forward stroke [72, 79] can be explained by looking at the difference in the drag between the two half cycles (D_f, D_b), this leads the backwards stroke to have a much lower contribution to the overall effect of the actuator. The authors in a subsequent paper [97] proposed that the difference is caused by the generation of the plasma closer to the surface during the backwards stroke and therefore incurring greater wall friction during the off phase than during the forwards stroke, see Figure 1.58 and Figure 1.62. In their paper they backed up this theory by running CFD simulations with plasmas with different volumetric constraints and densities and came to the conclusion that their initial postulation of both plasmas having similar ion numbers, but the forward stroke being more diffuse, largely agreed with the experimental data.

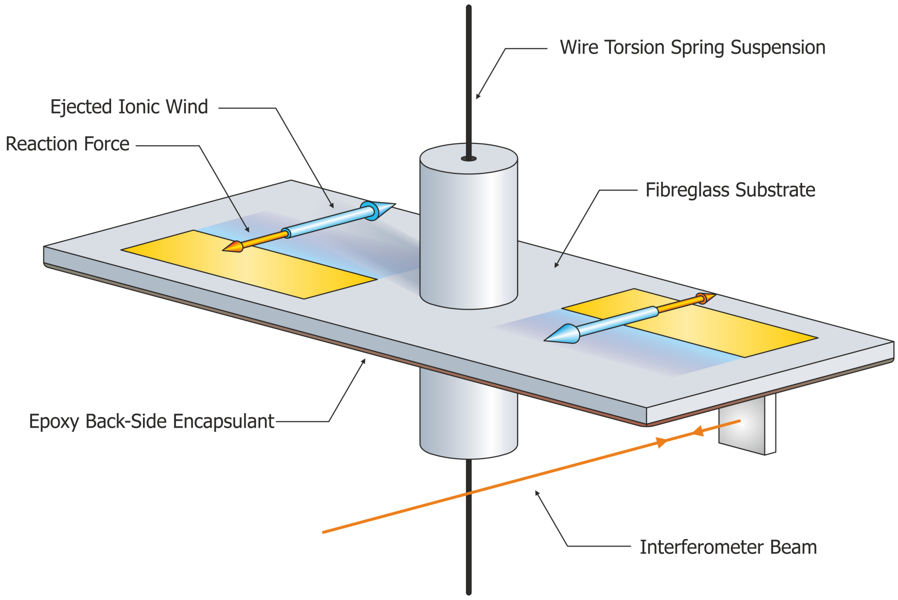

Figure 1.64 Torsion pendulum apparatus

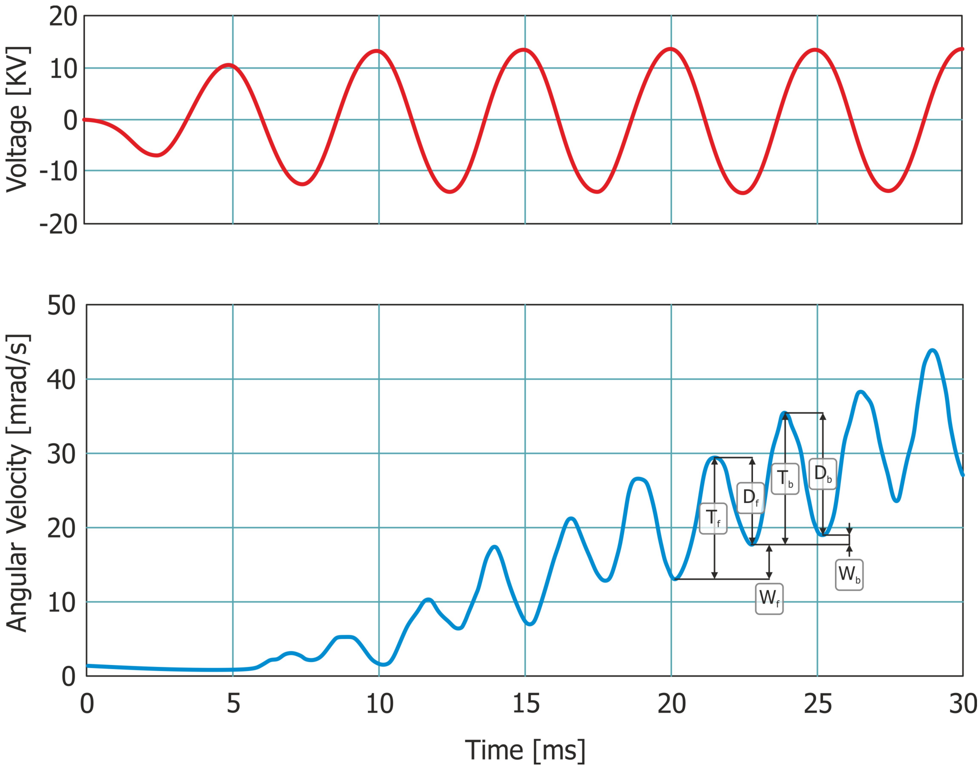

Figure 1.65 Torsion Pendulum Results (Replotted Based On [96])

Possible evidence of the creation of the plasma in different bounding volumes between the two half cycles from the wall can also be seen in the data shown in Figure 1.66. The traces shown were taken at specific points on time resolved particle image velocimetry (PIV) images, at a Y position of 1 mm from the wall and 2 and 5 mm downstream from the electrode edge as indicated. Close to the electrode edge there is only a significant input of velocity on the forward stroke; the negative stroke shows little effect to the velocity at that point as if the momentum addition is being generated lower in the boundary layer below the measurement point. However further downstream the backwards half cycle starts to show an input into the flow velocity as the added momentum is transferred further out into the boundary layer through viscous shear stress where the PIV can then pick it up.

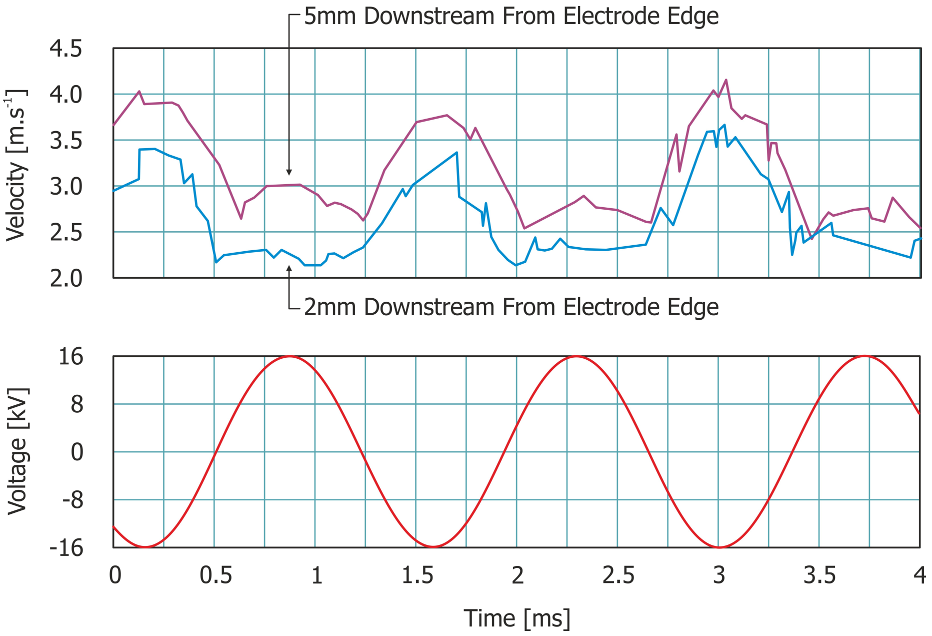

Figure 1.66 Time Resolved PIV Data (Replotted Based On [72])

Irrespective of the exact nano and micro second timescale structure and development of the plasma, the time averaged millisecond and beyond scale overall effect on the flow structure can readily be measured. Figure 1.67 shows a fairly typical velocity profile, in this case collected using a fine glass total pressure probe in the flow field 30 mm down stream of the actuator edge. The notable feature of this is the injection of most of the momentum within 1 mm of the wall.

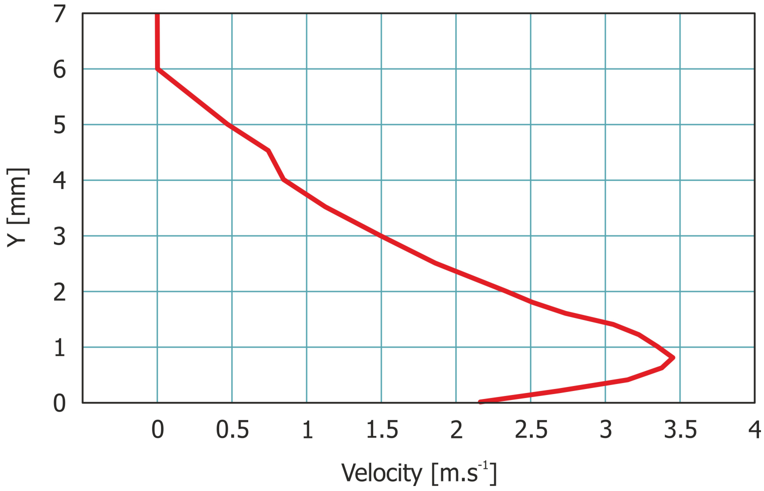

Figure 1.67 Velocity Profile (Replotted Based On [72])

1.4.2 Non Single Dielectric Barrier Discharge Plasma Actuators

1.4.2.1 DC Corona Discharge

The DC corona discharge is a simple plasma actuator consisting of two air exposed electrodes (see Figure 1.68); a high voltage at the anode creates an intense electric field which is able to ionise the air surrounding it. The ions then drift towards the cathode under the influence of the electric field, where they are neutralised. Because the wire to wire discharge does not have a capacitive element that becomes charged like the DBD the DC corona discharge, as the name suggests, is run continuously from a DC high tension supply. The advantages of the DC corona discharges are that they are simpler to manufacture and are more efficient at generating an ionic wind [98]. The disadvantages of the DC corona discharge when compared to the DBD is that because the electrodes are not separated by an insulator it can easily transition from a uniform glow discharge to a constricted arc, thus losing its efficacy as an actuator and risking damage to the power supply and actuator itself. As such, on balance, DC corona discharges are still a viable option for airflow control, see [99] for a good example of flow reattachment using this actuator.

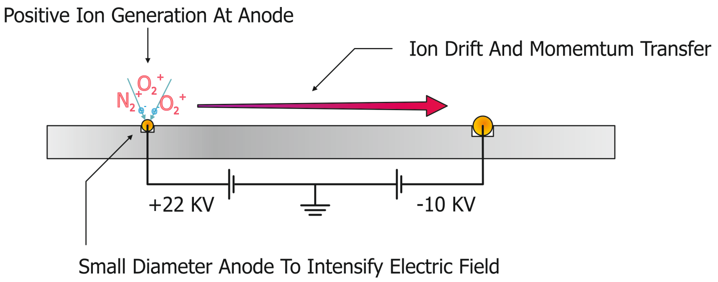

Figure 1.68 Corona Discharge

1.4.2.2 Sliding Discharge

Sliding discharges were first developed for generating excited species for pumping gas lasers and were only later applied to flow control. This type of discharge contains elements of both the DC corona discharge and the DBD. The plasma is initiated at the edge of the exposed electrode under the action of the DBD part of the actuator, and then streamers propagate under the influence of the electric field between the two air-exposed electrodes [100-101], see Figure 1.69. This means that the plasma sheet and therefore ionic wind region extends the full downstream width of the actuator (as in the DC corona discharge) enabling a much larger acceleration region than in a single DBD. However, because the reduced field strength between the air exposed electrodes does not need to be high enough to cause the breakdown of the air in the first place, as in the DC corona actuator, the discharge is much more stable and will not normally transition into an arc discharge.

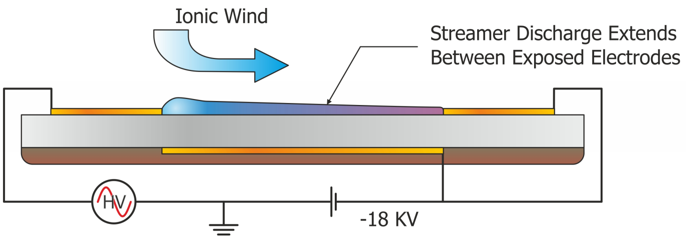

Figure 1.69 Sliding Discharge

1.4.2.3 Downstream Charge Neutralising DBD

In [73] it was shown that the dielectric surface downstream of the standard DBD becomes charged: sufficiently charged to distort the electric field and reduce the efficacy of the actuator. Their proposed solution is given in Figure 1.70: although similar to the sliding discharge in topology, the lack of a DC bias between the air-exposed sections of the electrodes prevents the plasma from extending that far, and merely allows ion species which have persisted in the airflow past the extent of the plasma to neutralise on the electrode surface and avoid depositing their charge on the dielectric.

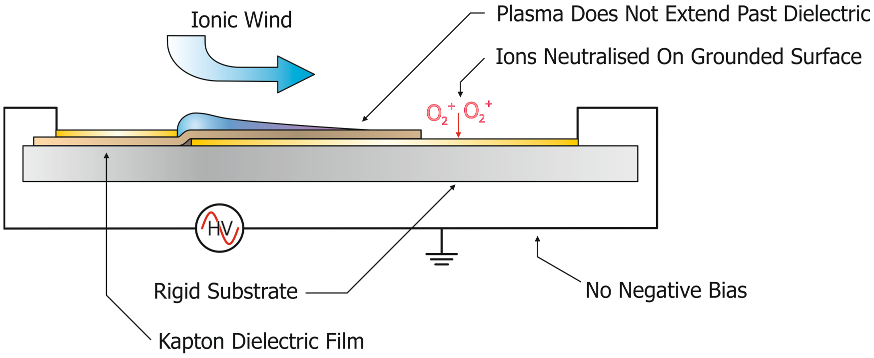

Figure 1.70 Modified DBD

1.4.2.4 Cascaded Multi Discharge DBD

Cascaded actuators are seen as a good way to create a larger actuation force over a greater area than a single actuator. A problem with multiple actuators is that a secondary plasma in the opposite direction to the desired flow is created; this is termed the crosstalk between the individual actuators, see Figure 1.71. This causes the air to roll up into vortices between the actuator segments [71]. The solution is to create an embedded plane at the same potential as the exposed electrode but covered by a dielectric immediately upstream of the exposed electrode. [102] did this explicitly by burying electrode strips under a Kapton dielectric, as shown in Figure 1.72, however [72] achieved a similar result by covering the trailing edge of the electrode with simple Teflon tape.

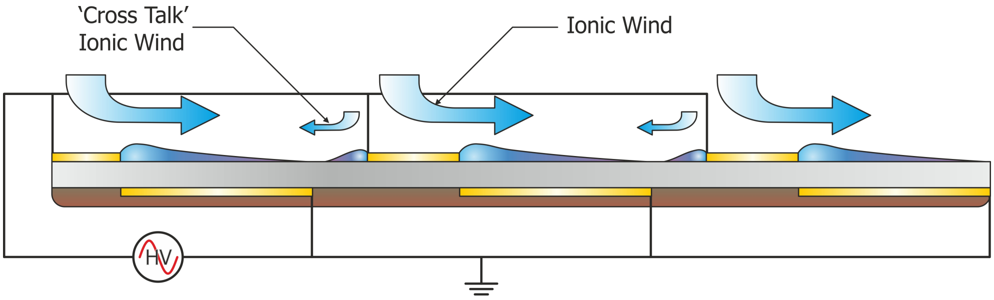

Figure 1.71 Cascaded Actuators

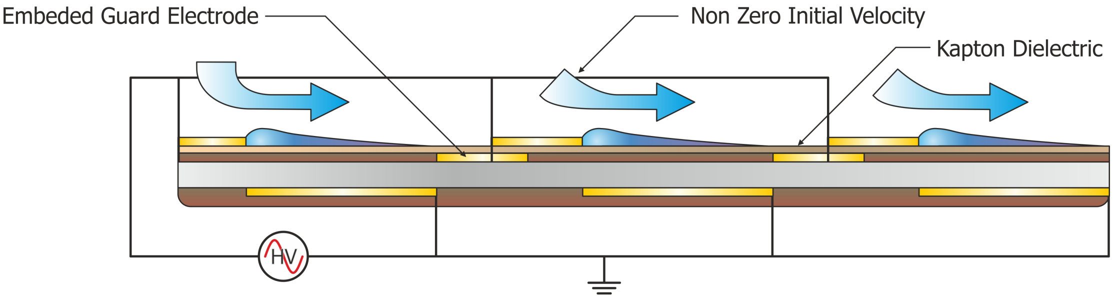

Figure 1.72 Cascaded Shielded Actuators

The efficacy of the guard electrode arrangement can be seen in the results shown in Figure 1.73 where it is clearly evident that the longitudinal velocity across the electrode array is much improved when the parasitic crosstalk plasma does not retard the jet between each actuator.

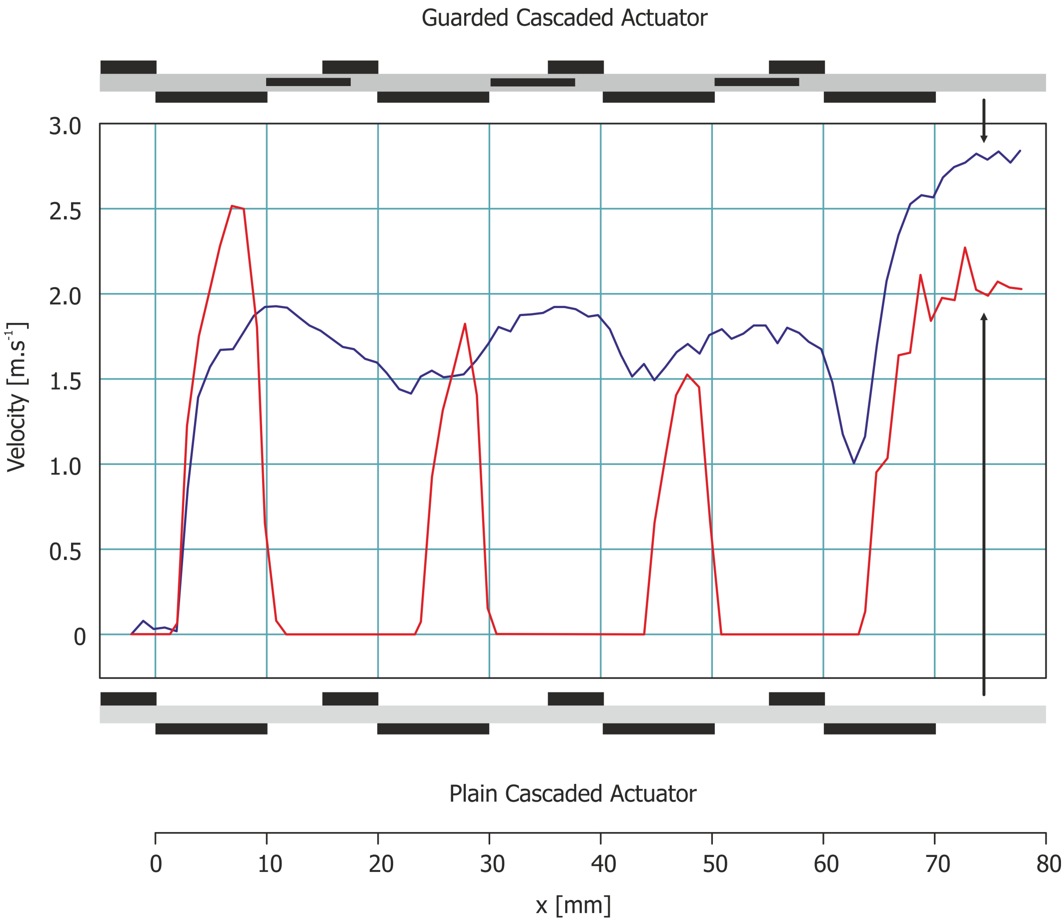

Figure 1.73 Longitudinal Velocity In Cascaded Actuators (Replotted Based On [102])

1.4.2.5 Wall Normal jet

The wall normal jet is an arrangement of a DBD actuator, either with two independent strips facing each other to create a curtain of wind jetting from the wall [103], or a single pair of electrodes arranged in an annulus to create a single point jet [104], see Figure 1.74.

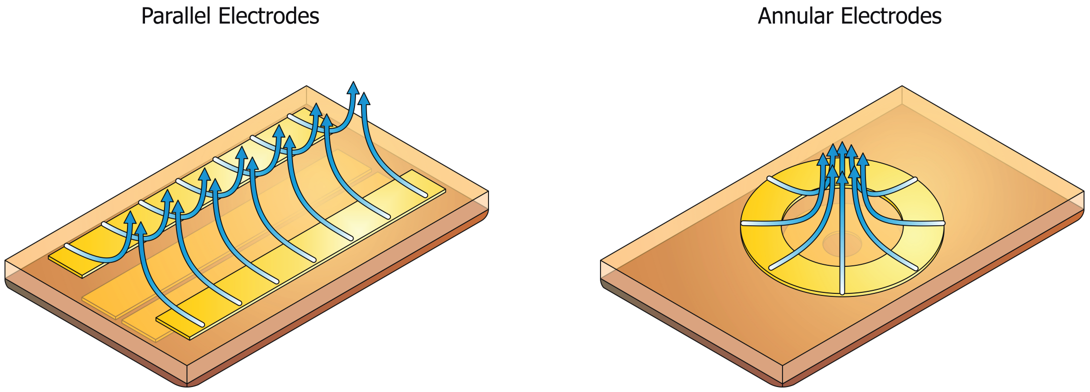

Figure 1.74 Wall Normal Jets

By placing the two plasma sheets, and therefore the associated ionic wind pointing at one another the resultant fluid motion is forced to create a jet normal to the wall. With the parallel strip topology it was found in [103] that they were able to vary the relative magnitude of the two plasmas by adjusting the drive voltage and vector the jet by ±20^o without significant loss in the jet strength (See Figure 1.75 and Figure 1.76).

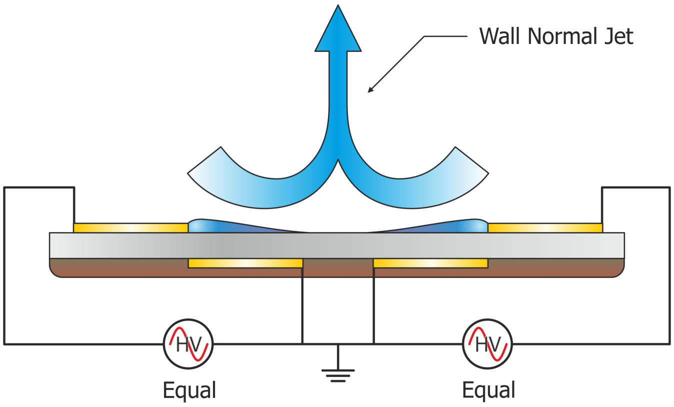

Figure 1.75 Wall Normal Synthetic Jet

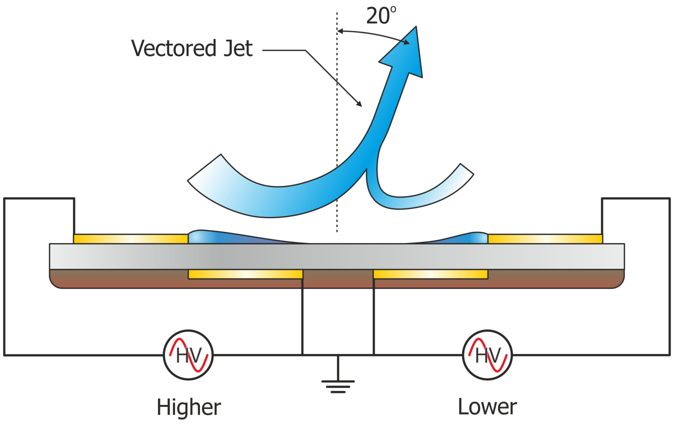

Figure 1.76 Vectored Synthetic Jet

Using multiple sets of actuator arranged facing each other and lying parallel to the airflow as shown in Figure 1.77 streamwise vortices can be induced in the flow . This has the effect of energising the boundary layer in the same way as fixed physical vortex generators do. Actuators with this construction have been demonstrated to be useful for preventing boundary layer separation in an adverse pressure gradient [105] and modifying the vortex shedding structure for cavity noise suppression [106].

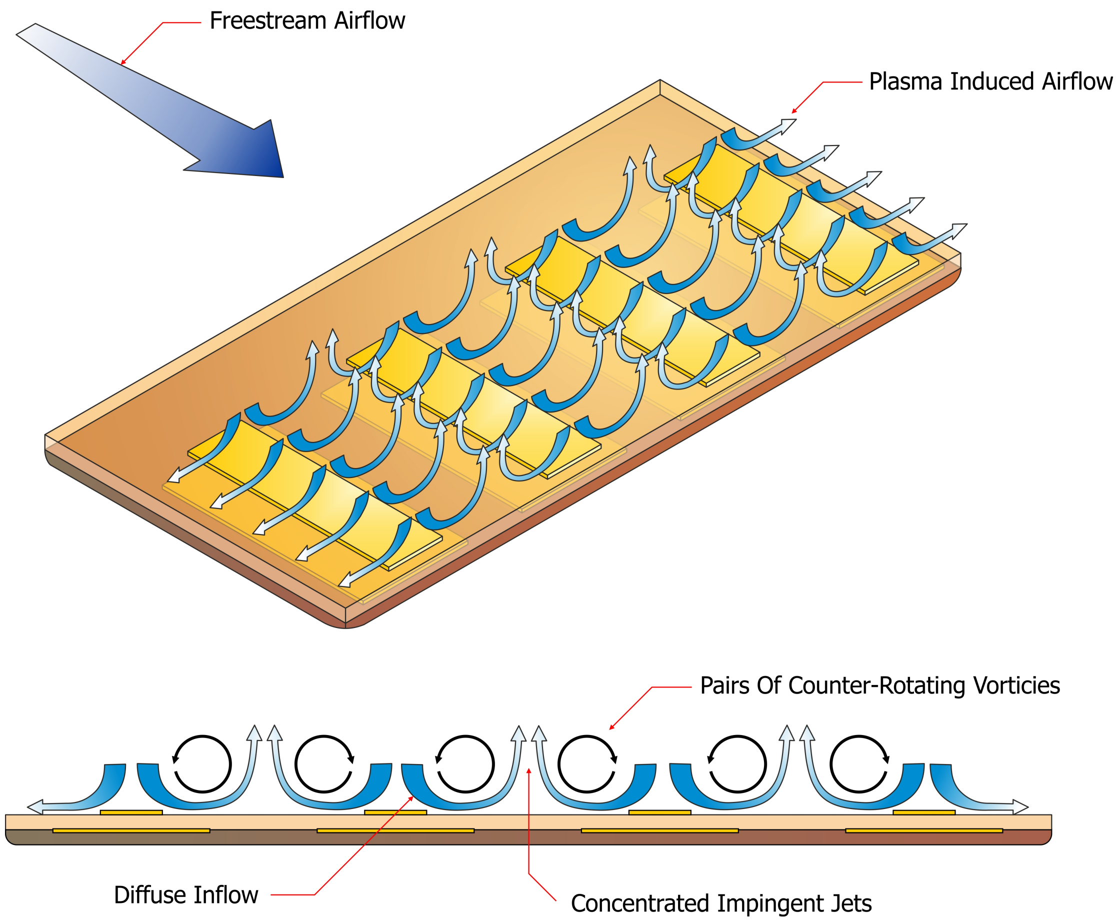

Figure 1.77 Plasma Streamwise Vortex Generator

1.4.3 Parametric DBD Studies

The following section details some of the effects that the drive voltage, bulk fluid conditions and actuator construction have been observed to have on single DBD actuators across several parametric studies presented in the literature. Figure 1.78 taken from [107] shows a proportional relationship over the given range exists between thrust, measured using an actuator mounted directly to a force balance, and input power measured using current and voltage probes on the supply line to the actuator. The actuator was constructed on GRP with 300mm long 15mm wide copper electrodes, and the drive frequency was 5 kHz.

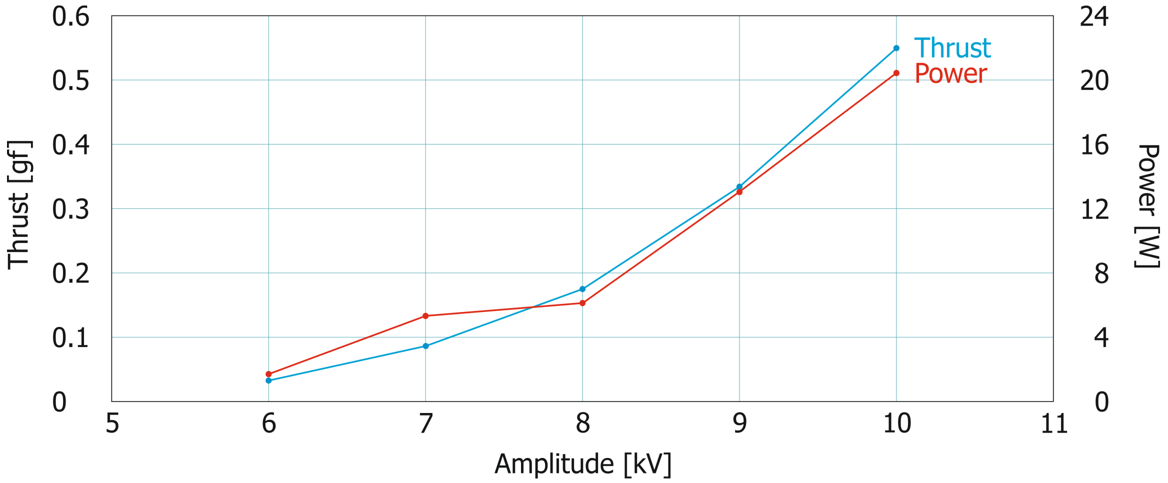

Figure 1.78 Thrust & Power Variation With Input Voltage (Replotted Based On [107])

Figure 1.79 and Figure 1.80 represent data from [72] collected using a 20 cm long actuator built on glass. Voltage and current measurements were collected using the high voltage supply internal probe and the voltage across a shunt resistor respectively. The bandwidth available from the shunt resistor allowed resolution of current spikes not visible on an internal HV supply current probe. The data sets clearly show the cubic relationship between input voltage amplitude and input power, and the linear relationship between frequency and power.

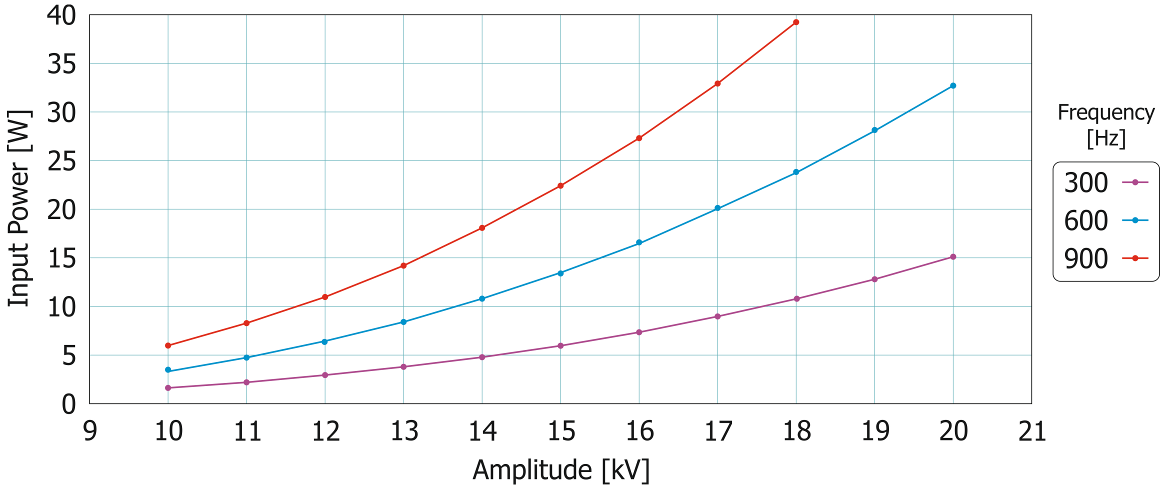

Figure 1.79 Input Power Variation With Input Voltage (Replotted Based On [72])

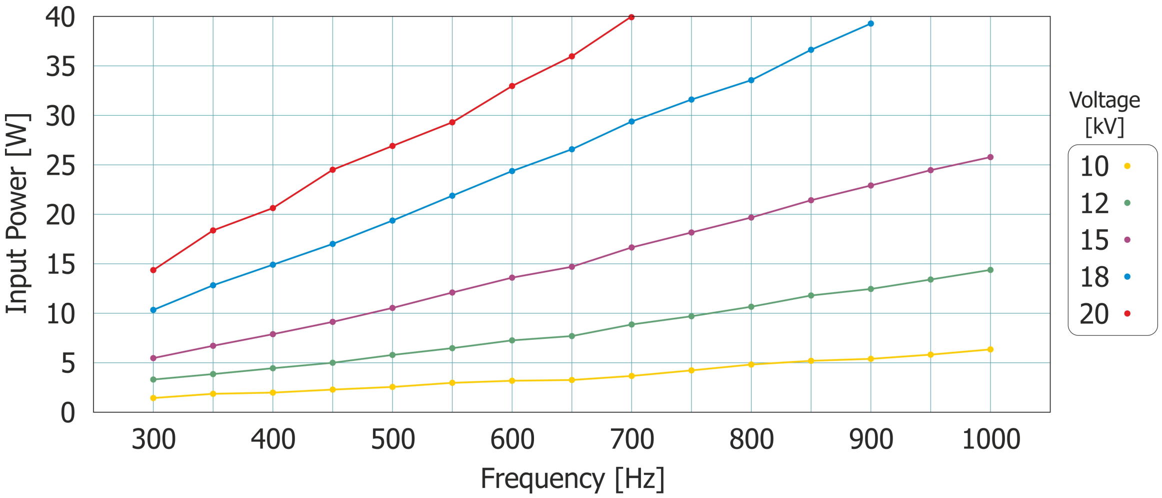

Figure 1.80 Input Power Variation With Drive Frequency (Replotted Based On [72])

Figure 1.81 taken from [108] shows the decrease in performance of a DBD actuator when subjected to an increase in relative humidity. The data was taken 20 mm downstream of the edge of the air exposed actuator; it was driven at 20 kV with a frequency of 1 kHz, and the dielectric was PMMA. Mass flow was calculated by integrating velocity measurements from laser Doppler velocimetry traverses and is plotted as $g.s^{-1}$ per linear m of actuator. Importantly this sensitivity to humidity suggests any application using a plasma actuator where high operational availability in a wide variety of climates is important must build in significant overhead in the system to be able to increase the voltage to compensate for the drop in performance.

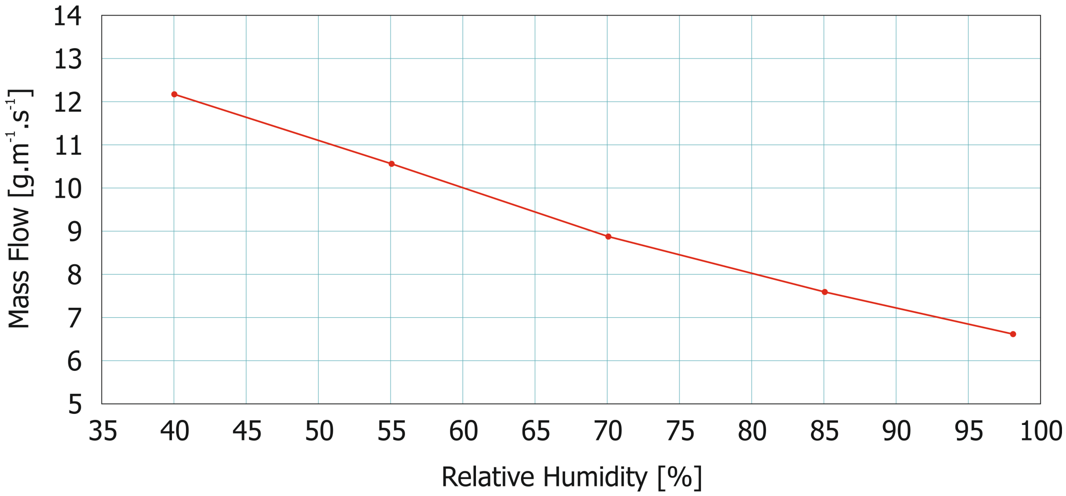

Figure 1.81 Change In Mass Flow With Relative Humidity (Replotted Based On [108])

In [107] Abe et. al. investigated the result of operating a DBD actuator at different ambient pressures. The actuator was run at 10 kV, 2 kHz. Figure 1.82 shows the results of their investigation. It can be seen that the results form part of a parabola; pre maxima the thrust increases with pressure as gas density increases and tape thickness has less of an effect. Post maxima the tape thickness begins to have more of an influence as the thrust drops off due to a decrease in ease of ionisation. The thinner tapes maintain maximum thrust at higher pressures because they generate a higher field density at the tip and therefore more readily ionise the air as the ambient pressure begins to approach 0.1 MPa. This decrease in thrust and therefore momentum addition to the fluid has implications on any applications which are designed to operate at altitude. However depending on the exact application the global flow which is being actuated by the DBD device will also be at a lower Reynolds number and have a subsequently smaller boundary layer which will therefore be easier to affect. It should be the case that the actuators shown in Figure 1.82 experience a peak in efficacy at approximately 70 kPa (3000 m altitude in the 1976 international standard atmosphere) even for the 0.01 mm thick actuator which shows flat line thrust performance from 70 – 100 kPa.

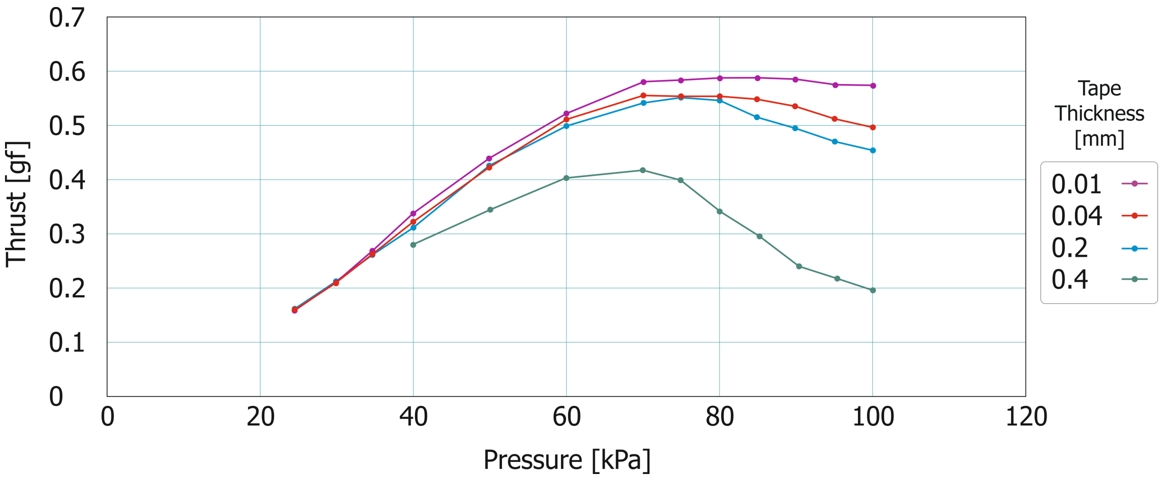

Figure 1.82 Thrust Variation With Ambient Pressure (Replotted Based On [107])

Abe et. al. also conducted the same pressure sweep with a stainless steel mesh electrode. The fine ends of the exposed stream-wise wires of the mesh served to create even higher electric field concentrations at the tip and provided even better high pressure thrust than the thinnest tape. This improvement based on maximising the local electric field at the electrode edge can also be seen in the work of Thomas et. al. [109]. Shown in Figure 1.83 is a comparison done between two otherwise identical actuators, one with 12.7 x 3.175 mm serrations in the electrode edge and the other one plain. The drive voltage amplitude sweep shows how the serrations particularly improve performance at lower voltages where the plain edged actuator is struggling to ionise the air.

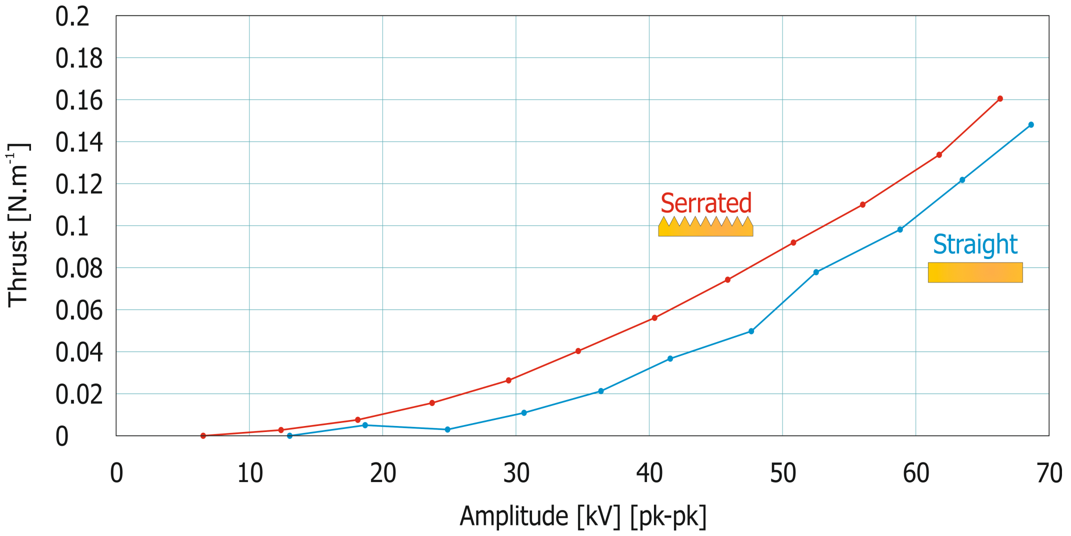

Figure 1.83 Electrode Edge Optimization (Replotted Based On [109])

Figure 1.84 and Figure 1.85 are taken form the work in [72], and the test data comes from an aluminium actuator built on 2mm thick PMMA driven by a 20 kV supply at 700 Hz. Figure 1.84 shows how the system responds to increase in electrode width. As the electrode width is increased, initially so is the extent of the plasma and therefore the length available for ion acceleration and momentum transfer to the neutral fluid. Once the width exceeds 22.5 mm the peak velocity then saturates. This is because the drive voltage can no longer overcome the internal resistance of the plasma and surface charge to push plasma streamers further out onto the electrode. Increasing the drive voltage would result in an increase in the electrode width to achieve saturation.

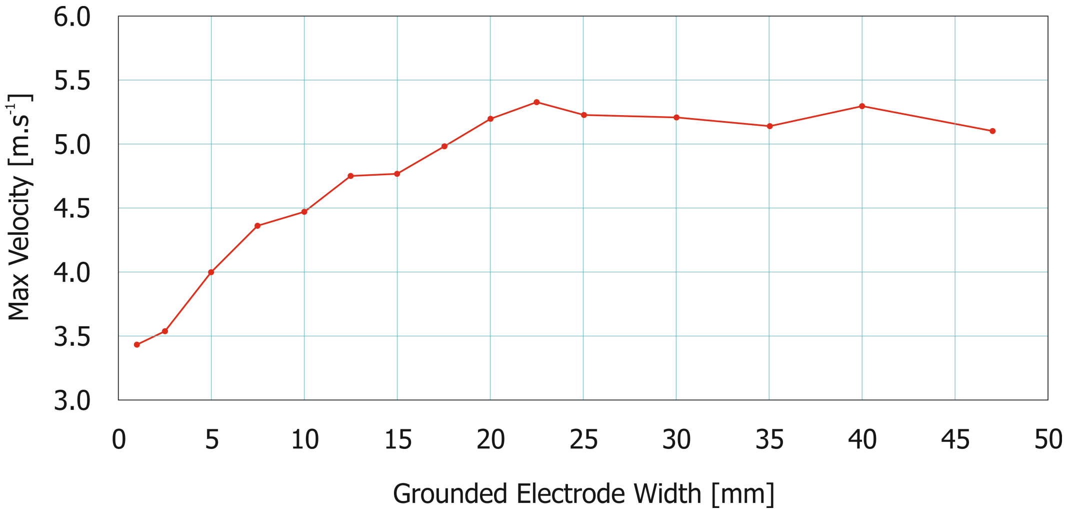

Figure 1.84 Effect Of Grounded Electrode Width (Replotted Based On [72])

When analysing the data shown in Figure 1.85 it is important to consider that the electrode width was 5 mm. When the electrode gap is shown as -5.0 mm the two are laid directly on top of each other and nominally no asymmetry exists in the electric field. It is difficult to separate the effect of the electrode overlap distorting or reducing the electric field from the effect of increasing the extent of the plasma. It would have been preferable for this test to have been run with a quasi-infinite grounded electrode so that the two effects could have been separated. As Forte et. al. note in the paper, [72] a 20 mm grounded electrode performed identically to a 15 mm grounded electrode with a 5 mm gap. It can then be argued that the performance increase from 0 to 2.5 mm separation is due to an increase in size of the plasma sheet and the length of ion acceleration available to transfer momentum to the fluid. The deterioration in performance post 5 mm separation can however be attributed to the increase in effective dielectric thickness between the two electrodes, reducing the electric field strength.

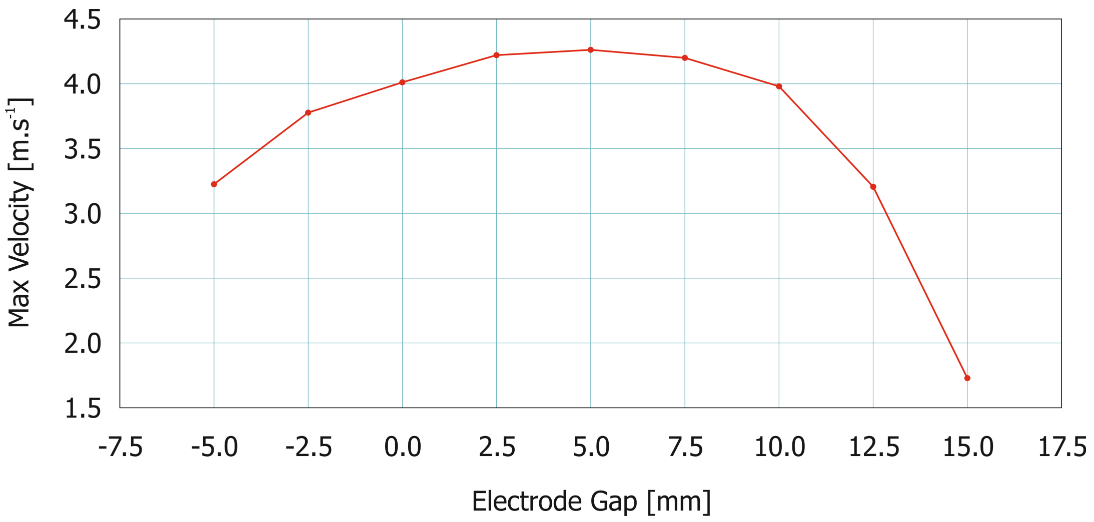

Figure 1.85 Effect Of Streamwise Inter Electrode Gap (Replotted Based On [72])

Figure 1.86 shows how the dielectric constant of the substrate affects the maximum thrust generated before the discharge mode saturates, and further increases in voltage and power yield no further increase in thrust. The dielectric constant for Kapton® HN is included as a point of reference on the chart merely because it is one of the most common dielectrics to use for DBD construction and was not a point in the original data set. By using the lower dielectric constant dielectrics the field concentration at the electrode tip is reduced, and therefore greater voltages can be applied before the discharge regime saturates and no further performance can be extracted from the actuator. Other data sets within [109] show how for a fixed voltage in the pre-saturation discharge regimen the higher dielectric constant materials provide better performance.

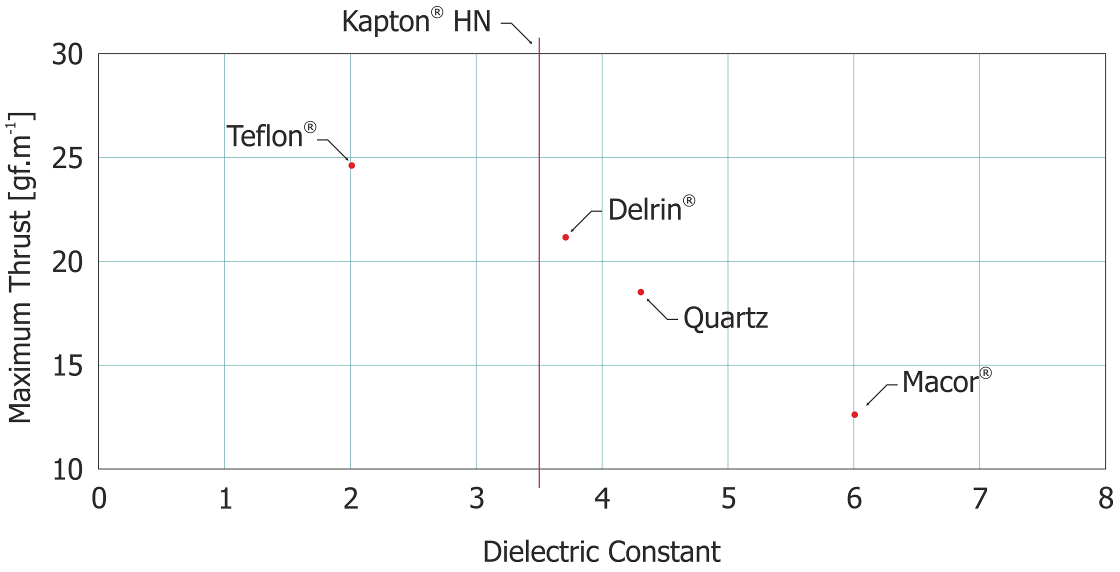

Figure 1.86 Thrust Against Dielectric Constant (Replotted Based On [109])

Figure 1.87 shows the behaviour of the actuator as the freestream velocity is increased, in this figure we see a decrease of a few percent over the test range. This figure is based on results which were reported in [110] and were taken for a 12 kV drive voltage at 10 kHz, similar interactions have also been reported in [111]

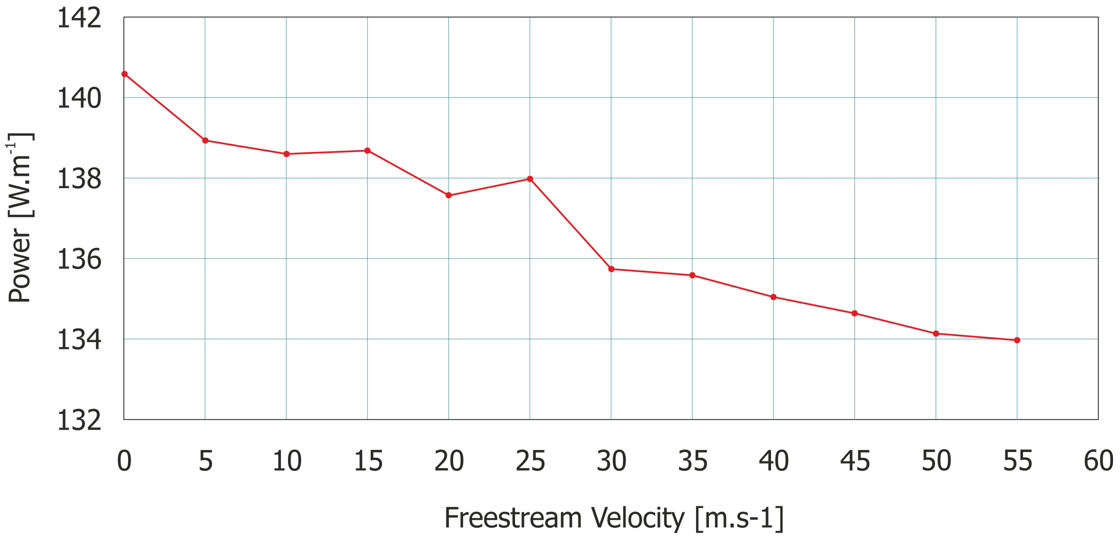

Figure 1.87 Actuator Power Against Freestream Velocity (Replotted Based On [110])

Recent work presented in [112] has also shown that the force production by a DBD actuator also varies with ambient temperature. The study used a direct force balance measurement of the thrust generated by accelerating the air jet inside a temperature controlled chamber, one of the key results is shown in Figure 1.88, the data is for the 20 kV, 9.4 kHz driven plasma but is representative of the trend in other conditions tested. A similar increase in performance with increasing temperature was also seen by Erfani et. al. in [113] where they used PIV measurements to show an increase in the plasma induced jet velocity with the temperature of the actuator dielectric. It should be noted that in contrast the work of Versailles et. al. in [112] these measurements were taken at constant ambient temperature and only the surface temperature of the dielectric was varied.

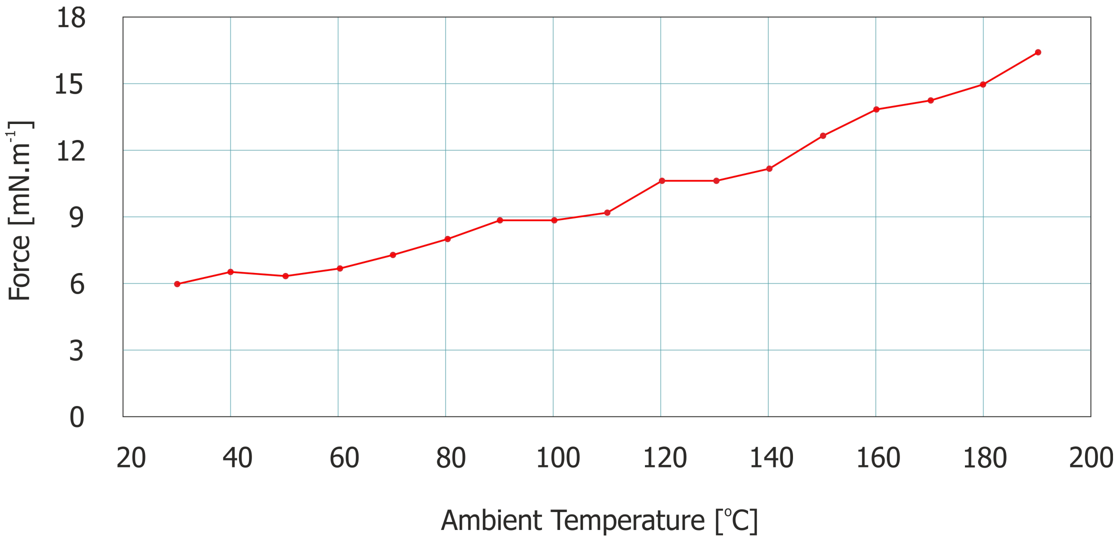

Figure 1.88 Actuator Temperature Dependence (Replotted Based On [112])

As can be seen from the results of parametric studies shown hereinbefore there are a large number of factors affecting the functioning of a DBD, many of which cannot be expected to be constant across the range of conditions a flight vehicle might be expected to operate under. As such it is evident that adapting to the changing efficiency of the actuator is necessary, the use of a closed loop control system for this purpose is examined at a proof of concept level in the paper presented by Kriegseis et. al. [114].

1.4.4 Summary Of Key Points On Plasma Actuators

Several types of plasma actuator have been detailed, all of which show simple construction and operation. The salient points of the operation of the DBD are:

The plasma structure is different for the two half cycles of the AC drive voltage, denoted as the forward and reverse strokes.

The structure of the forward stroke plasma is composed of many individual streamers which ignite and then quench on the order of micro seconds; these streamers are exceedingly localised but time averaged are spread across the whole surface of the actuator. The reverse stroke is a more diffuse discharge.

The plasma extent is self-limiting and will quench at the point that the change in voltage rise can no longer drive electrons onto the dielectric. The structure also means that the DBD cannot collapse into an arc discharge.

The structure of the forward and reverse discharges differs such that the operation is PUSH-push, a more effective forward stroke being augmented by a weaker backward discharge both of which contribute forward momentum addition to the fluid.

Momentum addition increases with both drive voltage and frequency.

1.5 Overview and Project Direction

1.5.1 Actuator Technology Comparison

An overview of 3 critical actuator characteristics for the various actuator technologies looked at previously in this review is presented in Figure 1.89. The key element to notice here is that no one actuator technology dominates across all three categories (i.e. produces a large deflection / output at a high operational frequency for a low input voltage), and therefore the choice of actuator is a compromise influenced by what is important for the intended application.

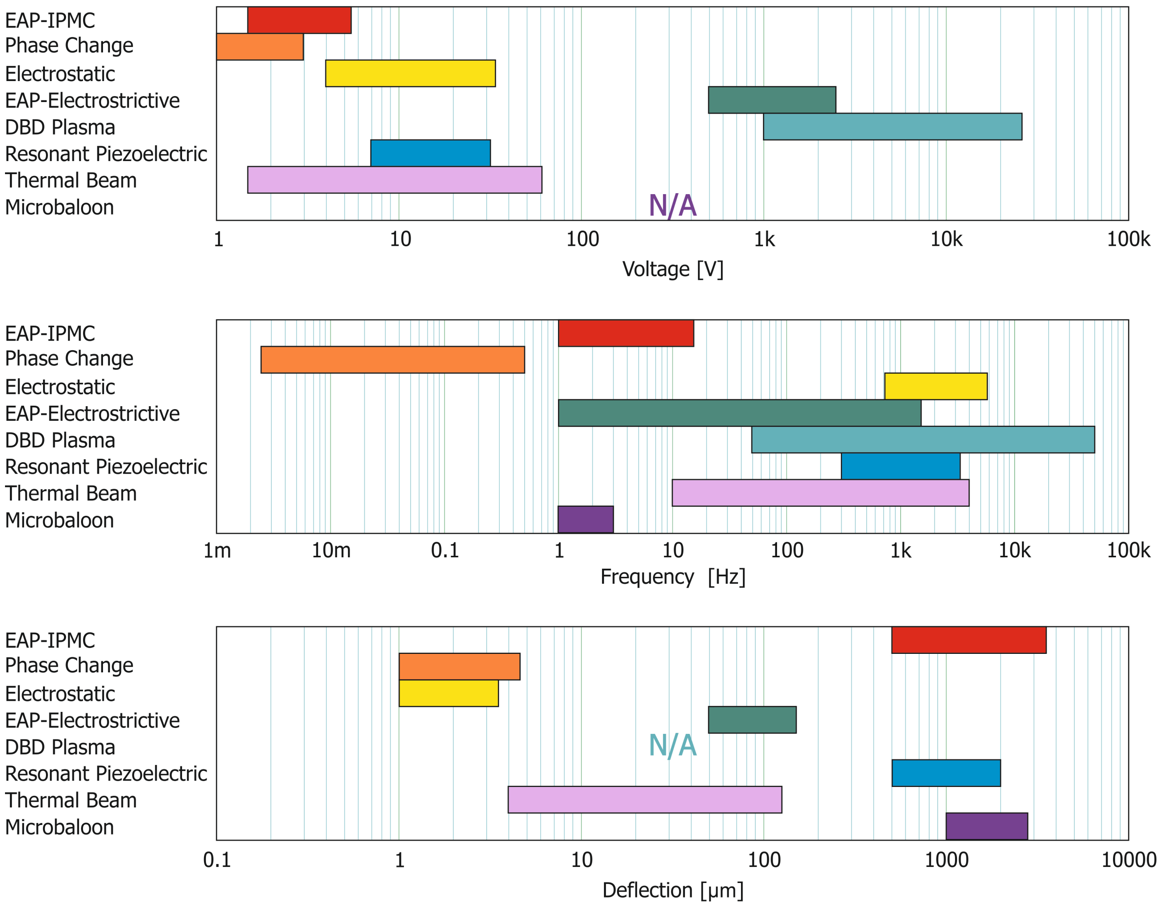

Figure 1.89 Actuator Technology Overview

Looking back at the applications for active flow control shown in section 1.2, it is useful to bear in mind not only their similarities but also their differences. The majority of the presented applications showed an interaction with a flow to produce an effect larger than pure force or effort applied by the actuator. However, different applications place different demands on the actuator characteristics required; for example, for high lift or stall delay devices which are only turned on during take off or landing a deployment time on the order of seconds is acceptable. Whereas, at the other end of the spectrum, skin friction reduction by direct opposition would require an actuator able to respond to individual eddies in the flow. Even the largest of these eddies within a turbulent boundary layer a few mm thick in a relatively low speed 20 $m.s^{-1}$ flow will have a time scale which corresponds to a frequency of the order of 5 kHz. Looking at how the plasma actuators compare to the other actuators reviewed in this section, at it can be seen that they are ideally suited for influencing flows on the scale of the individual eddies or vortices by being able to operate in the kHz region. However the compromise is the exceptionally high voltage which must be generated to activate them.

1.5.2 Summary

It has been shown that there are many possible active flow control applications and actuator technologies. However, of these, plasma flight control stands out as a particularly suitable candidate for further study. Plasma flight control contains elements of both a resonant interaction as evidenced by the fact that the pulsed actuation has been shown to out perform steady actuation (note differences between the two graphs in Figure 1.5), and additionally as it is actuating upon a flow separation it manages to produce a large shift in C_L for a small input energy. The DBD actuator at the heart of plasma flight control systems has the benefit of being simple, lightweight and robust when compared to other active flow control techniques as it contains no moving parts. Whereas there are many studies on the operation and discharge characteristics of DBD devices mounted on flat plates, those studies which relate to their application on aerofoils or under flight conditions are less well covered. Of those studies that have covered on-wing applications several have shown the benefit of pulsed actuation. However, there remains an open question as to how this unsteady actuation interacts with the flow and its effect on C_L at different frequencies. As such the scope of this project will cover the behaviour of trailing edge plasma actuators and their influence on the flow field around a 2D aerofoil at low angles of incidence. In particular it will concentrate on the behaviour of the aforementioned actuators at differing interruption frequencies and will look to better understand the method of increased actuation effect seen with pulsed over continuous actuation. In addition, this study will also look to develop the construction of the DBD actuator itself in order to move towards flight-ready systems for possible future MAV integration.

Chapter 2 Experimental Method

2.1 Overview Of Experimental Approach.

The general experimental approach was to investigate the effect of a plasma actuator on a 2D stepped aerofoil. To do this a model was run though an extensive battery of tests in a wind tunnel. The effect of powering the plasma actuator with various continuous and pulsed sinusoidal high voltage waveforms was investigated using a combination of force balance measurements, laser deflection sensors, probe traverses (both hot wire and 5 hole) and Particle Image Velocimetry (PIV) measurements.

2.2 High Voltage Generation

Throughout the project the high voltage generation system was developed and changed to improve available drive frequencies for testing, output power and to ensure proper integration and operability with the measurement and test systems being used during that phase. The HV system had to be able to produce the waveform shown in Figure 2.1, so that the plasma can be driven with an AC carrier wave, but at the same time pulsed on and off at a slower frequency, termed the interruption frequency.

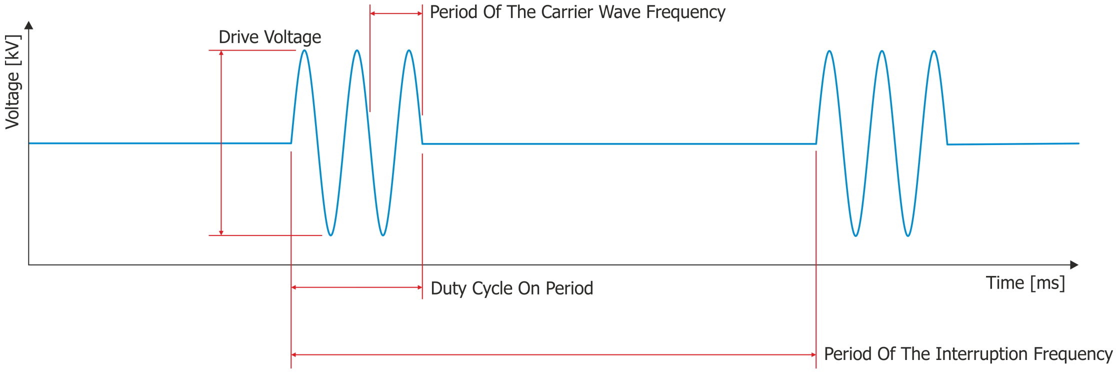

$$\text{Duty Cycle} = \frac{\text{Duty Cycle On Period}}{\text{Period Of Interruption Frequency}}$$

Figure 3.1 AC Plasma Drive Waveform

2.2.1 Preliminary Setup

The first phase of testing was carried out using a high voltage generation system consisting of a laboratory signal generator feeding a signal into a 250 W per channel power amplifier and then into an American 120 V - 15 kV neon sign transformer via a low ratio custom wound isolation transformer. Interruption was supplied by physically switching the feed from the signal generator using a reed relay controlled by the clock from a second signal generator and a pair of decade counters (see Figure 2.2 and Figure 2.3). The carrier signal was directly controlled by the primary signal generator, duty cycle (X/T) could be controlled by altering the reset switch point on the latch logic and T could be changed through the clock signal, (T = Clock x 0.01). This system was successfully used to test the longevity of different actuator constructions and to calculate ozone production rates. Its ability to run continuously and rapid development and assembly of the system allowed for these tests to be carried out quickly and efficiently. However, when moving to aerodynamic testing this setup was severely limited by two factors; firstly, the physical relay limited the switching frequency, and secondly the lack of computer control of the waveform made accurately setting the frequency a painstaking exercise involving the oscilloscopes, a process which precluded automatic logging sweeps and good repeatability; as such a subsequent system was required.

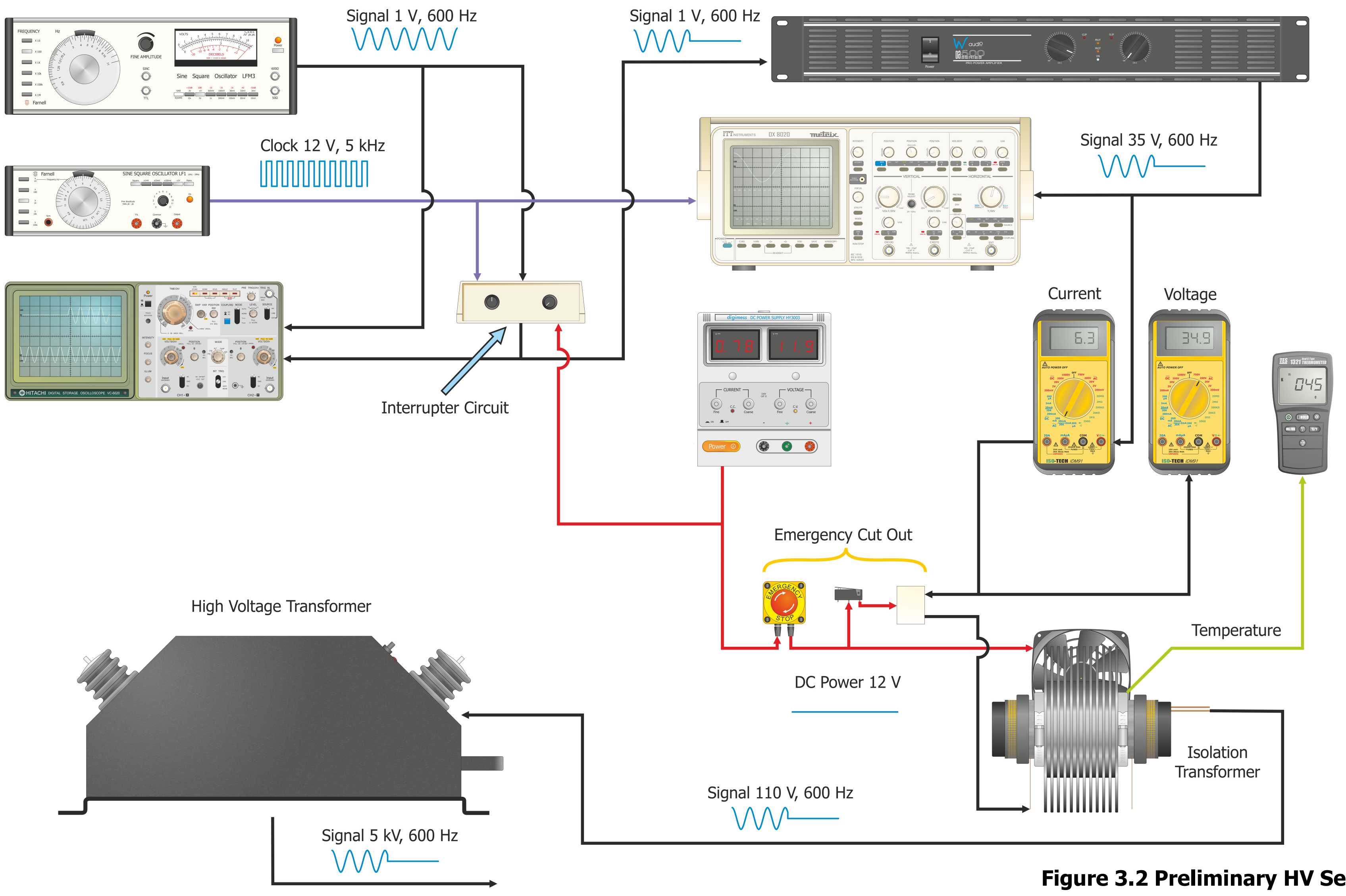

Figure 3.2 Preliminary HV Setup

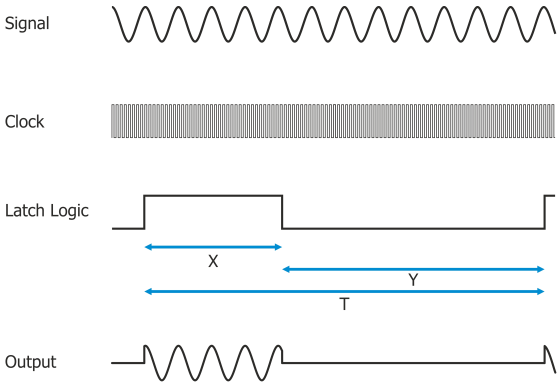

Figure 3.3 Interrupter Circuit Operation.

2.2.2 Automated 1st Generation

The 1st automated system used the same basic high voltage elements as the preliminary setup, i.e. power amplifier, isolation transformer and neon sign transformer. However the feed signal was generated in control software and fed out from the analogue output of a data acquisition (DAQ) module (USB-6218, National Instruments) (see Figure 2.4). This module was controlled using its native NI-DAQmx drivers within a C/C++ programming environment. By running everything from a single master control program (MCP) the generation of the HV signal could be synchronised to the force logging and allow the insertion of interleaved unactuated control data points within data collection runs. The disadvantage to this system is that the waveform is generated in an array and uploaded to the DAQ for output. Limits on the array size meant that maximum run time was limited, with the limit imposed depending on the sampling frequency required. For practical purposes with the frequency limits of the neon sign transformer (600 Hz), and the desire to capture a good approximation of the waveform without aliasing issues or distortion by sampling significantly above the Nyquist frequency, the maximum runtime was around 1.5 – 2 minutes. This system was used successfully for the majority of the uninterrupted runs. However the transformer network limited its potential for interrupted plasma testing. The neon sign transformer has a design frequency of 60 Hz (American power grid) and had a laminated iron core: this meant that past around 600 Hz carrier frequency it was so far from its design point that its output voltage had dropped off to a point where it could no longer support effective plasma ignition. This in turn limited the maximum interruption frequency at a 25% duty cycle to only 150 Hz which turned out to be insufficient to interact with the fundamental frequency of the aerodynamic system. This system also suffered from a massive power loss incurred in the primary of the isolation transformer. This energy loss was large enough to require a large heat sink and fan to cool it sufficiently to stop it melting the plastic former. The transformer network was designed to maintain safe isolation of high and low voltage sides in the event of a failure; this significantly compromised the electromagnetic efficiency of the system.

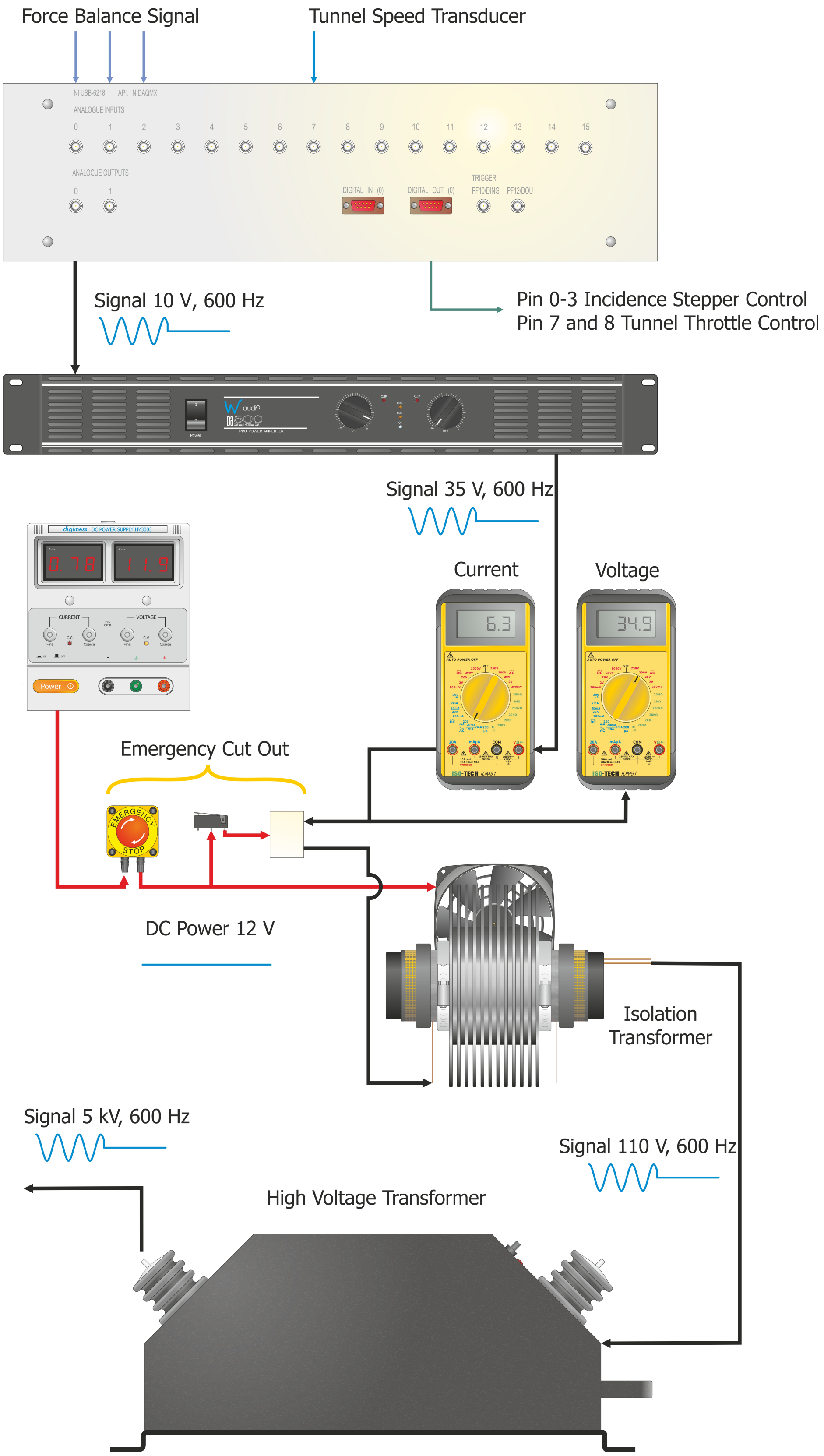

Figure 3.4 1st Automated High Voltage Generation System

2.2.3 Automated 2nd Generation

The 2nd generation automated system replaced the isolation transformer – neon sign transformer pairing with a single purpose built transformer from Amethyst Designs in Cambridge. The transformer has a design frequency of 1.2 – 7 kHz and a maximum insulation-limited output of 10 kV when operated in air. During this work it was run oil-immersed thereby ensuring breakdown voltages were well above the required level. The increased efficiency of the single stage design and higher carrier frequency resulted in a much more powerful plasma being achievable from this setup (Figure 2.5). The improvement in frequency response from the purpose built system is shown in Figure 2.6.

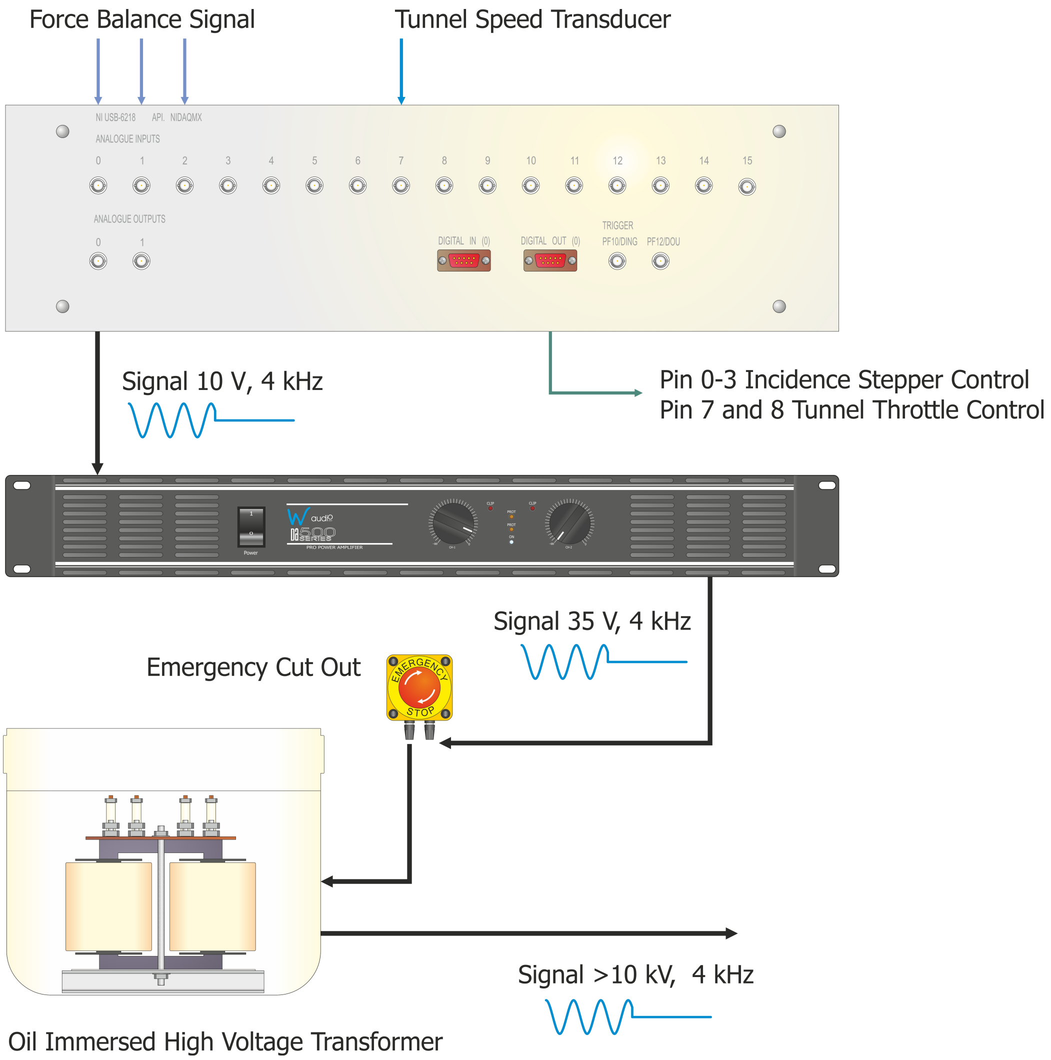

Figure 3.5 2nd Generation Automated High Voltage System

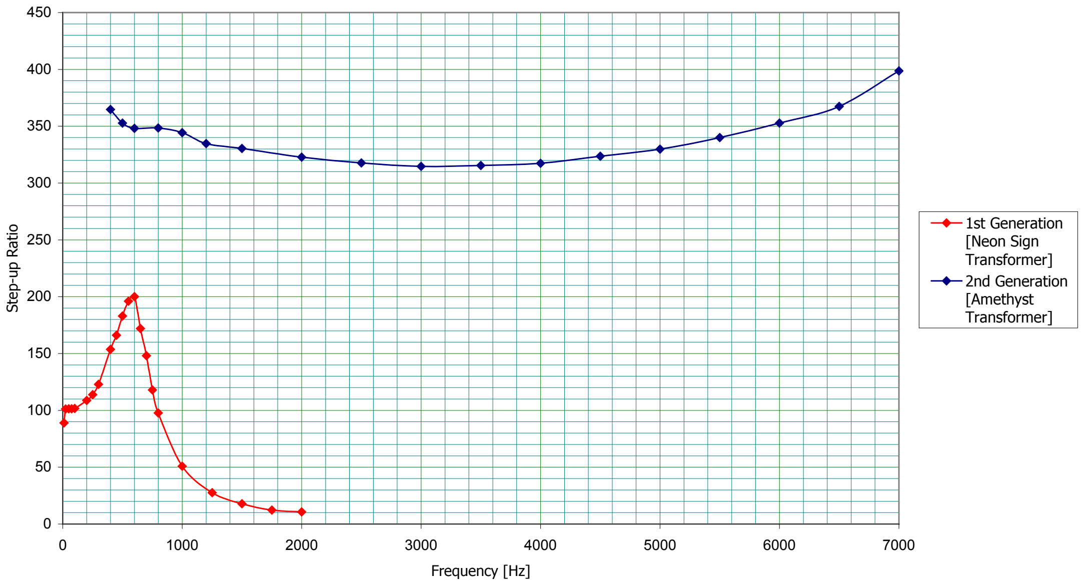

Figure 3.6 Comparison Of Transformer Frequency Response

2.2.4 High Voltage System For PIV

As was mentioned in section 2.2.2 the systems running from the NiDAQ logger analogue outputs suffered from limited run time. Also, running individual cases was more complicated than necessary due to the code being designed to run parameter sweeps whilst logging force data. To allow almost unlimited running the HV setup was changed to that represented in Figure 2.8. Firstly the waveform was generated by a program written in Basic and output as mono unsigned 8 bit data at 44 kHz into an intermediary file. This raw data file contained no heading data. The open source sound editor 'Audacity' was then used to import the raw data and export it as a correctly formatted Stereo 16 bit signed 44 kHz '.Wav' file. This file was uploaded to a personal music player (Walkman NWZ-SS369F, Sony). An audio amplifier was then used as a pre amp stage to increase the voltage to the same 10 V peak to peak delivered by the NiDAQ data logger to ensure parity with the signal coming from the power amplifier between the two final generation HV systems. Figure 2.7 shows the response of the system to differing demand values from the Wav file stored on the personal music player. The linear relationship shows that no significant alteration to the signal is occurring through any digital signal processing going on in the signal (audio) path.

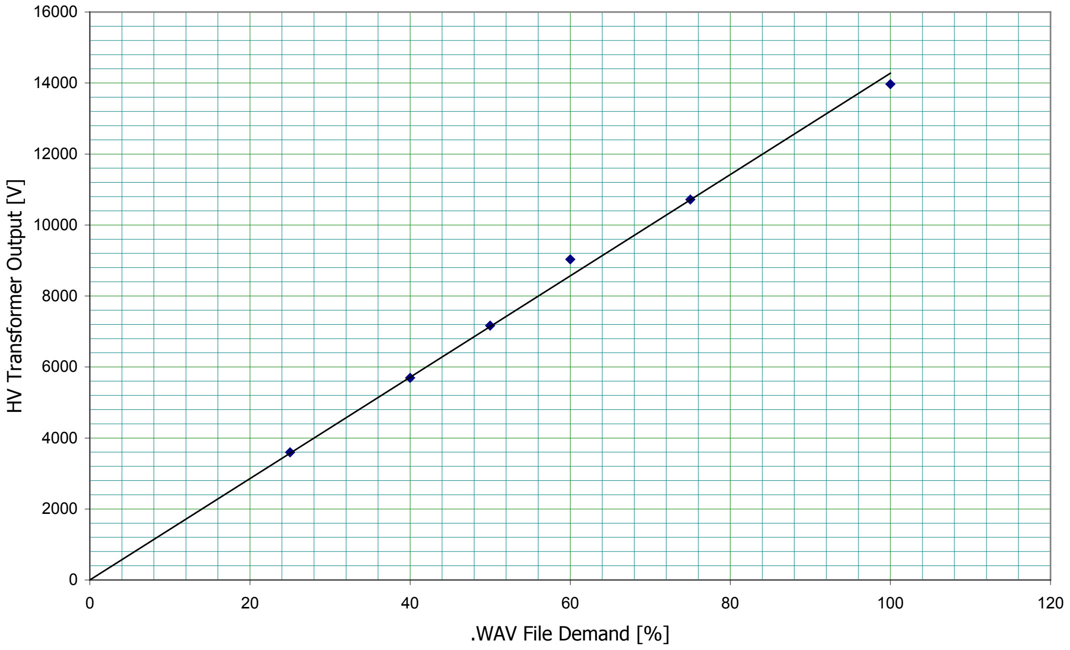

Figure 3.7 HV System Response At 4 kHz

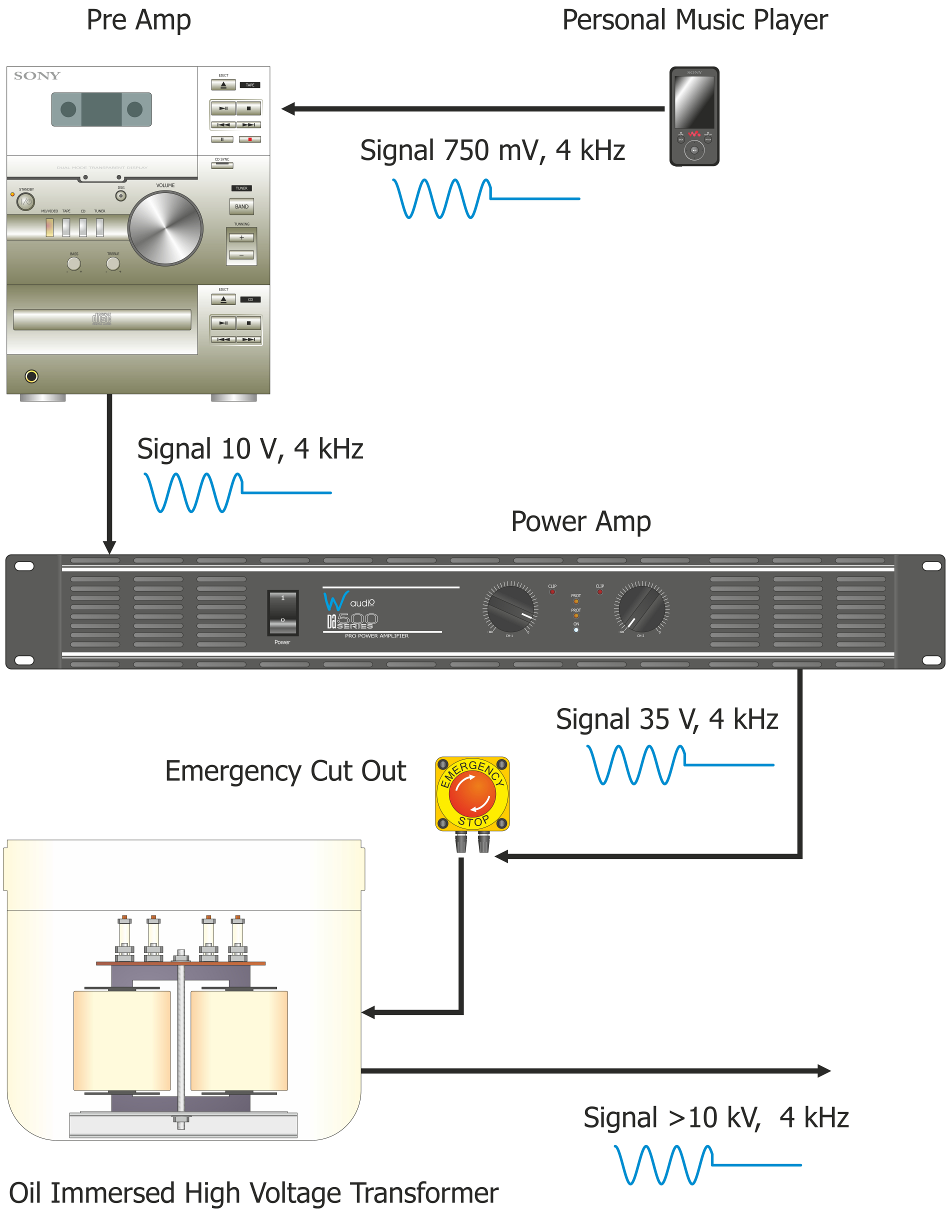

Figure 3.8 PIV High Voltage System

2.3 Actuator And Aerofoil Setup

2.3.1 60 mm Chord Design

The first generation wing design featured a 60 mm chord with a 180 mm width. The dimensions of the first generation wing were limited by the actuator construction technique. The electrodes were deposited using an e-beam evaporator (See chapter 3 Device Development for more information on the actuator construction) and as such any actuator width was limited to 220 mm. To keep the actuator within the area of the chamber which exhibits uniform deposition a value for the width of 180 mm was selected. Chord was decided by the need to keep the aspect ratio of the wing large enough for it to still be considered a

2D aerofoil and was therefore set at 3:1 giving a chord value of 60 mm. Figure 2.9 shows how the step and wing profile was created, with the base as a standard NACA 0012 aerofoil. High lift, specialised aerofoils were considered for the basis of this study and could be more directly applicable to MAV development. However, the generality, highly studied and well documented nature of the NACA 0012 made it a better candidate for this research and would provide a basis for comparison with published literature. Another consideration in choosing the profile was that the addition of the separation step was going to significantly modify the flow behaviour and characteristics from that of its parent aerofoil anyway, therefore it was considered an unnecessary complexity to choose anything other than a simple symmetric profile. The trailing edge separation ramp was specified using the angle from horizontal (20°) and the distance from the centreline as a percentage of chord (5%). The point this represented was then connected by straight lines to the trailing edge of the aerofoil downstream and the tangent point on the NACA 0012 profile upstream.

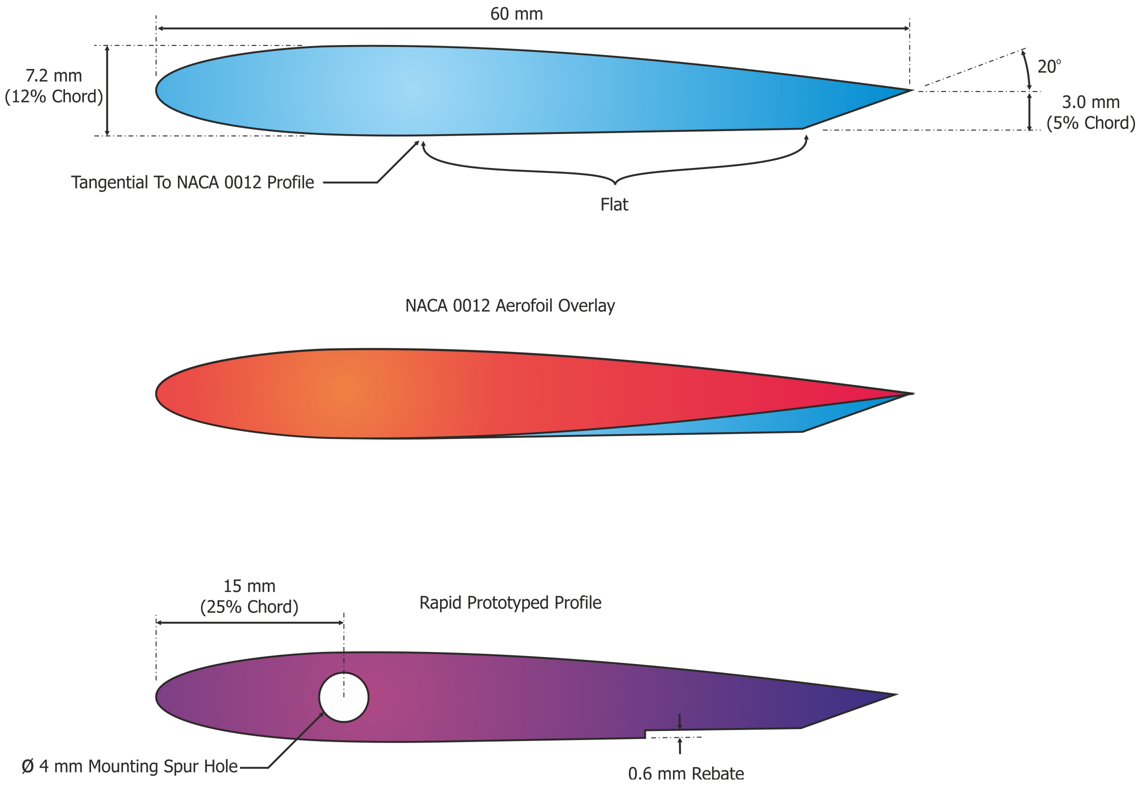

Figure 3.9 60 mm Chord Wing Profile

The wing was produced in a single piece on a rapid prototyping machine (Eden 500V, Objet) using the 'FullCure720' acrylic based UV cured polymer. The profile was generated by a computer program written in basic which took the equations that define a NACA 0012 wing, and the additional step angle and height information, and output a set of XY points which were then used to create the profile in SolidWorks. The additional mounting spur hole and rebate shown in Figure 2.9 were cut away and the resultant part was exported to the '.STL' format used by the 3D printer. The finished wing emerges from the printer encased in a soft support materiel which allows for complex structures and overhangs to be correctly printed. The bulk of this support materiel was simply pealed away form the wing profile. A subsequent sodium hydroxide bath followed by cleaning with acetone removed any remaining traces of the support materiel. Finally the surface of the wing was carefully rubbed smooth with 800 grit emery paper to remove any trace of the individual layers of the print.

To assemble the actuator onto the printed wing assembly, a gluing jig was used to force the actuator to follow the contour of the separation step (see Figure 2.10). The jig was CNC machined from aluminium using the same base profile as the wing itself. Meguiars number 8 mould release wax was used to prevent the wing bonding to the jig.

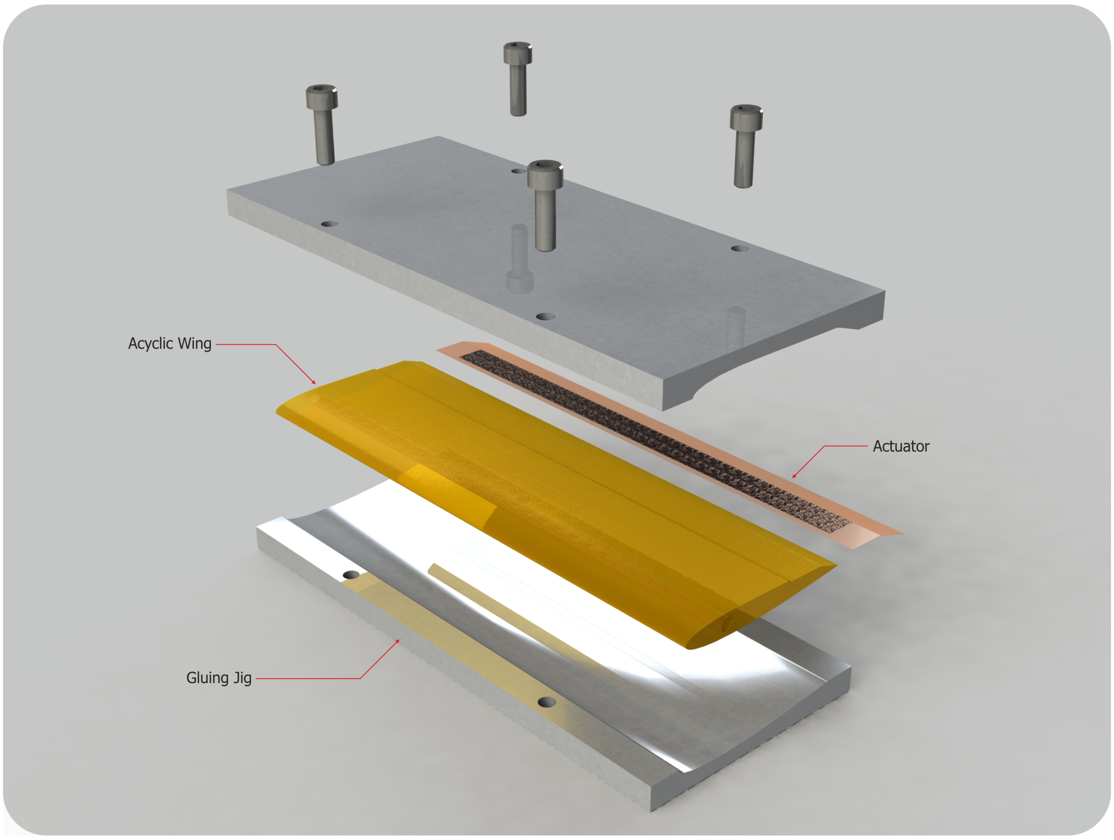

Figure 3.10 60 mm Wing Assembly Procedure

The aerofoil was mounted to the balance using a single sided spur. Two spur designs were used with the 60 mm chord aerofoil. To maintain the electrical isolation of the wing from the balance the spur had to be nonconductive. The first generation was constructed using GRP rod, a 4 mm diameter shaft into the wing and a 12 mm diameter bar from the edge of the wing into the clamp on the balance (see Figure 2.11). Although this worked, it provided unsatisfactory rigidity. The 2nd generation mounting spur provided a significant improvement on this; a 4 mm steel shaft went into the aerofoil and was attached to a steel cup with an interference fit. The steel cup then had a 14 mm diameter alumina shaft epoxied into it. The ceramic shaft was the only part of the assembly to protrude from the tunnel or contact the balance, thus ensuring sufficient electrical isolation even in the event of a trace wire failure electrifying the metal shaft and cup. The use of a lathe and tailstock to manufacture the assembly ensured that the two shafts remained aligned concentrically whilst they cured. For both 60 mm aerofoil spurs the wing was press fit into place and a drop of cyanoacrylate glue at the end of the wing shaft was used to lock it into place. Removal and replacement was performed manually by inducing failure in the glue joint.

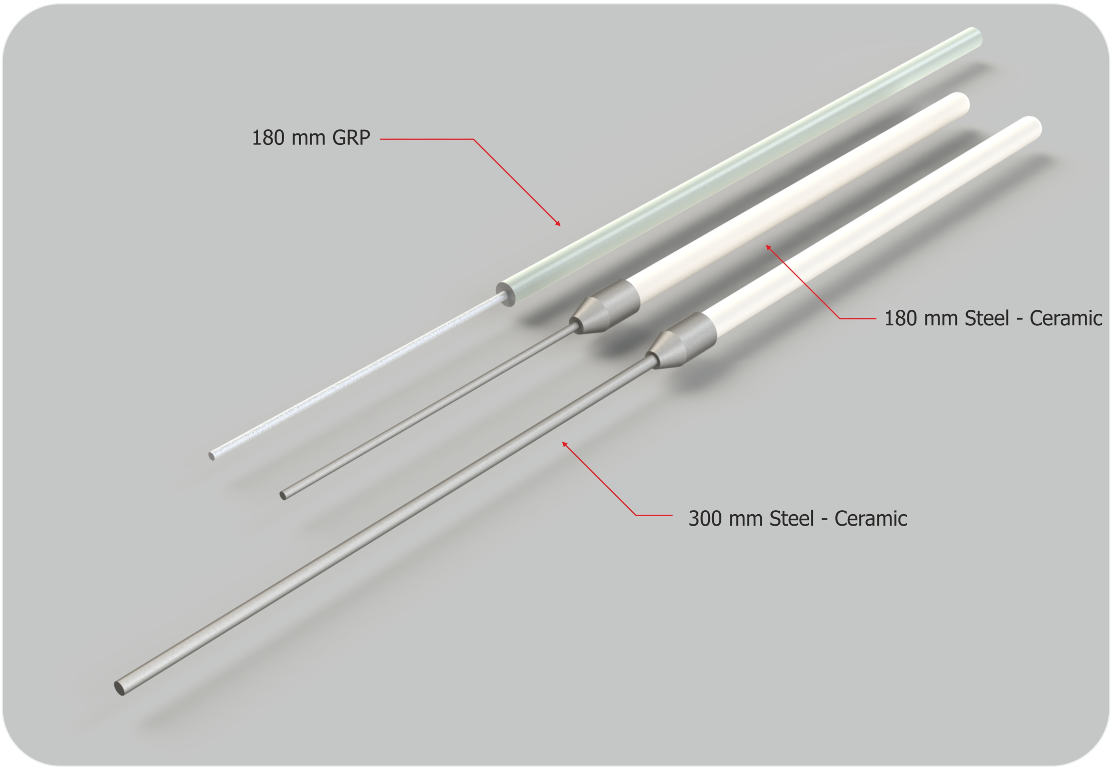

Figure 3.11 Mounting Spur Comparison

2.3.2 100 mm Chord Design

With new actuator manufacturing methods the limitations of the e-beam chamber and reactive ion etch platen size were removed (see Chapter 3 Device development), and so to improve the signal to noise ratio the wing size was enlarged (see section 2.5.3.1). Whilst increasing the wing size the characteristic dimensions of the step were also changed slightly to provide a larger angle and a stronger separation behind the aerofoil. Figure 2.12 shows the changes made to the wing profile and highlights the differences between 1G and 2G designs. The change in the rebate came as a result of some of the failures observed in the 1G wings where the epoxy had failed to fully encapsulate the backside electrode, which allowed sparking around the edge from the positive electrode. By introducing the step at the edge, the ground electrode was better sealed, the definition of the trailing edge of the aerofoil was improved and the positioning of the actuator during gluing was made easier.

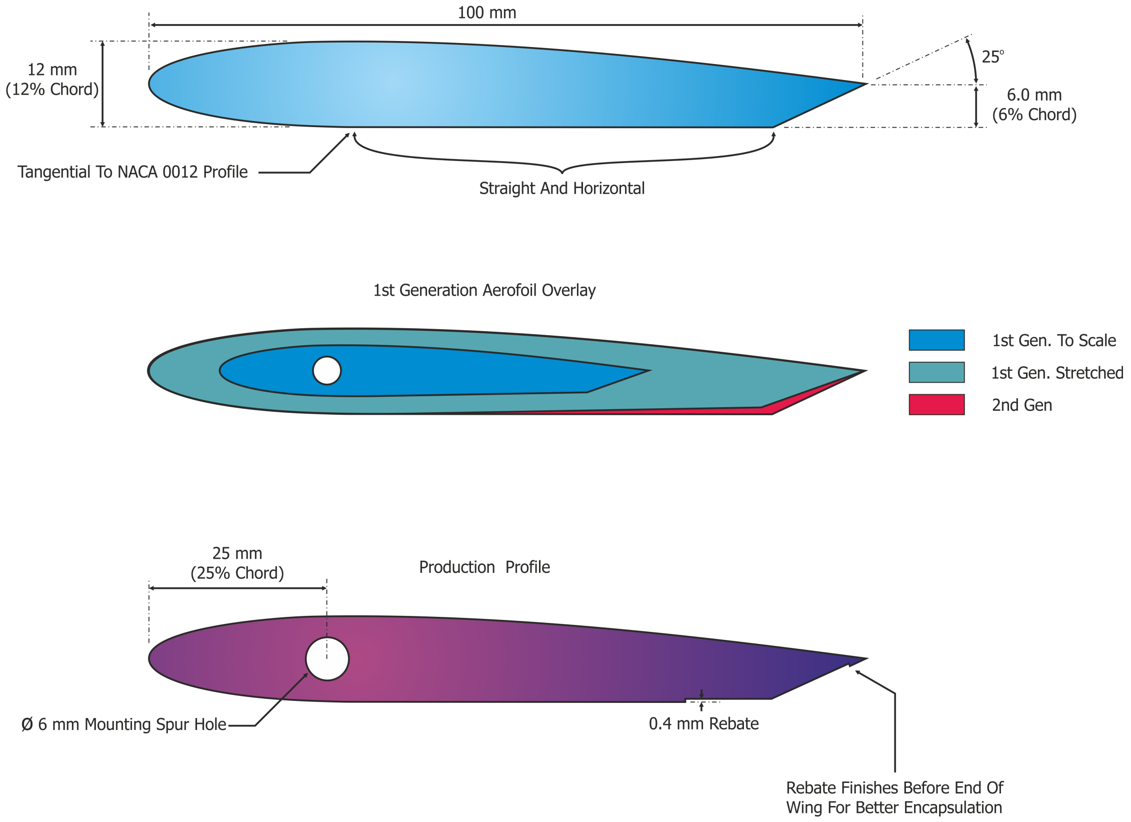

Figure 3.12 100 mm Chord Wing Profile

The actuator for the 100 mm wing, shown in Figure 2.13, was much faster to construct than those for the 60 mm wing. A simple construction from 150 µm Kapton® HN film and 80 µm thick 12 mm wide adhesive backed copper tape was used (Figure 2.13). Because each actuator had a short expected mean time between failure (MTBF) and the 2G wing was nearly 5 times larger, and therefore much more costly to produce on the rapid prototyper than the 1G wing, the use of a single piece disposable wing was impractical. A two piece wing was designed, a front section permanently epoxied onto a steel – ceramic spur and a removable tail section which was fixed in place by a set of pins and holes along the separating line (Figure 2.14). This rear edge has only 26% of the volume of the full wing and consequently a significantly reduced manufacture cost. The same hydroxide wash, acetone clean and smoothing process detailed for the preparation of the raw printed parts for the 60 mm wing-actuator assemblies was applied to both parts of the 100 mm wing. To smooth over the join between the two parts of the wing standard office issue Sellotape® was used as a suitable nonconductive alternative to the aluminium tape usually used for joint coverage on wind tunnel models.

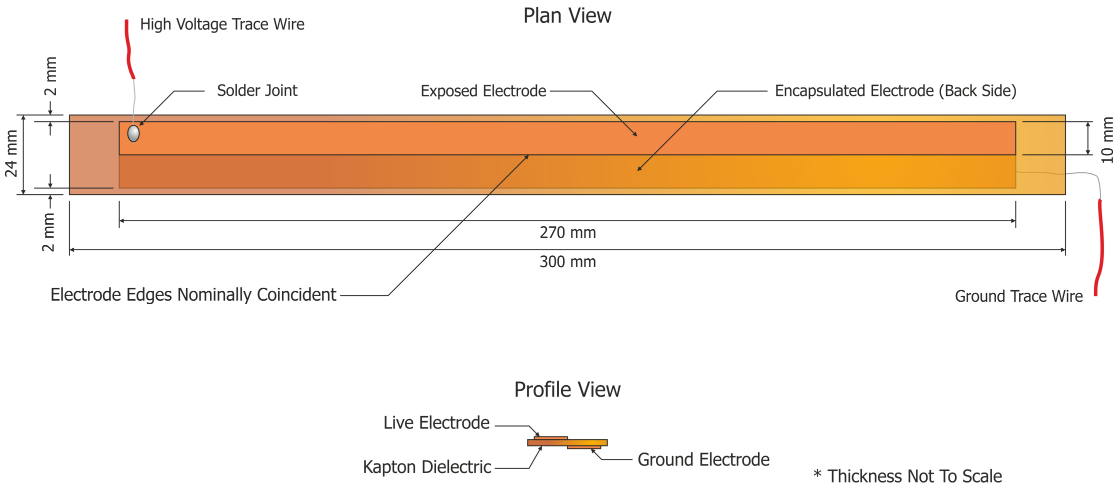

Figure 3.13 100 mm Actuator Construction

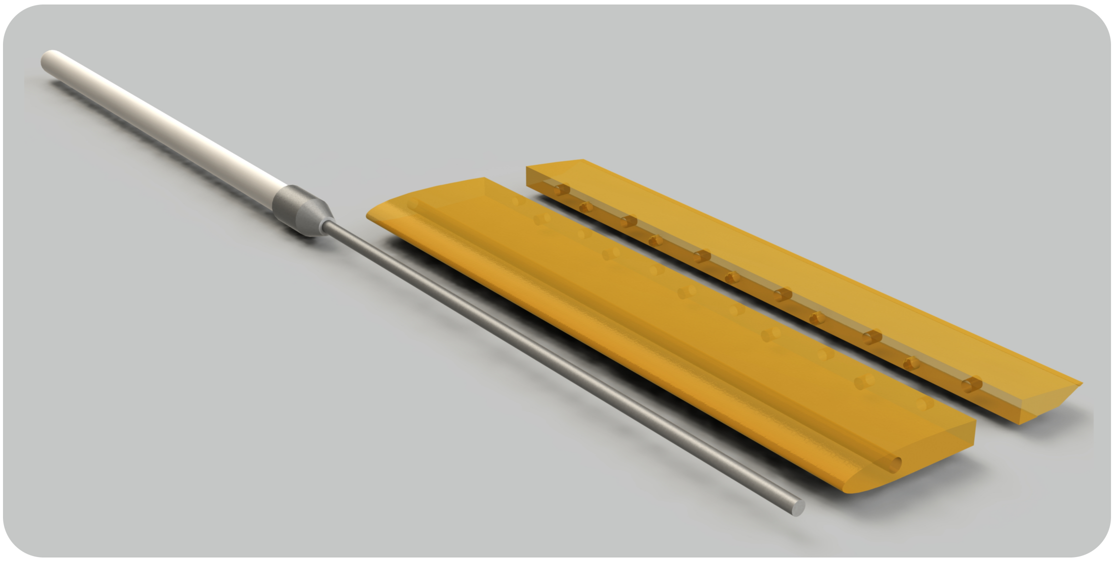

Figure 3.14 100 mm Wing Components

Due to the shape of the end section a simple 2 piece gluing jig could not be machined; the jig used was a four piece construction machined from aluminium, as shown in Figure 2.15. Again Maguire's mould release wax was used but additionally a medium viscosity silicone spray-on mould release agent was used to ensure clean release. Jig cleaning was accomplished using mechanical attack (scalpel) and, when needed, a heat gun to thermally destroy the epoxy.

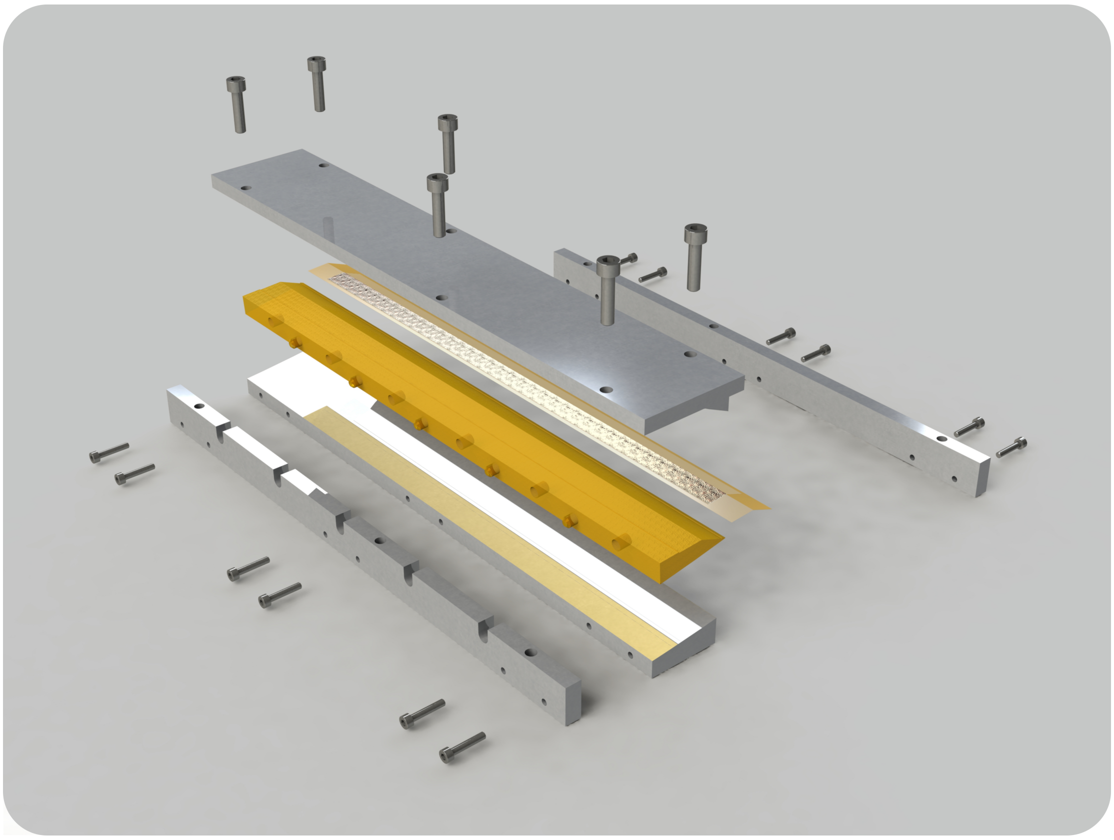

Figure 3.15 100 mm Gluing Jig

2.4 Ozone Management

Ozone is a highly reactive molecule formed when an intense electric field strips a diatomic oxygen molecule apart, forming an oxygen radical, which then reacts with another oxygen molecule according to Equation 1

$$O^{-} + O_2 \rightleftharpoons O_3 + e^{-}$$

Equation 1 - Formation Of Ozone

The high oxidation potential of ozone means that when it comes into contact with biological systems it chemically attacks them. It is used as a powerful and taste free biocide system to kill bacteria, mould spores and viruses [115-116] for swimming pools, drinking water and even medical instruments [117]. Ozone also reacts with tissues when inhaled. It attacks the lining of the lung leading to pneumonia and fluid build up.

Table 2.1 shows the effects of different ozone concentrations and exposure durations on the human body. With the possibility of death the build up of ozone in the lab needed to be assessed and monitored carefully.

	Concentration (ppb)	Duration	Effect
Acceptable	10-40	∞	Odour Threshold
	100	8 hr Exposure Limit	Eye, Nose & Throat Irritation
	>100	Few Minutes	Headache & Shortness Of Breath
Hazardous	250-500	2-5 hr	Reduction In Lung Function For Susceptible People
	300	15 min Exposure Limit	
	400	2 hrs	Reduction In Lung Function For All People
	>600	1-2 hrs	Chest Pain & Dry Cough
	1000	1-2 hrs	Lung Irritation
	>1500	2 hrs	Fluid Build Up In Lungs. Reduced Concentration.
	9000	Intermittent	Pneumonia
Lethal	10000	< 1min	Severe Heath Affects
	11000	15 min	Unconsciousness
	50000	30 min	Fatal

Table 2.1 Biological Effects Of Ozone [118]

Ozone also occurs naturally in the troposphere through the action of ultraviolet light at less then 240 nm [119] on nitrogen oxides (NO_x) and carbon monoxide (CO) released into the atmosphere by industry and vehicles. To deal with the health threat to the population posed by ozone levels, governmental and legislative bodies have come up with guidelines for the maximum ozone concentration which is can be considered safe for long term exposure. These values are in Table 2.2. Conversion between $\mu g.m^{-3}$ and ppb assumes ideal gas theory applies and is done at the atmospheric conditions present in the lab when the ozone rate testing was conducted of 99300 Pa and 295 K.

Organisation	8hr Limit µg.m^{-3}	8hr Limit (ppb)
World Health Organisation [120]	100	51.4
UK Environmental Protection [121]	100	51.4
EU Directive 2002/3/EC [121]	120	61.7
US Environmental Protection Agency [122]	145.9	75
UK Health and Safety Executive (1986) [123]	194.5	100
UK Health and Safety Executive (2005) [124]	389 (15 min)	200 (15 min)

Table 2.2 Atmospheric Ozone Exposure Limits

To ensure that ozone production in this experiment does not pose a health and safety threat the ozone concentration in the lab must not exceed 50 ppb; this is well below HSE guidelines and a figure considered clean air by all regulatory bodies. To assess the rate of production of ozone by the plasma actuator tests were run in a sealed system along with an Aeroqual S200 ozone monitor with a 0-500 ppb sensor head attached. The test actuator consisted of a 180 mm wide 1st generation actuator driven by the 1st generation HV setup detailed earlier. By running the plasma discharge system for a known time and using a fan to achieve a homogeneous ozone distribution within a small 0.0511 m^3 box measurable ozone concentrations can be generated rapidly and repeatability and a rate of ozone production can be calculated in mol.s^{-1}. Taken from the average of 10 concentration readings from 10 s of plasma run time the average concentration achieved was 0.2313 ppm. Using the known molar contents of the container used ozone production rate can be estimated at 4.97x10^{-8} mol.s^{-1}. The volume of air in the wind tunnel lab contains approximately 17330 mol. From this the amount of ozone required to give the critical concentration of ozone set at 50 ppb can be calculated as 8.67x10^{-4} mol. Assuming the worst possible case scenario of a zero rate on the reverse reaction to diatomic oxygen and zero ventilation loss the time to critical concentration can be calculated with the estimated production rate to be 18100 s. This equates to just over 5 hours of continuous running at maximum power. As the figures showed critical concentration would take a significant length of time to build up, standard operating procedure was established as to be to open one of the windows directly downwind of the tunnel exhaust jet, and another near the tunnel inlet to create a low level but constant forced ventilation of the room. In addition to this an ozone monitor was to be used to check in room ozone levels when running for extended periods. Whenever developments were made to the actuator design or HV generation system ozone levels in the room were carefully monitored during the first full length test run of a new configuration, ensuring that they remained below the safe limit with the ventilation system in place. In practice the ventilation level required to keep the lab at constant temperature due to the energy input from the tunnel exceeded the ventilation requirement for ozone removal.

2.5 Wind Tunnel Force Balance Measurements

2.5.1 The 'Plint' Tunnel

The Plint wind tunnel is a 0.46 m x 0.46 m test section tunnel in an upstream fan configuration, with a layout as shown in Figure 2.16. Manufactured by Plint and Company Ltd. in Wokingham it has a design speed of 20 $m.s^{-1}$ and a turbulence intensity of <0.25% [125]. The low turbulence intensity of this tunnel is achieved through a series of screens in the diffuser and settling chamber which ensure good homogeneity of the flow going into the high nozzle area ratio contraction before the test section. This 9:1 contraction serves to further suppress any fluctuations which were present in the settling chamber area before the flow reaches the test section. The tunnel is driven by a 20 kW radial fan blowing air through the tunnel. Flow velocity is controlled by a throttle, increasing restriction at the fan inlet and is continuously variable from 3.5 – 21 $m.s^{-1}$. Tunnel velocity is calculated from the built in upstream and downstream pressure taping rings which each average over 4 positions around the perimeter of the tunnel upstream and downstream of the contraction. A nozzle calibration was used to return the true static and dynamic pressures in the tunnel test section based on the data from the pressure tapings on the tunnel contraction. This calibration was generated using a Pitot-static tube placed in the tunnel test section as the reference.

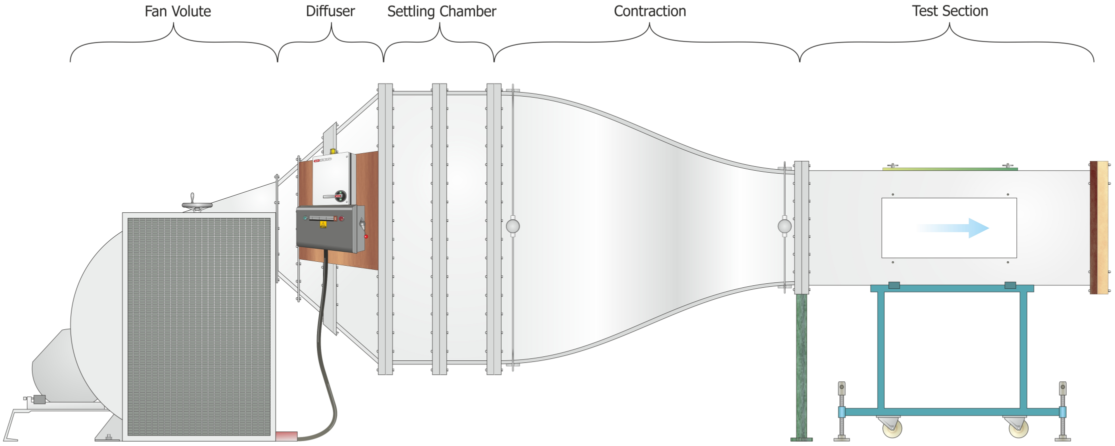

Figure 3.16 Plint Tunnel Sections

2.5.2 Tunnel Master Control Program (MCP)

The tunnel system is controlled by a National Instruments USB-6218, a 16 bit, 32 channel data acquisition module. It also possesses 2 analogue and 8 digital output lines, these are controlled by the MCP to fully automate and control the data collection process. The MCP was written in C using the NI-DAQmx windows USB libraries supplied by National Instruments, these libraries were used along with many proprietary in-house routines for handling standardised I/O, calibrations and corrections associated with experimental aerodynamics.

The 4 functions of the MCP are:

- Closed loop tunnel speed control
- Plasma waveform calculation and output
- Stepper motor indexing for incidence control
- Force balance & velocity transducer voltage logging

The program flow is laid out in Figure 2.17: of specific note is the way in which the program deals with tunnel speed control. Because the air flow is mechanically throttled rather than reduced by decreasing the fan speed a simple output demand voltage from the DAQ could not be used to set tunnel velocity. Speed was controlled by installing a 24 V DC, 100 W electric motor to the leadscrew of the wind tunnel throttle. The drive speed was reduced through a 50:1 worm - wheel gearbox integrated onto the front of the motor housing. The motor was fed from a current limiting power supply - this was set to allow sufficient current to start and move the shutters under normal conditions, but if the motor runs into the end stops the stall current and torque are sufficiently low so that the motor does not overheat and the threads on the lead screw or teeth on the gears would not strip. The motor direction and operation was controlled using 2 of the digital output pins from the DAQ. These feed into a relay box which could change the polarity of the power supply connections to the motor as well as disconnect it completely. Standard tunnel control systems would apply a PID control strategy to a fan speed demand voltage to get to a set point. However this mechano-electrical solution being tri-state only offers 3 options; making the tunnel faster, slower or leaving it as it is. PID control cannot be applied to a tri-state device like this: to approach the set point with speed and accuracy a two stage approach was implemented in software. When the deviation from set point was greater than 0.75 m.s^{-1} the motor was turned on continually and short sample time average velocity readings were repeatedly taken as the throttle valve was being moved. When the deviation from the set point fell below 0.75 m.s^{-1} the control program moved into its fine tuning routine. The fine tuning routine turned on the motor for a fixed 0.15 s pulse to turn the throttle lead screw by a fraction of a revolution. The program then takes a long sample time average tunnel reading, and further pulses were applied until the velocity reading was within 0.075 m.s^{-1} of the target point. During this process the software was watching for a lack of change in the tunnel velocity despite powering the motor: this was to safeguard against running the throttle control motor for too long in a stall condition if it runs into the stops at the end of the throttle travel.

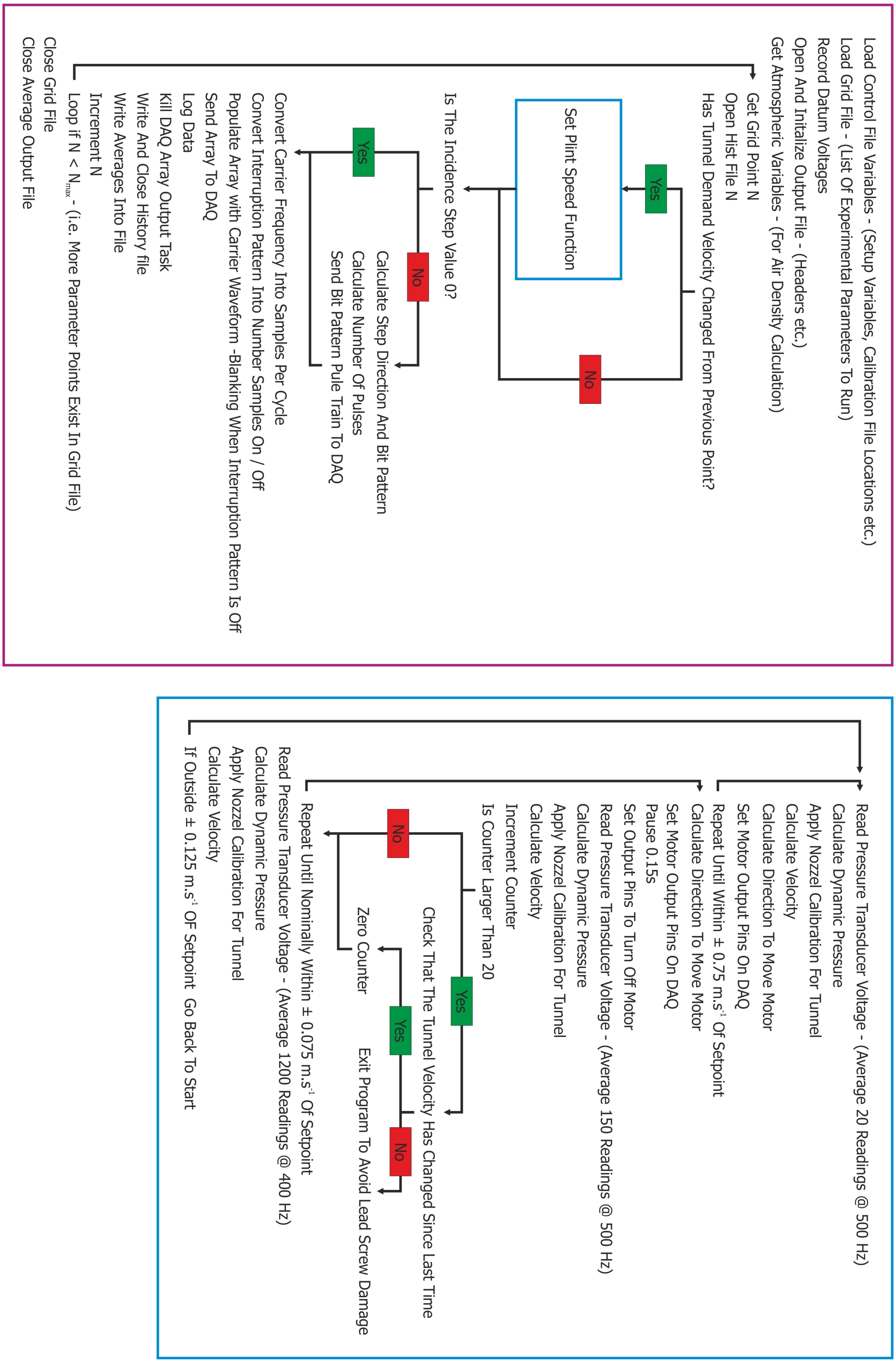

Figure 3.17 Tunnel Control Flow Chart

2.5.3 Three Component Balance

An existing 3 component balance was used. This was manufactured in-house from DS Europe load cells (model 535, full scale deflection of 6 kg). These load cells are an externally amplified strain gauge based design with a z fold construction - these can be seen labelled in Figure 2.18. The balance is configured to give lift, drag and pitching moment as the 3 resolved components. The construction uses 1.2 mm steel piano wire flexures to support the live plate and transfer the force to the strain gauges. The piano wire flexures provide a more repeatable resistance to displacement than the stiction of a tribological joint (Figure 2.18).

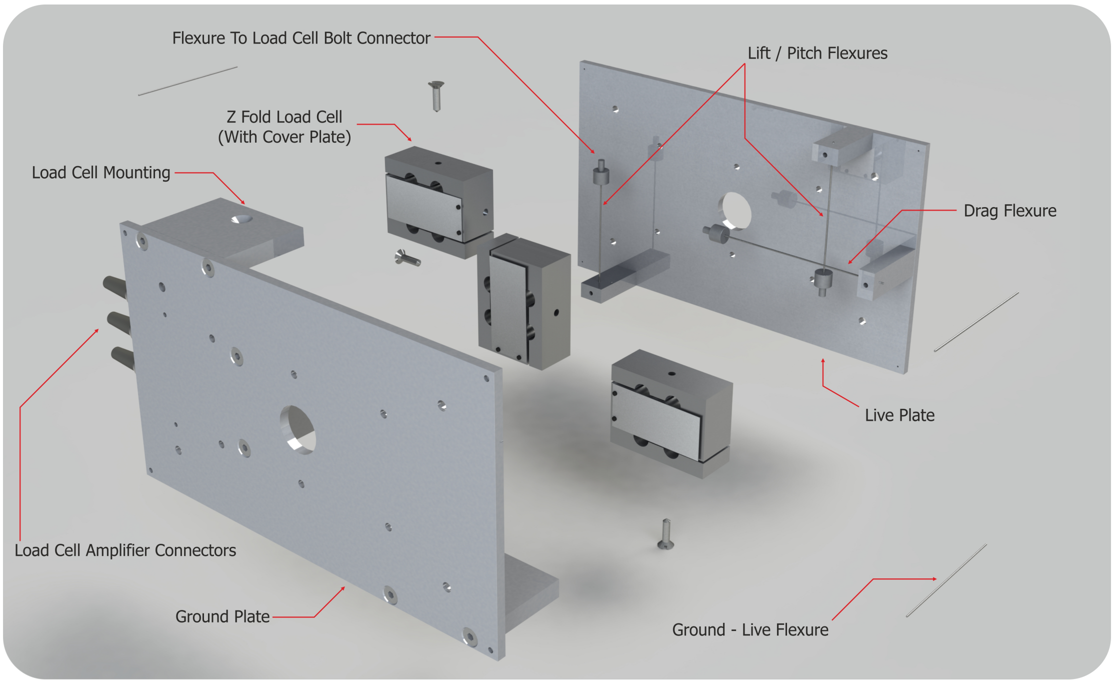

Figure 3.18 3 Component Exploded View

The balance was mounted to the side of the tunnel via an access panel (Figure 2.19). Connected to the live plate of the balance is a Time and Precision turntable. The advantage of putting the turntable on the live plate was that the resolved forces from the balance stayed in the same reference frame: the disadvantage is that the control wire for the stepper motor had to bridge the live and static sides of the balance. To minimise the effects of this a special extension connector cable was constructed, with each of the 4 conductors for the section bridging the gap between the tunnel side and the turntable consisting of 8 individual lengths of very fine gauge lacquer insulated magnet wire. These wires were not bound together but were loosely coiled into a long spring like structure on a per conductor basis. This provided very low weight and negligible stiffness whilst also being able to carry the 1.5 A holding current of stepper. The reduction ratio of the turntable (100:1) and 3.75° ½ step angle of the stepper driver – motor combination allowed turntable repeatability to be less than the 0.1° resolution of the inclinometer (Smart Tool Level, Mecklenburg-Duncan) used to set up the aerofoil incidence. Turntable drift was assessed by zeroing the inclinometer on the wing and then continuously driving the wing backwards and forwards through $\pm 10^o$ with the wind tunnel at maximum velocity for over an hour, cycling between the two incidence angles approximately 400 times, wing incidence angle was then re-measured and found to have returned sufficiently accurately to 0^o for any difference to be unresolvable with the inclinometer.

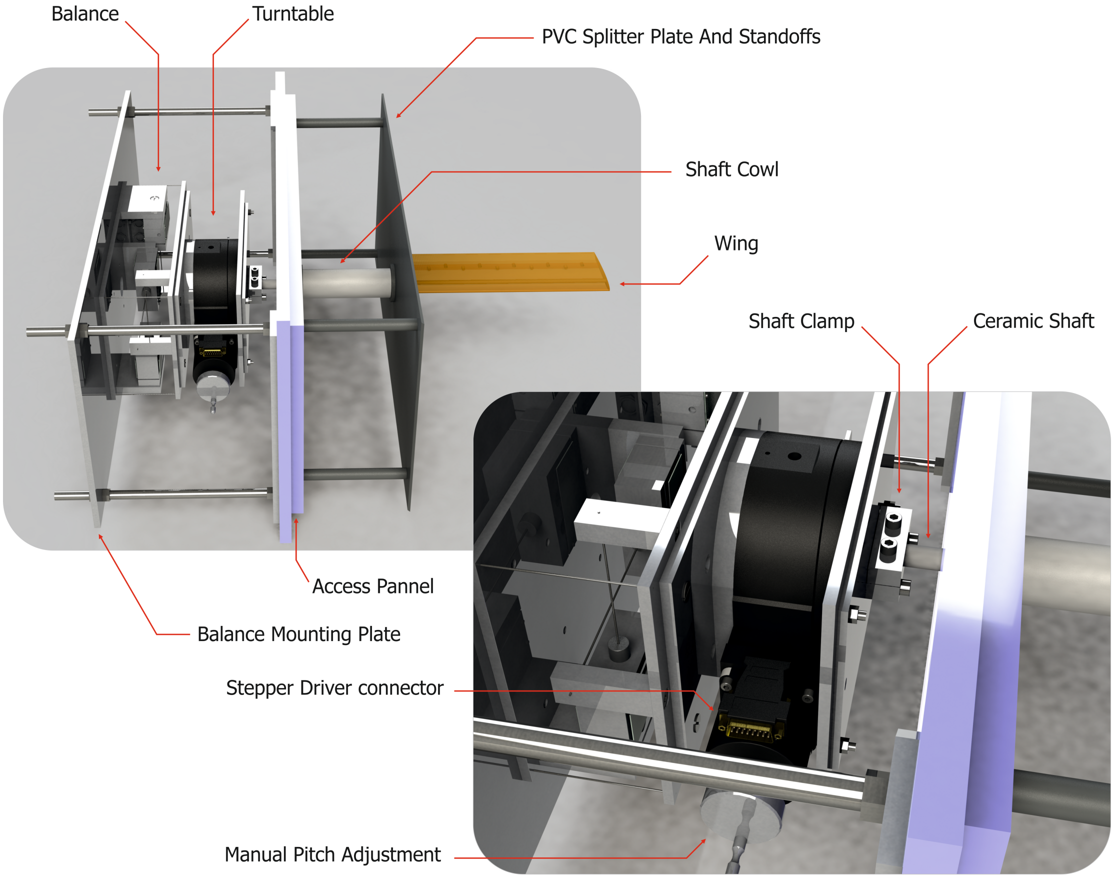

Figure 3.19 3 Component Balance On Tunnel Access Panel

Figure 2.20 a & b show how the tunnel control and experimental measurement systems fit onto the wind tunnel.

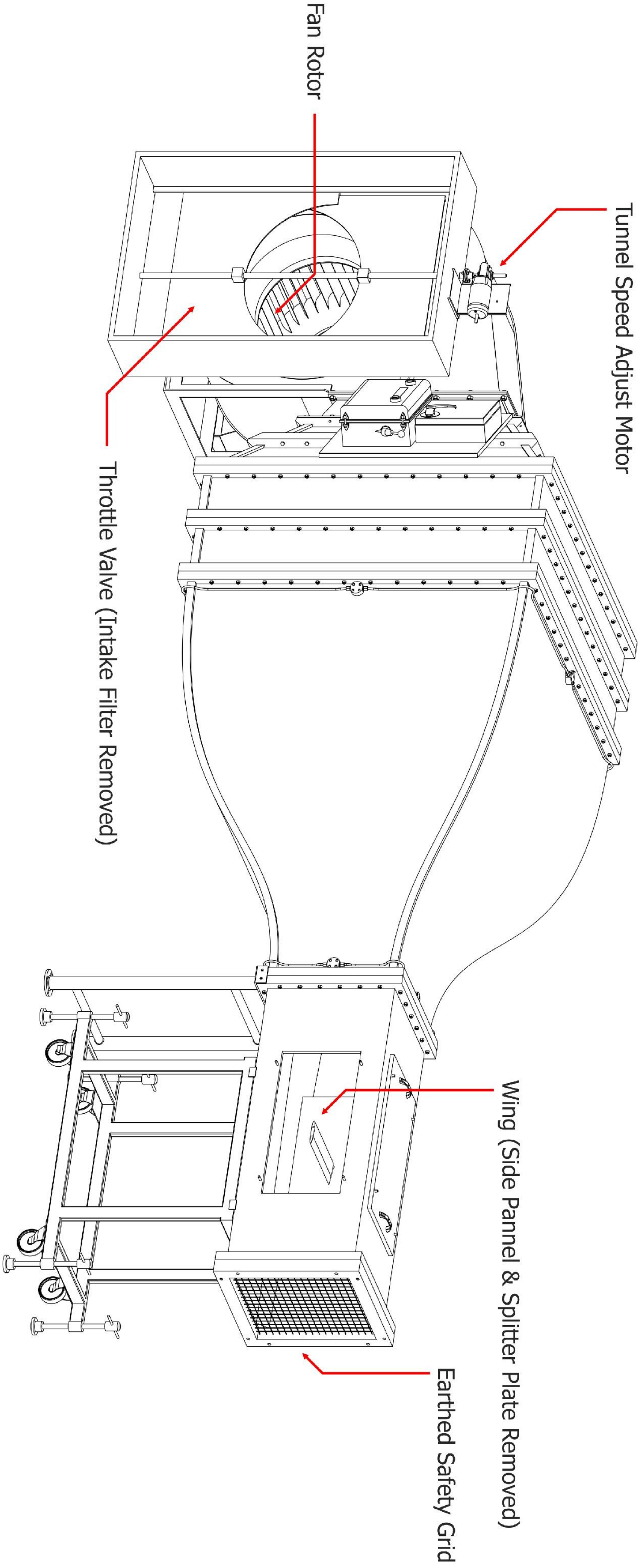

Figure 3.20a Force Measurement Tunnel Setup

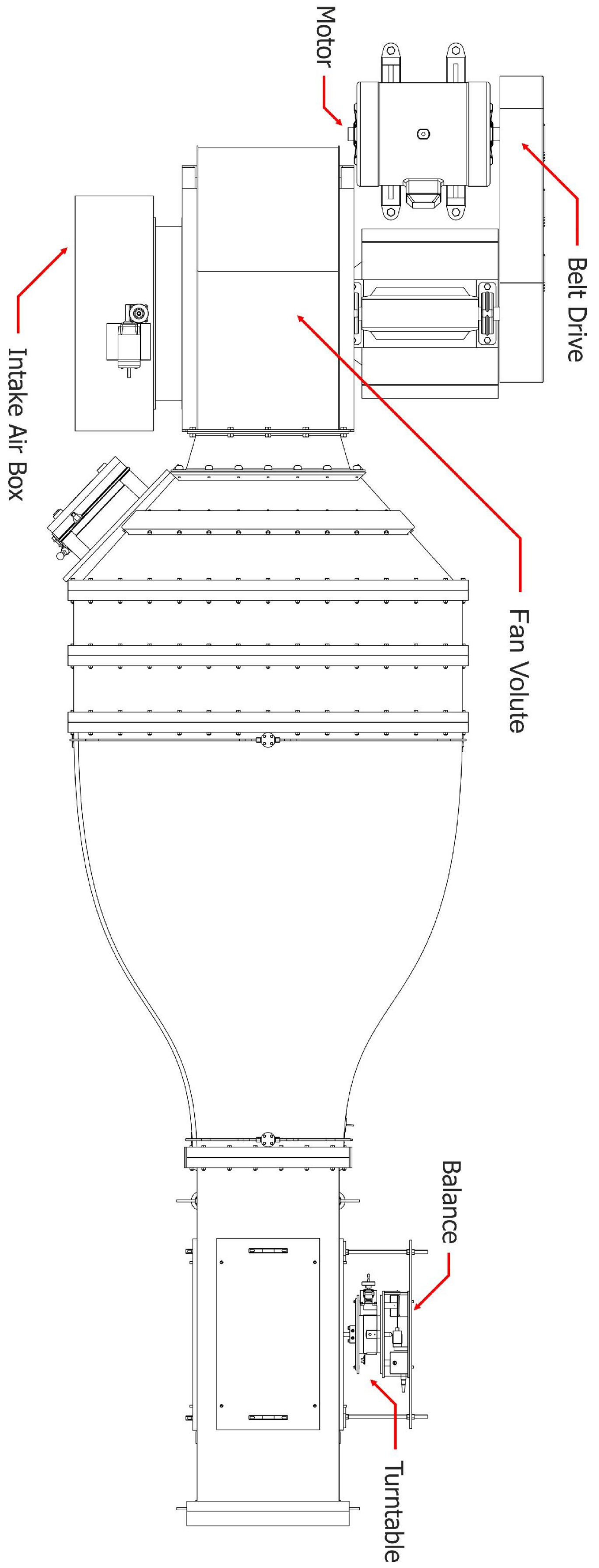
Motor
Belt Drive
Intake Air Box
Fan Volute
Balance
Turntable

Figure 2.20b

Figure 3.21 shows the blockage ratio for the tunnel with the 100 mm chord wing installed along with the splitter plates and shaft cowl. As can be seen no matter which way you calculate the blockage for the tunnel the value for the 0° incidence case is within the accepted normal range. At 15° incidence the blockage ratio is fractionally high when considering the total blockage level in the test section, however 15° is beyond the stall point for the aerofoil and data was only taken at this incidence for lift curve characterisations, the maximum incidence used for plasma actuated runs was 10°. At 10° incidence the figures become 10.05% and 5.72% for the 3D flow and 2D flow blockage ratios respectively, as such blockage in the tunnel shouldn't be considered to be a problem.

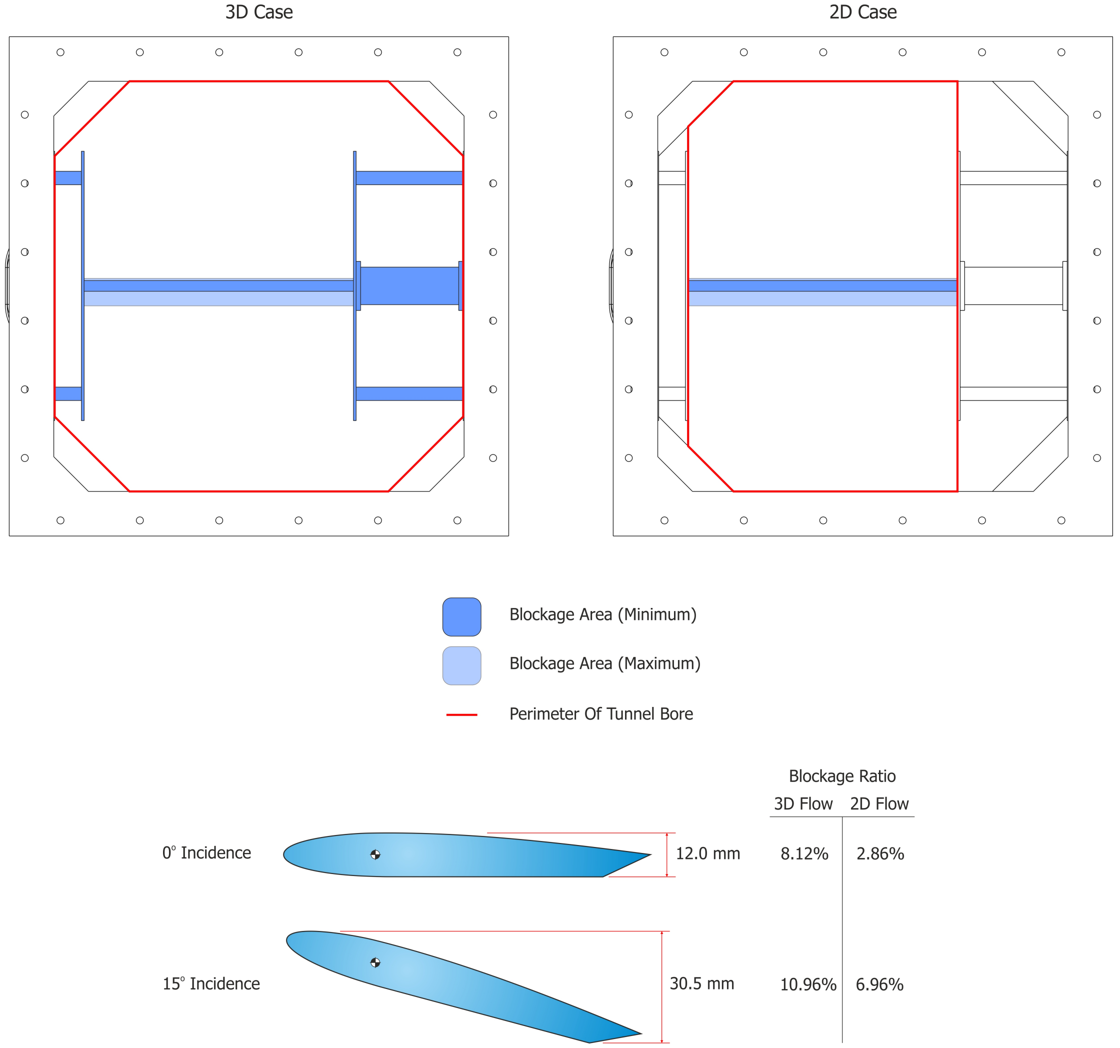

Figure 3.21 Blockage Ratio Calculations

2.5.3.1 Calibration & Repeatability

The calibration of the balance was carried out by sequentially adding reference weights up to the maximum loading and then removing them one by one. For the final calibration the balance was cycled through loaded and unloaded states 3 times to ensure the readings repeated and no hysteresis issues were present. Voltages were logged at each point for 16 kibi samples (KiSa) and averaged. To calibrate the lift load cells, the masses were applied directly to a 12 mm steel shaft secured in place of the wing spur. Drag calibration was achieved by running monofilament fishing line horizontally from the steel shaft and then over a very low friction pulley running on dual open cage unlubricated ball bearing races: weights were then hung from this to provide known drag force. Pitch response of the 2 lift load cells was calibrated by hanging the weights off the end of 100 mm arm fixed to the central steel shaft. As the expected experimental forces were very small special care was taken to ensure that all possible hysteresis effects in the balance were eliminated. Hysteresis showed up on the original calibration charts as differences between the load cell voltages for the two readings at the same applied load as the balance was loaded and then unloaded (see Figure 2.21 and Figure 2.22). The balance had to be stripped down and rebuilt before the final detectable hysteresis source was eliminated: a small piece of aged Sellotape which had peeled off a wire and was brushing gently against the live side. During the strip down the load cell sensitivity and zero points were also reset.

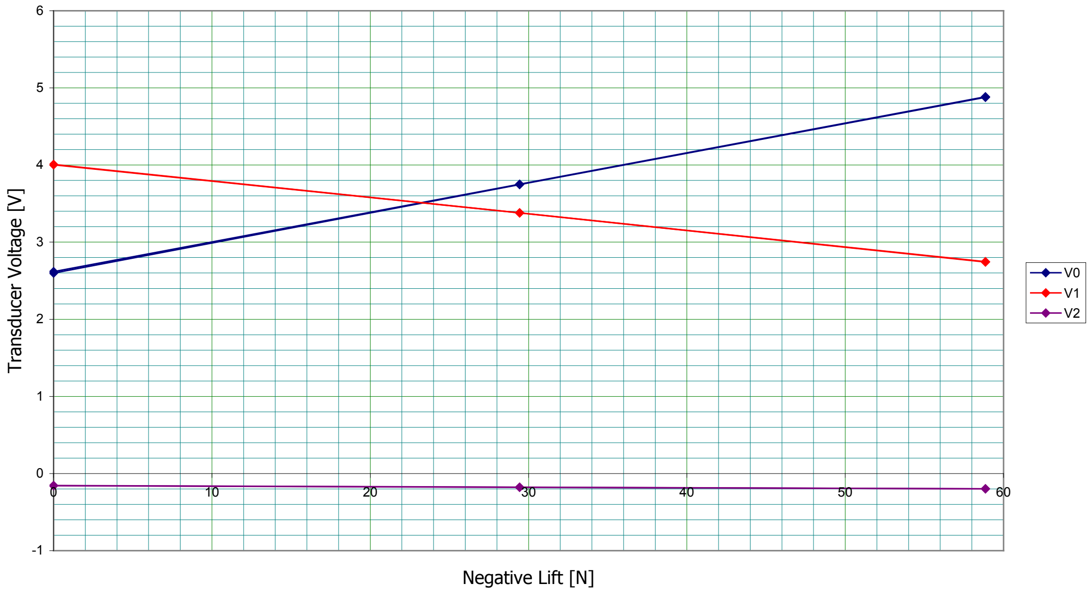

Figure 3.22 Original Calibration Load Cell Measurements

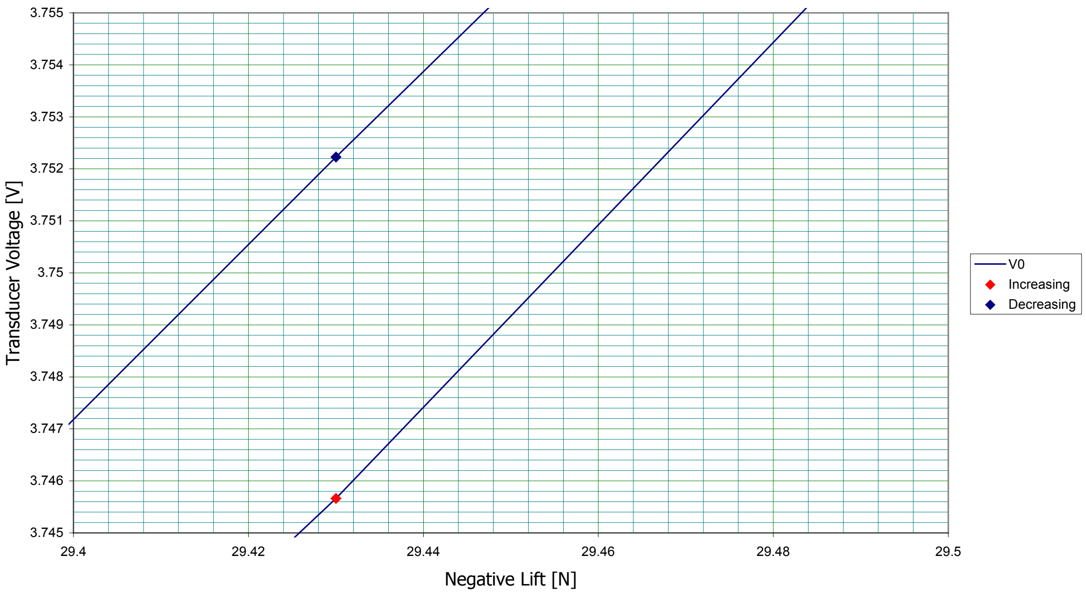

Figure 3.23 Zoomed In View Of Hysteresis In Original Calibration

The final raw calibration data is shown in Figure 2.23 and Figure 2.24; note the order of magnitude improvement in the voltage scales between the zoomed in sections shown in Figure 2.22 and Figure 2.24. From this data the calibration matrix was calculated in accordance with Equation 2. As the wind tunnel software is set up to work with 6 component balances, unused components of the matrix are zeroed out.

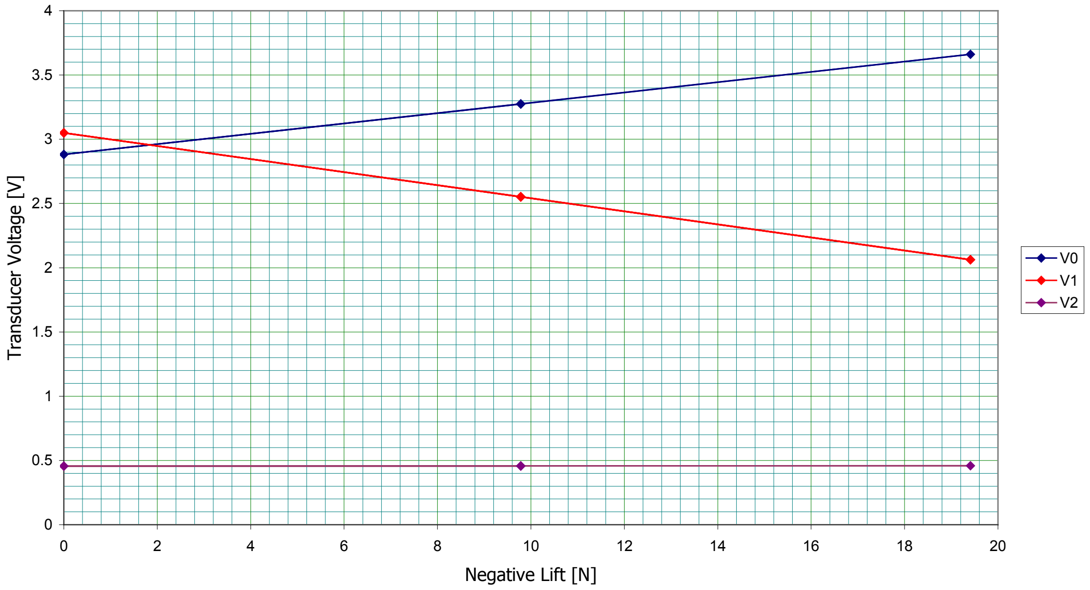

Figure 3.24 Rebuilt Balance Calibration Measurements

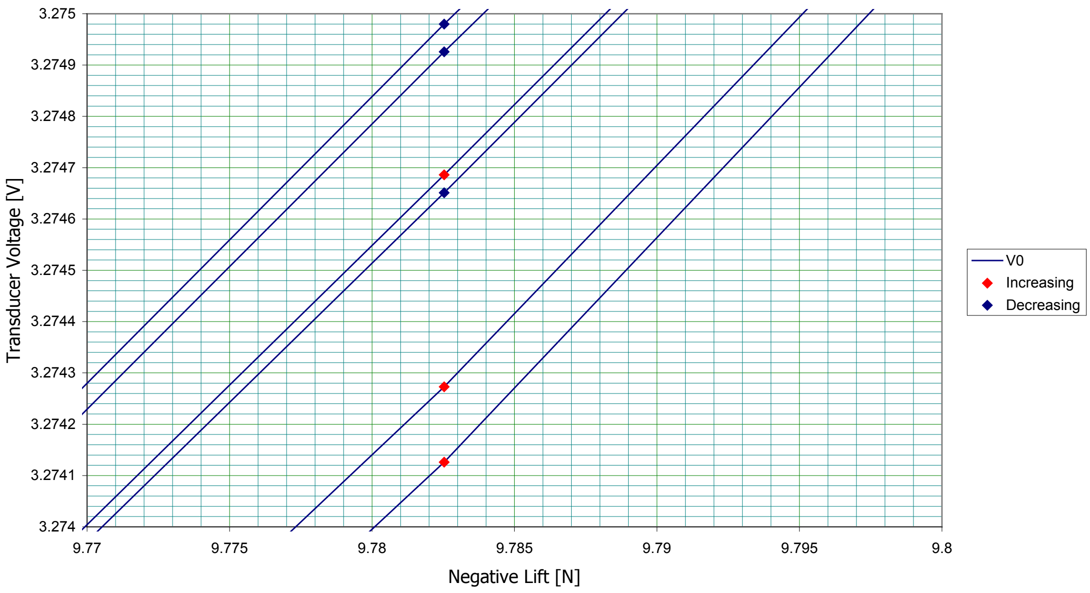

Figure 3.25 Hysteresis In Final Calibration

$$
\begin{bmatrix} \\ \mathrm{Cal} \\ \\ \end{bmatrix} = \begin{bmatrix} \nabla(V_o = f(\mathrm{Drag})) & \nabla(V_1 = f(\mathrm{Drag})) & \nabla(V_2 = f(\mathrm{Drag})) \\ \nabla(V_o = f(\mathrm{Lift})) & \nabla(V_1 = f(\mathrm{Lift})) & \nabla(V_2 = f(\mathrm{Lift})) \\ \nabla((V_o - f(\mathrm{Lift})) = f(\mathrm{Pitch})) & \nabla((V_1 - f(\mathrm{Lift})) = f(\mathrm{Pitch})) & \nabla((V_2 - f(\mathrm{Lift})) = f(\mathrm{Pitch})) \end{bmatrix}^{-1}
$$

NB: Pitch = Lift * Moment Arm Length

Equation 2 - Balance Calibration Matrix

The repeatability of the balance was assessed by taking 75 pairs of readings, first with no mass applied and then with a nominal 30 g mass applied. Each reading consisted of 2048 samples at 512 Hz. A high precision microbalance was used to calculate the actual mass applied each time was 29.9227 g this gives a force of 0.29368 N when g is adjusted for Durham's latitude and elevation according the formula provided by NPL (see Equation 3) [126] to give g = 9.81669 $m.s^{-2}$. Calculating the difference between the two readings and subtracting either the mean reading or the actual applied load and then ordering the data produced (Figure 2.25 and Figure 2.26 respectively). Figure 2.25 shows that the noise introduced by the balance follows a normal distribution with the characteristic S shaped plot crossing the y axis at 0.5. From this we can calculate the 90% confidence interval to be approximately ±0.022 N with this logging configuration.

$$g = 9.780\,327\,(1 + A \sin^2 L - B \sin^2 2L) - 3.086 \times 10^{-6} H \,\mathrm{m \cdot s^{-2}}$$

Where:

$A = 0.0053024$
$B = 0.0000058$
$L =$ latitude
$H =$ height in metres above sea level

Equation 3 - Variation In Local Gravitational Field

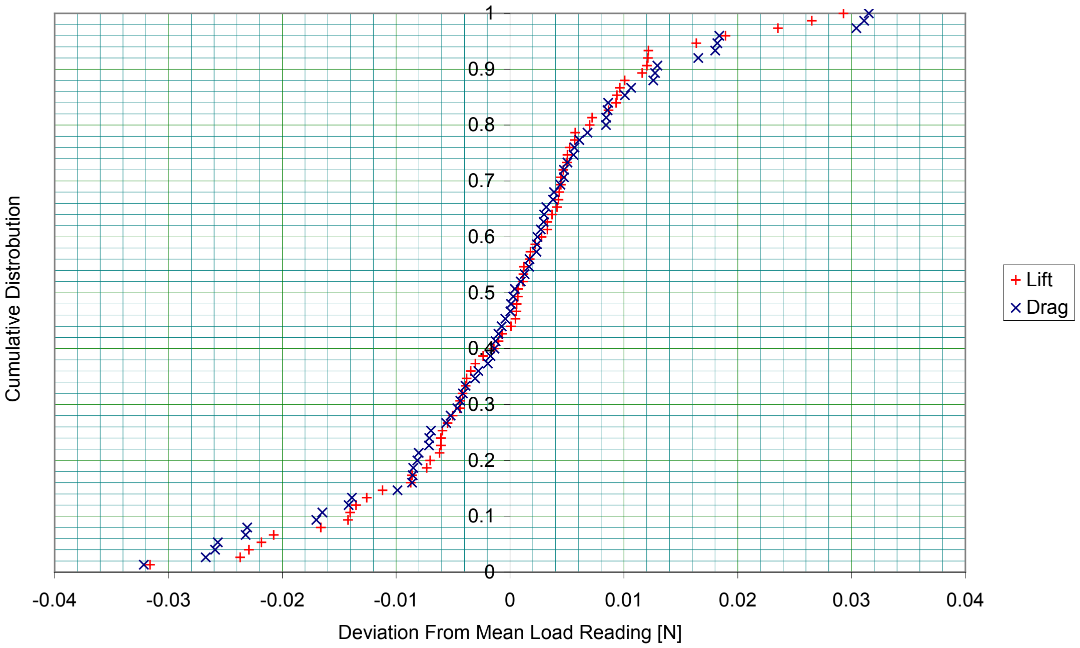

Figure 3.26 Deviation From Mean Load

From Figure 2.26 it can be seen that the calibration is slightly off at this loading, as when the data is compared to the true value for the load a slight shift of +0.002 N is observed. It is also notable that the noise on the lift and drag channels is almost identical, despite the fact the balance was set up horizontal and perpendicular to the ground and the mass was only applied along the lift axis. This indicates that noise at that level is load independent and the true resolution of the logging equipment and load cells is being shown.

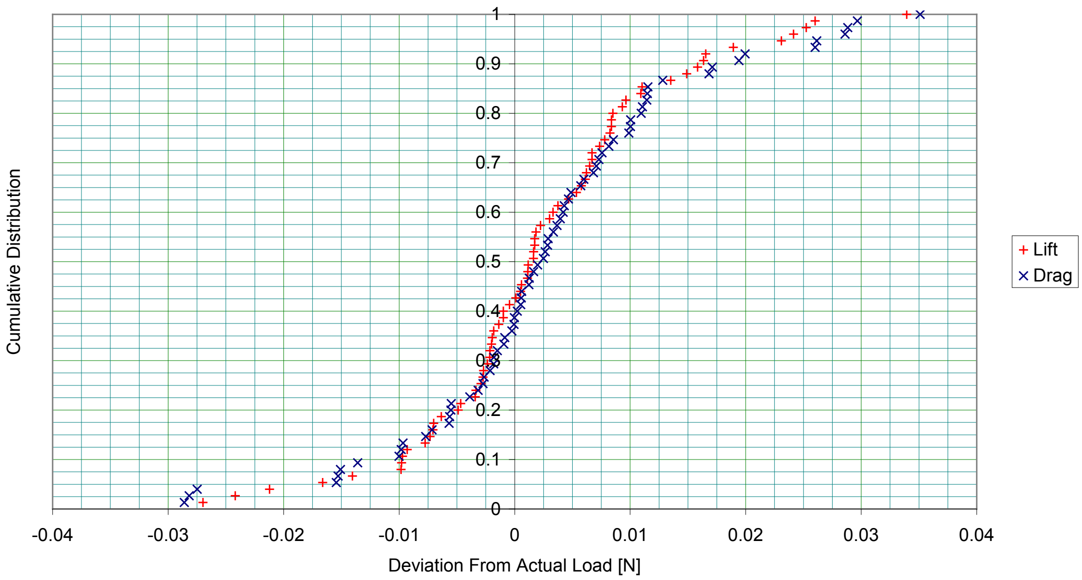

Figure 3.27 Deviation From Applied Load

Repeatability of the whole tunnel, balance and turntable system was also assessed. Using the 60 mm chord aerofoil in a 20 m.s^{-1} airflow the foil was set at 0^{o} incidence and then pitched through 2.0^{o} to give a change in lift and then pitched back to take another 0^{o} baseline reading. Again the difference between pairs of readings was taken to eliminate thermal drift effects. Because the process was automated, this allowed for a larger sample size of 150 reading pairs per test to be used. The logging frequency and time were changed to optimise experimental procedure to maximise precision. The data was processed by calculating the change in lift between the two incidence angles, subtracting the mean and then sorting the residuals from smallest to largest. A goal seeking algorithm was then used to fit the cumulative distribution function for a Gaussian distribution to the data by minimising the sum of the squares of the deviation of the experimental data from ideal (Figure 2.27). The standard deviation used to fit the cumulative distribution data was then used to produce the Gaussian distribution which best described the data set and compared between sampling rates and sizes.

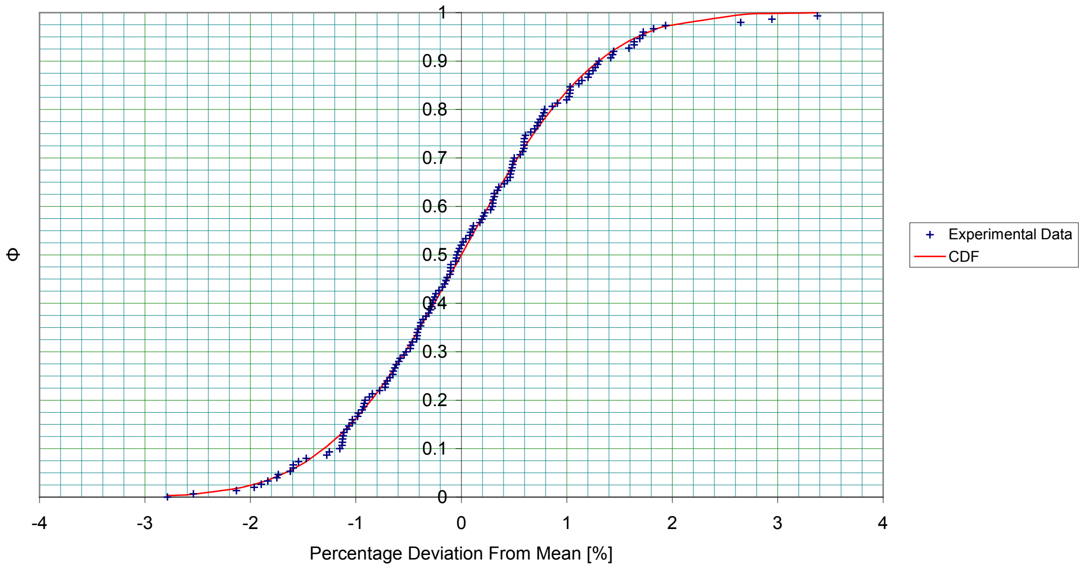

Figure 3.28 Example Of CDF Fit To Experimental Data

Figure 2.28 shows how the data grouping tightens as the sample size increases. Unfortunately due to the memory allocation coding in the Durham wind tunnel software suite 16 KiSa (Kibi Samples) is the maximum continuous sample size achievable. To overcome this multiple bursts of 16 KiSa can be recorded consecutively with a brief pause to write the data to disk, and this is how the larger sample size data sets in Figure 2.29 were collected. Figure 2.29 shows two things; firstly that repeatability is sample size rather than rate dependent when not taken to extremes; the difference produced by doubling sample time alone between 16 KiSa over 32 s and 16 KiSa over 64 s is almost indistinguishable when compared to difference introduced by doubling both sample time and sample size seen in Figure 2.28. It also shows that sampling time cannot be minimised drastically and compensated for by increasing sample size as shown by the steep decrease in performance by taking 64 KiSa at the much increased rate of 5120 Hz. The final trace in that graph shows the minimal improvement provided by increasing sample size to 64 KiSa at the expense of doubling sample time again to 64 s. Due to the limited runtime offered by the actuators it was decided that it would be better to increase the individual independent repeats rather than increase sample time beyond 32 s.

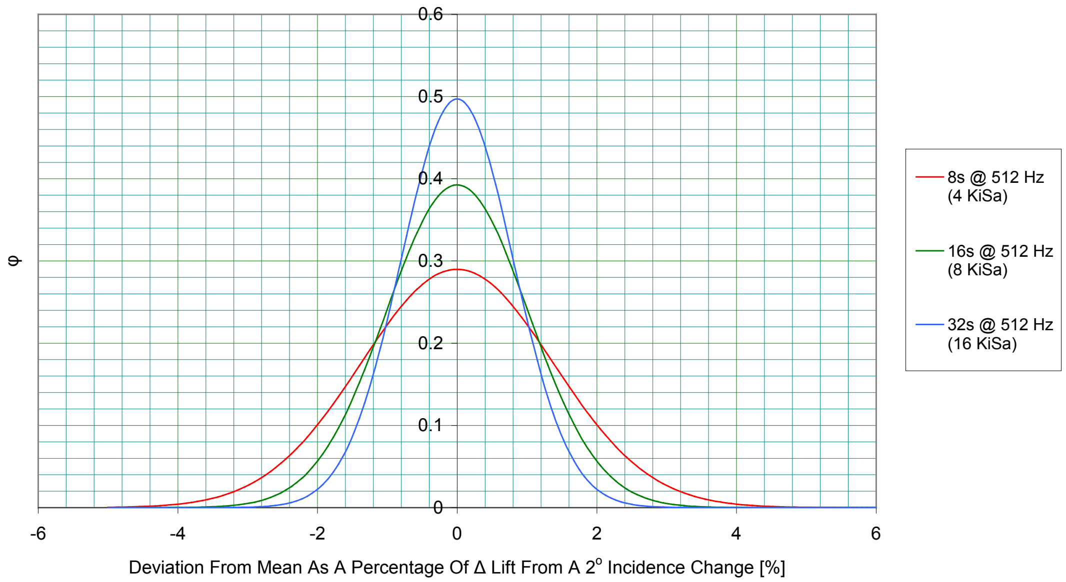

Figure 3.29 Effect Of Sample Size On Repeatability

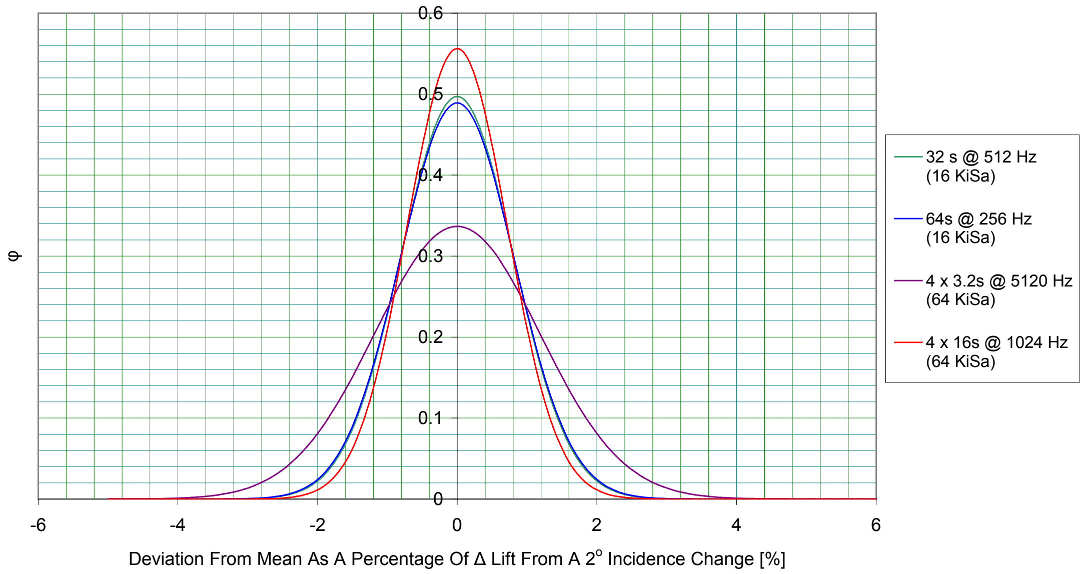

Figure 3.30 Effect Of Sample Rate On Repeatability

The preceding graphs were produced using data collected using the 60 mm wing. Following the switch to the larger 100 mm chord wing a comparison data set was compiled containing 436 data point pairs. The normal distribution best describing the data is shown in Figure 2.30: when expressed as a percentage of the 2^o sweep it is obvious that the larger wing provides a much better repeatability. As the $0\text{-}2^o$ incidence change lies on a linier portion of the lift curve it is possible to equate the percentage deviation to an equivalent change in incidence angle. With the 100 mm chord wing 99.7% of the data points lie within ±1.02 % of the mean or a change in incidence equivalent to 0.0204°. Figure 2.31 shows the repeatability of the balance for the 16 KiSa 32 s logging regimen. Although this does not give overall accuracy it shows that the 95% confidence interval for a single reading pair is around ±0.008 N from the mean.

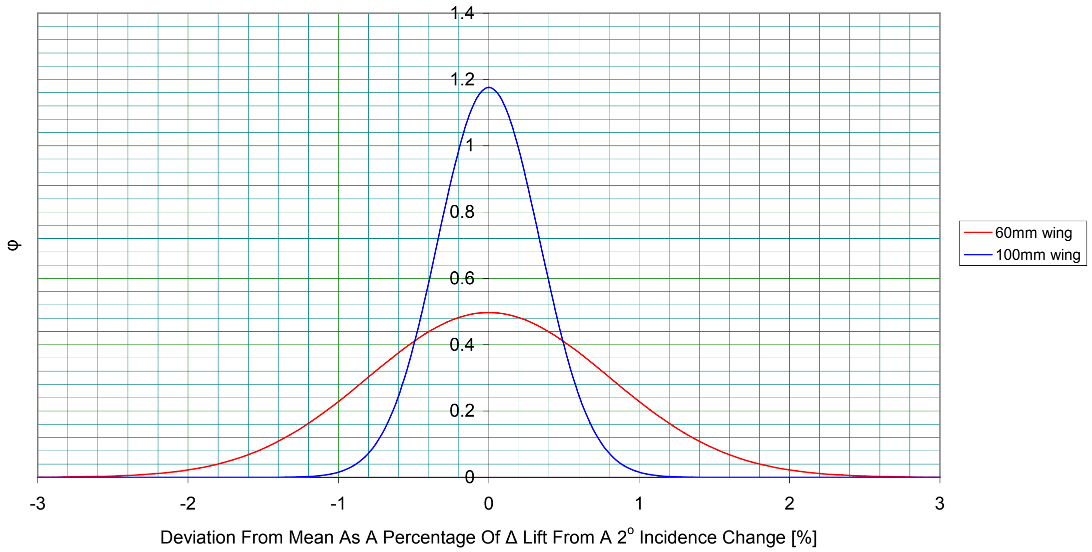

Figure 3.31 Effect Of 100 mm Chord Wing On Repeatability Compared To the 60 mm Chord Wing.

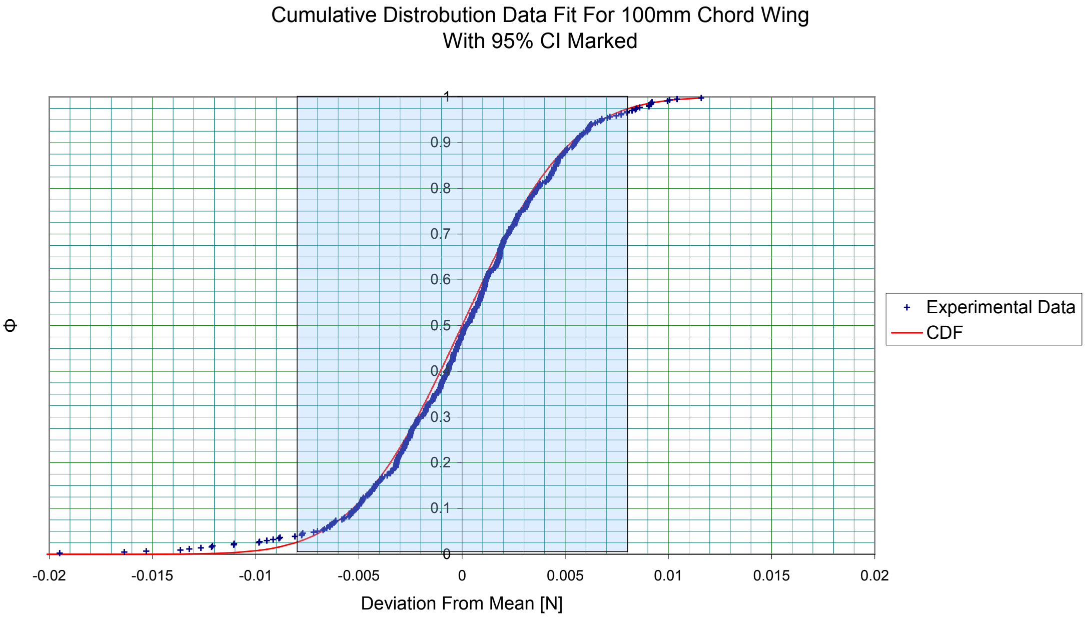

Figure 3.32 Balance Repeatability Expressed In Newtons For The 100 mm Chord Wing With 95% Confidence Interval Marked

2.5.4 Laser Linear Transducer

A pair of Baumer optical angle distance measurement (OADM) transducers were firmly bolted to the inside of the top tunnel access panel which itself is bolted in place; so although they were in the airflow they remained immune to aerodynamic vibration. The sensors were positioned with the laser dot for the respective transducer just off the leading and trailing edges of the aerofoil (Figure 2.32). The areas on the aerofoil where the laser dot impinged had a small section of white tape attached. This was to prevent confusing sub-surface reflections and multiple laser returns from the translucent RP material. Logging the location of the leading edge and training edge of the aerofoil as it moved against the spring suspension provided by the load cells of the 3 component balance allowed the change in lift and pitch to be verified, and made it possible to identify the deflection of the aerofoil and mounting system under aerodynamic load.

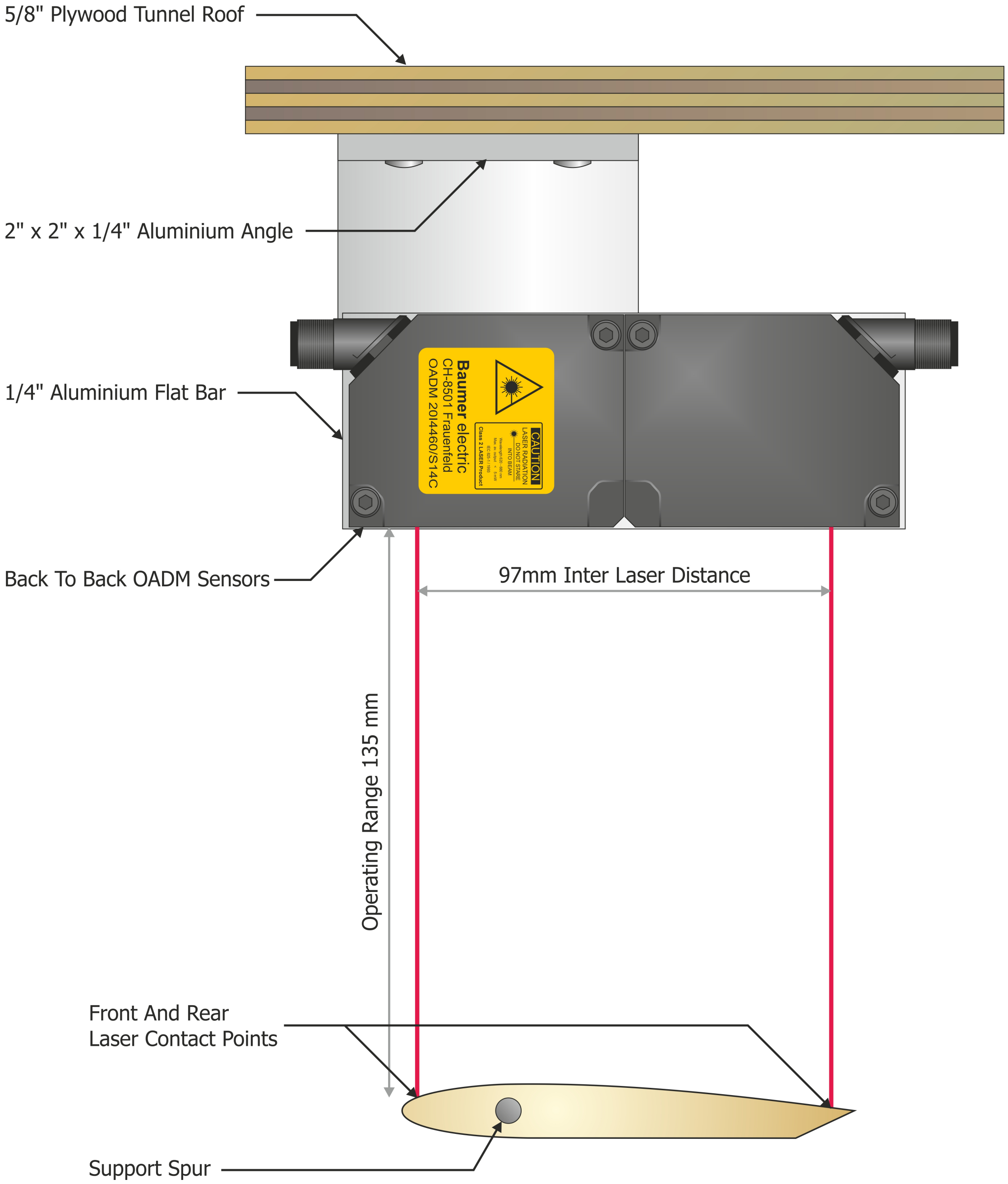

Figure 3.33 In Tunnel OADM Positioning (To Scale)

OADM transducers track the angle subtended between a projected laser dot and a horizontally offset imaging sensor. As the distance changes so does the position of the image on a linear CCD. A calibration curve is applied in the device and an output generated (Figure 2.33). The Baumer OADM 20I4460/S14C transducers are rated for measurement from 30 mm to 130 mm at a resolution of 0.05 mm and provide a proportional current output based on this distance. Although operated just outside the rated distance, the setup had no trouble resolving the motion of the wing. A pair of cables containing high tolerance resistors was used to convert the current signal to a voltage drop which could be logged simultaneously with force balance strain gauge data by the NI-DAQmx. Although the transducer has a nominal 50 µm resolution, logging and averaging 16 KiSa of data superimposed over the Gaussian positional noise induced by aerodynamic vibration of the wing allowed a greater degree of precision to be achieved in practice.

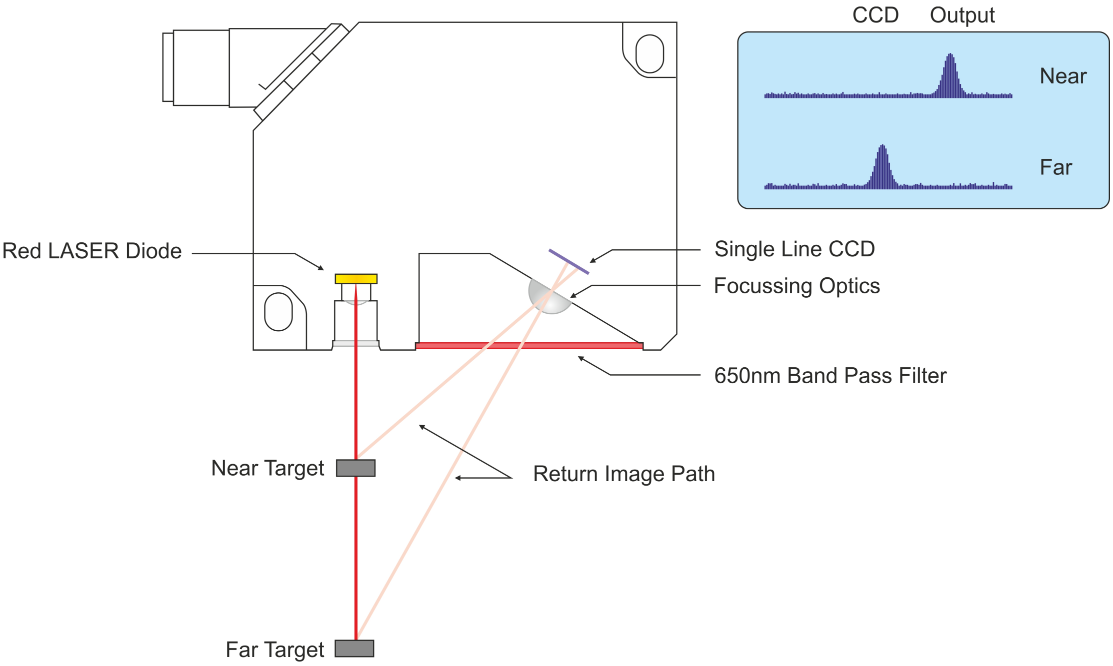

Figure 3.34 OADM Operation

The OADM transducer was calibrated across its operating range and found to have excellent linearity (Figure 2.34) and, even with the very small deviation at extremes, the full scale linearity is not all that important. It is the relative motion between points a few µm apart that is critical, so as long as the consistency and repeatability holds for this short range the data will be of good quality.

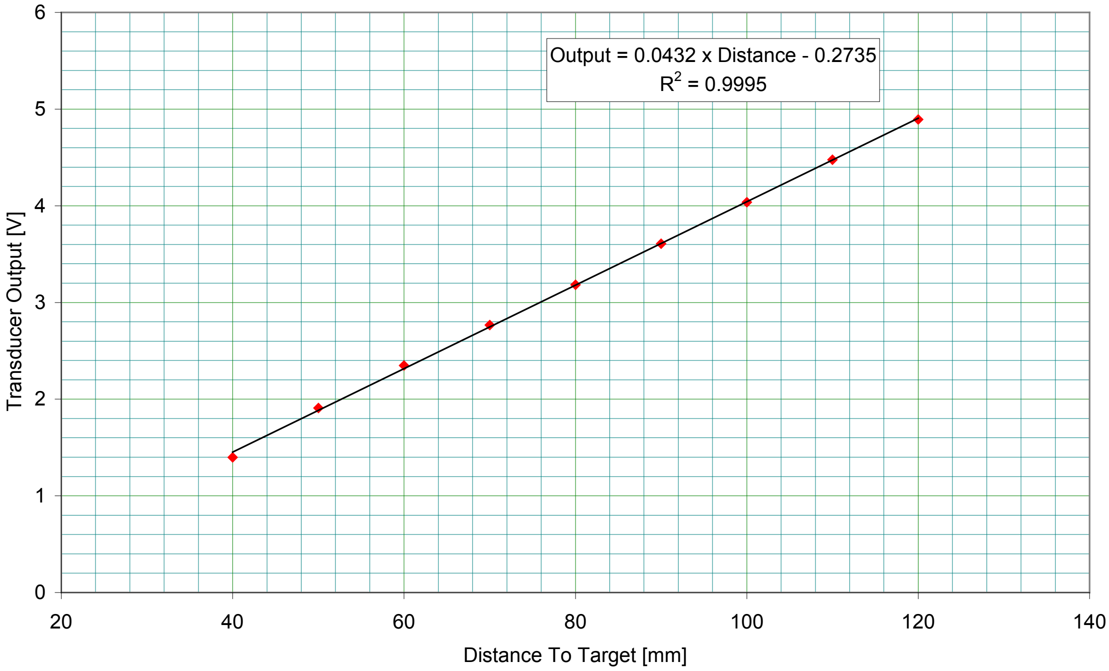

Figure 3.35 OADM Calibration

2.6 Hot-Wire Probe

Hot-wire anemometry senses fluid speed from the rate of energy loss from a wire, the faster the fluid flow the greater the power loss. Constant temperature anemometry, which was used here, heats up a wire until it reaches a given resistance. Because the wire has a positive temperature coefficient this means that at that given resistance the temperature of the wire is fixed. A Wheatstone bridge circuit containing the hot-wire as one of its elements is connected to a servo amplifier which also feeds the circuit (Figure 2.35). Resistors R_1 and R_2 are trimmed to be identical, variable resistor R_{set} is set by the user to equal the desired probe operating resistance. In this way when the probe is resistively heated to that point the voltage V_{error} is driven to zero. R_{set} is calculated from Equation 4. In this equation α_{20} is the temperature coefficient of the probe at 20 ^{o}C, which for the probe used was 0.0036 $^{o}C^{-1}$. Additionally $R_{probe@20}$ = 3.5 Ω, R_{leads} = 1 Ω - these values are measured when the probe is manufactured and supplied along with it. In principal T_{set}, the set point temperature can be chosen by the user. However the probe has a maximum specified temperature, in this case 300 ^{o}C, and by the running probe as hot as possible noise introduced by fluctuations in ambient temperature is reduced [127].

$$R_{set} = (R_{probe@20} + R_{leads}) + (\alpha_{20}.R_{probe@20}.(T_{set} - T_{ambient}))$$

Equation 4 - Hot-Wire Probe Operating Temperature

In operation, as the flow speed increases the temperature and resistance of the wire dips due to an increase in the forced convective cooling component of energy loss from the wire. This induces a non-zero error voltage output from the bridge causing the amplifier to increase the applied voltage until sufficient power is being dissipated into the hot-wire element to heat it back up to its resistive set point in the increased fluid flow. The output of the system is the required feed voltage. Because the thermal mass of the wire is so low this process has a very short time constant and bandwidths of several hundred kHz are achievable.

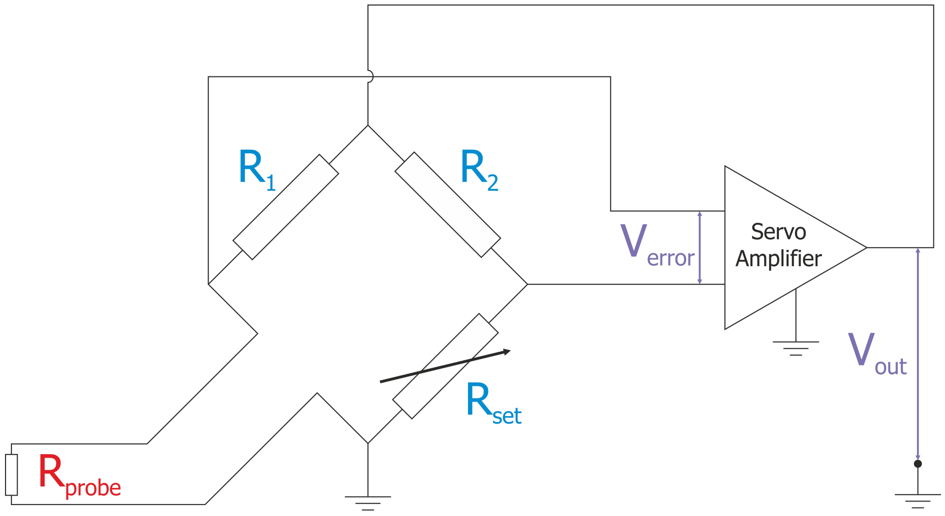

Figure 3.36 Hot-Wire Control Schematic [128]

A DISA hot-wire probe control system (Type 55M01) was used in this research. A one dimensional Dantec probe head 55P01 was used - this uses a 3 mm long 5 µm diameter gold plated tungsten filament with a 1.25 mm active section in the middle designed to reduce interference from the wire supports. Its single wire was aligned parallel to the trailing edge of the wing along the Y-axis. The probe was operated at its maximum temperature, T_{set}, of 300 ^{o}C with the controller response tuned to provide a bandwidth of up to 3 kHz.

The probe was calibrated against a reference Pitot-static probe in a wind tunnel. An unmodified King's law approximation for the behaviour of the wire was fitted to the data and used for the calibration see Figure 2.36. King's law describes the relationship between voltage and the flow normal to the wire [129] (see Equation 5). However, it is a basic derivation based solely on convection from an infinitely long wire. It therefore does not take account of any end effects, and it also ignores energy losses through conduction to the support prongs and losses through radiation to the environment. Fortunately the operating Reynolds number and probe design mean that the effect of these approximations is minimal.

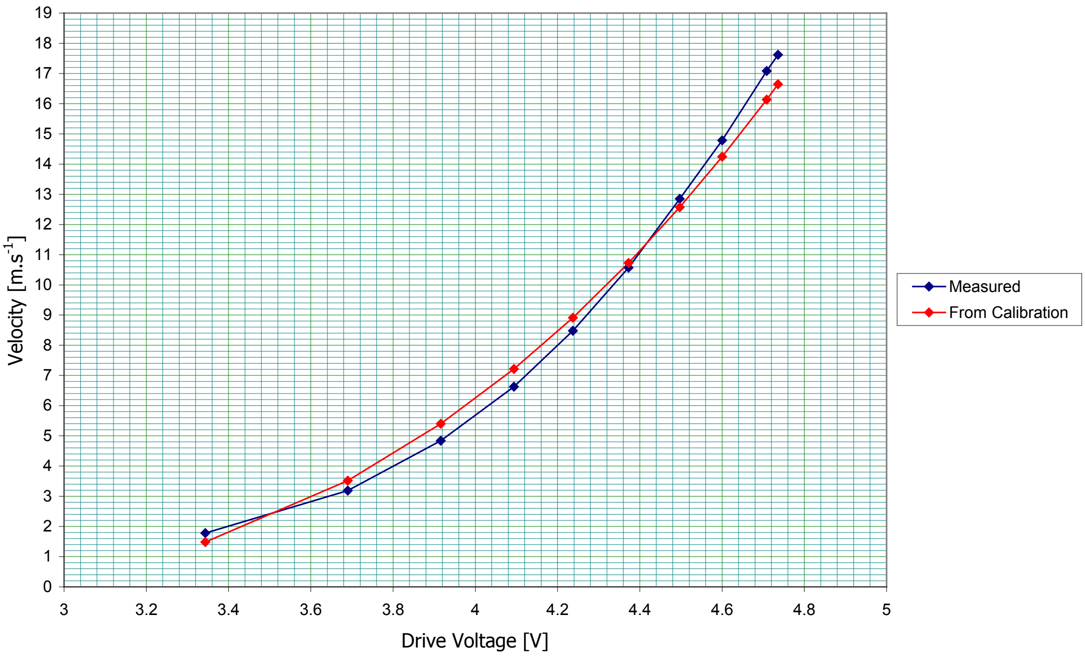

Figure 3.37 King's Law Constant Temperature Hot-Wire Probe Calibration

$(V_{out})^2 = A + B.(U_{normal})^N$

Where:

A, B and N are experimentally determined constants.

With N ≈ 0.45 to 0.5 [129]

Equation 5 - King's Law

2.7 5 Hole Probe

2.7.1 Probe Design

A new 5 hole probe was designed, developed and constructed as part of experimental work for this thesis, in order to allow measurements to be taken concurrently with the plasma actuation. The required design parameters were; a small head size to facilitate a good spatial resolution in the relatively small wake region behind the aerofoil, an electrically isolating construction to eliminate the possibility of the high voltage sparking to the probe head and grounding to a point outside the tunnel, and finally good dimensional stability to allow reliable positioning within the flow. To meet these requirements a probe was manufactured using a 2.7 mm diameter sintered alumina shaft. This shaft contained 5 x 340 µm holes which were formed along its length during the extrusion process. Originally intended as a high temperature insulator for carrying thermocouple wires this provided the excellent electrical isolation and rigidity that would be expected from a ceramic at the expense of the inherent brittleness and difficulty in machining also associated with this material. According to [130] at the intended operating Reynolds number of 3240 both truncated cone and truncated square based pyramid designs were likely to suffer from Reynolds sensitivity affects. As such the probe head design was chosen as a truncated cone, shown in Figure 2.37, as this could be easily manufactured symmetrically by slowly rotating the alumina shaft whilst bringing it into contact with a diamond grinding disk.

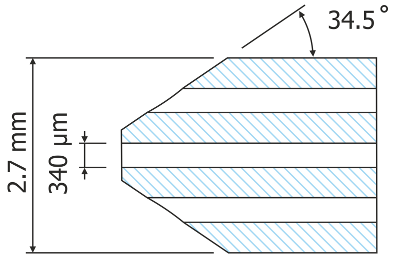

Figure 3.38 Probe Head Section View

To allow connections to the 5 alumina tubes to be made a 2 part boss was manufactured using a rapid prototyping machine, shown in Figure 2.38. The boss used slits ground through the tube wall at different axial positions lined up with circumferential cavities connected to tubes running through the RP material and eventually into stainless steel hypodermic tube used to connect to the standard small bore silicone pressure signal tubing used in the lab (2 mm OD, 1mm ID, Nalgene). Small copper wire plugs were used to seal off the ends of the circumferential tubes and allow the central tube to be fed straight out of the back. By using the split design the areas which were to be in contact with the shaft could be carefully epoxied and then closed together around the shaft ensuring proper sealing without clogging the holes in the ceramic. The locating lugs at the front of each half ensured the boss remained aligned during the gluing process.

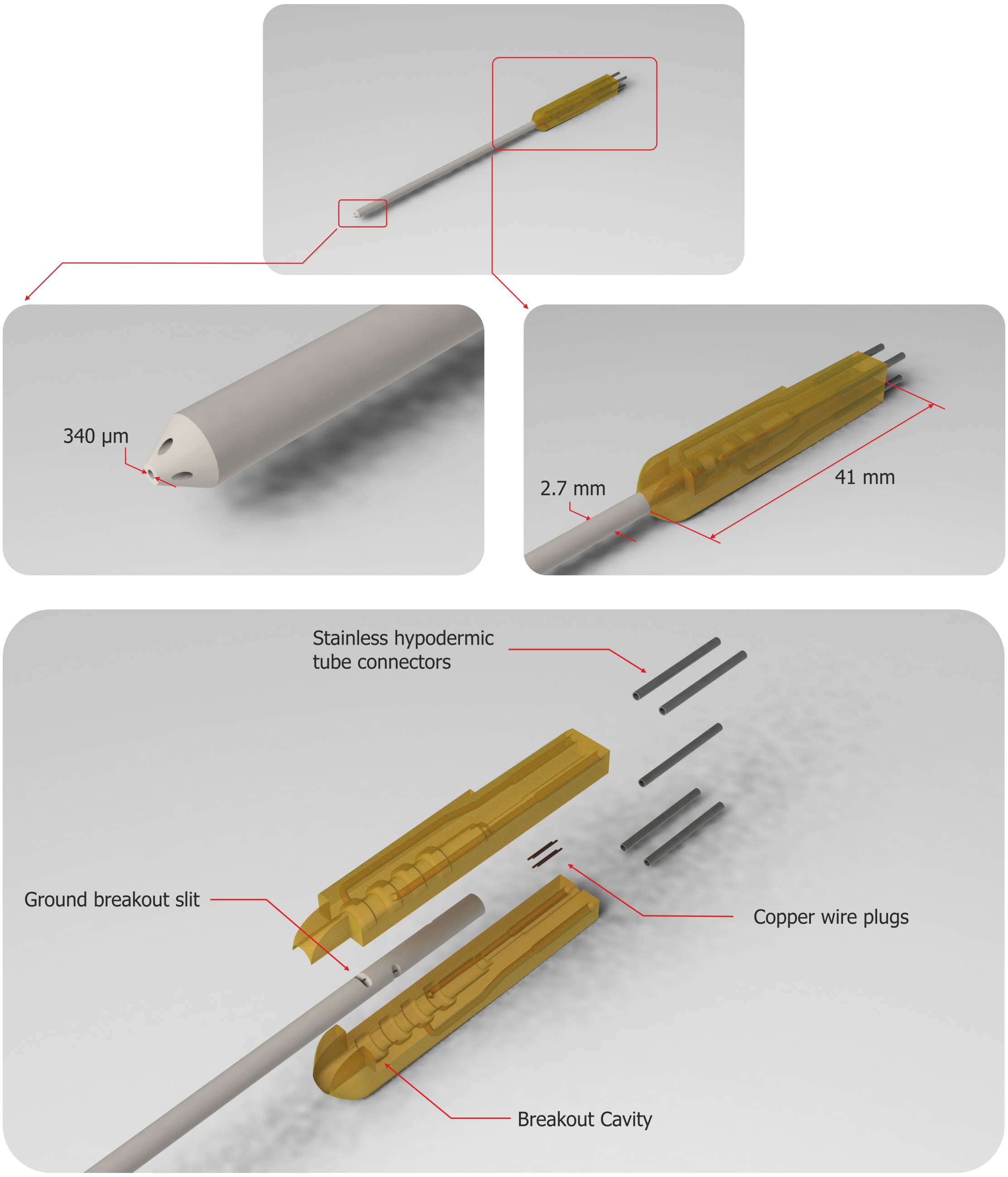

Figure 3.39 Probe Construction

The probe was calibrated using an automated facility within the department - an open jet wind tunnel with a 2 degree of freedom roboticised positioning system. A calibration grid with a 2.5^{o} step size over $\pm$ 35^{o} on both pitch and yaw was used, and in order to minimise any inaccuracies caused by Reynolds effects, the probe was calibrated in an airflow equal to its intended usage point of 20 m.s^{-1}. The raw pressure tube readings are shown in Figure 2.40, and Figure 2.41 shows the processed calibration file. The coefficients plotted in Figure 2.41 are defined as given in Figure 2.39:

P_{dyn} = Dynamic Pressure

P_{tot} = Total Pressure

$$P_{ave} = \frac{P_1 + P_2 + P_3 + P_4}{4}$$

View Onto Probe Head.

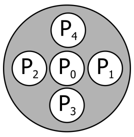

$$CpTot = \frac{P_0 - P_{tot}}{P_0 - P_{ave}} \qquad CpDyn = \frac{P_0 - P_{ave}}{P_{dyn}} \qquad CPitch = \frac{P_3 - P_4}{P_0 - P_{ave}} \qquad CYaw = \frac{P_1 - P_2}{P_0 - P_{ave}}$$

Figure 3.40 5 Hole Probe Coefficient Definitions

The four lobed distortion seen on the CpDyn plot in Figure 2.41 is due to the compromise accepted by manufacturing the probe head by grinding tube stock which already contained extruded holes. This created the geometry shown in Figure 2.42, labelled parallel tubes. Ideally the axis of the circumferential tubes would have been perpendicular to the slope of the cone, as labelled perpendicular entrances in the same figure, which would have provided a much more uniform CpDyn distribution and better sensitivity at low angles of pitch and yaw. However from the yaw and pitch coefficients shown in Figure 2.41 the probe still retains good sensitivity and uniformity over a wide range of incident flow angles.

As the probe was used to collect time averaged pressure readings, and because the exceptionally small diameter, high aspect ratio tube within the probe shaft would severely damp the dynamic response anyway, the transfer function of the probe was neither calculated nor corrected for.

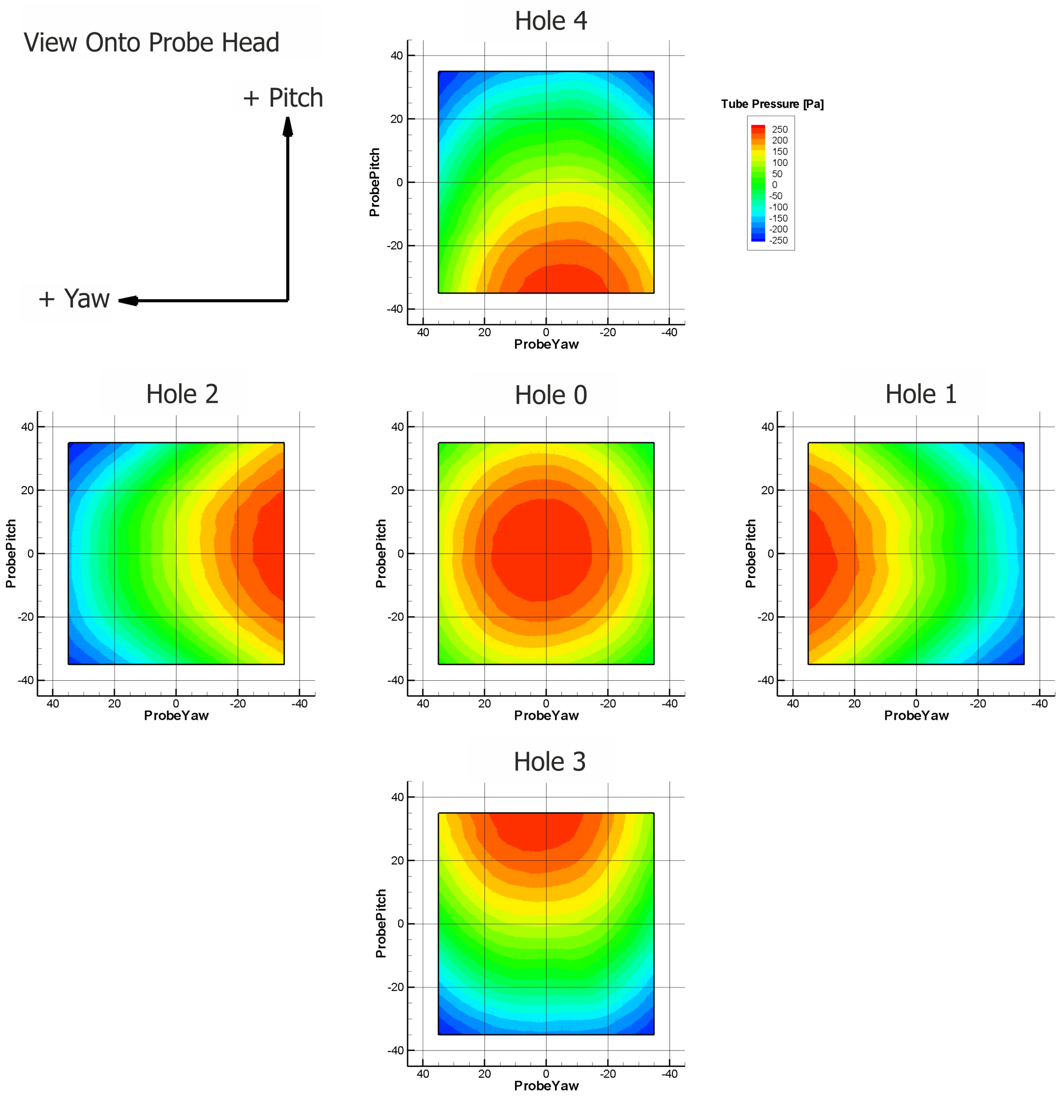

Figure 3.41 Raw Probe Calibration Data

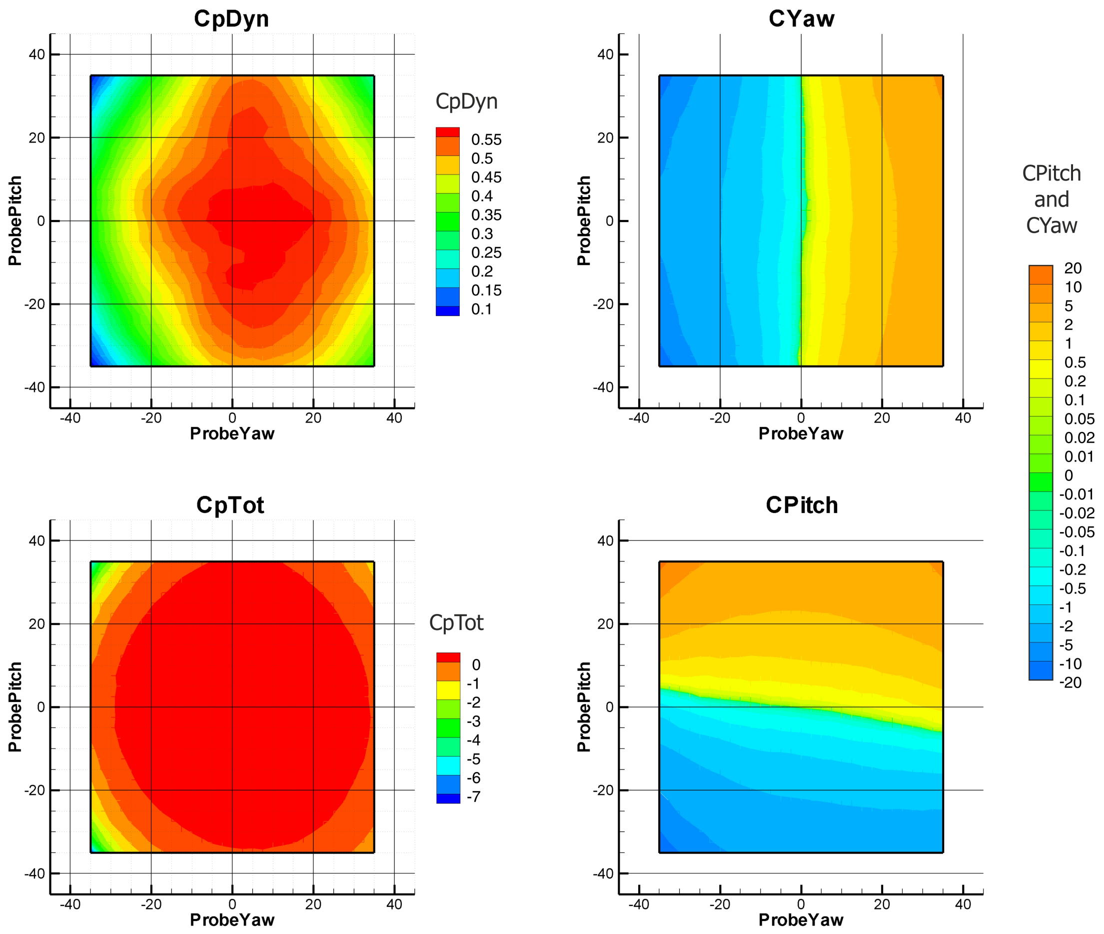

Figure 3.42 Probe Calibration Maps

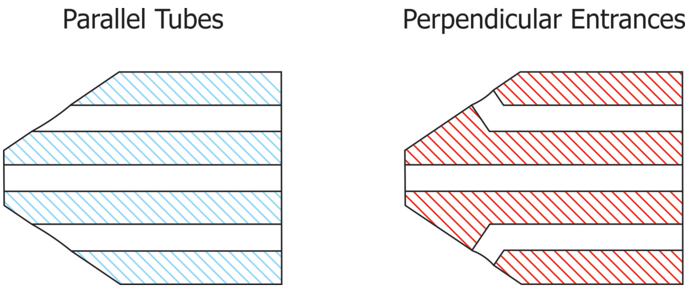

Figure 3.43 Differing Conical Probe Head Geometries

2.7.2 Probe Usage

The completed probe was mounted in a 90° rapid prototyped boss which was epoxied into a 12mm Ø stainless steel tube, (Figure 2.43). This construction allowed the tubing to be fed out through the centre of the support tube to a bank of 5 SensorTechnics HCLA12X5B pressure transducers located outside the tunnel. The HCLA12X5B is a miniaturised amplified pressure sensor with a ±12.5 mbar range and a nominal sensitivity of 6.25 mBar.V^{-1} on an analogue voltage output. The signal from the transducers was logged by the NI-DAQmx USB-6218 controlled by the MCP detailed previously.

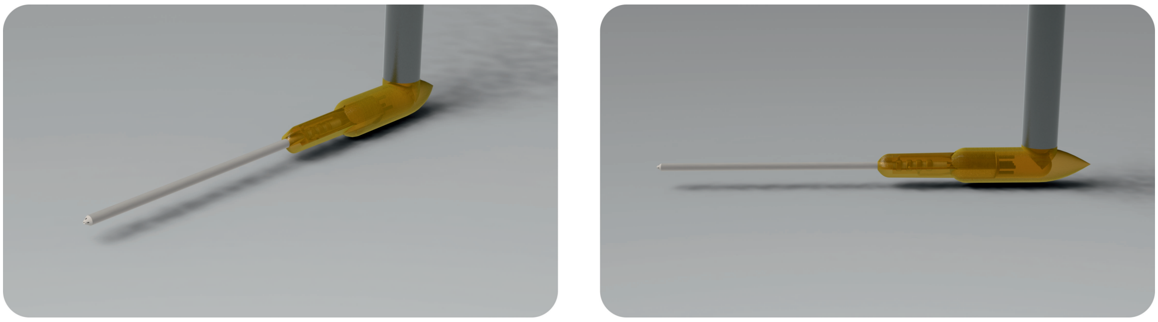

Figure 3.44 Probe in Mounting

Probe tip position was controlled using a 3 axis linear traverse attached to the top access panel on the wind tunnel. The X & Y Axis were locked off to improve the rigidity of the traverse but could be repositioned manually, and the Z axis was controlled by stepper motor using the output channel usually reserved for the aerofoil pitch turntable. This provided a 0.02 mm.step^{-1} resolution and allowed for automated wake traverses synchronised with interleaved control and actuator-active readings.

2.8 Particle Image Velocimetry

2.8.1 PIV Theory & Operation

Particle image velocimetry (PIV) is an almost entirely non-intrusive technique for measuring the flow field in a plane. Unlike probe based methods, where the probe head will inevitably interfere with the flow field to some degree, the only interference to the airflow is the introduction of the microscopic seeding medium. Seeding particles are small enough that the droplets remain suspended in the flow and do not significantly affect its path, nor does particle charging due to the DBD affect the measurement [72]. The non-invasive nature of the PIV system also allowed measurements to be taken much closer to the electrified surface of the plasma actuator. In comparison to the 5 hole probe which could only produce wake traverses 40 mm from the bottom edge of the exposed electrode due to the possibility of arcing to the grounded probe tip, the PIV system is capable of providing data within approximately 0.5 mm of the actuator surface.

PIV as a measurement system relies on capturing two images of the seeded flow separated by fractions of a second, in this case 10 – 100 μs dependent on velocity. These image pairs are then post processed in software using a technique based on cross-correlation (Figure 2.44)[131].

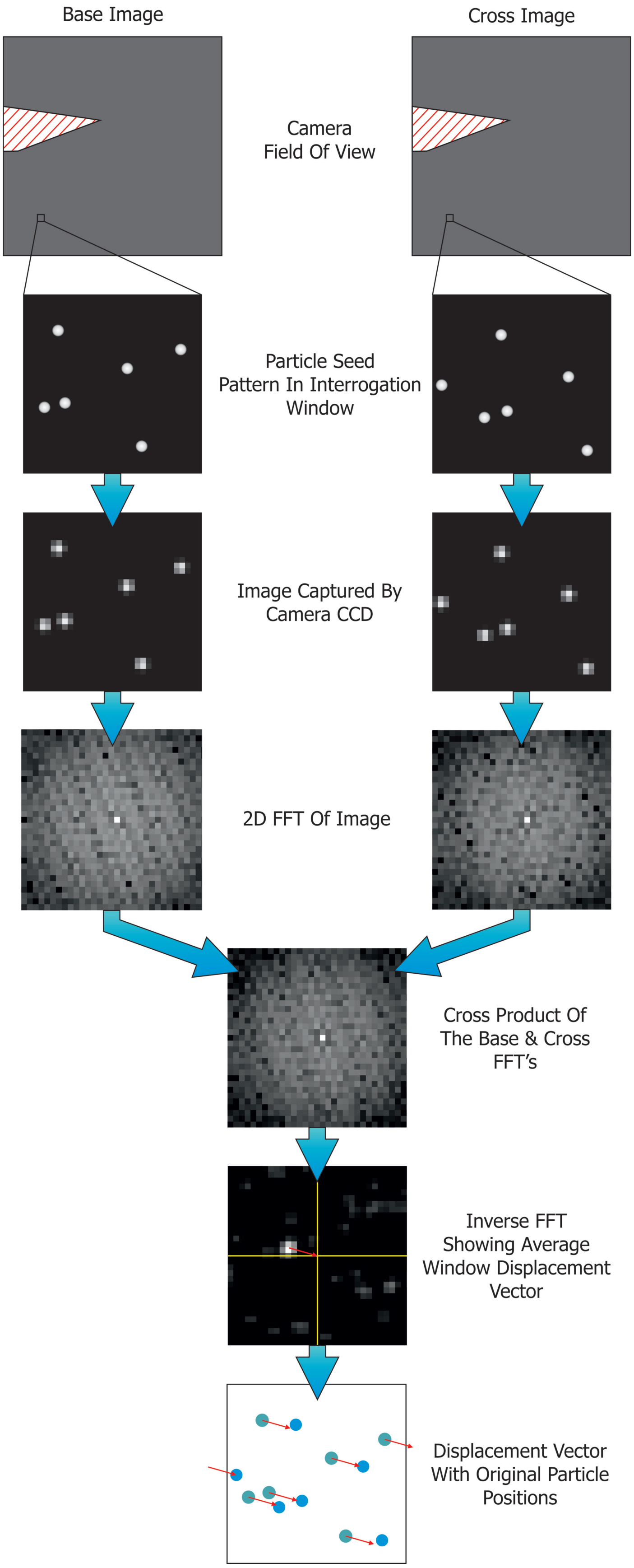

Figure 3.45 Cross Correlation

In PIV the two images are termed the base image, the first one to be taken and the cross image, the second, slightly delayed image. Cross correlation takes the original images and breaks them down into multiple interrogation windows of size 2^n pixels square. 2D fast Fourier transforms (FFT) are applied to the individual interrogation window sub-images. Taking the cross product of the FFT from the base image and the corresponding FFT from the cross image and applying an inverse FFT yields an average displacement vector for the particles in that interrogation window. The inverse FFT will have the same resolution as the interrogation window. To avoid severe discretisation of the displacement vector, sub-pixel positioning of the point is employed by fitting Gaussian distribution curves to the pixel intensities around the peak (Figure 2.45) [132-134]. Repeating this process with interrogation windows tiled across the whole of the original image provides the full instantaneous flow field map.

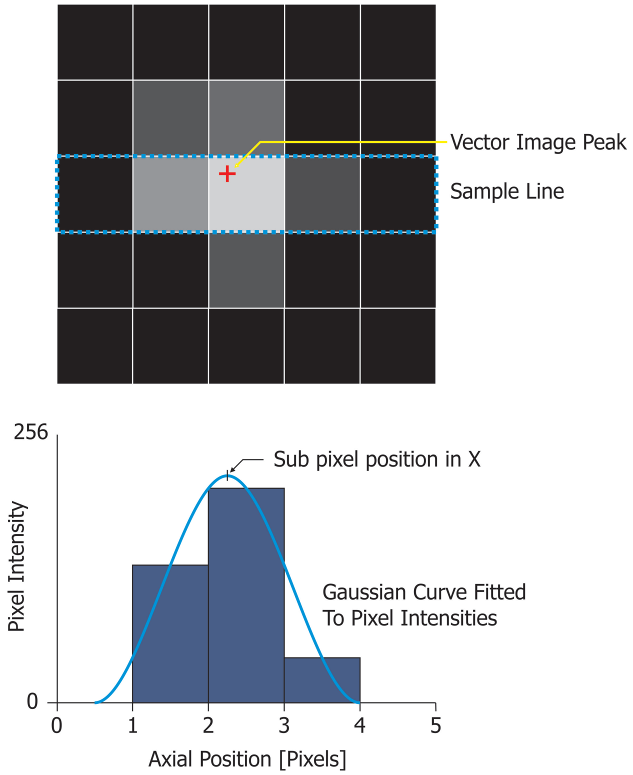

Figure 3.46 Sub Pixel Positioning

Once the cross correlation is completed the vectors are filtered to remove those which are likely to be incorrect. Firstly a window filter removes all those vectors which lie outside of pre defined U & V velocity limits. These limits are set based on the freestream velocity and whether or not any recirculation is expected. Secondly a local velocity filter is applied and vectors which differ significantly from their neighbours are removed. Values for the removed vectors are then interpolated from the surrounding unfiltered ‘valid’ vectors.

Adaptive cross correlation is then applied (see Figure 2.46) [134-136]. Discrete window shift adaptive cross correlation is useful for increasing the number of valid vectors returned from the analysis. As more tracer particles move into and out of the set interrogation window between base and cross images (circled red and orange in Figure 2.46) the cross correlation becomes more noisy. Although the example cross correlation shown would have still given the correct fluid motion, it must be noted that this is an idealised case. The particle motion is perfect homogenous translation, the particle size is consistent and when the window is resampled to 32 pixels square each particle covers a 3x3 pixel area with a Gaussian intensity profile. Also the signal to noise ratio of particle to background is a perfect white on black, no particles exhibit out of plane motion and there are no stray laser returns - and yet the noise is still almost enough to return an incorrect motion vector. To improve the signal to noise ratio adaptive cross correlation takes an approximation of the fluid motion, either from the first cross correlation or in the case of that returning an invalid vector the interpolated vector from its neighbours. The interrogation window in the cross image (shown outlined in blue in Figure 2.46) is shifted by this vector and the cross correlation redone. It can be seen in the diagram that this improves the number of particles present in both interrogation windows. It can be seen that in the idealised example that this massively improves the signal to noise ratio, which leaves more headroom to cope with out of plane particle motion etc. before the fluid motion signal becomes swamped by noise. The detected fluid motion is gained by vector addition of the shift applied to the window and the cross-correlation from that interrogation window and the original base image interrogation window.

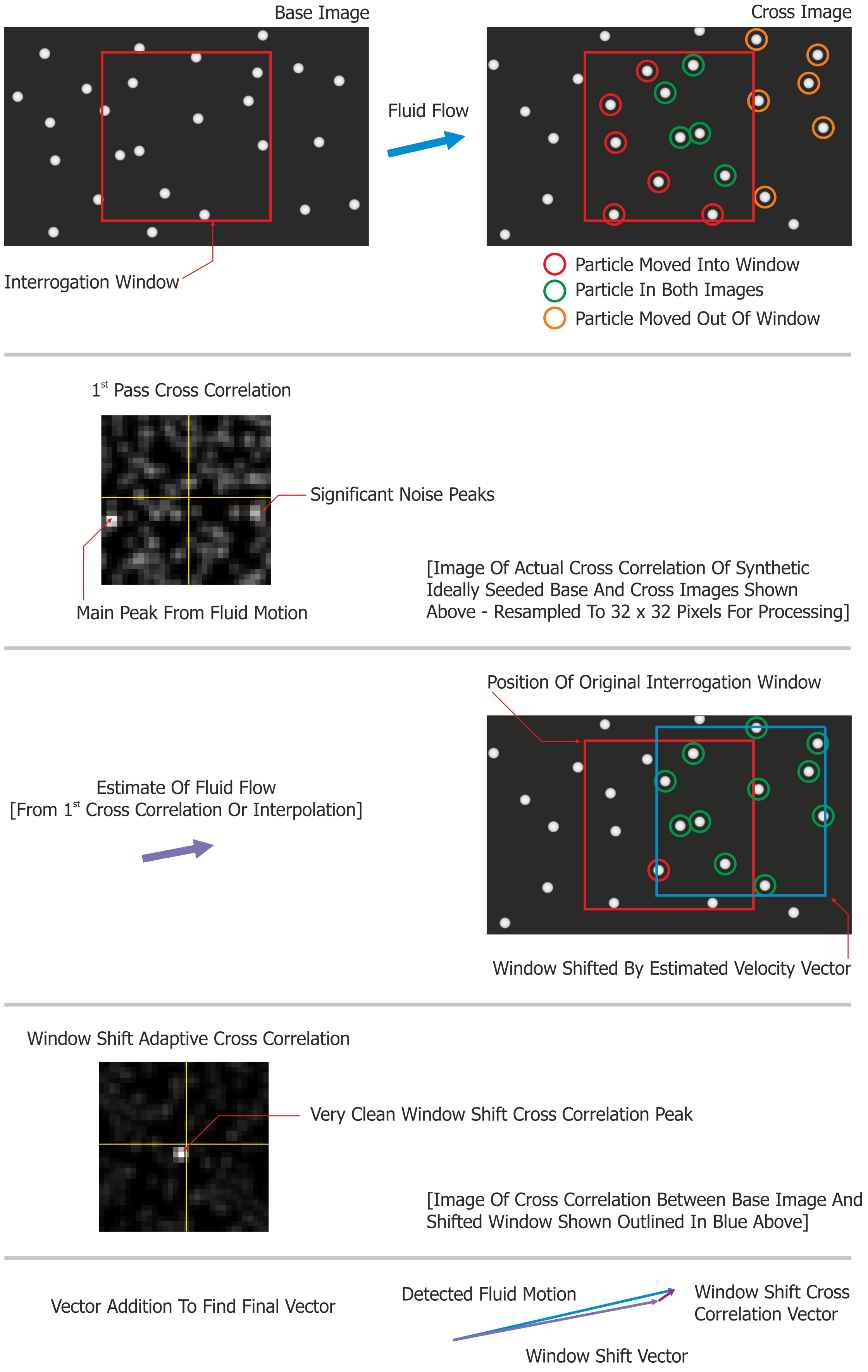

[Image Of Actual Cross Correlation Of Synthetic Ideally Seeded Base And Cross Images Shown Above - Resampled To 32 x 32 Pixels For Processing]

[Image Of Cross Correlation Between Base Image And Shifted Window Shown Outlined In Blue Above]

Figure 3.47 Adaptive Cross Correlation

2.8.2 PIV Hardware, Setup and Operation

2.8.2.1 PIV System Specification

The PIV system used supplied by Intelligent Laser Applications GmbH (ILA) and sold by Oxford Lasers in the UK. The system is capable of doing 3 dimensional PIV using a pair of cameras to give stereoscopic image quadruplets. The cameras themselves (PCO sensicam) contain 1.2 M-Pixel greyscale charge coupled device (CCD) sensors thermostatically cooled to -12 ^{o}C using Peltier elements. The Peltier element hot sides are cooled by simple heat sink fan arrangements. The cooled sensors reduce thermal noise, which can be a major problem when operating at the extremely short exposure times required to capture the image pairs of a small interrogation area in a fast moving flow. The cameras are capable of both 8 bit (256 levels) and 12 bit (4096 levels) output precision. The camera bodies take standard Nikon F-mount lenses but feature no capacity to drive the available autofocus features: they do however feature adjustments for Scheimpflug focal plane corrections. The standard lenses were Nikkor 85mm f/1.4D's. Images are streamed from the camera to the host PC in real time via a fibre optic interconnect, image bursts are buffered on ram local to the PCI interface card before being transferred into a swap file for use by the analysis software. These two factors limit the capture rate (4 Hz), and maximum burst size (approximately 300 image pairs).

Illumination is provided by a New Wave Research Solo 120, dual head, flashtube pumped Nd:YAG laser designed specifically for PIV. The laser cavities are actively q-switched by a Pockels cell to allow precision beam shaping and pulse separation. Output pulse energy is 120 mJ at a wavelength of 532 nm (green) after the infrared Nd:YAG has been passed through a frequency doubler. The Beam has a pulse width of 3 - 5 ns. Maximum pulse repetition rate is 15 Hz. The light sheet optics consist of 3 elements, a standard focusing lens, and horizontal and vertical cylindrical lenses to form the sheet. The unit used a light guide arm to steer the beam through a series of 4 rotating joints from the exit of the laser cavity to the light sheet optics located in the tunnel test section. Sheet width is approximately 2 mm.

The seeding system which was used utilised atomised droplets of Di(2-EthylHexyl) Sebactate (DEHS), a non-toxic ester with the formula $C_{26}H_{50}O_4$. Although commonly referred to as a 'smoke' system it is instead an aerosol. The atomiser system uses a series of 40 laskin nozzles to produce a high volume output with an average droplet size of approximately 1 µm [137].

2.8.2.2 Wind Tunnel Modification & Additional Hardware For PIV

Achieving good PIV results is a combination of creating sufficient seeding particle density and uniformity, maximising laser power and controlling unwanted laser returns from non seed particle sources. Increasing seeding density at a given laser power provides a greater number of particles above the minimum size required to return a strong enough signal for the camera to pick up at that illumination intensity. Increasing the laser power allows the camera to pick up smaller seed particles in the flow, providing better images. However, as laser power increases, pixel bloom from where the laser strikes the aerofoil edge starts to become a problem. Pixel bloom is where the individual pixels on the CCD receive sufficient photon flux so that the accumulated charge overflows to neighbouring pixels altering their value to 255 or fully white. Once these pixels then fill, the uncontained charge can spread to more and more generations of neighbouring pixels, and dependent on the level of illumination at the source pixel or area, a significant portion of the image can become saturated.

Several variations on tunnel flow seeding were tried. Firstly the 'smoke' stream was injected upstream of the fan, marked 'Injection Point 1' in Figure 2.47. The thorough mixing provided by the fan produced a very homogenous but sparse seeding across the whole test section. Using the light guide arm to generate the laser sheet the seeding density in the images was acceptable up to a velocity of around 10 m.s^{-1}. To improve the image quality it was attempted to increase the seeding density in the plane of the laser sheet. Seeding rakes were tried at both rake position 2 and simultaneously at rake positions 1 & 2 along with several combinations of foam and fine stainless steel mesh diffusers. These seeding methods vastly increased the seeding density by only seeding the small strip of flow which tracked onto the laser sheet position in the test section. All however suffered from very poor uniformity of distribution of the seed particles due to the low turbulence intensity flow into which they were introduced. To provide homogenous seeding concentrated along the laser sheet stream line, seeding at 'injection point 2' between the fan and settling chamber, was tried. Although mixing was improved relative to rake seeding it too could not produce satisfactory seeding uniformity. The final adaptation to the seeding scheme that was tried was the use of a large diffuser and temporary wind tunnel return leg to recirculate the pre-seeded exhaust flow back to the tunnel inlet. Although initially promising, this proved too cumbersome and fragile to be used in an extensive test campaign.

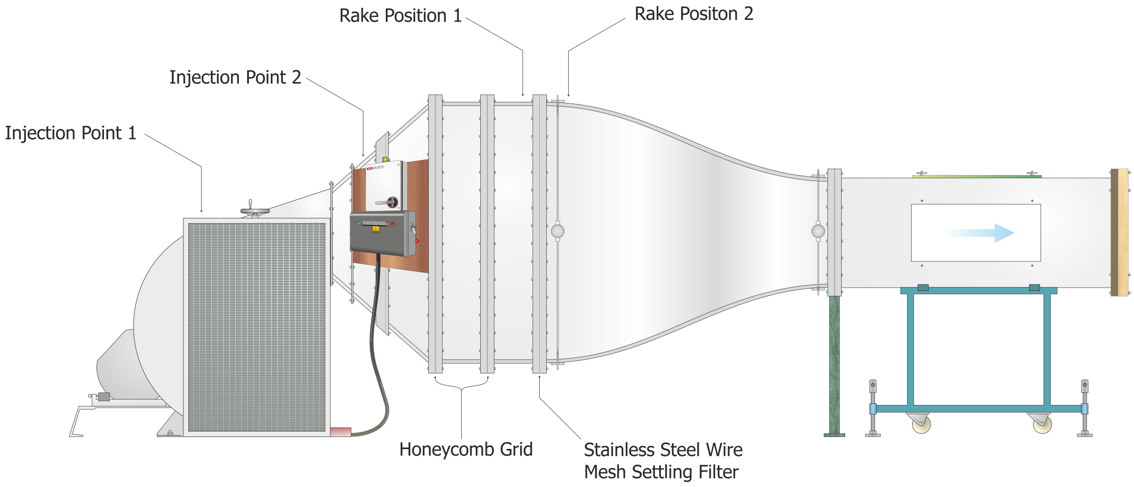

Figure 3.48 PIV Seeding Locations

The solution to the seeding/image quality problem was achieved by modifying the laser source. By removing the laser light guide and the losses associated with its mirror pairs usable laser power was significantly improved, the light sheet optics were instead bolted directly to the front of the laser cavity and this whole assembly was placed inside the tunnel. The improvement in laser sheet power came at the cost of increased tunnel blockage (see Figure 2.48). The laser was however situated a significant distance downstream, with the tip at over ten chord lengths from the trailing edge and the point of peak blockage a further two chord lengths downstream. It was confirmed though comparisons of the aerofoil force data with and without the laser head in the test section that any effect of the increased blockage could not be detected in the lift of the aerofoil. With the higher power laser sheet the tunnel could be seeded from 'injection point 1' and achieve near perfect image pairs at full tunnel speed. It was able to do this because the higher power laser illumination reduced the minimum size of droplet required to appear as a defined particle in the image pairs and in so doing showed up many of more of the smaller droplets present in the flow, thus effectively increasing the seeding density.

In conjunction with the search for the best possible seeding solution the position of the cameras was very tightly controlled. By ensuring that the camera was positioned inline with the axis of the wing, the visibility of the point where the laser struck the wing surface was obscured by the perspective view of the wing tip, in this way stray surface reflections affecting the images was all but eliminated.

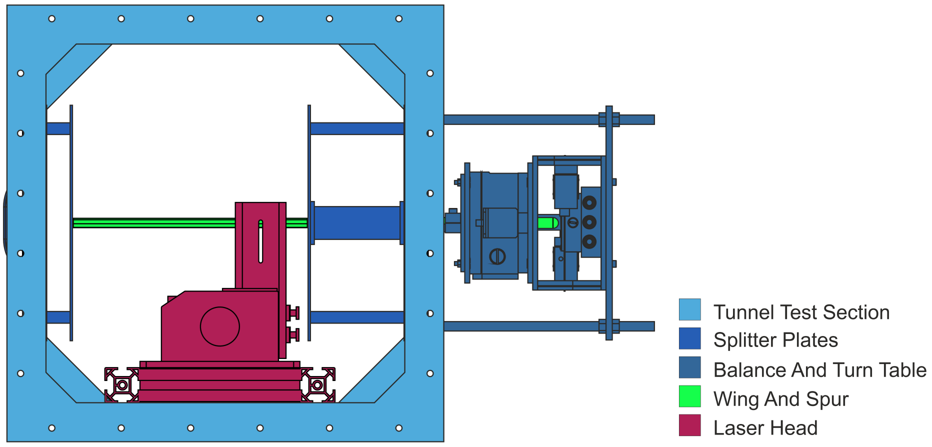

17.4% Blockage

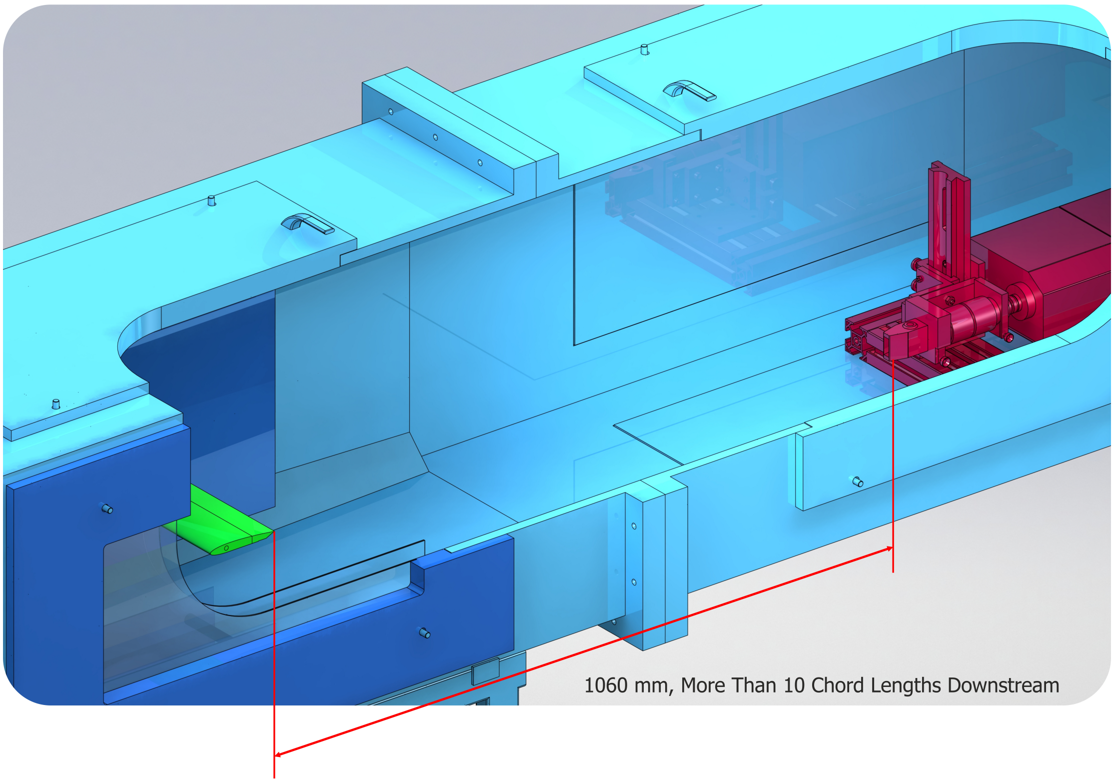

Figure 3.49 Laser Head Tunnel Blockage

The wind tunnel is not located in a dedicated laser safe environment, and to eliminate the possibility of stray laser light making it out into the room and the access road that runs by the lab windows a light trap was built that attaches to the end of the tunnel (Figure 2.49). The trap was constructed from lightweight black Corex® fluted plastic with the edges reinforced by 10 mm x 10 mm aluminium angle. The diamond shaped centre body completely blocks any line-of-sight exit from the tunnel test section. Because the centre body had to cause significant deflection to the flow the shell was designed to diffuse the flow to recover wasted kinetic energy from the exhaust jet to offset the blockage effect and maintain maximum tunnel speed. Testing showed that the diffuser did not negatively affect test section velocity and, as a by product of slowing the exhaust jet, reduced tunnel noise.

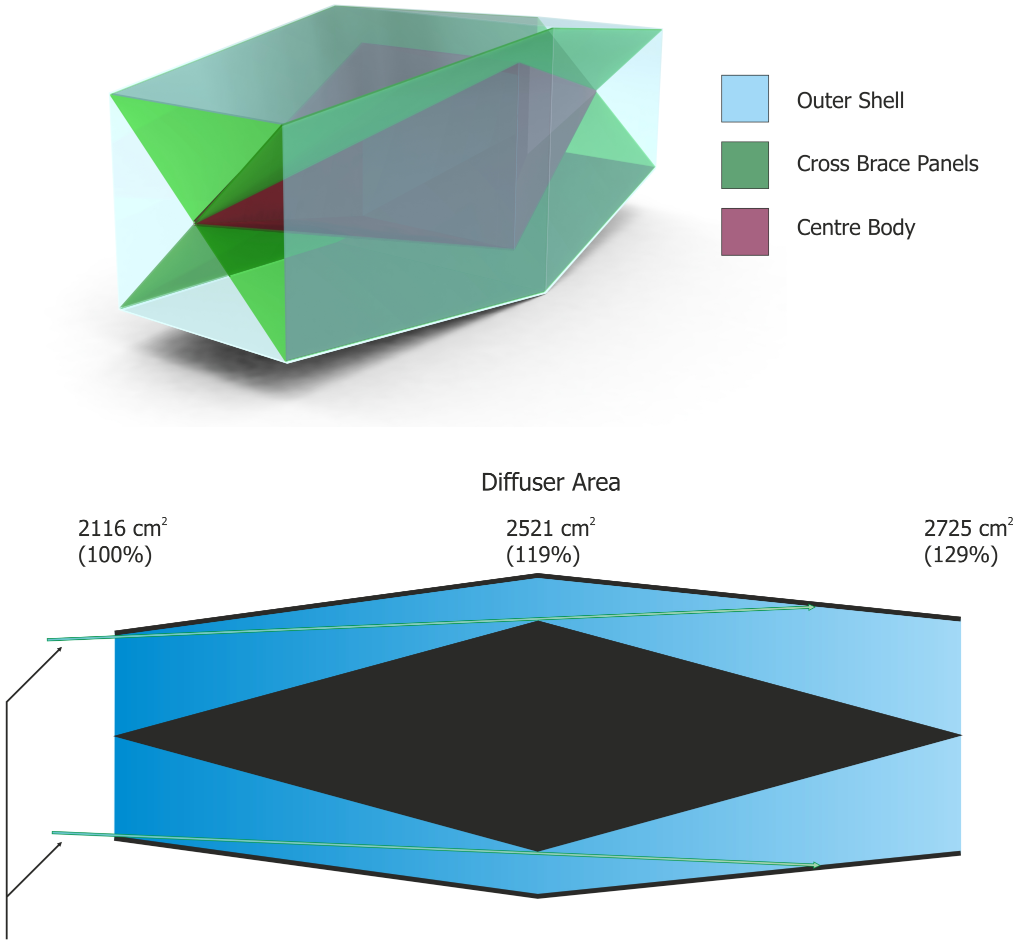

No Direct Exit Path From Tunnel Exists For Stray Laser Beams

Figure 3.50 Laser Light Trap

A fitting was manufactured for the laser sheet optics which eliminated the deposition of an oil film from the impingent seeded airflow (Figure 2.50). By passing a low pressure air stream from the front of the slit the contaminated air is deflected away from the lens without the laser sheet being affected. Air feed was adjusted by using an inline pneumatic throttle designed for controlling piston speed, using this it was possible to adjust flow rate to be appropriate for the tunnel speed. This completely eliminated the need to clean the lens in-between runs. The fitting was also designed to control the shape of the laser sheet, the part was painted matt black and the slit designed to clip the sheet such that only the interrogation area for the PIV study was illuminated. By firing the beam through the slit the amount of light hitting the white tunnel walls was reduced significantly. By reducing this, ambient (scattered) illumination of the test section was minimised. This cut down the optical return of smoke particles out of the interrogation plane. Eliminating this unwanted return maximised contrast between the intentionally illuminated particles and dark background in the camera image. Also important to control was the light which was scattered horizontally by dust, oil and imperfections in the laser optics. Unchecked this caused significant illumination of the background splitter plate. Although nominally coincident, fractional differences between the alignments of the two beams in the dual head laser changed the way the light was scattered by the imperfections in the optics altering the light pattern on the splitter plate between base to cross images. This obviously introduced large areas of changing intensity, which was sufficient to swamp the seed particle signal when the lateral beam clipping provided by the fitting was not in place.

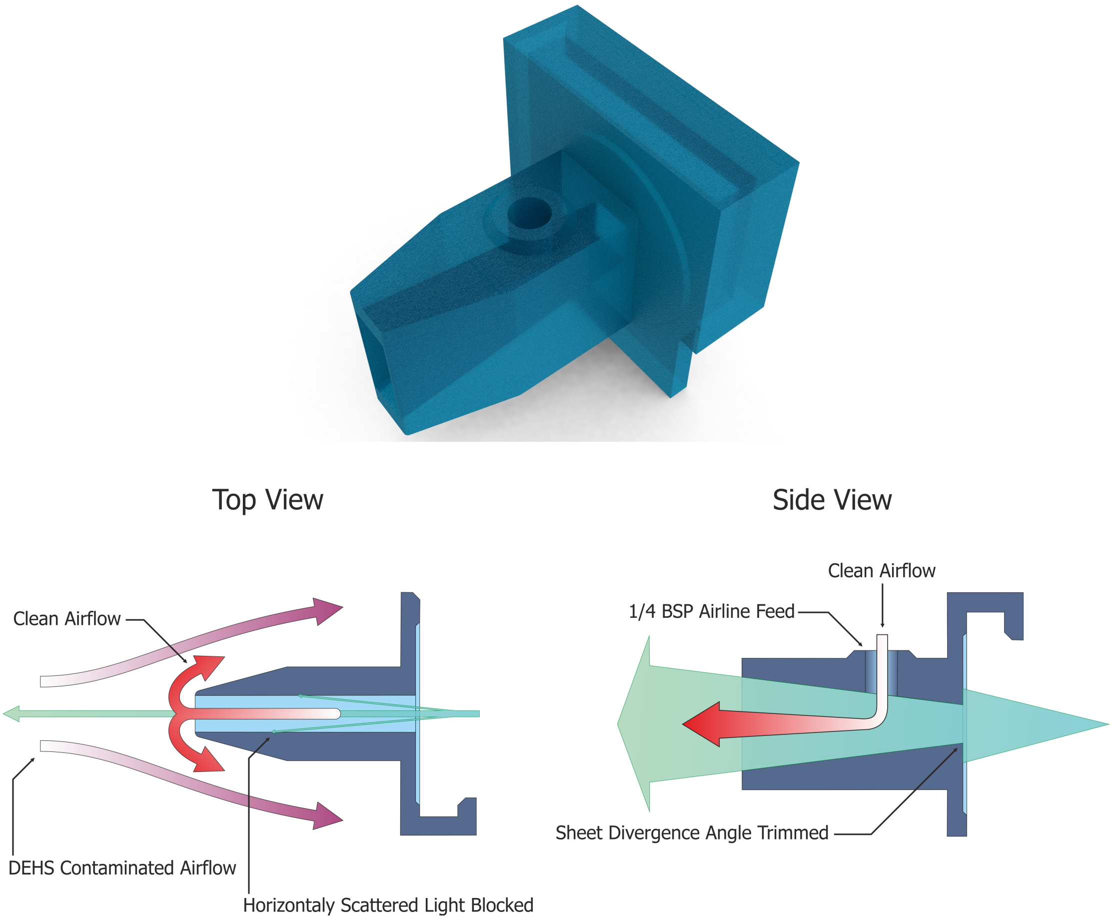

Figure 3.51 Air Lens Protector

To allow the illuminated particle sheet to be imaged a transparent side access panel had to be used in the tunnel: this also needed to incorporate a clear splitter plate to maintain a 2D flow field over the aerofoil. To minimise image distortion and maximise optical transmission the 2 clear panels (see Figure 2.51) were made from 2 mm thick TRU-VUE ® AR Reflection-Free® multi coated picture framing glass. Although this is optimised for broadband antireflective performance it was still quoted as having >97% transmission per panel. The use of rigid, flat glass panels also provided a much reduced level of distortion to the image when compared to the Plexiglas side panels previously used for optical tunnel access.

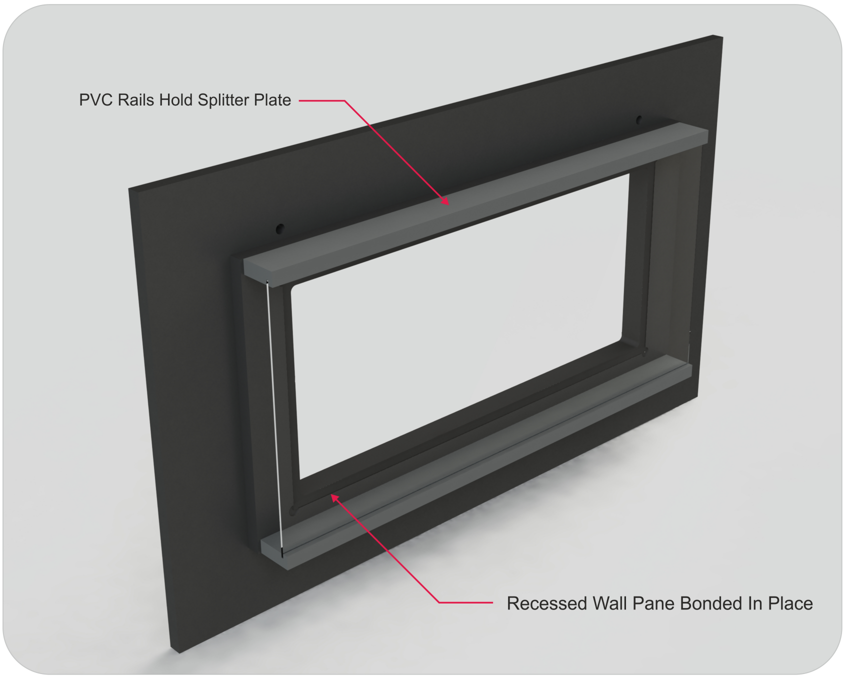

Figure 3.52 Glass Splitter Plate

How all this equipment fits together can be seen in Figure 2.52 parts a & b.

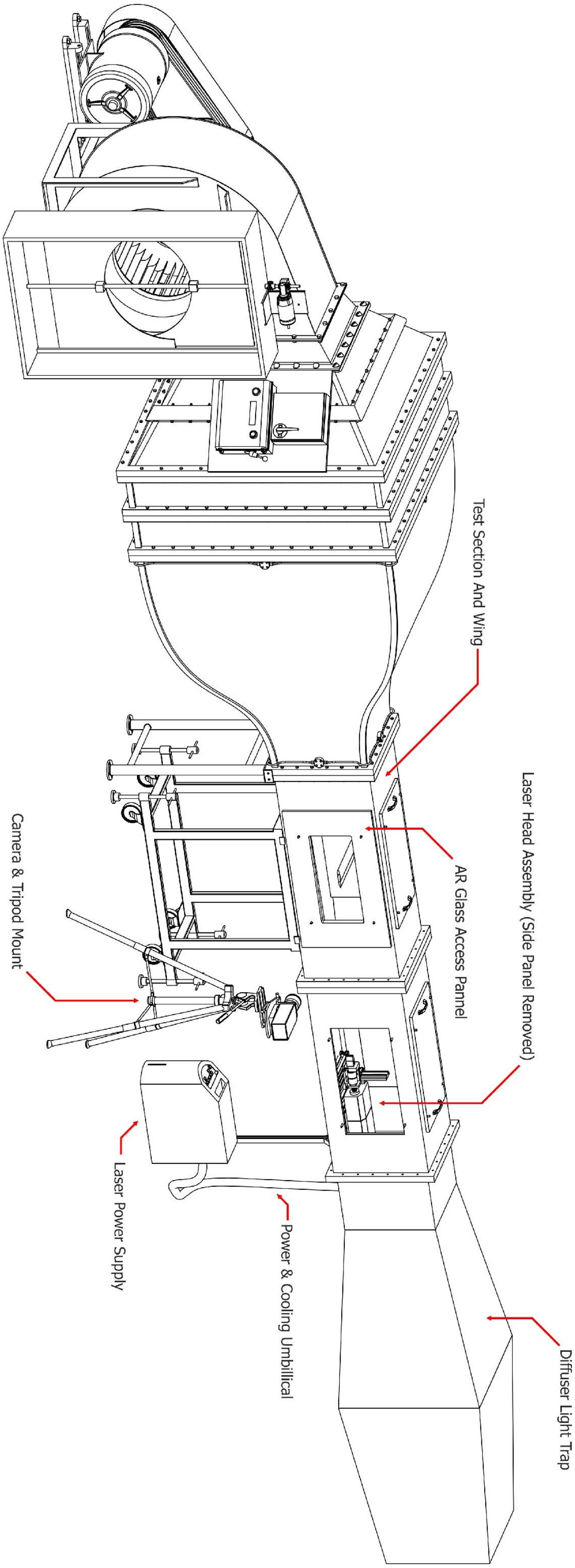

Figure 3.53a Wind tunnel PIV Setup

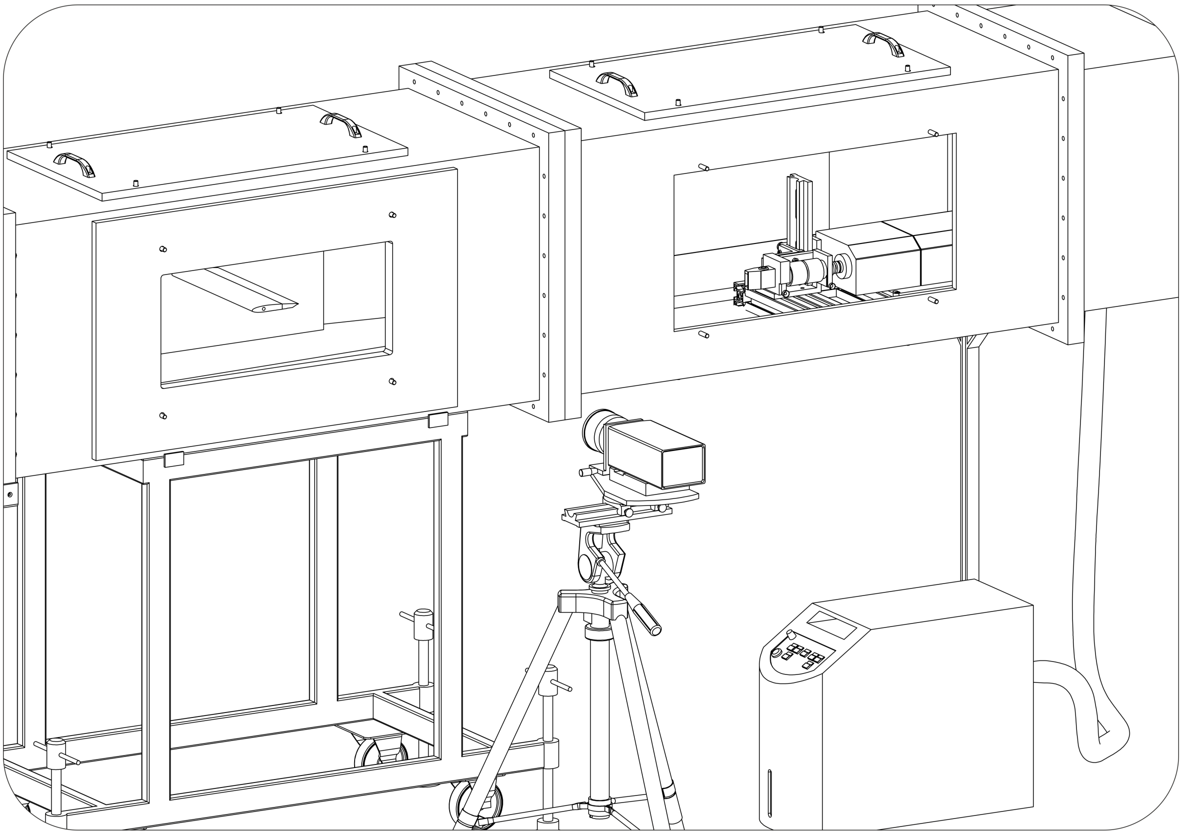

Figure 2.52b Wind Tunnel PIV Setup Detail

To allow the PIV software to translate the cameras field of view in the laser plane onto a useful user coordinate system and calculate velocities in m.s^{-1} rather than pixel.s^{-1} a calibration image is required. Figure 2.53 shows the calibration image used, superimposed over the outline of the incidence levelling tool to which it was attached. The rapid prototyped prismatic section of the incidence levelling tool was specified to precisely conform to the shape of the upper side of the wing: in this way its flat top section was ensured to be parallel to the centreline of the wing for seating the inclinometer, and the calibration image was fixed to the wing coordinate system and ensured to be parallel to the XZ plane. The range of markings allowed for the same calibration image to be used for both wide angle (most of the aerofoil) and close in (trailing edge only) PIV runs.

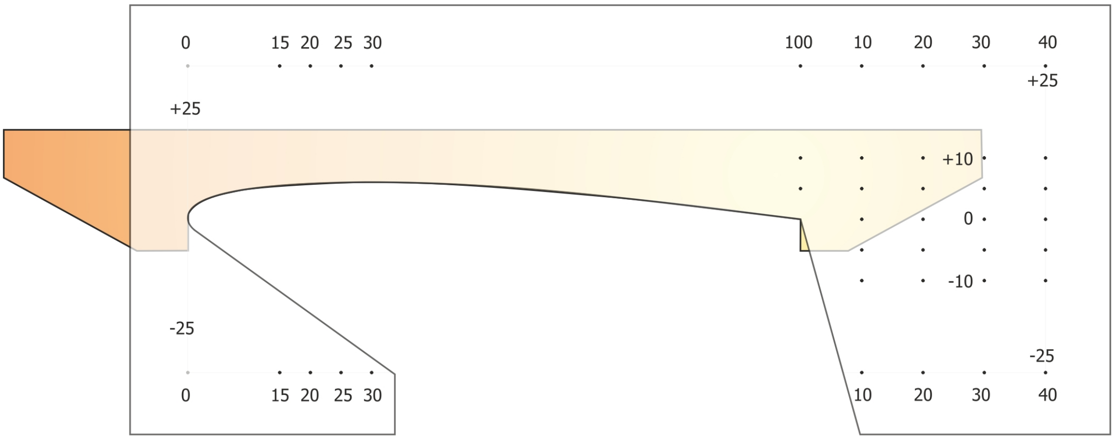

Figure 3.54 Calibration Plate

2.8.2.3 PIV Experimental Technique

2.8.2.3.1 PIV Measurement Procedure

The following list details the capture and analysis procedure for the PIV measurements, assuming calibration and camera / laser focusing has already been carried out:

- Capture 250 Image Pairs – At The Appropriate Separation (See Table 2.3)
- Export Raw .BMP Images To Hard Drive
- Manually Remove Dead Image Pairs – Approximately 3% of Images
- Load Remaining Image Pairs Into ILA Vid PIV 4g
- Load Calibration Image
- Map Calibration Grid To Image Pairs – Linear Rather Than Perspective Mapping
- Annotate Exclusion Zone Within Body Of Wing
- Cross Correlation - 32x32 Pixel Window Size At 16 Pixel Grid Spacing
- Window Filter Vectors
- Local Median Filter Vectors
- Interpolate Outliers
- Adaptive Cross Correlation – 32x32 Pixel Window Size At 16 Pixel Window Spacing
- Window Filter Vectors
- Local Median Filter
- Interpolate Outliers
- Export Vector Fields
- Average Valid Vectors Across All Image Pairs

This procedure was followed for PIV runs with the exception of the phase locked results (see Section 2.8.2.3.2 below) where step 3, ‘remove dead image pairs’ , had to be eliminated so that the images were kept synchronised to their position relative to the plasma pulse.

Tunnel Velocity (m.s^{-1})	Base-Cross image Separation (μs)	
	Expanded Field Of View	Trailing Edge Only
20	20	8
10	40	16
8	-	20
7	-	23
4	80	36

Table 2.3 Image Separation

2.8.2.3.2 Phase Locked PIV Measurements

Once the PIV process was sufficiently finely tuned to allow single frames to be meaningful (>96% valid) it was possible to look at different ways of taking the data to allow for better insight into the plasma actuator operation. One of the techniques used in gathering PIV data for the pulsed or interrupted plasma runs was to almost phase lock the individual PIV images to the plasma drive waveform such that the point in the wave cycle at which the image was taken precessed through exactly one cycle. From this the location of any given image pair in the drive cycle could be identified and from the sequence of image pairs it can be shown whether or not the vortex shedding from the separation step was locked into the plasma interruption frequency. The ILA PIV synchroniser only allows for integer Hz firing rates for the data acquisition, so taking 400 Hz nominal interruption (driven at 399 Hz as the nearest node) the plasma drive frequency had to be adjusted so that as precisely as possible 132.996 drive cycles occurred between camera flashes (Figure 2.54). At 3Hz capture the fractional difference between 132.996 drive cycles and 133 cycles (which would synchronise perfectly with 399 Hz) stacks up to ensure that that over the 250 image pair acquisition the full waveform was covered in sequence. However because the clock in either the synchroniser, personal media player or both were not 100% accurate and the accuracy achievable from measuring it on an oscilloscope was not sufficiently precise the exact value for requested interruption frequency initially had to be determined experimentally through incremental improvement. By careful analysis of the precession with the oscilloscope locked into the q-switch signal pulse for the laser it was found that the degree of accuracy necessary to land within < 1% of the full waveform over the 250 image pairs was approximately ±50 μHz necessitating working to the 7th or 8th significant figure on the interruption frequency setting.

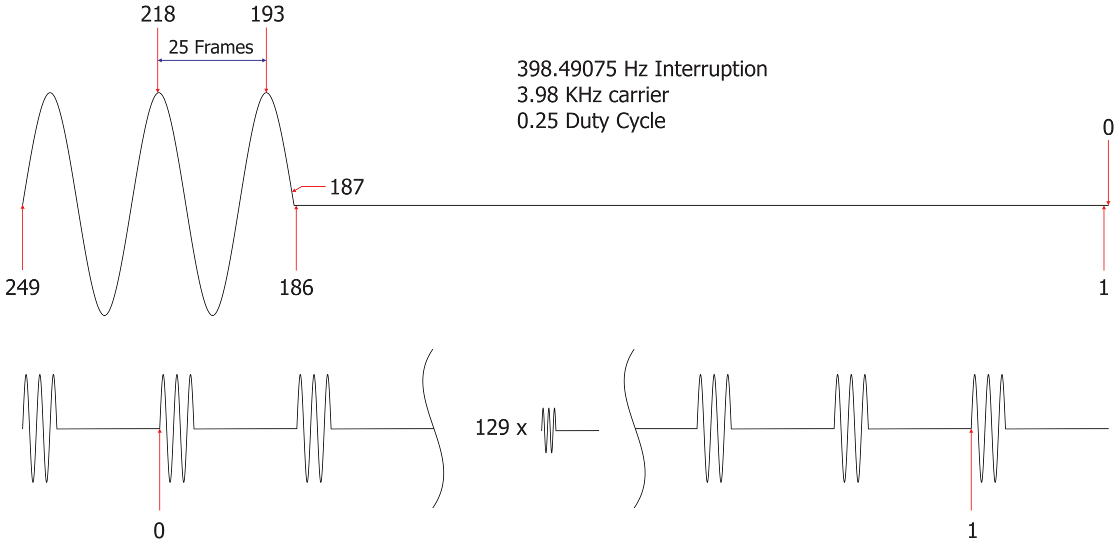

Figure 3.55 Phase Locked Frame Locations At 400 Hz

Once the beating frequency had been found to sufficient accuracy for 3 different interruption frequencies by trial and error, calculating the offset from the required interruption frequency in the digital source file to the nearest node frequency (i.e. nearest whole multiple of the nominal image capture frequency) showed a perfect straight line relationship (Figure 2.55). From this fitting it was possible to calculate the desired plasma interruption frequency for any nominal node frequency (see Table 2.4). The carrier frequency was also adjusted fractionally for each one so that an integer number of carrier (as distinct to interruption) cycles occurs in each 'on' section of the whole drive cycle. A modification to the waveform generation program automatically did these calculations and adjustments from the requested node frequency and output the raw data to form the .WAV file.

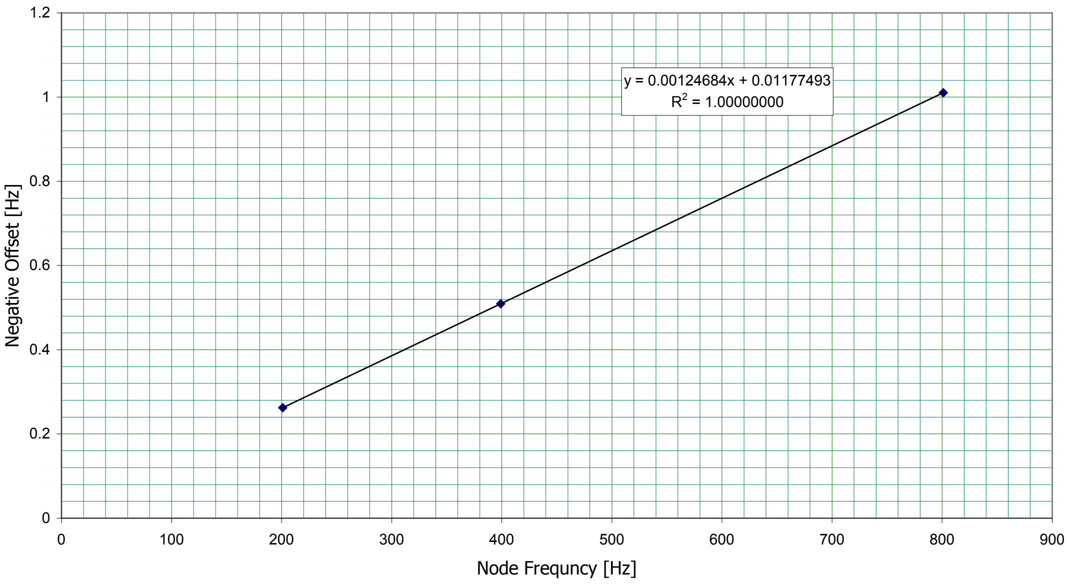

Figure 3.56 Phase Locked Beating Frequency

Nominal Frequency (Hz)	Nearest Lock-In Node (Hz)	Actual Frequency (Hz)
800	801	799.9895
700	699	698.1167
650	651	650.1765
600	600	599.2401
400	399	398.4908
300	300	299.6142
273	273	272.6478
261	261	260.6628
249	249	248.6778
237	237	236.6927
225	225	224.7077
213	213	212.7226
200	201	200.7376
150	150	149.8012

Table 2.4 Lock-In Frequencies

Data from these phase locked experimental runs were processed in 3 different ways; firstly individual frames were shown sequentially as a video. These showed whether or not the shedding was locked into the plasma interruption. Secondly, the sets of sequential frames were processed into 5562 time histories, one for each vector location in the field of view. These could then be plotted to give quasi sequential values in time for X,Z and absolute velocity components at any given point. Thirdly, because the lock-in forced the capture period to average over exactly one cycle, eliminating the possibility of unwanted partial lock-in overemphasising one part of the cycle in the average vector fields, the average vector fields returned from the phase locked results turned out to have better repeatability than those taken without lock-in.

Chapter 3 Plasma Actuator Development

3.1 Section Overview

This section details the trials, failure mode analysis and incremental improvements in the process of developing a long life dielectric barrier discharge actuator which could resist the thermal, chemical and electrical stresses placed upon it by the formation of the plasma. The concept was that the actuators would use thin metallised films for the electrodes; this is potentially desirable as electrode edge shape can be defined almost arbitrarily through the use of shadow masks during the metallisation. This could be used to improve plasma actuator performance, as was later reported in [109]. In addition to this, thin film electrodes possess an inherent flexibility and low weight advantage over macroscopic films applied with adhesives.

3.2 Thin Film Electrode Configuration, Patterning and Deposition

The initial choice for dielectric film was Kapton® HN (DuPont). It was selected for its high dielectric resistance (177 kV.mm^{-1})[138] and good mechanical and thermal properties. The electrodes were configured as strips 10 mm wide and 150 mm long; they were arranged on the substrate such that they were staggered to form the DBD actuator with their trailing and leading edges coincident for the live and ground electrodes respectively (Figure 3.1). They were produced using electron beam physical vapour deposition (EBPVD). EBPVD is used for film deposition in the MEMS and integrated circuit industries: the Durham University EBPVD chamber is shown in Figure 3.2.

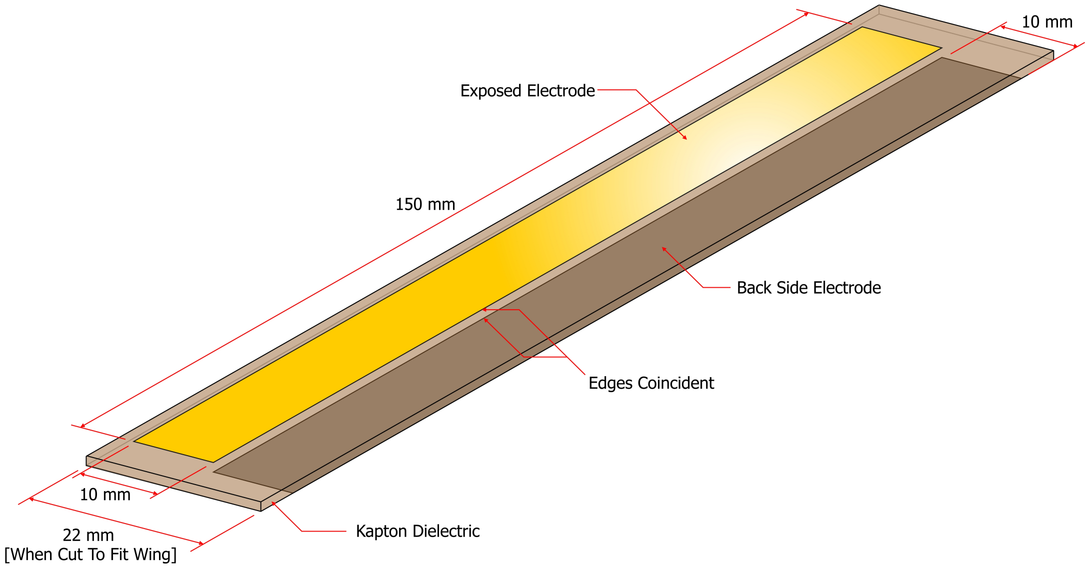

Figure 3.1 Thin Film Actuator Layout

EBPVD uses a thermionic element to generate an electron beam which is then used to bombard a sample until it is heated to the point where either the sample vapour evaporates from a molten pool contained in the crucible or pelletized material reaches its sublimation point. This vapour then travels to the substrate where it condenses. As the deposition is done under high vacuum, the mean free path of the vaporised atoms is much longer than the crucible – substrate distance, this means the atoms mostly arrive at the substrate surface without interacting with any of the residual atmosphere. A consequence of this is they arrive with line of sight directionality with respect to the crucible and with a $BCos^N \theta$ thickness distribution across the face of the substrate where θ is the angle subtended to the surface normal of the evaporation source and B and N are empirically derived constants [139]. The simplicity of operation of e-beam deposition allows for a wide variety of different materials to be deposited including pure metals, amorphous semiconductor films and some ceramics. Metal alloys can also be deposited but differences in the vapour pressures of the constituent elements can lead to the deposited material not having the same composition as the sample.

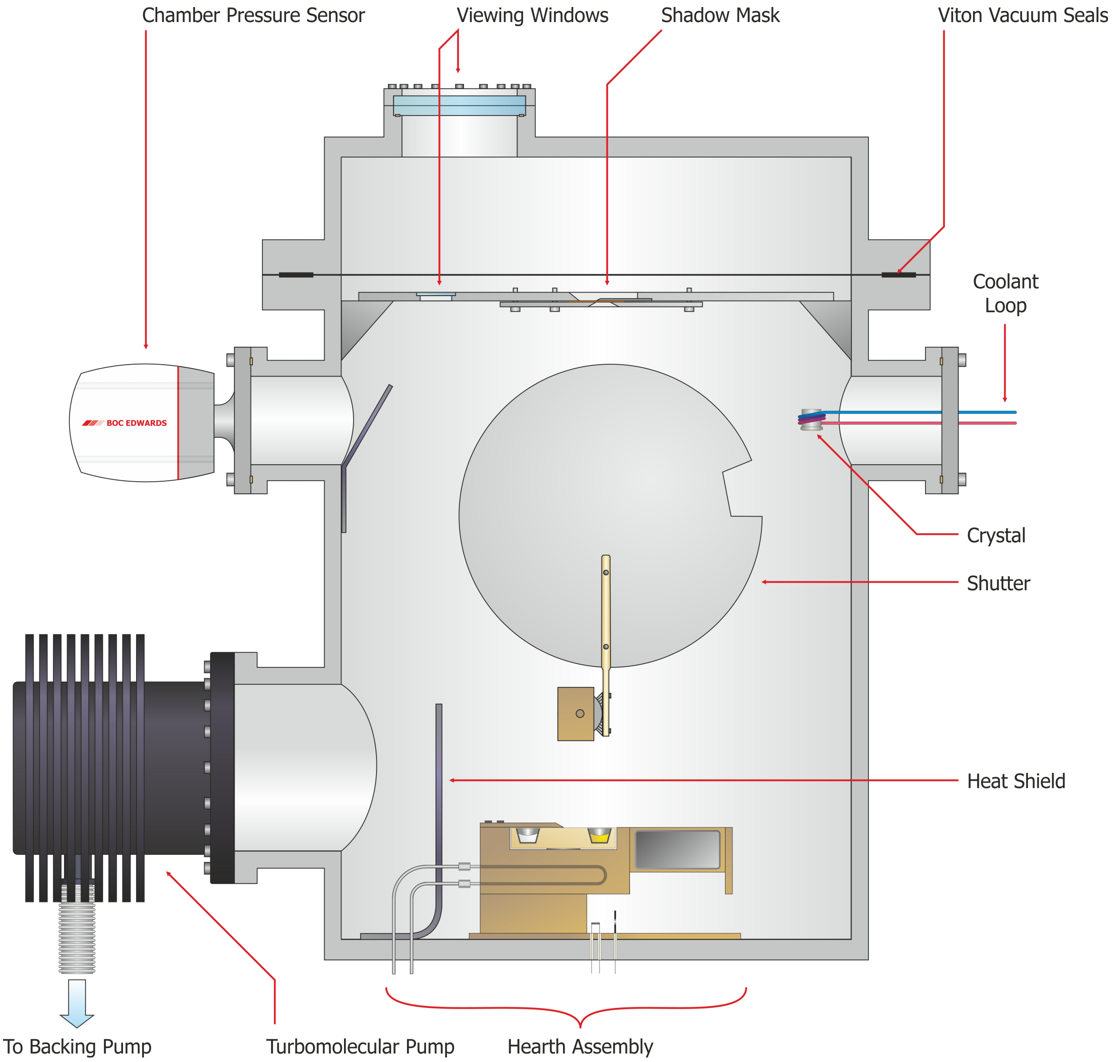

Figure 3.2 EBPVD Chamber

Figure 3.3 shows a diagram of the hearth. The complex arrangement of bending the beam through 270^o using magnetic fields is necessary to avoid metal deposition on the electron gun and thermionic element which would cause the system to short circuit. The crucible indexer allows for several different samples to be loaded at once and then rotated to deposit films of different materials without having to let the chamber back up to atmospheric pressure.

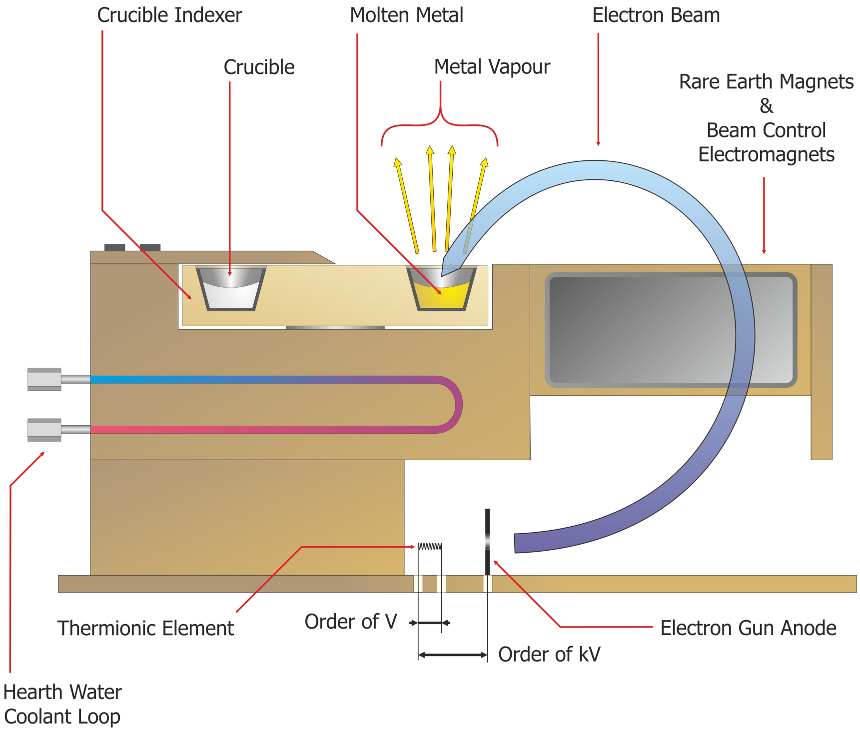

Figure 3.3 E-Beam Hearth

Film thickness is controlled using a combination of a quartz crystal monitor and the shutter (see Figure 3.2). The shutter allows the melt pool to be established and any surface oxides on the sample to be removed before the substrate is exposed to the vapour flux. It also allows the flux to be cut off more rapidly than de-energising the electron beam and is therefore used at the end of the deposition when the correct film thickness is reached before the electron gun is shut down. Film thickness is determined using the quartz crystal monitor, where changes in the resonant frequency of a piezoelectrically driven quartz disk can detect the addition of mass to the exposed crystal face as material is deposited. By knowing the density and acoustic impedance of the material being deposited the rate of change in frequency can be related to a rate of deposition with a resolution of less than 1 atomic layer per second.

Figure 3.4 shows a schematic of the shadow mask used to define the electrodes on the substrate. The mask consists of a metal plate which fits into the top of the e-beam chamber and a smaller clamping plate. Both of these contain precisely machined windows in the shape of the desired area over which metal is to be deposited on the substrate. A recess exists to take a microscope slide so that the position of electron beam can be seen to enable adjustment during operation so that it hits the centre of the crucible. In use the substrate is clamped in place and the first electrode deposited. The chamber is then brought up to air and the mask turned over without releasing the substrate. As the two windows in the mask are machined to have their edges coincident, the edges of the patterned electrodes are ensured to be aligned in the finished actuator.

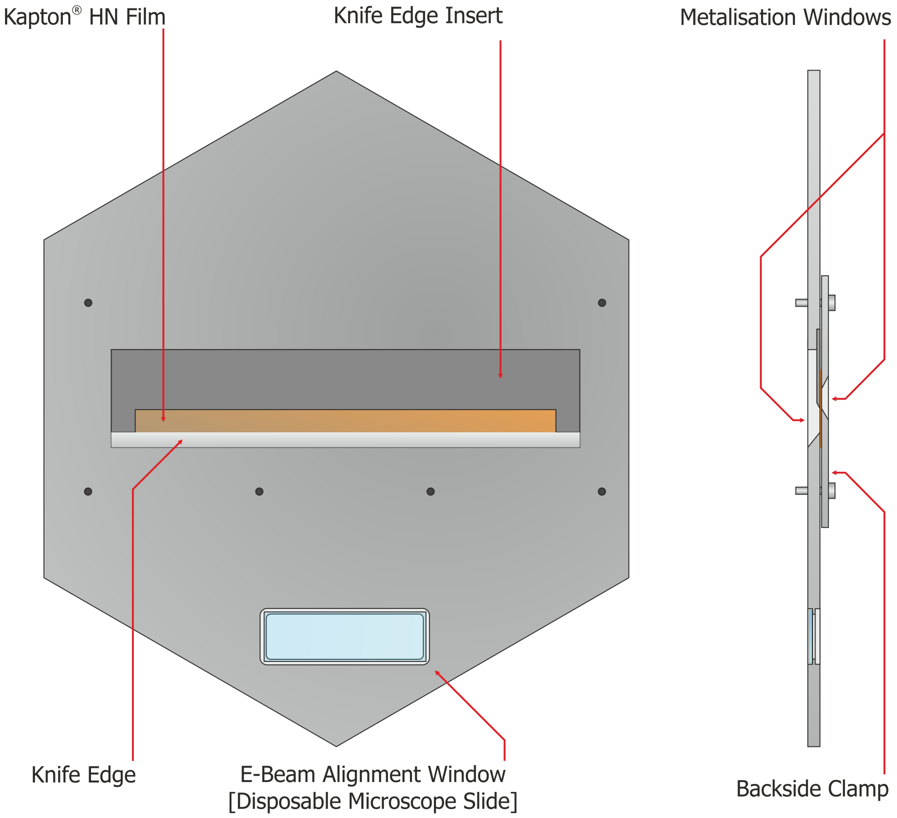

Figure 3.4 Shadow Mask

3.3 Electrode Failure Modes And Materiel Selection

Initially devices were created with electrodes made from 300 nm thick aluminium: these had an exceedingly short life span, in the region of 2-3 minutes. The failure mode the actuators were undergoing consisted of having the metal electrode eroded away from the downstream edge of the exposed film (see Figure 3.5 for the effect of 2 minutes of actuation). To enable the production of a better actuator an investigation into the process causing this failure was carried out.

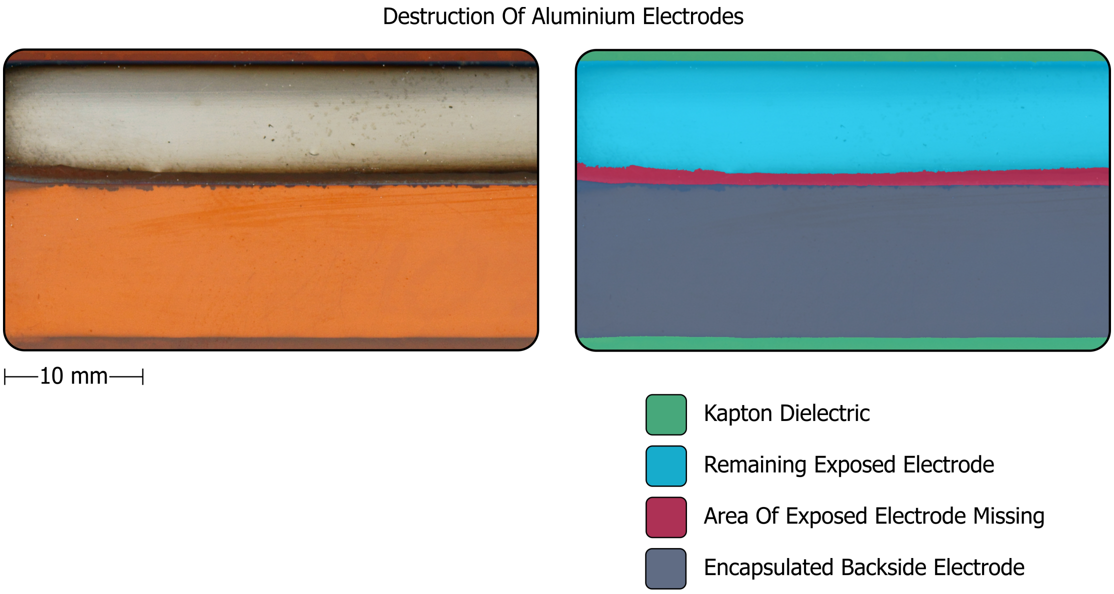

Figure 3.5 Macro Photograph Showing Aluminium Electrode Failure

3.3.1 Electrode Erosion Testing.

3.3.1.1 Ion Sputtering

Ion sputtering was the least likely of the three possible explanations proposed for the loss of electrode area. Ion sputtering is observed when a charged gas ion is accelerated towards a target by a bias voltage. If the impact has sufficient energy an atom at the centre of the collision and possibly some of those in the vicinity will be removed from the bulk material (see Figure 3.6). As the initial poorly performing electrodes were made from aluminium, to provide suitable contrast in susceptibility to ion bombardment a set of 300 nm thick gold electrodes were produced: to get the gold to adhere to the substrate a 15 nm chromium seed layer was used. Sputter yield is the metric by which ease of material removal by ion bombardment is measured. It is defined as the number of atoms removed from a target for a given incident ion and is a function of incidence angle and ion energy. A high sputter yield is indicative of rapid material removal. Gold has a particularly high sputter yield when compared to most metals, but when compared to the surface oxide which will have formed on the aluminium electrodes it is over 70 times quicker to sputter (see Table 3.1). If ion sputtering was the cause of electrode loss when the test was run the gold should have been eroded significantly quicker than the aluminium electrodes. This was not the case with the gold electrodes, which in fact performed significantly better than those made from aluminium, lasting approximately 15 times longer and failing through a different mode whilst showing no macroscopic signs of electrode degradation.

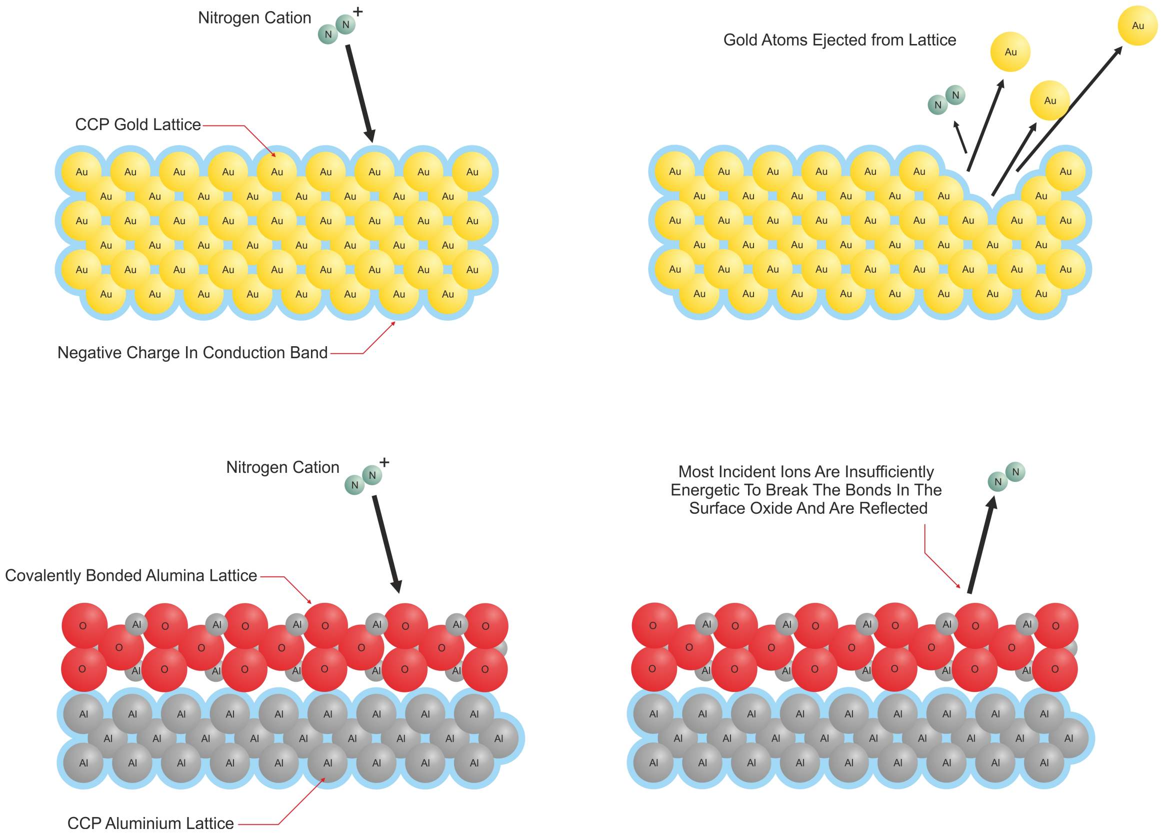

Figure 3.6 Ion Sputtering

Metal	Sputter Yield (Atoms.Ion^{-1}) (Ar^{+}, 5 keV)
Gold (Au)	7.9
Aluminium (Al)	2.0
Aluminium Oxide (Al_2O_3)	0.11

Table 3.1 Sputter Yields [140]

3.3.1.2 Oxidation

A second theory about how the electrodes were being eroded was that they were being oxidised and slowly burnt away by the reactive oxygen species in the plasma. Two tests were performed to determine if this was the case. Looking at the results of the test carried out to rule out ion sputtering we see that using a noble metal to form the electrodes eliminates the type of failure seen in the aluminium: this supports the oxidation hypothesis. To confirm this, an actuator constructed with aluminium electrodes was run inside a small Plexiglas box purged with dry nitrogen. By running the actuator in an environment with a very low oxygen content the reactive species should have been all but eliminated from the plasma thus severely reducing or eliminating the electrode erosion. This was not observed experimentally, as the actuator run in the nitrogen environment deteriorated at the same rate as those run in air thus ruling out oxidation as the cause of the electrode erosion.

3.3.1.3 Vaporisation

The final hypothesis for the mechanism of the destruction of the aluminium electrodes was that the metal was being locally heated to the point of vaporisation. Although time averaged the plasma extends across the whole length of the actuator edge and therefore power density is low; Instantaneously individual streamers are exceedingly localised. Due to the thin nature of the electrode film it has a low thermal mass and relatively high resistance; this could lead to significant Joule heating at the site of streamer formation. To test this, actuators were patterned with electrodes made from the refractory metals tungsten and molybdenum as well as titanium all of which have melting points in excess of gold and significantly greater than that of aluminium. A comparison of the melting points of these metals is shown in Table 3.2

Metal	Melting Point (^oC)	Boiling Point (^oC)
Aluminium (Al)	660	2519
Gold (Au)	1064	2856
Titanium (Ti)	1668	3287
Molybdenum (Mo)	2623	4639
Tungsten (W)	3422	5555

Table 3.2 Melting Points Of Selected Metals

Tungsten and molybdenum proved very difficult to deposit, the exceedingly high melting points of these metals meant that heating the sample in the e-beam crucible whilst preventing the hearth itself from melting could not be sustained for long. The coolant system could only maintain an acceptable coolant temperature for long enough to put down a layer a few 100 Å thick before the deposition had to be stopped and the equipment left to cool. Both tungsten and to a lesser extent molybdenum also presented a secondary practical problem which resulted in the resistance of the film produced being of significantly higher resistance than was expected. For the tungsten electrodes the resistance was over 2 orders of magnitude greater than for the gold. Figure 3.7 shows the two dimensional sheet resistivity of the deposited films. The values were calculated from a 4 wire resistance measurement at 20 mA constant current. Measurements were taken over the film deposited on the glass microscope slide window as this provided a more stable surface for making an electrical contact to, and these resistance values were then normalised to represent the resistance of thin film 1 m^2. It should be noted that the film thickness is not consistent, it was too difficult to deposit tungsten to the same thickness as the aluminium and gold films which deposit easily therefore these resistivities are representative of the films used on the actuators. The high resistance of the refractory metal electrodes is thought to have been caused by inclusion of co-evaporated carbon in the film, because the melting point of the tungsten is close to the sublimation point of the graphite crucible (3642 °C) in which it was contained. Significant portions of the wall of the crucible were also vaporised along with the metal.

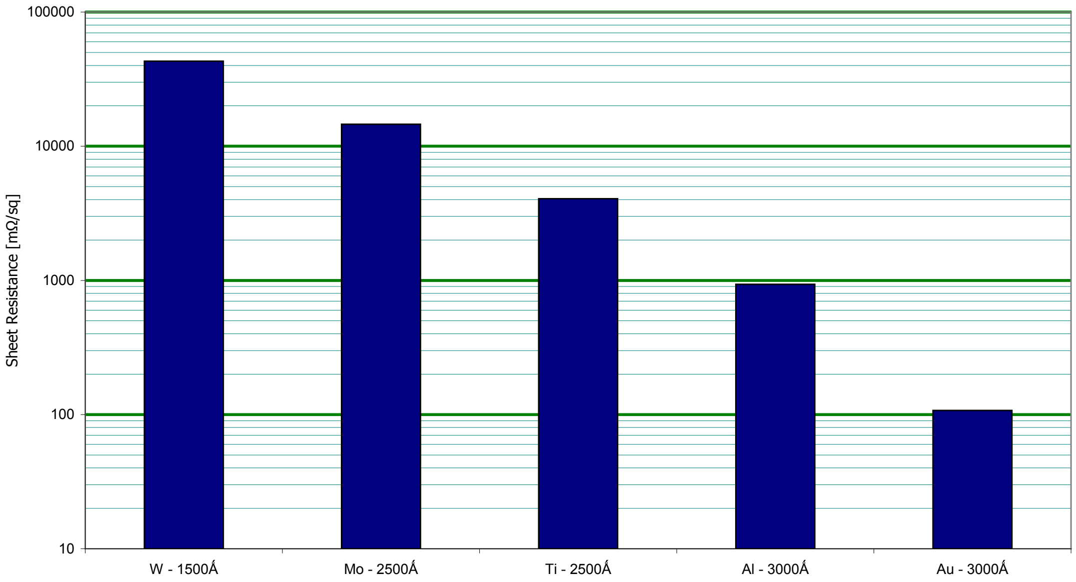

Figure 3.7 Electrode Sheet Resistance

The result of this increased resistivity was that especially in the case of the tungsten the parasitic resistance of the electrode was sufficient to provide a voltage drop great enough to reduce the strength of the ionic wind formed by the actuator.

With respect to electrode degradation, all four non-aluminium metals performed very similarly showing no elimination of the electrode surface despite the more reactive nature of the metals when compared to gold. Figure 3.8 shows the electrodes from the gold and the most reactive of the non-aluminium test metals, molybdenum. Both these actuators have experienced 50-55 minutes of running; compare this to the state of the aluminium electrodes shown in Figure 3.5 with only 2 minutes of running. This, combined with the results of the oxidation tests indicates that low reactivity is less of an issue than having a low melting point.

Figure 3.8 Macro Photographs Of Gold And Molybdenum Electrode States Post Use

3.3.1.4 Conclusions On Electrode Construction.

The conclusions which can be taken from these tests are that the most important attributes for the film to posses are a relatively high melting point for electrode endurance and a low sheet resistance to minimise parasitic resistive losses in the electrodes. The standard electrode configuration became 150 nm gold with 15 nm chromium as a seed layer. The reduced thickness was a cost saving measure and did not significantly affect the actuator performance through increased electrode resistance. Gold was primarily chosen for its ease of deposition in relatively thick unstressed layers.

3.4 Dielectric Failure Modes And Design

3.4.1 Kapton Plasma Erosion

With the chromium – gold evaporated electrodes improving actuator life expectancy into the 30 – 55 min area, the failure mode shifted to the next weakest part. Actuator breakdown occurred by going short circuit with respect to the high voltage potential applied across the two electrodes, although they did not necessarily show a conduction path to low voltage test equipment. When used actuators were examined they were showing a degradation in the condition of the surface of the Kapton downstream of the exposed electrode. The transparent smooth Kapton surface became increasingly matt and opaque with increased run time and proximity to the edge of the electrode. Examining the surface under the optical microscope showed surface pitting. Using images from the scanning electron microscope (SEM) it can be seen that the Kapton surface downstream of the actuator has been attacked, with the majority of the material removal occurring at the edge of the electrode (see Figure 3.9).

Looking more closely at the Kapton surface further downstream from the area immediately behind the electrode, the effects of micromasking on the surface can be seen (see Figure 3.10). Micromasked areas show up as areas which have not been attacked, due to being protected by surface contaminants, for example grease from fingerprints. This suggests that the Kapton is being etched by the plasma. As the plasma is known to contain ozone and oxygen radicals these were the most likely agent to be attacking the organic Kapton polymer. Comparing the actuator surface to a sample exposed to a known oxygen plasma in a reactive ion etch (RIE) system (Plasmalab 80 plus, Oxford Plasma Technology) showed that both test sample and exposed electrode had the same pitted surface and micromasking. The RIE test sample also produced a well defined copy of a finger print placed on the sheet to test for contaminant induced micromasking.

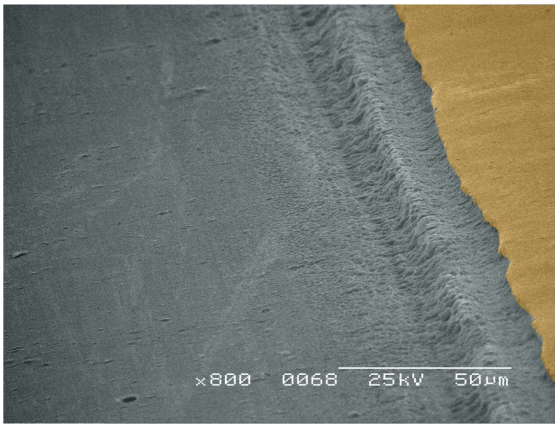

Figure 3.9 SEM Micrograph Of Downstream Kapton Plasma Etching

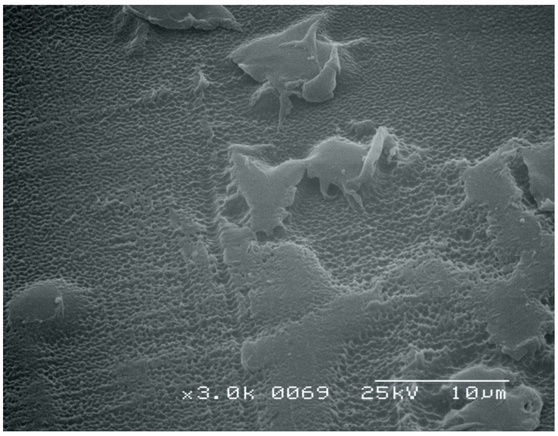

Figure 3.10 SEM Micrograph Of Micro-masking In Kapton Etching

Although the evaporated electrodes were no longer showing the same dramatic electrode vaporisation seen with the aluminium electrodes, SEM images of the electrode edges do show that there is still a small level of loss from the edge due to undercutting of the support material. Figure 3.11 shows the difference between the malleable gold electrode, gently drooping down into the trench being carved out underneath it and the much more brittle titanium electrode which can be seen to remain cantilevered out over the trough and then fracture as the undercut becomes too large.

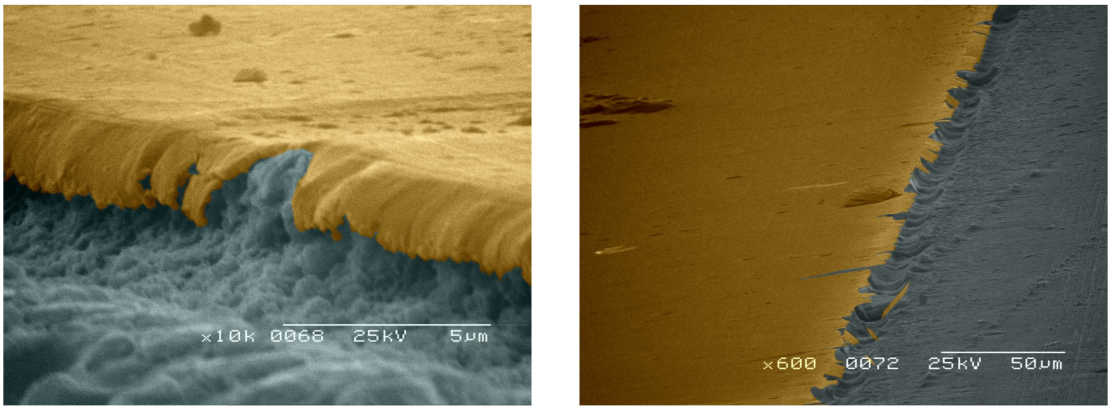

Gold Electrode

Titanium Electrode

Figure 3.11 SEM Micrograph Of Plasma Etched Trench Electrode Undercutting

3.4.2 Kapton Through Hole Formation

Having had several actuators fail with no obvious damage done, other than the trenches and surface roughening shown previously, a titanium electrode actuator failed as shown in Figure 3.12. A spark formed between the two electrodes through a hole formed in the Kapton and continued to spark, ablating the electrode around the hole and slowly progressing to carve out a circle as it sparked to the nearest connected part of the electrode. Removing the PVC tape encapsulating the rear electrode, and examining the backside of the actuator, showed that in addition to the single through hole visible from the top that caused the actuator to fail there were many more sub-thickness blind holes forming at the edge of the encapsulated electrode. This showed the direction of formation of the holes was from back to front (see Figure 3.13)

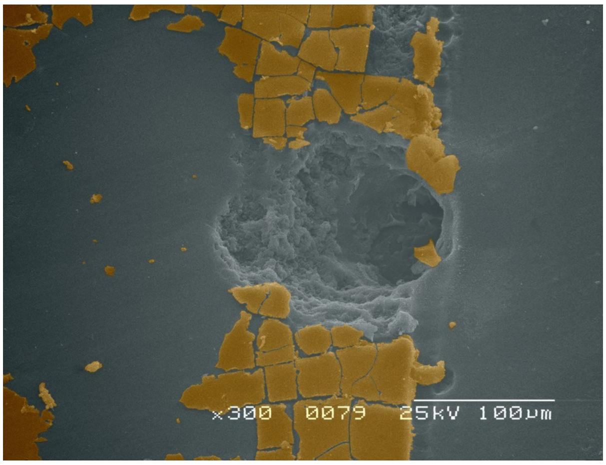

Figure 3.12 SEM Micrograph Of Through Hole In Kapton With Resultant Ti Electrode Spark Ablation

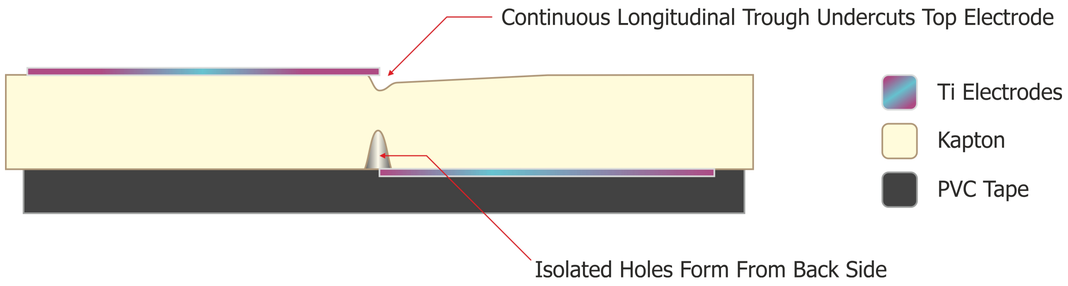

Figure 3.13 Backside Hole Formation

Visually the holes appeared blackened and using a precision probe station a resistance measurement was taken across the surface of one of these blind holes. Across the 130 μm diameter the modified surface showed a resistance of 58 kΩ, the front side surface showed no such change in conductivity after plasma attack, and from these observations it is reasonable to assume that the Kapton was being carbonised. Kapton becomes carbonised in an inert atmosphere from around 500 – 550 °C [141-142] giving off oxygen and nitrogen containing volatile molecules formed from the imide functional group in the Kapton polymer backbone. Given the semi-sealed nature of the back of the electrode a small defect in the encapsulation allowing the plasma to initially strike and start the process would give rise to a pocket of gas being generated, which was inert enough to allow the Kapton to carbonise rather than to burn. This correlates well with the favoured theory for the erosion of the aluminium electrodes which would require instantaneous temperatures in the region of 660 °C at streamer formation sites. The limited number of defects in the encapsulation limits streamer formation to a limited number of nodes, concentrating the effect to the point where the temperature of the bulk Kapton film can increase to the necessary point. In support of the thermal carbonisation of the film is the presence of tracking marks, tunnels of de-bonded PVC tape leading away from the streamer formation sites to the tape edge: this could be the pathway for the eventual release of the evolved gases (see Figure 3.14).

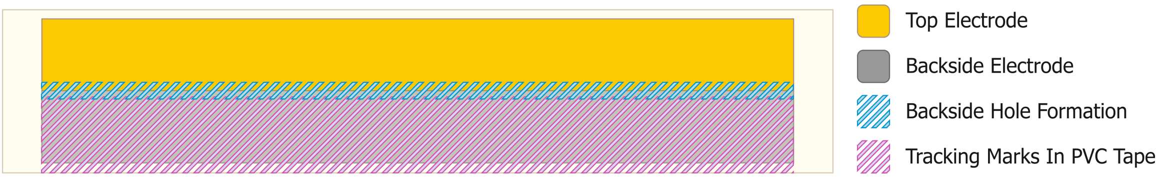

Figure 3.14 Location of Gas Induced Tracking Marks

The conclusion from this is that a major role in the failure of the initial development devices can be credited to the imperfect encapsulation of the backside electrode provided by the PVC tape which was being used. However this would be relatively easy to fix with a truly hermetic encapsulation by a suitably strong dielectric: this would totally suppress formation of the backside discharge. Development continued with PVC tape backside encapsulation as the relative erosion rate of the exposed side could still be observed without the need to epoxy encapsulate every actuator.

3.4.3 Improving Oxygen Plasma Resilience

Having found the new failure mode for the actuators to be due to the chemical attack of the Kapton by the plasma a series of attempts were made to improve the resistance of the dielectric substrate and therefore extend useable actuator life.

3.4.3.1 Silicon Dioxide Coated Kapton

The etching of silicon dioxide in an RIE requires a fluorine based chemistry to work [143]. The plasma created by the DBD will contain very few reactive fluorine species due to the low prevalence of fluorine containing contaminants in the atmosphere. Therefore the etch rate of an SiO_2 layer should be virtually nonexistent in an atmospheric plasma.

Creation of an SiO_2 layer on Kapton film was done using an e-beam evaporator and pelleted target material in a graphite crucible. This gave excellent deposition rates; however, this method suffered from low uniformity, evidenced by colour gradients produced by interference fringing across the substrate. Deposition using the EBPVD also produced a film with a high level of intrinsic stress which, over a series of trials, would lead the protective layer to delaminate from the substrate on occasion. To reduce the delamination problems the film thickness was reduced from 150 nm to a nominal 75 nm, along with the introduction of an improved surface preparation procedure involving washing the substrate in Decon® 90 detergent in an ultrasonic bath to dislodge particulate contaminates, followed by acetone and propan-2-ol washes to remove organic oil / grease deposits. The substrates were then washed in deionised water and force dried with nitrogen. This resulted in a film which was stable enough to survive the subsequent processing to produce an actuator from the coated material.

Figure 3.15 shows the results of running an actuator prepared with SiO_2 coated Kapton. The actuator was run without any backside encapsulation, which meant that the two sides would be subjected to equal plasma discharges. Comparing the protected and unprotected sides clearly shows the macroscopic efficacy of the SiO_2 layer in protecting the Kapton from attack by the plasma. When the backside was sealed with PVC tape in the standard way single side coated actuators showed marginally improved longevity of 40 – 70 min due to the Kapton only being eroded from one side. The logical path forward from positive single side coated tests was to protect both sides with an evaporated SiO_2 layer. However, unfortunately when run, these did not provide the improvement expected. The high stress and low substrate adhesion of the SiO_2 meant that the layer was especially prone to damage. This, along with the line of sight deposition of the e-beam, made it difficult to both deposit in the first place and then maintain after further processing a defect free protective layer. Although the double sided protected actuators exhibited the same broad resistance to attack shown in Figure 3.15, defects in the layer let the oxygen species contact the bare Kapton and cause failure at these points. It would have been interesting to be able to test actuators prepared with more conformal, lower stress protective oxide layers with potentially greater robustness created using RF magnetron sputtering. However the deposition area in the available sputter system (Mini Lab, Moorfield) was not large enough to coat the required dielectrics.

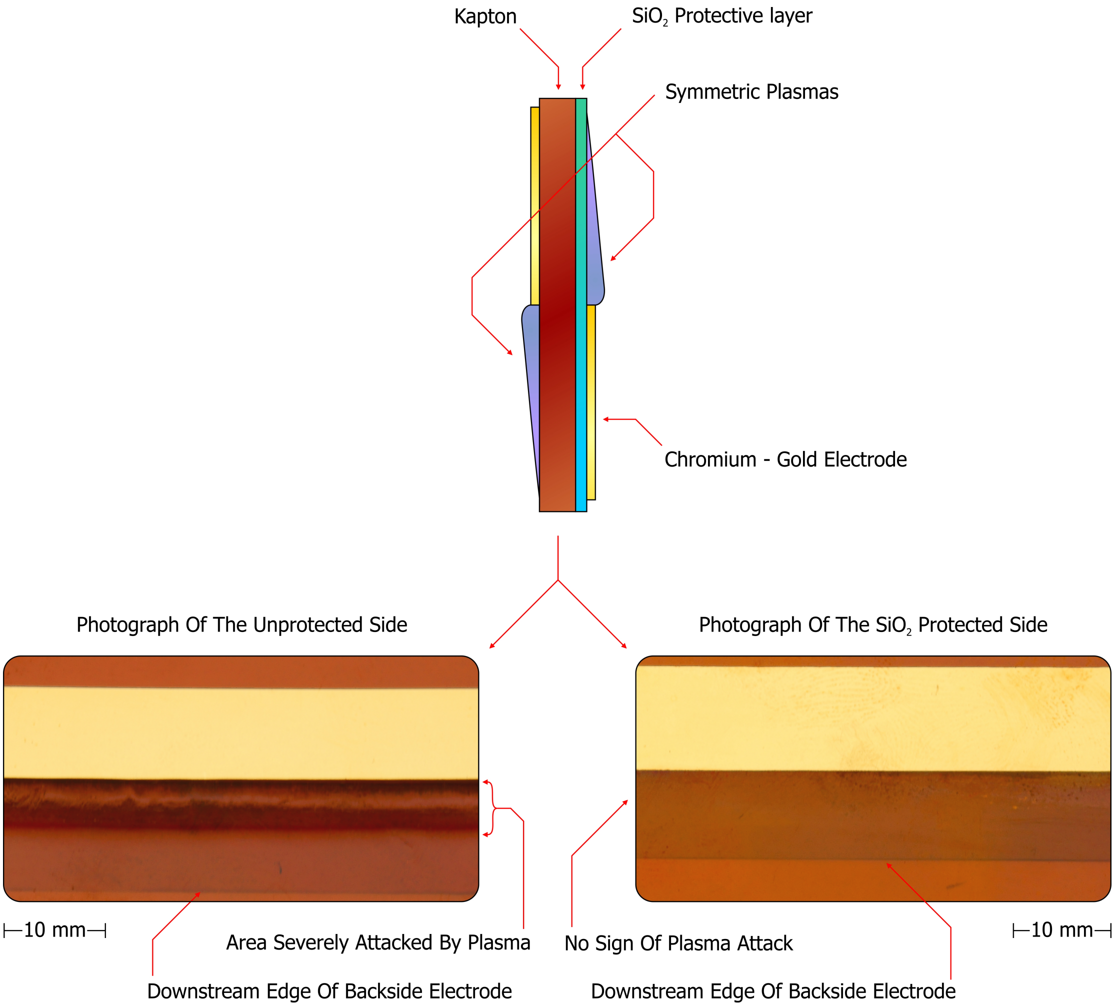

Figure 3.15 Comparison of Protected and Unprotected Surface Attack

3.4.3.2 Fluorinated Ethylene Propylene (FEP)

DuPont Teflon-FEP is a random co-polymer of Hexafluropropylene (HFP) and Tetrafluroethylene (TFE) (see Figure 3.17). It contains a CF_2-CF_2 backbone with CF_3 branches from the HFP [144] and is very similar in its chain structure to Polytetrafluoroethylene (PTFE).

Fluropolymers like this are very thermally stable and highly resistant to chemical attack. These characteristics stem from fluorine's high electronegativity and small atomic radius and because of this the C-F bond formed in fluoropolymers has a very high bond dissociation energy [145-146] and is therefore energetically unfavourable to break apart. The bond is therefore exceedingly difficult to break down even by powerful oxidising agents. The small atomic radius of fluorine atoms allows the carbon backbone of the polymer to take an unstressed dihedral angle. However, it is large enough that the fluorine atoms form an almost perfect shield around the carbon backbone protecting it from chemical attack [144] (see Figure 3.18). On this basis FEP sheet was selected as a suitable test material likely to resist the chemical attack by the oxygen plasma which had been seen in the Kapton. The DuPont FEP sheet chosen was 0.127 mm thick, from reference [147] DuPont specify a dielectric strength of approximately 150 kV.mm^{-1}, a thickness which translates to a breakdown voltage of 19 kV. This should have equated to almost a factor of 3 safety margin over the approximately 7 kV available from the signal generator amplifier setup used to test it. Two devices were patterned. The first failed instantly, sparking straight through the substrate, and the second lasted only 1:30 of running before the device again failed through the breakdown of the dielectric (Figure 3.16). It is suspected that the initial instantaneous failure was caused by structural compromise of the soft polymer during the processing and patterning to form the electrodes.

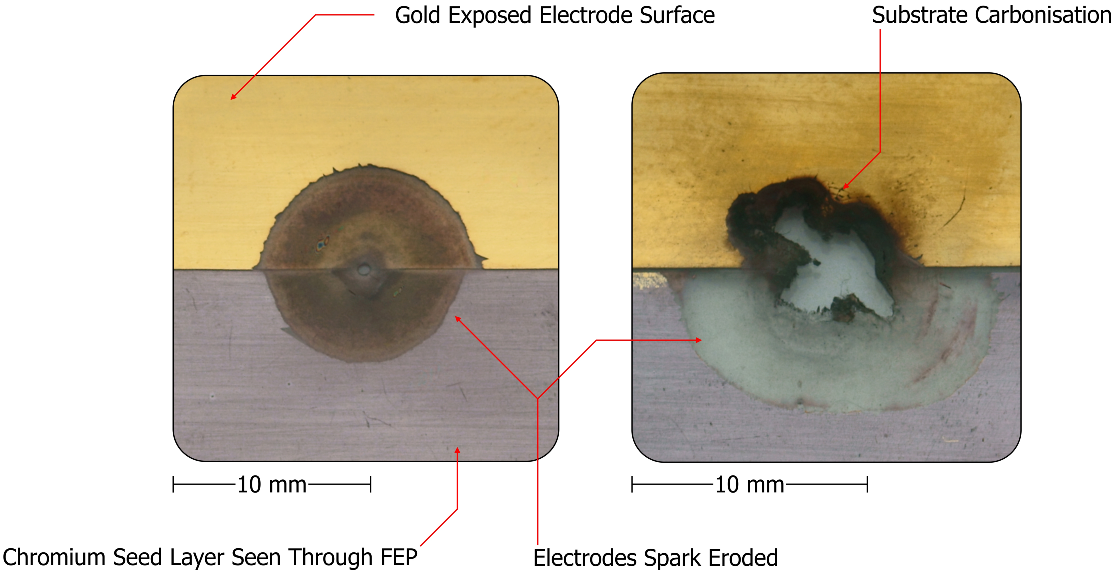

Figure 3.16 Macro Photographs Of FEP Dielectric Failure

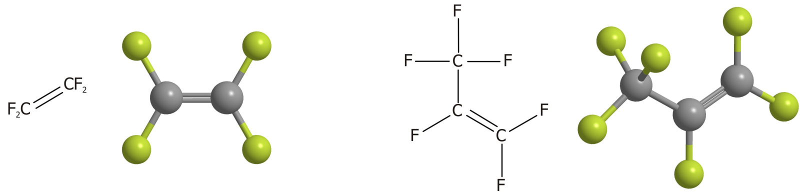

Tetrafluroethylene

Hexafluroproylene

Figure 3.17 FEP Monomers

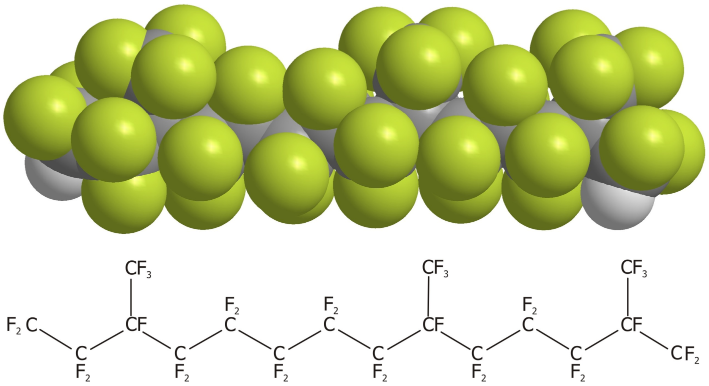

Figure 3.18 Space Filling Diagram Of A Section Of FEP Polymer

As the actuator had failed electrically any improved plasma resistance couldn't be verified in the standard timed bench-top test. To get around this and investigate its suitability without having to procure thicker FEP sheet, samples of FEP and Kapton were cut and placed in the RIE. The samples were partially masked with a silicon wafer and then simultaneously exposed to an oxygen plasma at 350 W, 50 sccm O_2, 150 mT for 15 minutes. Examining the thickness of the unexposed and exposed material showed that the etch rate of the FEP sheet was actually higher than that of the Kapton (see Figure 3.19). Following failing to live up to expectations in both plasma resistance and electrical insulation, further investigation of fluropolymer dielectrics was dropped.

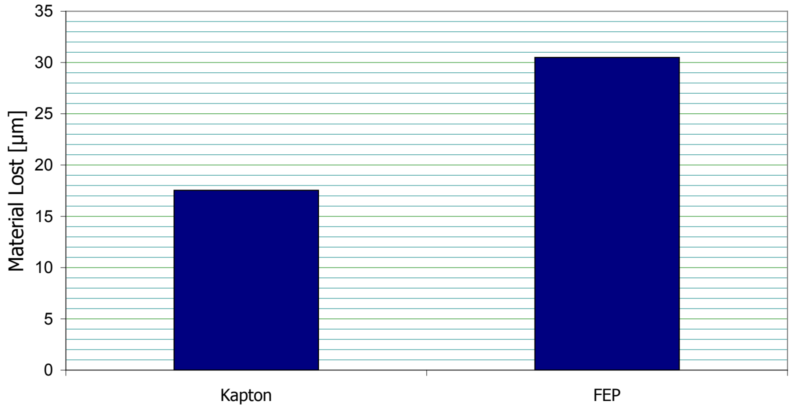

Figure 3.19 Controlled O_2 plasma Erosion Test In RIE

3.4.3.3 Polydimethylsiloxane (PDMS) Glass Reinforced Plastic (GRP) Composite

To create an actuator which would resist erosion by the oxygen species present in the DBD plasma sheet a ruggedized flexible silicon based solution was investigated. PDMS is a widely available commercial polymer containing a backbone of Si-O-Si bonds. For these experiments Dow Corning® Sylgard® 184 elastomer was used; it is sold as a 2 part kit containing the monomer in one part and a crosslinking agent with a platinum catalyst in the other.

When PDMS is attacked by an oxygen plasma, silanol groups (Si-OH) are formed on the surface. Adjacent silanol groups then undergo a condensation reaction to eliminate a water molecule leaving an inert silicone dioxide film on the surface [148] and as such also require fluorine based chemistry to dry etch [149]. This means that an actuator containing a PDMS surface will have the benefits of the inherent flexibility of a polymeric elastomer coupled with the plasma resistance of an SiO_2 layer, but with the ability to regenerate itself at any cracks. To confirm its plasma resistance a sample of cast, unreinforced PDMS was subjected to the same test as FEP and Kapton samples underwent for Figure 3.19. The result for the PDMS sheet is not shown on that chart as no detectable step was formed between exposed and unexposed parts of the sample, and only a slight hazing of the previously clear surface could be seen.

PDMS on its own as an elastomer exhibits an extraordinarily low elastic modulus and poor structural properties. This makes cast PDMS sheets unsuitable for patterning electrodes on, as elongation during processing would compromise the integrity of the electrodes. A very low tear strength for thin sheets would also have complicated processing and produced problems in handling and attaching the sheet to the rear of the aerofoil. To address this, and create a PDMS sheet which was structurally sound enough to take an evaporated electrode and withstand processing, reinforcement was required. Exceedingly thin woven glass fibre mat with an areal density of only 25 $g.m^{-2}$ was impregnated with the elastomer. Initially samples were prepared by degassing the liquid PDMS in a vacuum oven before pouring onto the fibre matt, degassing again in the vacuum oven and then heat curing under vacuum whilst being compressed between two glass plates. This provided unsatisfactory defect levels in the finished sheet as the degassing was not absolute; the small amounts of residual gases were set in the cast sheet at maximum possible size due to the low pressure. The solution to this was to degas the sample once it had been poured and then bring it back up to atmospheric pressure and allow it to cure at room temperature; this produced sheets with a negligible level of defects. The composite produced was a 0.10 mm thick sheet with a high on-axis Young’s modulus and good mechanical durability whilst still maintaining the necessary compliance to be attached to an aerofoil profile (see Figure 3.20).

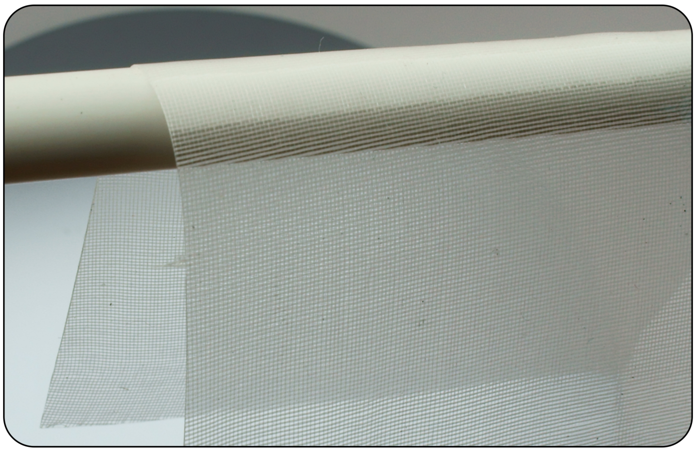

Figure 3.20 PDMS Composite Sheet Draped Over a 12 mm Diameter Rod

A sample of this single layer composite was placed between two high voltage terminals to investigate its breakdown properties; unfortunately it was unable to withstand the voltages it would experience in an actuator. This was the expected outcome as the sheet had turned out thinner than expected and with a stated dielectric strength of only 14 $kV.mm^{-1}$ for the PDMS [150] it was not expected to survive the test.

A second PDMS GRP sheet was constructed using 5 layers of the fibre matt arranged with alternating layers at 45° to each other. This produced a much stiffer composite with increased theoretical dielectric strength (0.47 mm, 6.58 kV). This dielectric also failed rapidly before the full test voltage could be reached. Examining the sheet revealed that it had been compromised during the manufacture process, as the sheet was separated from its mould by peeling it away from the glass plate it is necessarily bent through a tight angle. With 5 lamina the composite was sufficiently thick that the bottom layer of fibre mat would go taut around the outside of the bend and the material on the inside would buckle causing localised delamination to occur (see Figure 3.21, noting the fibre structure within the laminate). This also occurred whenever the composite was bent around any sharp corner giving potential problems when being fitted to a separation step on an aerofoil. With an inability to avoid structural compromise in the manufacture process and the limits of acceptable dielectric thickness being reached this led to the idea of a single sheet PDMS actuator being deemed unusable.

Figure 3.21 Buckling Induced Delamination

3.4.3.4 Kapton – (PDMS GRP) Laminated Composite

To create an actuator capable of withstanding both the chemical and electrical stresses experienced during operation, development moved to creating a dielectric with a single layer fiber-reinforced PDMS composite as a skin, selected for its plasma resistance properties and a Kapton sub-layer to provide the electrical insulation.

The first assembly method tried was to cure the PDMS glass fibre on top of a roughened Kapton sheet. This resulted in immediate separation of the two halves as the adhesion of the PDMS to the glass plate was greater than that to the Kapton and could not be released intact from the casting process.

Looking for a suitable glue, initial small scale tests of Polymethylmethacrylate (PMMA) dissolved in chlorobenzene proved positive providing a Kapton to PDMS bond stronger than the tensile strength of the PDMS. The high cost of the MicroChem PMMA photoresist used for testing prohibited its use for manufacture, and therefore a solution of Plexiglass® (PMMA) dissolved in chlorobenzene was prepared. When attempting to assemble the dielectric sheet with the bulk PMMA glue, the composite deformed, curling up and stressing off the surface of the Kapton before it could dry. Examination of the surface showed that where the cast composite had been smooth the surface was now dimpled between thread bundles of the glass fibre weave. Looking at the way the film distorted, its mass gain in solvent (see Table 3.3) and the ability of the film to return to its original shape if the sample was baked dry, it was apparent that solvent absorption combined with the anisotropic properties of the film had caused the buckling (see Figure 3.22). Differences in where the glass fabric lay within the z axis of sheet caused differential expansion around what was the relatively fixed datum of the fibre reinforcement, which also led to the dimpled surface due to pinning and reduced material for adsorption and expansion at the warp - weft nodes. Anasol® solvent was tested for its uptake into the PDMS as an alternative for forming the PMMA glue. Although offering a massive improvement in comparison to the chlorobenzene, it still produced some distortion. This, combined with the difficulty in drying the solvent whilst held between plates to maintain uniform distribution, and a failure to replicate the initial success from the small scale tests, led to the elimination of solvent based glues.

Solvent	Anasol®	Chlorobenzene
Initial Mass	0.358g	0.365g
Mass + Absorbed Solvent	0.416g	0.621g
% Change	16.2	70.1

Table 3.3 Solvent Absorption Test

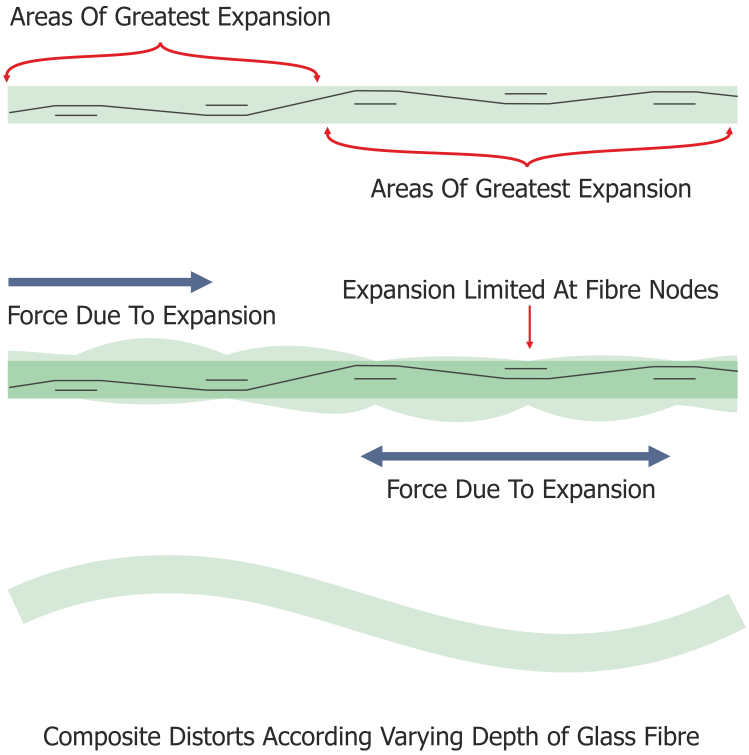

Figure 3.22 Solvent Absorption Buckling

One of the reasons PDMS is exceptionally hard to bond to is because it has a very low free surface energy of 19.8 mN.m^{-2}. This is even lower than explicitly 'non-stick' coatings like Teflon® (20.0 mN.m^{-2}) [151]. To enable bonding to this material surface functionalisation of the sheet can be accomplished using an oxygen plasma etch in the RIE [152]. To investigate the effect of the plasma etch and formulate a successful recipe, test samples were run. They were placed in the RIE chamber with the quartz glass platen. A 6" silicon wafer was used to support the composite sheet and ensure that it did not contaminate the chamber: the equipment settings are listed in Table 3.4.

Sample	Power (W)	O2 (sccm)	Time (min)	Pressure (mTorr)
1	350	50	2	100
2	350	50	20	100
3	350	50	5	100
4	75	50	60	100
5	75	50	2	100

Table 3.4 Surface Functionalisation Test Conditions

Control The sample adhesion was tested using double sided tape, and showed that the tape was incapable of fixing an untreated sample with the bond being weaker than that of the tape to its backing strip.

Sample 1 showed vastly improved adhesion, capable of fixing the two layers together sufficiently for manufacture and aerodynamic tests. It also showed a couple of small areas where the film had become damaged by fusing to the silicon carrier wafer.

Sample 2 was run to see if increased exposure would result in a stronger bond. The outcome of the test was that at 20 minutes the film had become distorted and stiffened and also managed to fuse itself to the silicon wafer over a much larger area. In addition to this, subjectively the bond strength had not improved.

Sample 3 consisted of three sub-samples. These were used to test the bond strength as it aged. Plasma treated PDMS shows a hydrophobic recovery; as the shorter more mobile polymer chains diffuse towards the surface, the functionalised groups on the surface return to the bulk polymer and it regains its original properties [153]. This process occurs on a timescale of hours to days and so samples were tested immediately after plasma exposure and bonding with the tape, then after 12 hours and again after 2 days; there appeared to be no significant degradation in the bond strength. All three suffered minor damage to the film during the RIE etch due to adhesion to the silicon carrier.

Sample 4 was run at a much lower power but for a longer time to compensate to allow the same level of surface functionalisation; the resulting film showed no signs of adhesion to the carrier wafer and yet retained the desirable adhesion improvement to the tape.

Sample 5 was used to see if it was possible to use a much shorter plasma exposure and still achieve the same surface properties as were obtained in test 4. The resulting film adhered as well as the film that had had the hour long exposure and again was free from the carrier wafer bonding issues. The RIE settings used for sample 5 were used to treat all subsequent samples.

Once the PDMS had been successfully functionalised, this allowed the assembly and patterning of the first actuator stacks with a PDMS plasma resistant layer for use on a wing. As it had shown good adhesion to the functionalized PDMS surface during testing double sided tape was used for both the inter layer bond between the two films and for adhesion of the Kapton to the aerofoil structure (see Figure 3.23). Because the tape was not vacuum compatible and thus could not be put into the EBPVD chamber the electrodes had to be patterned individually on their respective substrates and then assembled later. This is obviously undesirable from an alignment perspective but it allowed for rapid testing of the composite structure.

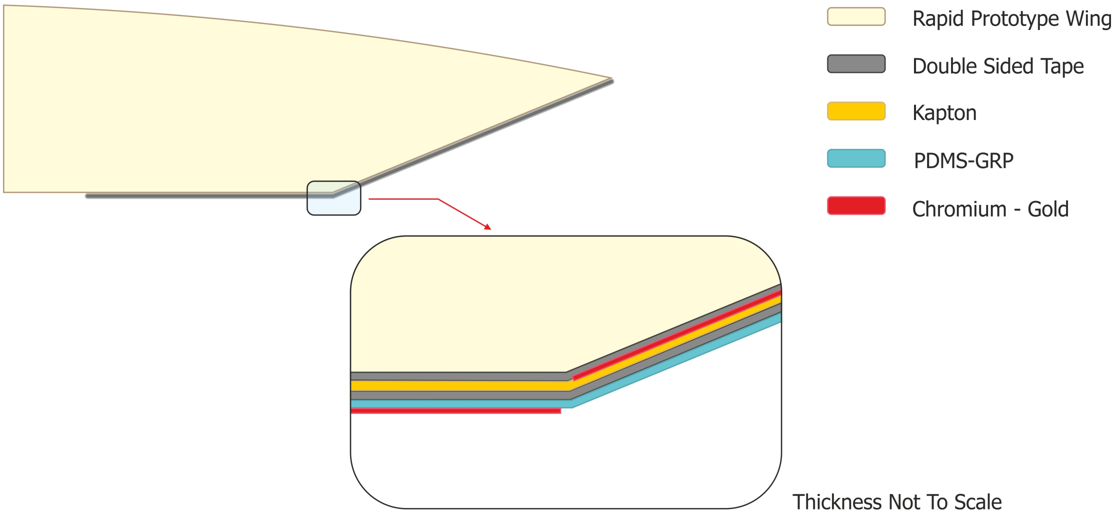

Thickness Not To Scale

Figure 3.23 Taped PDMS - Kapton Actuator

These initial actuators demonstrated increased endurance over the best-to-date Kapton actuators which had showed a maximum endurance of around 55 minutes. The laminated composite actuators survived for between 1.25 and 2.5 hours of operation; however, the failure method was the same as the unmodified actuators (backside holes formed by carbonisation of the Kapton). Although some of the improvement will have come from the lack of front side attack, the reduction in electric field strength due the increased electrode separation is likely to have reduced the plasma strength and also contributed significantly. However the surface showed no plasma attack and, unlike the SiO_2 coated devices, it was robust to handling, comparing the first three image pairs from Figure 3.25 demonstrates the improvements made in this respect. The taped actuators were also compromised by a tendency for the Kapton film to peel itself away from the trailing edge of the aerofoil due to the stresses incurred by conforming the relatively stiff and non compliant film to the sharp step in the aerofoil.

The solution to both these problems was to move to a glue based construction; firstly, properly sealing the actuator onto the rear of the wing using an epoxy eliminates any reactive breakdown products causing the backside hole formation. Secondly, a flexible polyurethane binary adhesive provided the vacuum compatible assembly for the two halves of the composite actuator prior to patterning so that the alignment issues were removed. The use of the polyurethane also allowed the actuator to remain compliant enough to conform to the shape of the rear wing without cracking. The functionalised PDMS-Kapton bond was achieved using Araldite 2018. Whilst the bond strength to the Kapton polyimide surface is strong enough to hold the highly compliant PDMS sheet in place, in the same way that the taped actuators tended to peel away from the rear of the wing due to the stiffness of the Kapton sheet, actuators constructed with both interfaces bonded with 2018 also failed in this way.

Araldite 2011, a rigid epoxy, was used for the Kapton to rapid prototype bond as this has better adhesion to the Kapton surface, and once the actuator has been patterned and bent into shape over the rear of the wing the concern for flexible construction materials is no longer relevant (see Figure 3.24)(see section 2.3.1 for assembly details).

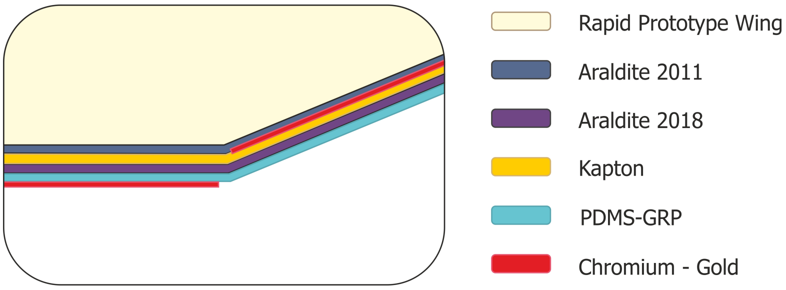

Figure 3.24 Glued Laminate Actuator Cross Section

These modifications to the construction process increased viable actuator life to in excess of 5 hours although the failure point was less sudden due to a shift in the failure mechanics. The new failure mode reverted to the electrode film itself, with the PDMS surface showing no signs of degradation before the electrode became crazed and broken up. Figure 3.25 shows the similarities and differences between the plain Kapton actuators with both Au and Mo electrodes, and the improvements made with the two iterations of composite laminate actuators. The only non self-explanatory point on the images are the areas of debonding observed on the glued actuator; this is the result of rough handling during the casting process, the debonded areas did not adversely affect performance and were only present over small areas of the composite.

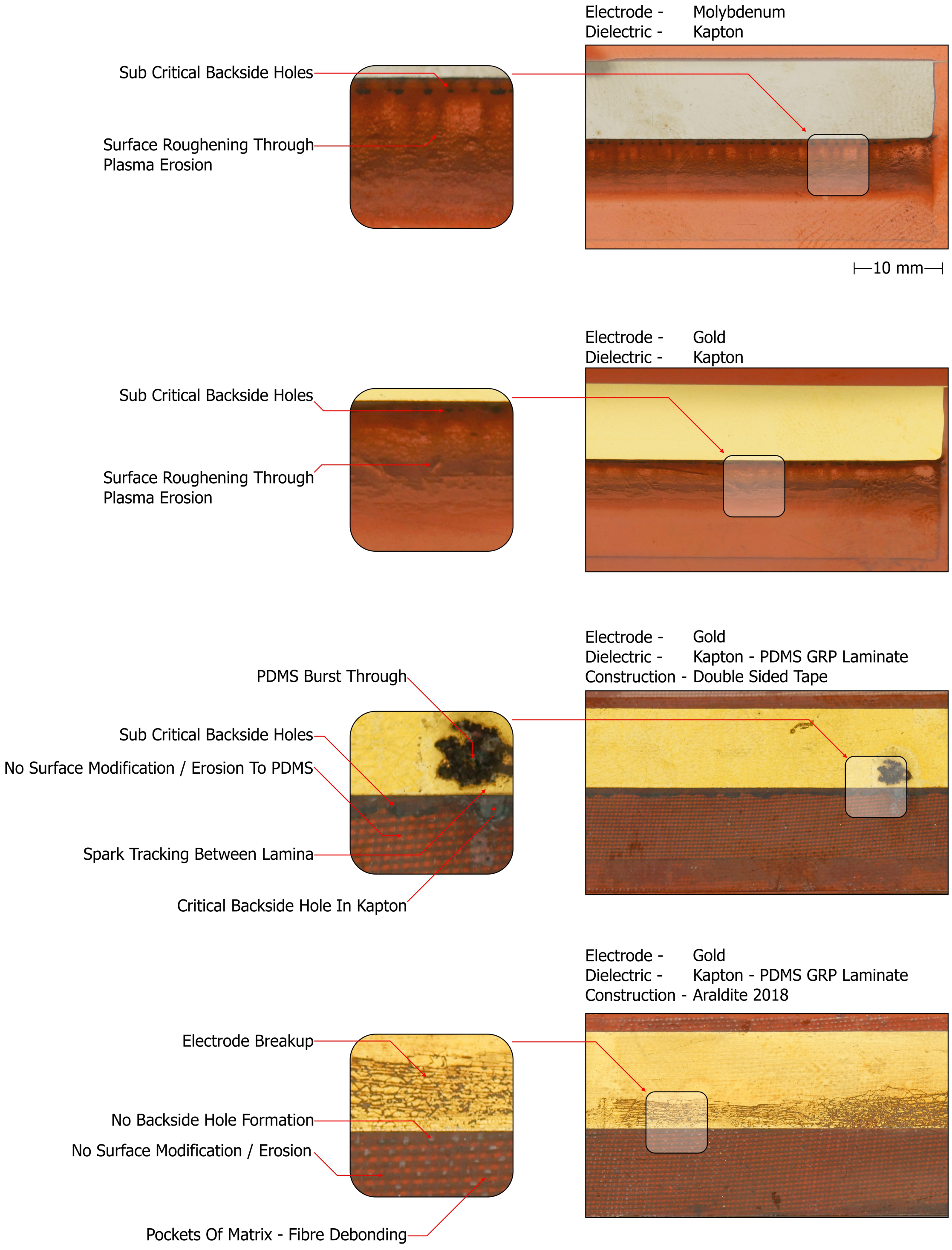

Figure 3.25 Photographic Comparison Of Composite Laminate Dielectrics To Unprotected Kapton

3.5 Conclusions On Actuator Construction and Integration Into Wind Tunnel Testing.

In conclusion, thin film actuators do not seem to be a viable solution for indefinite run time applications (see Figure 3.26), although this does not rule out certain applications like guided missile actuation where time of flight is a matter of seconds. As such for general applications it is recommended that either macroscopic metal foil based actuators or possibly patterned thin film electrodes which are then electroplated should be used. Either of these should offer greater structural rigidity, higher thermal mass and lower resistance when compared to the thin film actuators investigated here. More work is needed to determine minimum metal thickness for electrode survival. The second part of the developed actuator shown here, the bi-layer composite structure for the dielectric does appear to have real applications to improving actuator failure rates, allowing for thin, light weight, highly O_2 resistant and most importantly flexible actuators to be constructed which can be conformed to aerodynamic surfaces. Having shown no signs of dielectric degradation in the tests, it is possible that given the right macroscopic electrode configuration and attachment, under certain circumstances (i.e. small battlefield drones, or as part of high lift devices only used on takeoff / landing) they could provide lifetimes in excess of the air frames they are mounted to.

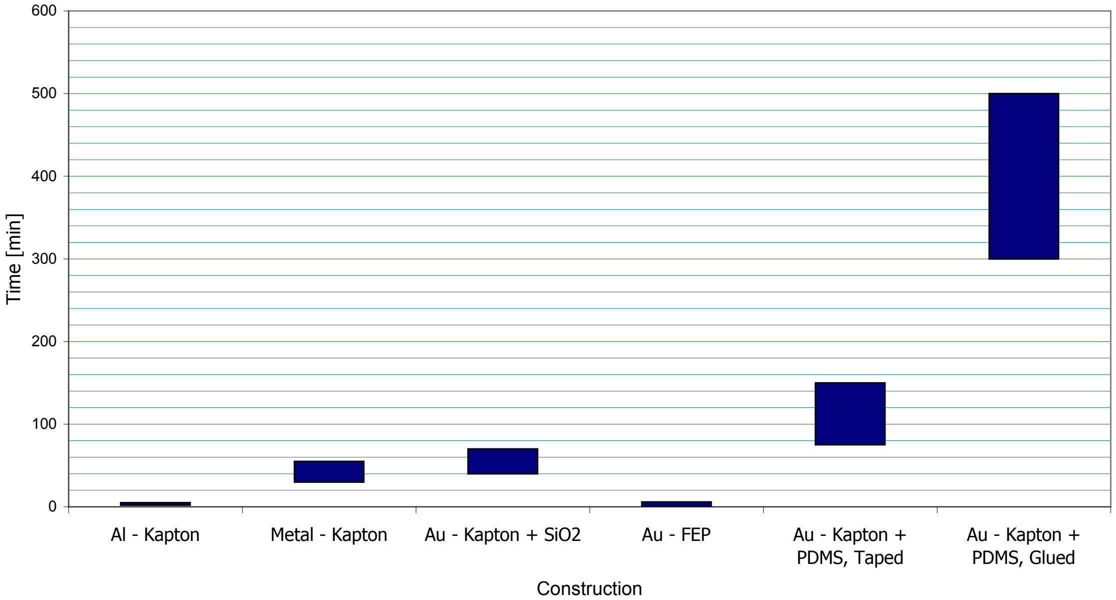

Figure 3.26 Expected Actuator Run Time Before Failure

Having developed a plasma resistant dielectric and electrode patterning technique, active plasma testing was started in the wind tunnel. It rapidly became apparent that due to the small plan form area of the wing which the developed actuators attached to, the forces involved were bordering on irresolvable by the balance system. To improve the signal to noise ratio of the wind tunnel test data a larger wing was required. However, the actuator membranes were already at the limit of the chamber sizes for the production equipment used in the methods detailed within this chapter, and although it would have been desirable to scale up the composite actuators to a larger wing it was simply not possible in house. As the purpose for the alternative larger actuators was to be used purely for wind tunnel testing, the longevity of the actuator although important was not critical, as long as it lasted long enough to get through a set of results. Therefore the decision was made to use simpler lower life actuators which did not include any of the developments detailed here, but which were designed to be rapidly replaceable and crucially could be constructed in much longer lengths. The construction of the devices used for the wind tunnel testing programme is covered in the experimental method (see section 2.3).

Chapter 4 Wind Tunnel Results And Discussion

4.1 Introduction

This chapter is broken down into four sections. The first of which gives the flat plate PIV results which will show the baseline performance of the actuator configuration and power supply system, but without the complexities of the aerofoil geometry or obfuscation that the wind tunnel airflow produces. Secondly, unactuated results for the aerofoil are presented; these characterise the natural unmodified response of the aerodynamic system. Thirdly, in the bulk of this chapter, are the plasma active results, and these cover the effect of the actuator on the aerodynamic performance of the test aerofoil. Lastly analysis of the results, particularly with respect to the implications that the combined datasets have on the suggested mechanisms of aerodynamic interaction with the actuator, are presented at the end of the chapter.

It should also be noted that throughout this chapter many of the graphs presented use a line to connect data points from the same set, even when the sampling on that particular data set is not sufficient to conclusively prove the trend which is implied by the line is real, and not noise on a different trend line fit. This is done as an aid to the eye for following datasets and to help in the identification of patterns in the data across different datasets.

Figure 4.1 reiterates the naming convention used for defining the drive waveform, and marked are the respective periods of the key frequencies. When describing figures in this chapter the following abbreviations are used for the test conditions: carrier wave frequency, CF; interruption frequency, IF; duty cycle ratio, DC; drive voltage, DV; wing incidence angle, Inc. and nominal wind tunnel velocity, Vel. Continuous (uninterrupted) actuation is demarcated as a 100% duty cycle ratio.

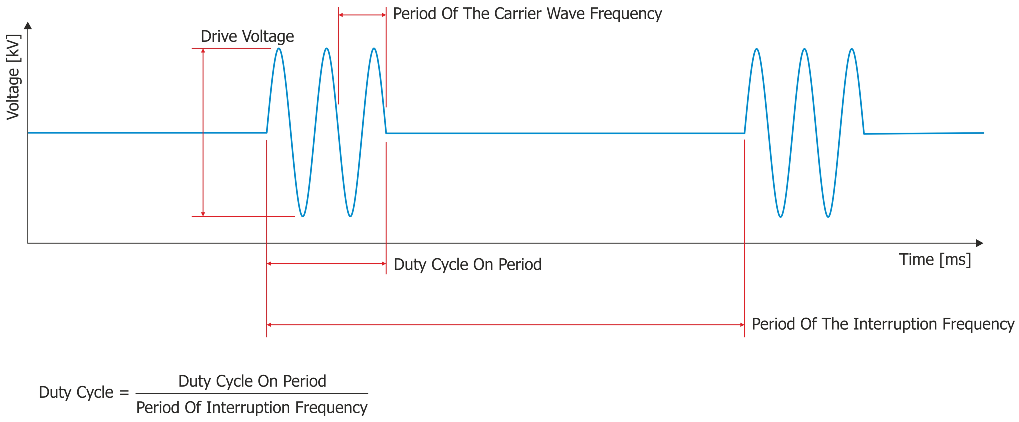

Figure 4.1 Recapitulation Of The Naming Convention

4.2 Quiescent Air Flat Plate PIV Results

This section details the results obtained from using the PIV system to measure the response of an actuator placed on a flat plate; this allowed for comparison with the literature in assessing the output obtained, and the characterisation of the actuator performance. The actuator's construction was identical to those used on the 100 mm chord wing. The data presented here were all taken at zero tunnel velocity, although tests were conducted in both quiescent air and at a variety of wind speeds. Only those at zero tunnel velocity showed a change in the flow above the detectable limit for the PIV system. Figure 4.2 is a typical vector map; from these tests, it can be seen that the actuator presents the expected behaviour seen in [80], with the air being drawn down and in from above the actuator and then accelerated downstream over the embedded electrode. As the flow diffuses downstream some of the quiescent air is entrained into the flow.

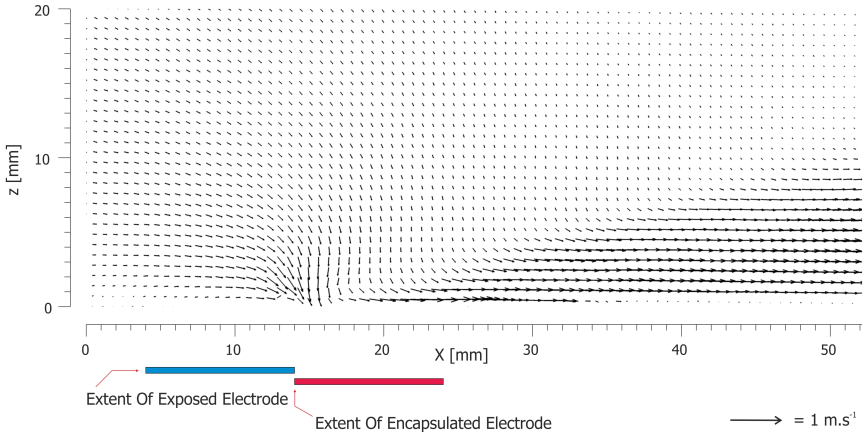

Figure 4.2 Vector Map Of DBD Actuation On A Flat Plate, (CF 4 kHz, DV 14 kV, DC 100%, Vel. 0 m.s^{-1})

Figure 4.3 shows PIV images of the absolute velocity of the actuator jet with increasing voltage. The actuator was driven with a continuous (uninterrupted) high voltage waveform at a carrier frequency of 3 kHz and varying peak to peak amplitude. From this we see that for this actuator there is a switch-on voltage below which no actuation effect is seen, and then from this point (7.2 kV) jet velocity increases with applied voltage.

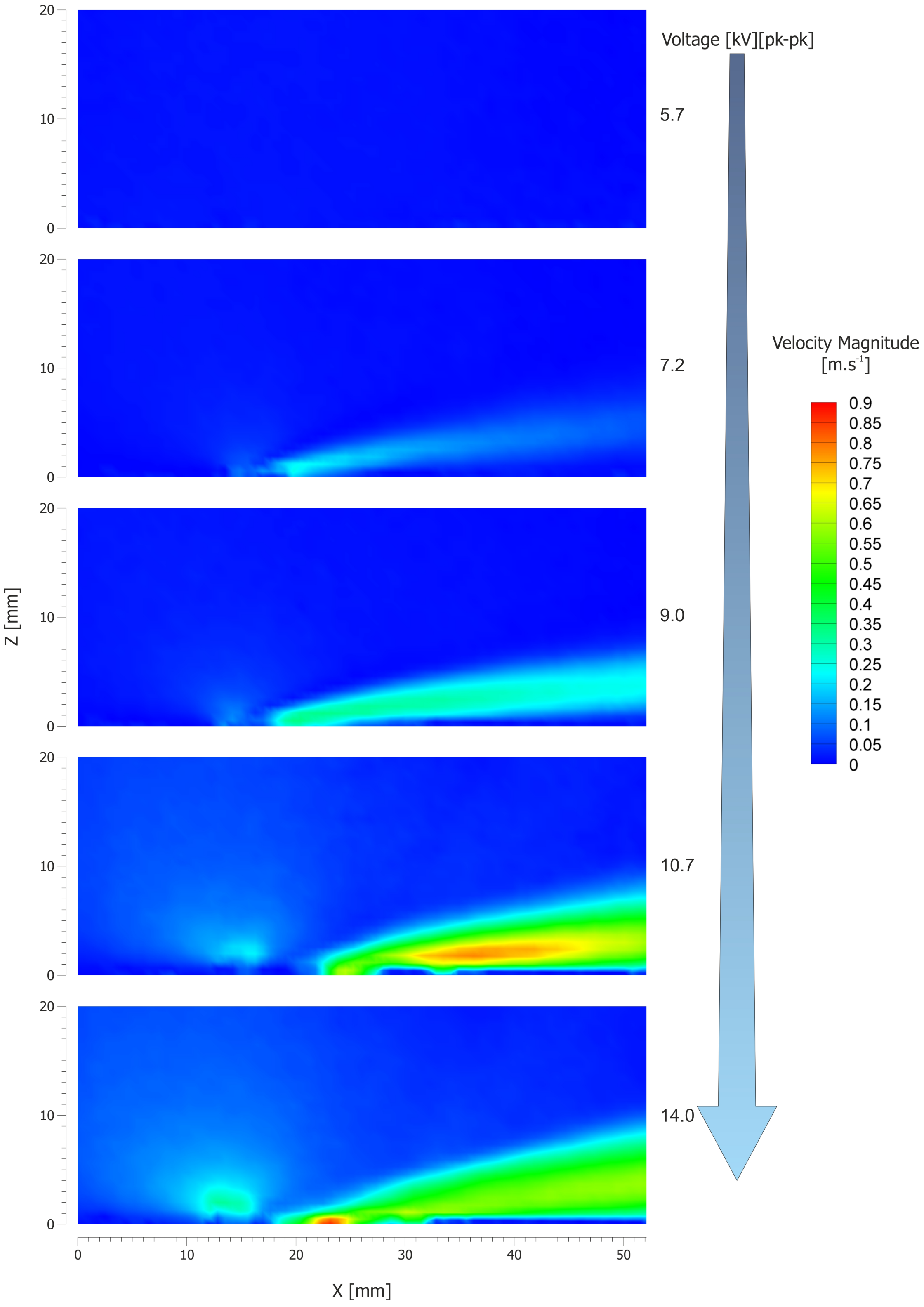

Figure 4.3 Increase In Actuation Effect With Voltage, (CF 3 kHz, DC 100%, Vel. 0 m.s^{-1})

Figure 4.4 plots the momentum integrals from the 5 test conditions. Momentum integral is approximated by integrating over a vertical line at each horizontal cell position in the discrete grid of velocities available from the PIV data, as explained in Equation 6; this gives a value normalised to represent the momentum addition created per linear metre of actuator. It is evident that each trace is following a very different pattern; the closest to the expected behaviour is the 7.2 kV trace (shown yellow) with the integral peaking as it crosses the actuator, and then decaying slowly as momentum is transferred to the wall through skin friction. It is not surprising that this trace approximates closest to the ideal behaviour, as the two main shortcomings of the data collection and analysis method are minimised at low speed. The first source of error is the inability of the PIV system to image the section of high velocity fluid within 1 mm of the wall. As such, initially much of the momentum added to the fluid by the actuator remains unseen by PIV image until it has moved slightly away from the wall through viscous entrainment, this leads to an error associated with the failure of the system to be able to integrate to the wall. This entrainment of the momentum and reduction of the integration error occurs quicker for lower jet velocities, and it can be seen that within 5 mm of the edge of the actuator at 7.2 kV the jet has moved away form the wall, and therefore all the momentum added by the actuator and not yet lost to the wall is being registered in the vector field. Also there is variation in how close to the wall the system manages to produce valid vectors; it can be seen looking at the 14 kV image that when the PIV system does measure right next to the wall it produces the spike in the momentum integral trace at 24 mm. The second source of error is the approximation that pressure is uniform across the domain; this had to be done as the data for this could not be collected. However this error will also be lower at lower velocities. Looking at Figure 4.4 with these limitations in mind, the near wall imaging inconsistency can be used to explain the spike in the 14 kV trace at x = 23 mm. Also the trace is still rising when it leaves the field of view; this suggests that it has not yet fully entrained all the unmeasured flow, whereas the others are all decreasing by the position x = 40 mm. In this way it can be argued that, had the field of view been larger, that the 14 kV trace would have levelled out at a point inline with its expected level of actuation compared to the 10.7 kV trace.

Maximum Vertical Cell Index [Z = 3.6 x 10^{-2} m]

Air Velocity For Cell

Cell Area Per m Of Actuator [Constant][m^2]

$$\int P \approx \sum_{J=0}^{J=67} (V^2 * 1.18 * 6.934 \times 10^{-4})$$

Cell Index [Z = 0 m]

Nominal Air Density [Assumed Constant] [$kg.m^{-3}$]

Equation 6 - Momentum Integral Approximation

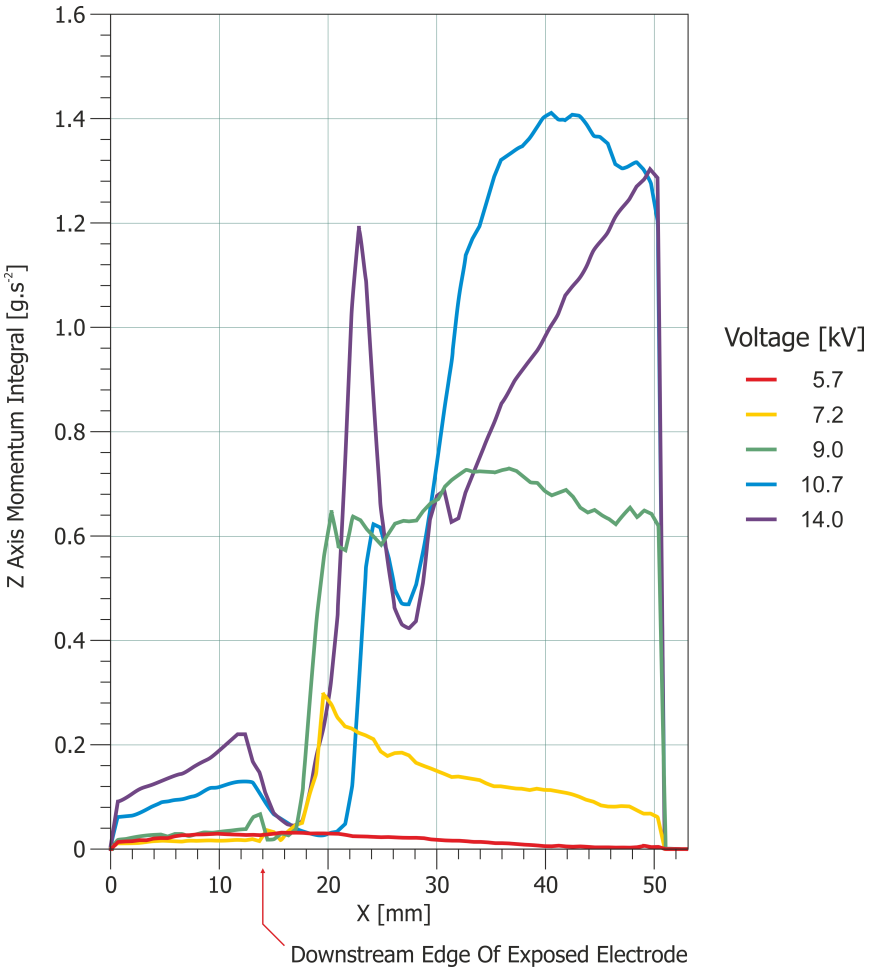

Figure 4.4 Change In Momentum Integral With Voltage

The effect of carrier frequency on the DBD jet is shown in Figure 4.5 and Figure 4.6. It should be noted that the blank section at approximately x = 32 mm is an artefact introduced by a reflection from a cable on the tunnel wall overpowering the seed particle laser return and disrupting the analysis. This reflection problem was rectified for all other runs. Also, the images show signs that the row of cells next to the wall have been compromised and are not reading the true velocity. What can still be seen in these images is that there is an increase in jet energy with increasing carrier frequency. This occurs because the DBD plasma actuator is primarily a capacitive load; as such, as the carrier frequency increases the actuator impedance drops allowing greater charge flow to be driven into the system. Increased current increases the frequency of streamer formation, driving the charge onto the dielectric surface and as a consequence ion creation and momentum coupling to the fluid are also increased.

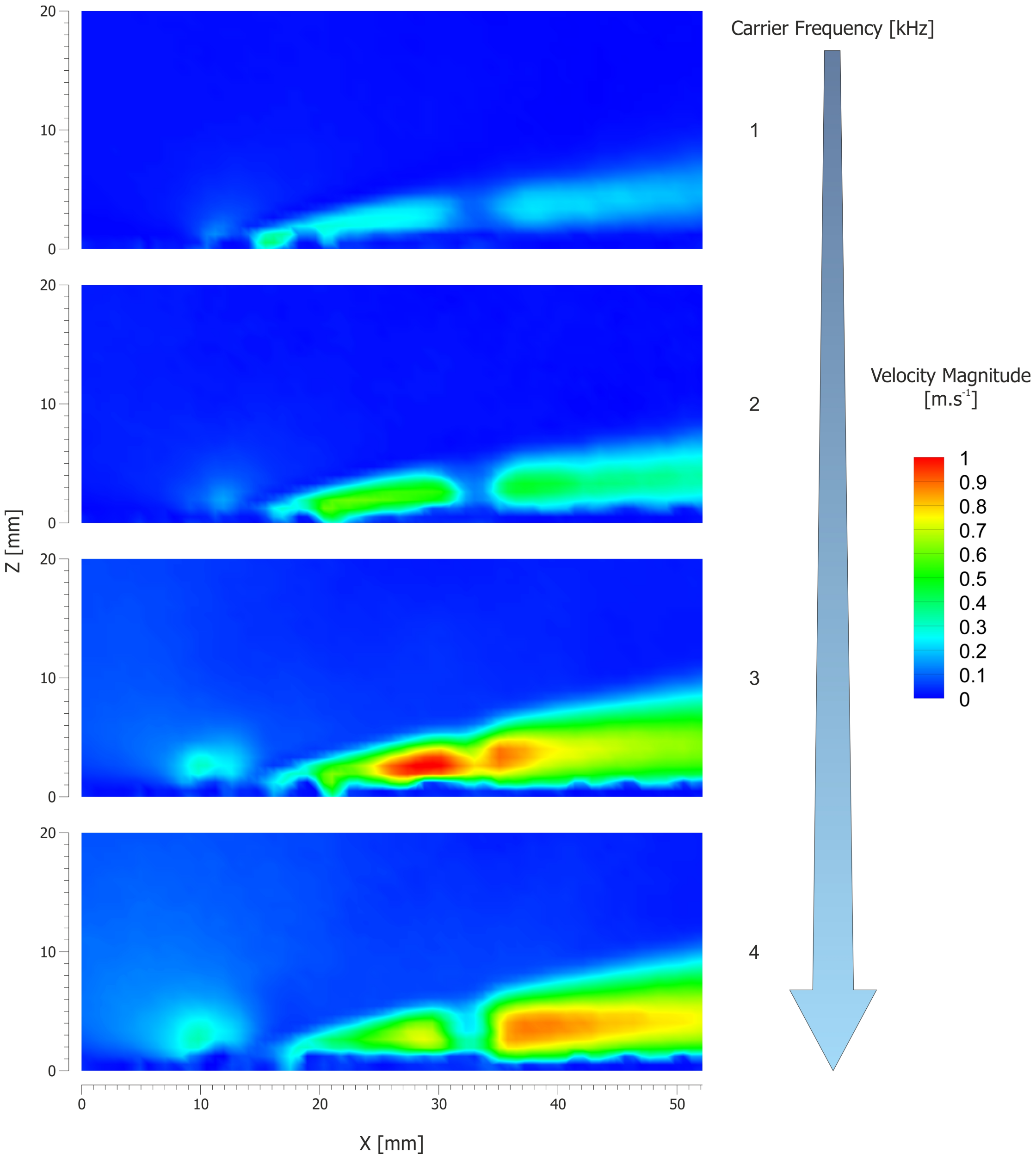

Figure 4.5 Increase In Actuation Effect With Carrier Frequency, (DV 14 kV, DC 100%, Vel. 0 m.s^{-1})

Figure 4.6 shows the associated momentum integrals for the data shown in Figure 4.5. Ignoring the dip caused by the stray laser return at x = 32 mm, the same pattern of longer entrainment times for the higher velocity jets up to a peak, followed by a loss of momentum to the wall, is seen again as it was in Figure 4.4. Without being able to accurately measure the momentum integral directly after the actuator it is difficult to draw anything more than a qualitative analysis that actuator force increases with carrier frequency as expected.

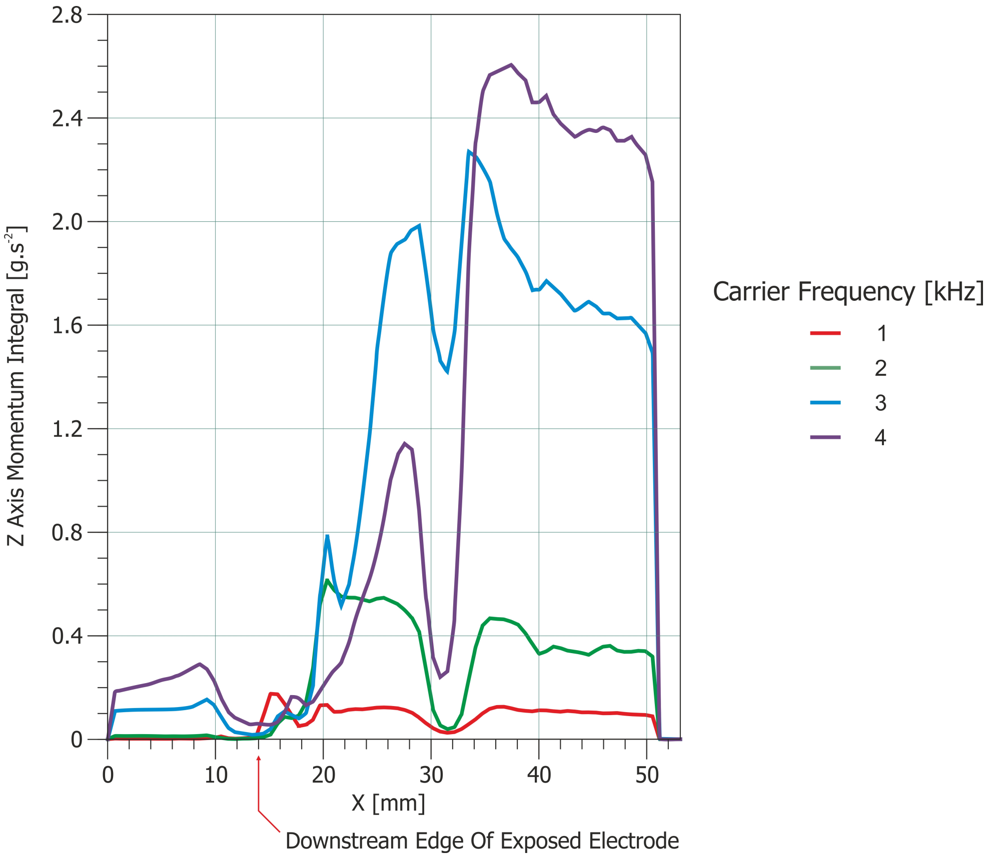

Figure 4.6 Change In Momentum Integral With Carrier Frequency

Figure 4.7 shows the behaviour of the actuator with changing interruption frequency. Ideally this would have been invariant, and it can be seen that although not constant the effect is small when compared to that of the carrier frequency; this pattern is also evident in Figure 4.8. As the drive frequency was a constant 4 kHz for all runs in this test, along with the duty cycle being a set 25%, the total power delivered to the flow would have been identical, and the explanation offered is as follows. The lower interruption frequencies accelerate the flow for a longer continuous period and therefore attain higher peak speeds. These higher peak jet speeds in turn incur greater viscous losses with the wall. This therefore leads to lower time-averaged amount of momentum coupled into the ambient fluid when compared to the more continuous push of the higher interruption frequencies. No further tests were performed to validate this theory.

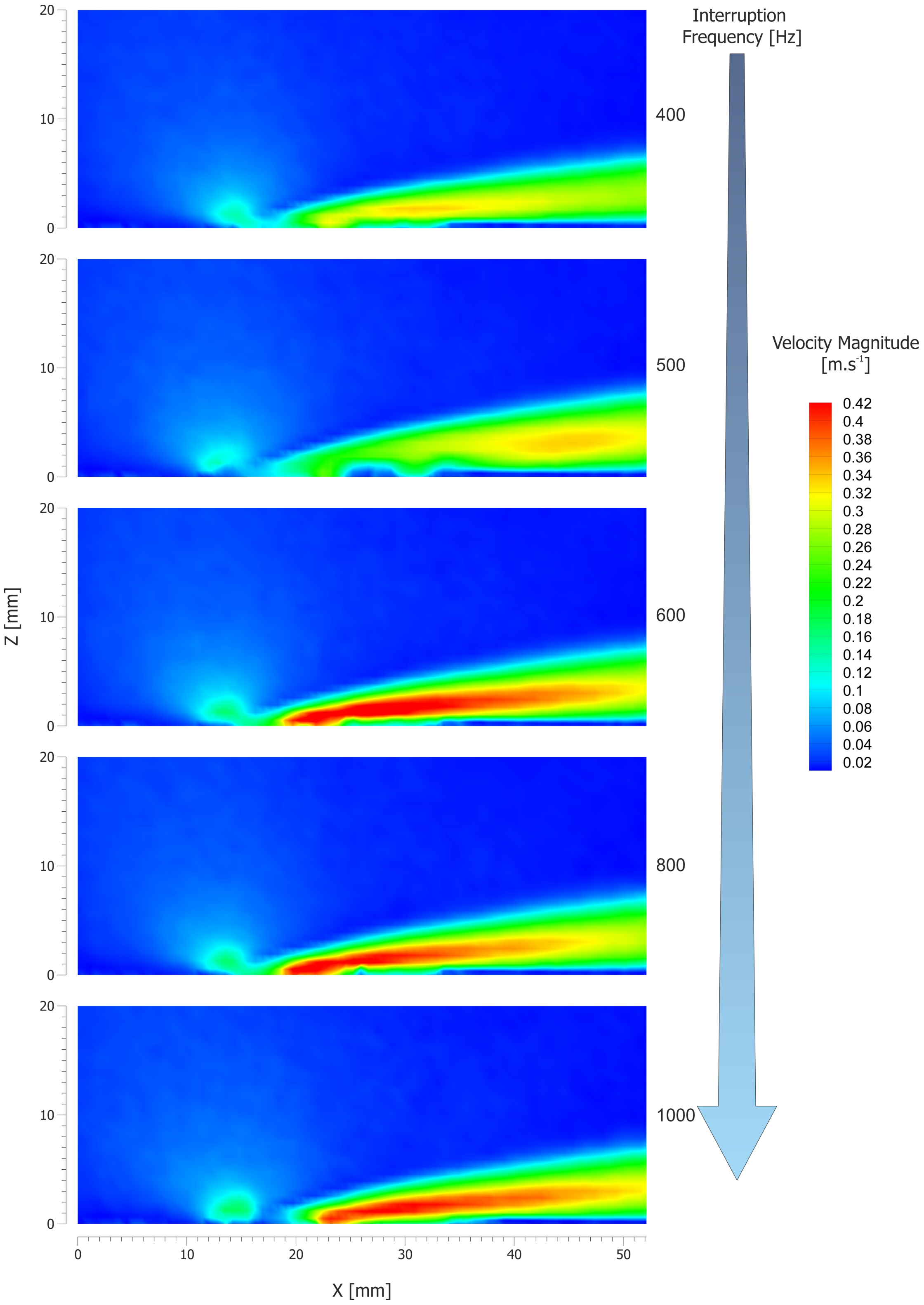

Figure 4.7 Change In Actuation Effect With Interruption Frequency, (CF 4 kHz, DV 14 kV, DC 25%, Vel. 0 m.s^{-1})

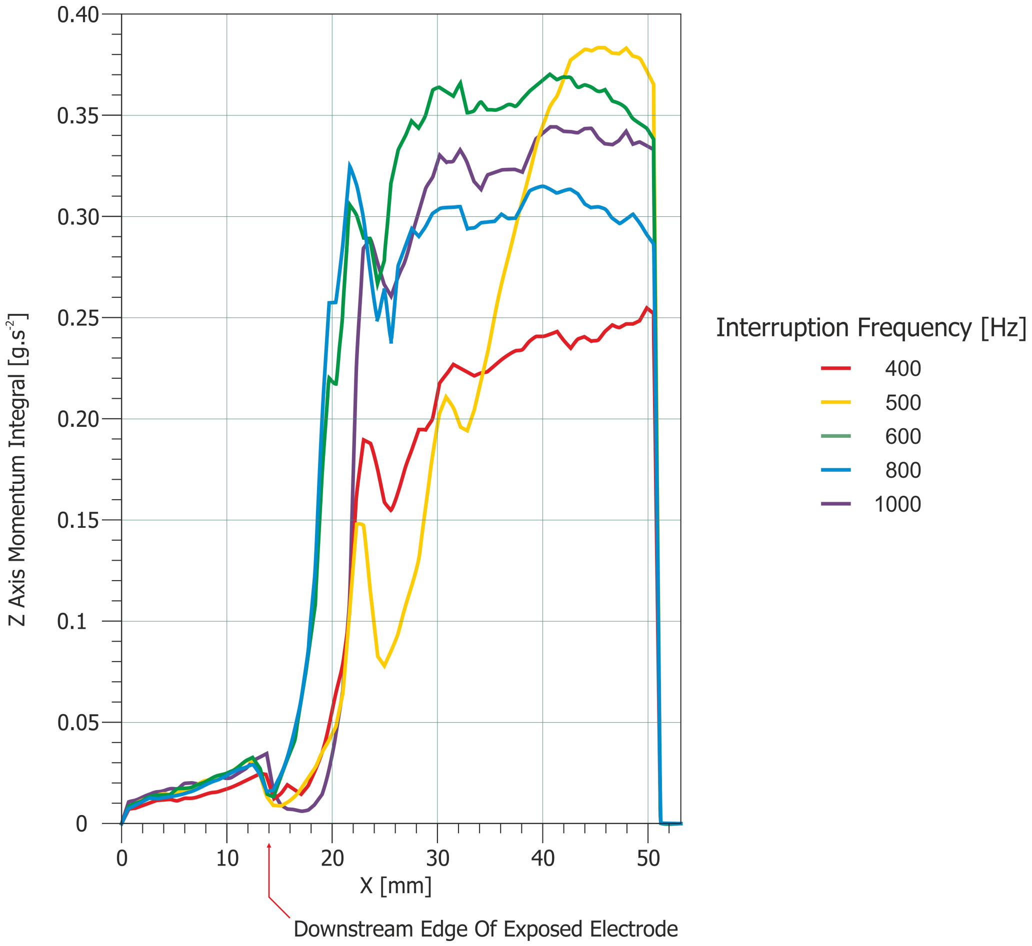

Figure 4.8 Change In Momentum Integral With Interruption Frequency

One of the things that can be take from the previous sequences of images is that the velocity of the jet is low, peaking at around 1 m.s^{-1}, this is slightly lower than most studies [72, 102] (2.5-3.5 m.s^{-1}) and significantly lower than a few have achieved e.g. [106] (8 m.s^{-1}) . This is despite the drive frequency, voltage and construction being comparable to those used by others, the only explanation offered is that the particular drive set up gave exceptionally poor impedance matching between plasma and transformer/amplifier reducing the power transferred to the plasma. However it is not common place in the literature to use power matching networks although some have e.g. [111].

4.3 Unactuated Baseline Data For The Stepped Aerofoil

The following section details the investigations into the underlying unactuated aerodynamic characteristics of the 100 mm chord, stepped aerofoil (detailed in section 2.3.2). This aerofoil was used to take all further results, both actuated and unactuated, which are detailed in this chapter. The data comprises high resolution incidence sweeps, frequency domain data from wake traverses with a hot wire probe and PIV images of the flow.

4.3.1 Unactuated Lift Curve

The unactuated lift and drag curves for the stepped aerofoil are given in Figure 4.9, testing was carried out at 19.8 $m.s^{-1}$ which equates to a Reynolds number of $1.33x10^5$ at this Reynolds number so far from the turbulent transition point it is assumed that at zero and positive incidence where there is no adverse pressure gradient that the flow over the pressure side remains lamina until it is tripped by the separation step. The two areas of interest on this graph are the stall point at 11^o and also a step in the lift curve between -3^o and -3.5^o, the latter of which is assumed to be due to a change in flow regime over the separation step. The normalised data for lift coefficient is plotted in Figure 4.10, along with the lift curve for an unmodified NACA 0012 aerofoil at a Reynolds Number of $1.70x10^5$; this latter data was taken from [154]. It is interesting to note the way in which adding the step to the underside of the aerofoil has not only introduced effective camber to give lift at zero incidence, but also altered the way in which the aerofoil behaves as it enters stall, suffering a much more abrupt loss of lift than the symmetric profile on which it is based.

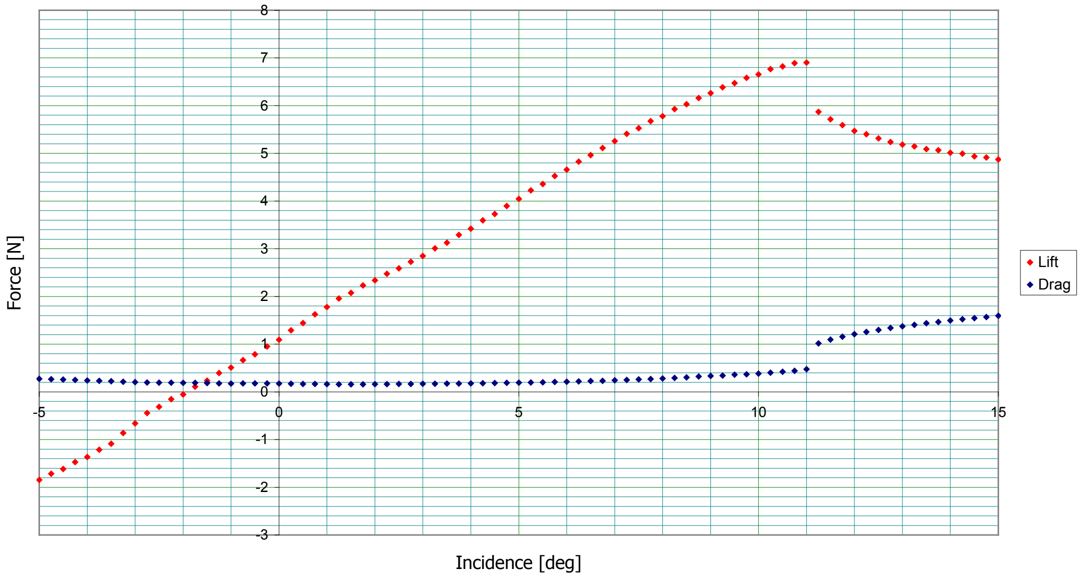

Figure 4.9 Lift And Drag Curves, (Vel. 20 $m.s^{-1}$)

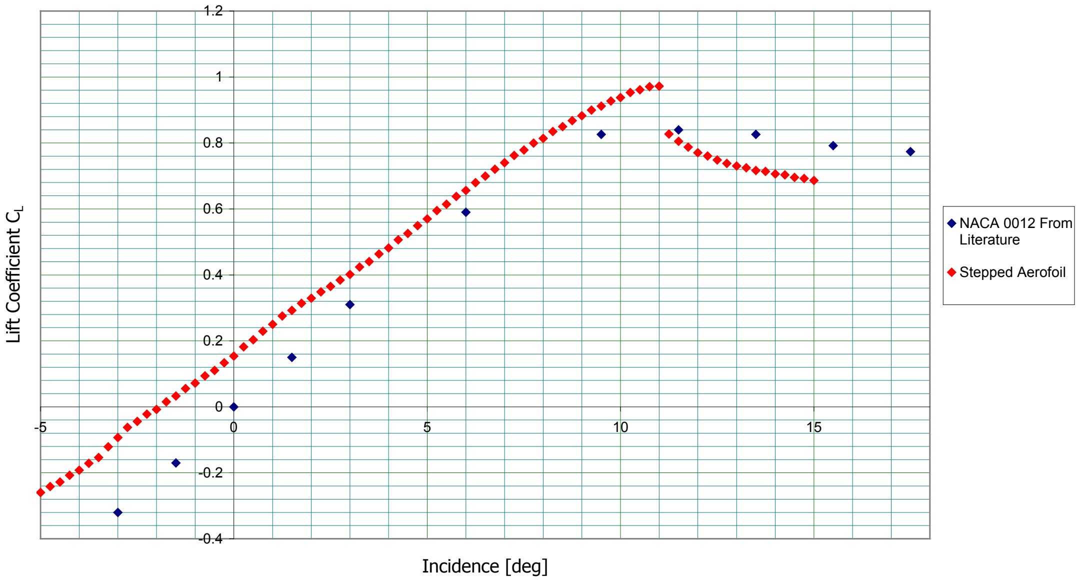

Figure 4.10 Non-Dimensionalised Lift Curve Compared To Literature [154]

Figure 4.11 shows the lift slopes of the modified stepped aerofoil and the unmodified NACA 0012 with the incidence expressed in radians. The unmodified aerofoil comes close to the infinite 2D thin aerofoil theory idealisation of the lift slope of, $C_L = 2\pi\alpha$, where C_L is the coefficient of lift and α is the incidence in radians [155]. The modified aerofoil however is further from the idealised behaviour, despite the efforts to maintain a truly 2D flow over the aerofoil. If the expected lift slope for the same wing experiencing simplified full 3D flow is computed by numerically solving the Prandtl lifting-line formulae using 3rd party software, then with a square planform and an aspect ratio of three the lift slope is calculated to be $1.16\pi\alpha$. This shows that the effect that the splitter plates are having on the aerofoil load distribution lies, as could be expected, between the values for idealised 2D and full 3D flow.

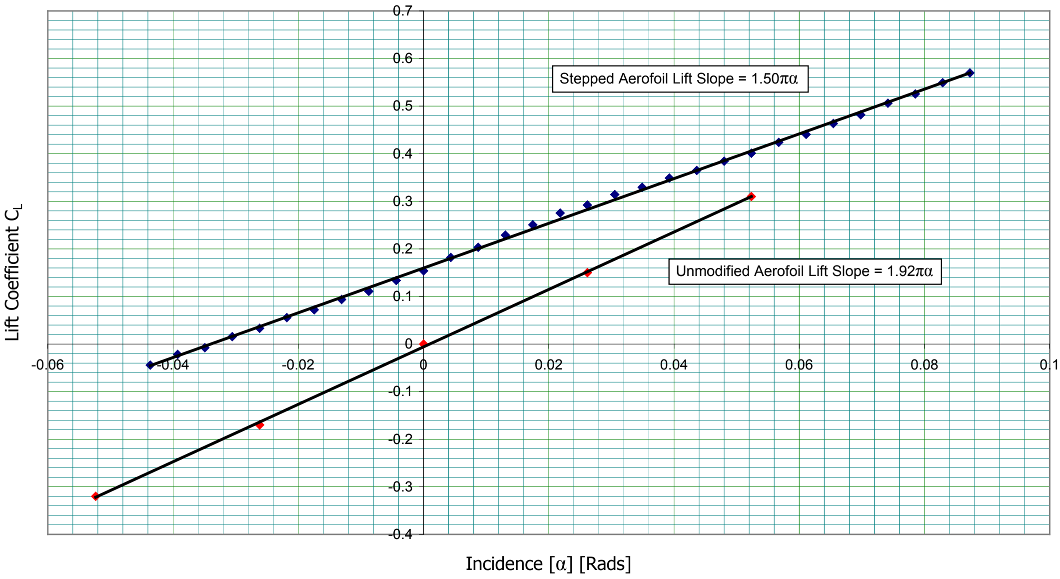

Figure 4.11 Comparison Of Lift Slope To Literature [154] And Thin Aerofoil Theory

Figure 4.12 shows a higher resolution sweep over the incidence where the step in the lift occurs. The near perfect linear fit of the two sections of the curve before and after the step (blue lines) along with the almost invisible 95% confidence interval error bars (black) show that it is a real feature of this aerofoil and not noise on the balance.

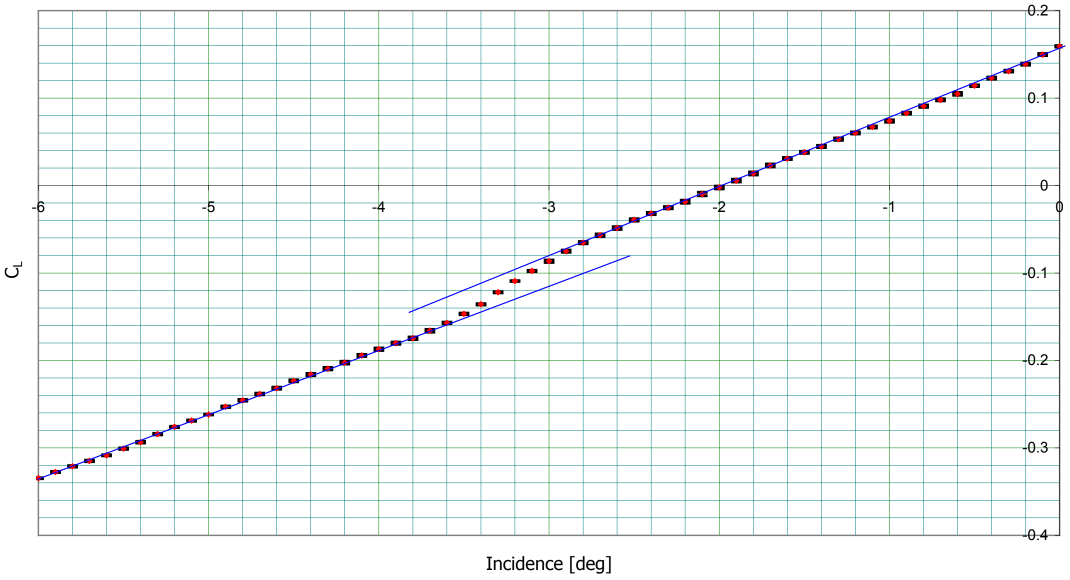

Figure 4.12 High Resolution Incidence Sweep Over The Separation Region, With 95% Confidence Interval Error Bars on C_L, (Vel. 20 m.s^{-1})

Figure 4.13 shows the hysteresis present in the lift curve when transitioning into and then out of stall. It should be noted that the whole hysteresis effect spans only 0.6° on incidence, a far greater degree of precision than is usually reported in the literature. it is assumed that the stall occurs over the suction surface with a mechanism is very similar to that of the NACA 0012 reported in [156], which states that at low Reynolds numbers that the flow separation is a combination of both a leading edge separation bubble failing to reattach and trailing edge stall. It is mostly included to provide context for the variation seen in the actuation effect plots shown later in this chapter. The accuracy of the balance when shown relative to the lift curve is clearly capable of resolving changes in lift arising from a change of less than 0.1° on incidence in absolute terms with a single 16 KiSa logging point and, as was covered in section 2.5.3.1, standard logging procedure when assessing actuation effect was to take 3 repeated points each relative to their own control so as to produce even higher levels of repeatability.

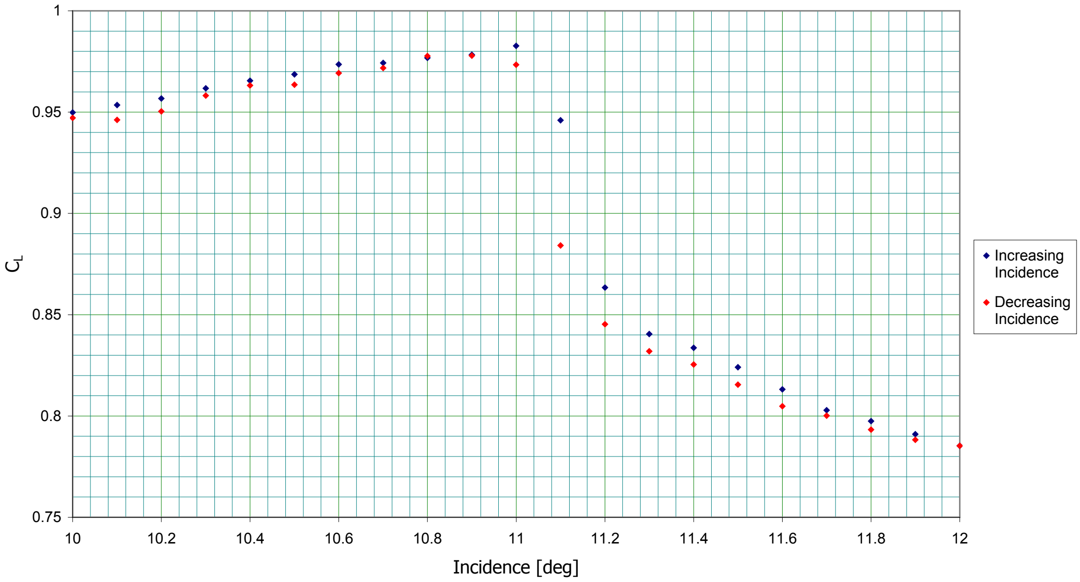

Figure 4.13 Hysteresis Around Stall Point (Vel. 20 m.s^{-1})

4.3.2 Hot-wire Measurements

Hot-wire traverses of the wake were taken at a single x-axis location with 5 different incidence angles from -10 to +10 degrees. Data was only collected in the pre-stall region as this corresponded to the incidence range over which the overwhelming majority of the plasma actuated data was taken. Figure 4.14 shows the average wake velocity deficits recorded; these are displayed relative to the wing at the appropriate angle. The pattern of increasing energy loss from the flow as the incidence angle moves away from neutral is immediately evident. However this is not the most interesting data to come from the hot-wire tests; for that we must look in the frequency domain.

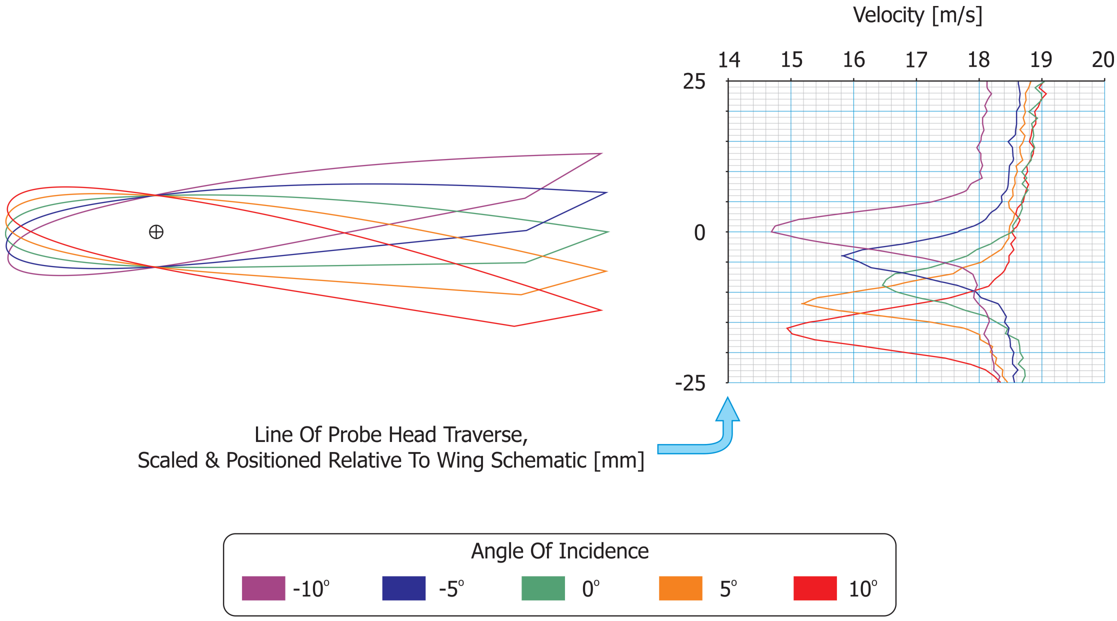

Figure 4.14 Hot-wire Wake With Wing (To Scale)(Vel. 20 m.s^{-1})

Fast Fourier Transforms (FFTs) of the data from the hot wire traverses showed that the wake contained a periodic signal generated by vortex shedding from the back of the aerofoil, this was initially thought to be originating from separation over the step on the pressure side of the aerofoil, later PIV plots would confirm this (see e.g. Figure 4.21). Figure 4.15 and Figure 4.16 show this frequency domain data. The first thing that should be noted is the strong vortex shedding peak at around 825 Hz; this equates to a Strouhal number of 0.248 based on the step height perpendicular to the freestream flow (6 mm). It should also be noted that not only does the frequency of the peak shift with both increasing and decreasing incidence from the zero degree case, but at the same time the peak also becomes broader and more spread out indicating that the vortex shedding is becoming less clearly defined and more variant. Figure 4.17 plots the Vortex shedding frequency against incidence, showing the decrease in shedding frequency with increasing incidence.

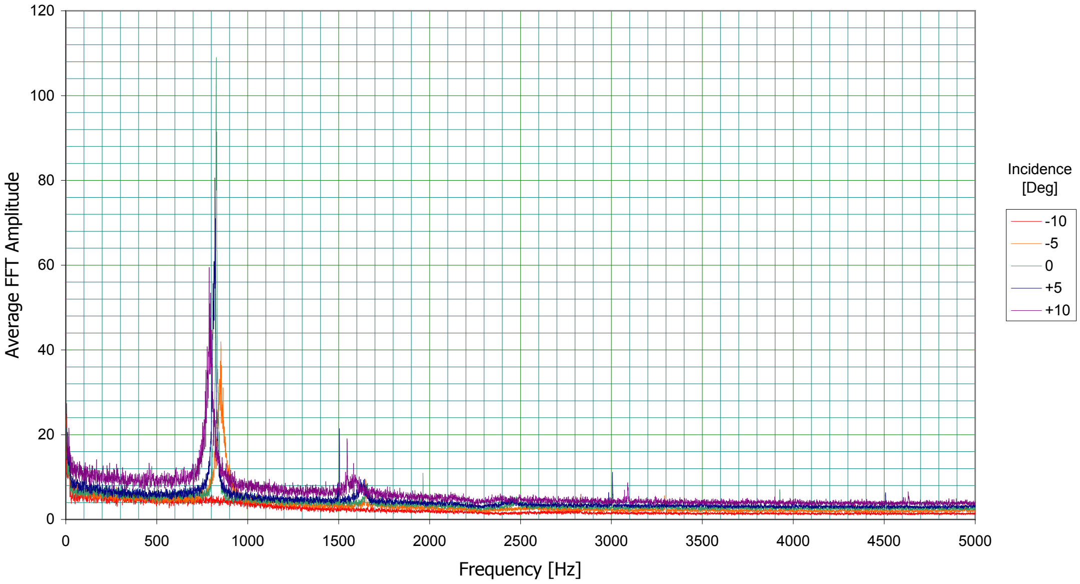

Figure 4.15 FFT Of Velocity Data At Varying Incidence, (Vel. 20 m.s^{-1})

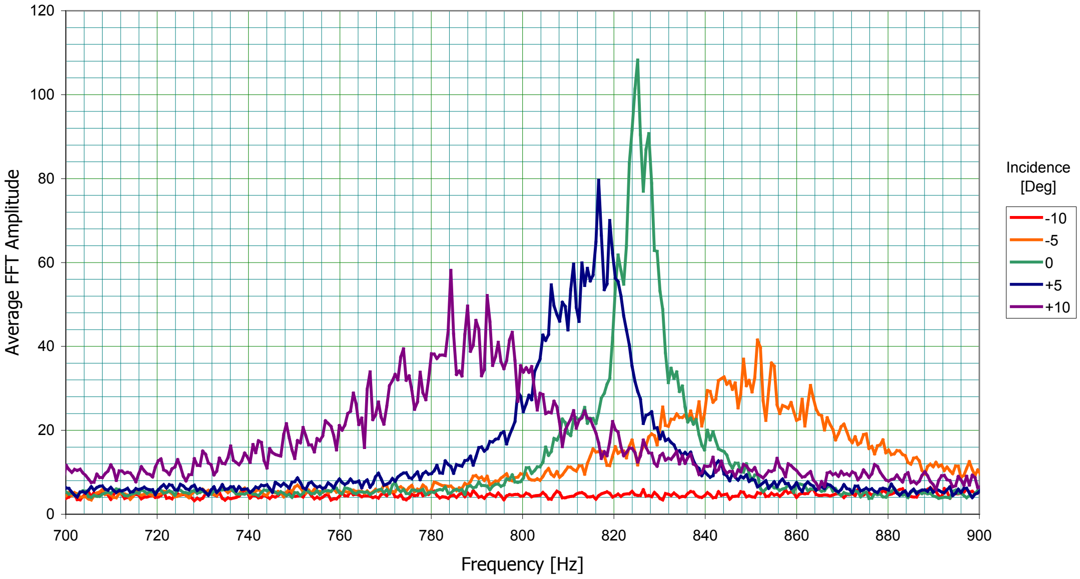

Figure 4.16 Close Up Of Shift Of FFT Peak With Incidence, (Vel. 20 m.s^{-1})

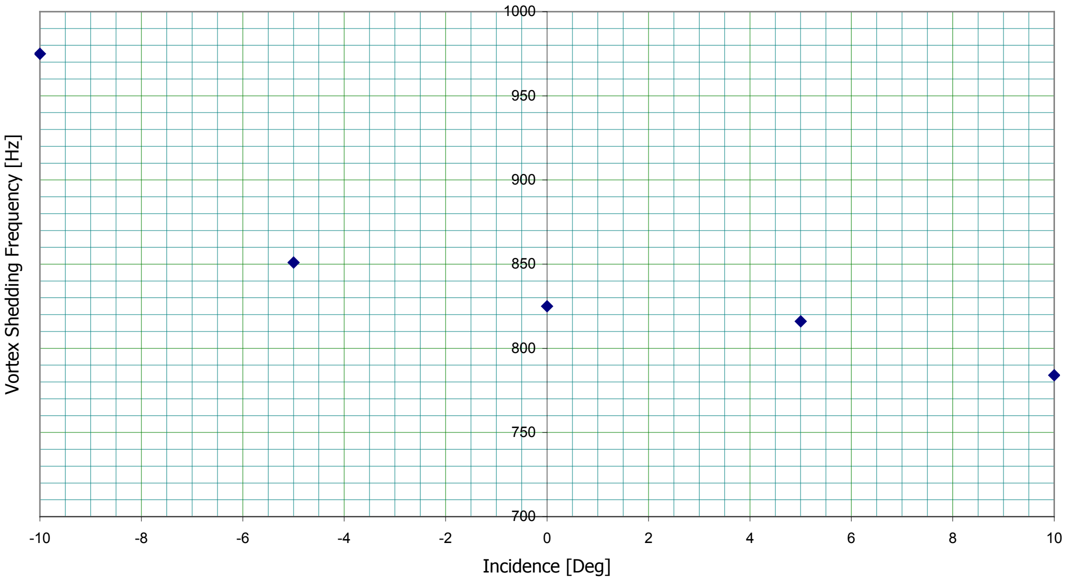

Figure 4.17 Hot-Wire Probe Shedding Frequencies Against Incidence, (Vel. 20 m.s-^{1})

Figure 4.18 shows that the position of the fundamental shedding frequency is insensitive to the position within the wake where the data for the FFT is taken from: However, there is clearly a significant difference in the strength of the signal, with the data taken at the edge of the wake showing a relative peak nearly 10 times larger than for the point in the centre of the wake. Of course for a symmetric 2D bluff body it would be expected that along the plane of symmetry you would observe a velocity pulsation of twice the frequency at which vortex shedding cycle was occuring. This occurs as the alternating clockwise and counter clockwise vortices from the upper and lower surfaces pass the wire, each causing their own pulse. The existence of the fundamental shedding frequency at ≈ 800 Hz is confirmed by the synchronised PIV results shown later in the chapter. The fact that the double pulse rate is not seen here is possibly a peculiar product of the geometry and the operation of the hot wire. As the hot wire is only sensitive to the absolute magnitude of flow velocity it is possible to have periodic flows which varies in direction vector but not magnitude which will not show up as a change on the hot wire, some evidence of this is visible in the consistency of the vector magnate arrows shown later on in Figure 4.20, this leads to the generally low level of periodicity. Also, as the geometry is asymmetrical, logically so to is the shedding pattern, this leads to a small asymmetry whereby only one of the 2 halves of the vortex pair registers with the hot wire leading to the small pulse at the natural shedding frequency. This observation is important for the extraction of shedding waveforms from the PIV phase locked data which is covered later in this chapter (see Figure 4.51).

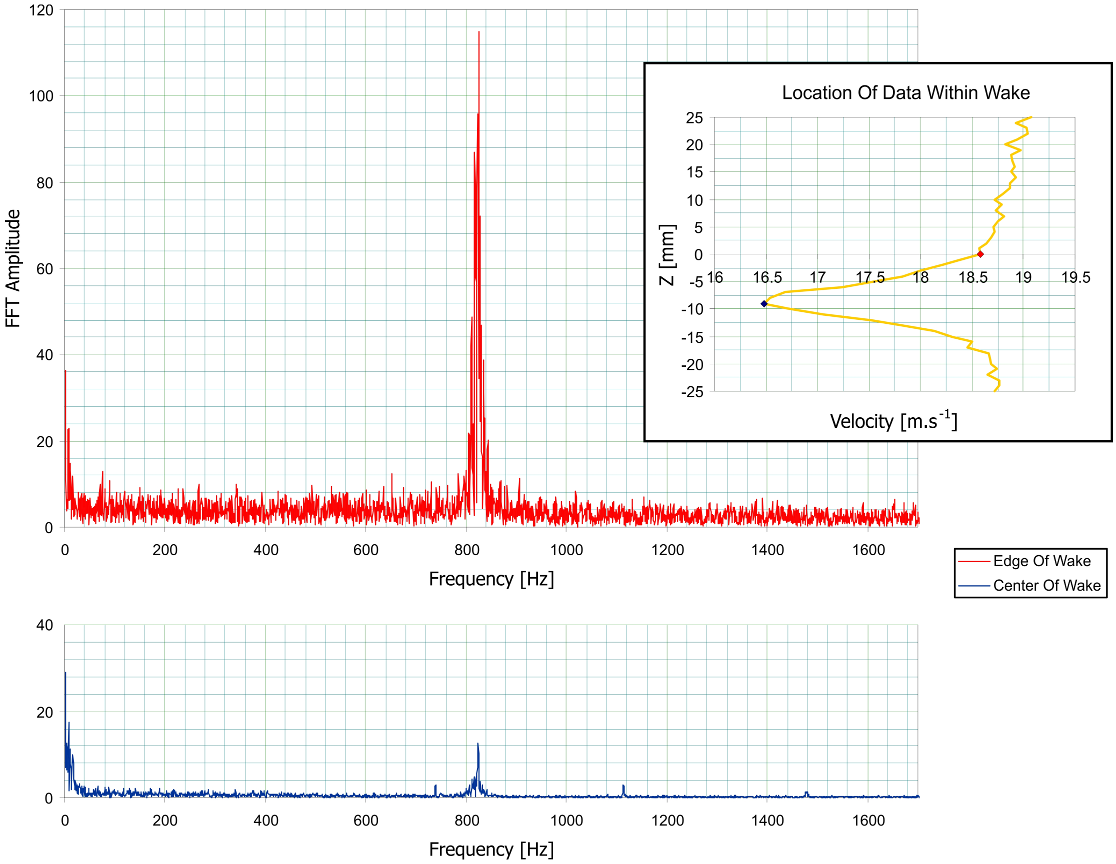

Figure 4.18 Insensitivity Of FFT Peak Location To Position In Wake (Sampling Location Within The Wake Inset), (Inc. 0°, Vel. 20 m.s^{-1})

4.3.3 Unactuated Aerofoil PIV measurements

Figure 4.19 uses data from the particle image velocimetry system to plot velocity vectors for the flow around and behind the aerofoil. These images are based on averaged values from datasets of 1000 image pairs. Section A shows a wide angle view of the aerofoil; resolution is limited and the actual deviation in the flow vectors from the free stream is minimal. However, a slight upwash can be seen in the wake behind the aerofoil. Section B shows the detail view of trailing edge step with the upwash more visible at this vector resolution. Vectors are coloured by absolute velocity and the velocity deficit is clearly visible in the wake. Also visible in section B and enlarged in section C is the recirculation bubble formed behind the step. It should be noted that in section C, to highlight the low speed bubble, the vectors are of uniform length, whereas in the other two sections they are sized relative to velocity.

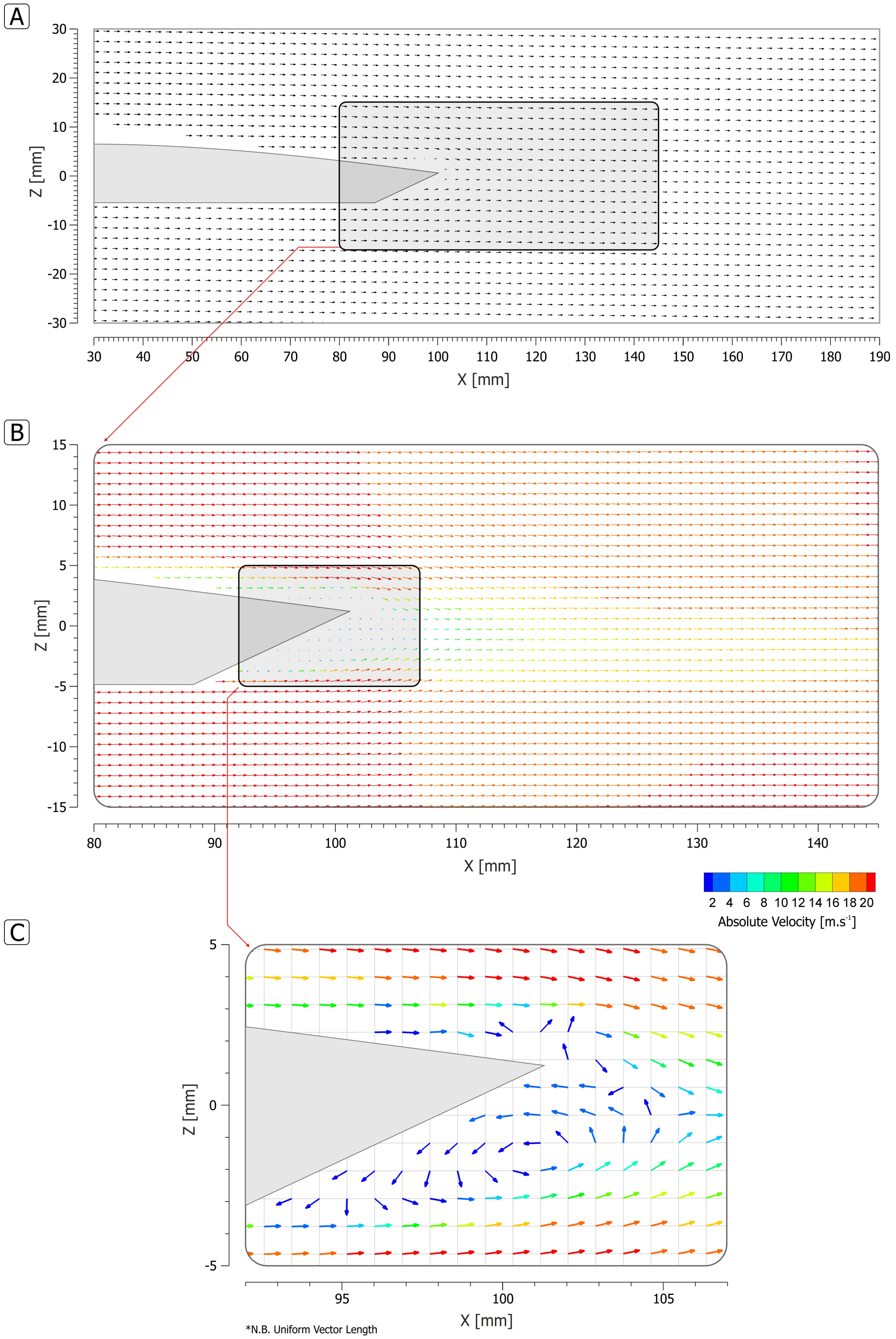

Figure 4.19 Velocity Vectors From Averaged PIV Data (Vel. 20 m.s^{-1})

Figure 4.20 shows a single instantaneous vector field; clearly visible is the vortex street forming behind the aerofoil. In this figure vectors are coloured by z-axis velocity component. It should be noted how this coloration/value correlates to the actual flow direction within the wake, as for clarity in smaller figures contour plots of this velocity component are used to demarcate the shedding patterns.

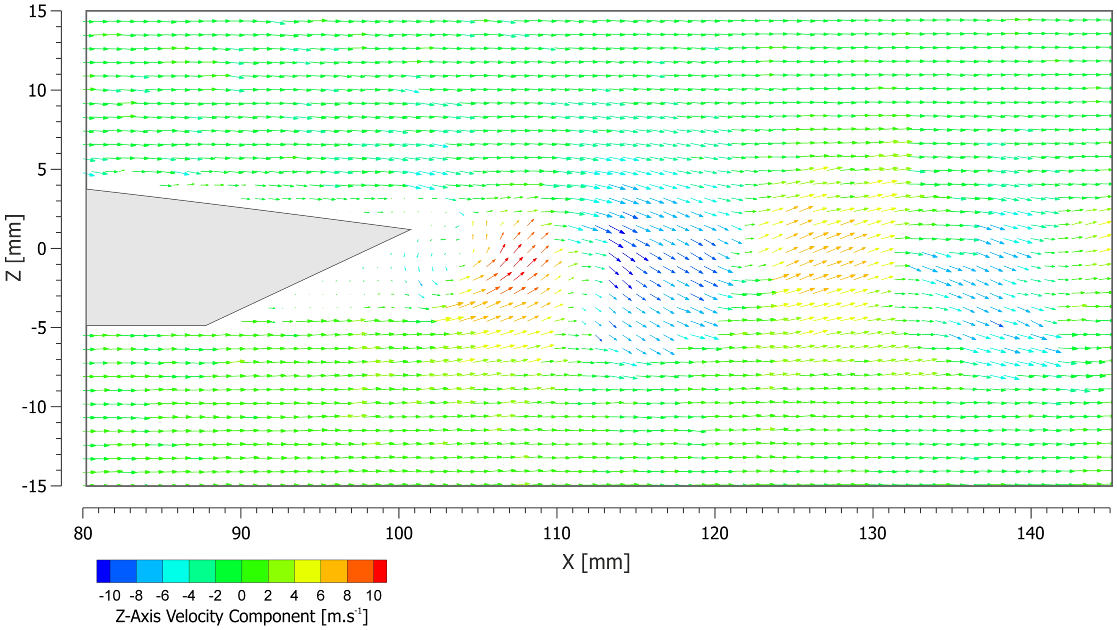

Figure 4.20 Instantaneous Velocity Vectors Showing Vortex Street (Vel. 20 m.s^{-1})

By looking at the available set of individual instantaneous images it is possible to sort them based on where within the vortex shedding cycle the capture occurred, and selecting a suitable subset of these images yields the sequence seen in Figure 4.21. It should be noted how the aerofoil naturally shows strong well defined vortex shedding in its wake.

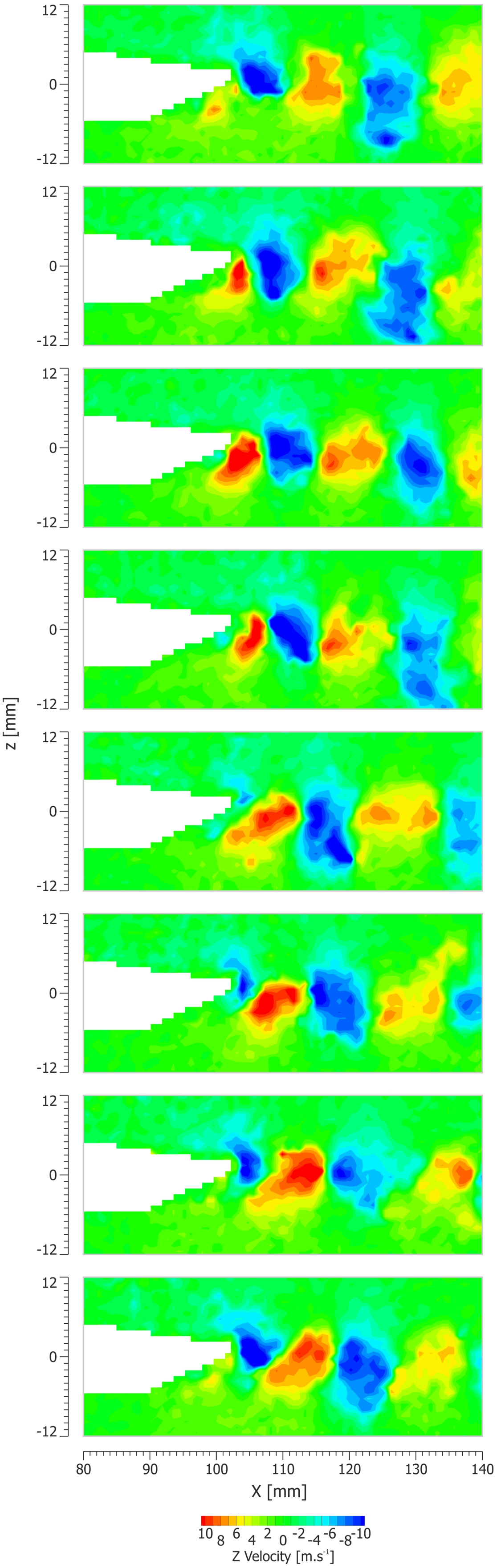

Figure 4.21 Manually Assembled Unactuated Vortex Shedding Sequence (Vel. 20 m.s^{-1})

Figure 4.22 shows plots of Reynolds stress and turbulent kinetic energy (TKE) in the flow. Reynolds stress was defined as $\overline{u_i'.u_j'}$ where u_i' is the Reynolds decomposition of the fluctuating part of the velocity vector in x and u_i' is the same measure along the z axis, this definition ignores the fluid density which is assumed to be constant therefore leading to the units of $m^2.s^{-2}$. As would be expected, these plots show that the unsteadiness in the flow is totally dominated by the vorticity in the wake.

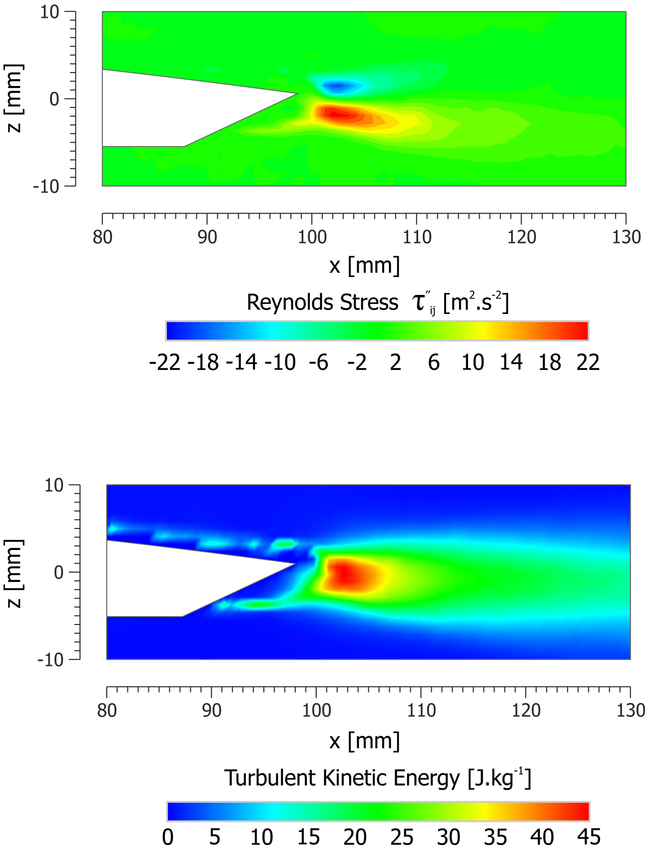

Figure 4.22 Reynolds Stress and Turbulent Kinetic Energy Plots

4.4 Continuous Plasma Results

4.4.1 Force Balance Measurements

Shown in Figure 4.23 is a high resolution incidence sweep with a continuously driven plasma at a carrier frequency of 600 Hz. This dataset was taken with the 1st generation automated high voltage supply. As such, care needs to be taken when making comparisons with other datasets elsewhere in the thesis. However, as the low maximum carrier frequency and lower drive voltage associated with that power supply created a much lower power plasma, the resolution and level of repeats contained within this figure could not be replicated within the lifetime of a single actuator when running at the full power of the 2nd generation automated

HV system. This graph contains 3 repeats of 0.1° incidence steps over 25.1° for a total 753 data points, each with its own local control reading with both active and control reading being 16 kiSa averages logged at 512 Hz. This gives a total logging time (excluding time to write the data to the disk and index the wing) of 13 hours 23 minutes. It is important to note that when a graph is listed as having repeated data sets that this means that the experimental setup was indexed through all test nodes once and then reset to its start point to index through them again, and so on for each repeat. This is in contrast to having one point logged at node one, then immediately logging the 2nd and 3rd points at node one before changing the parameters to node two and so on. In this way the spread on the data also represents any positional inaccuracies, actuator degradation and temperature drift encountered over the run; this increases the reliability of any trends evident in the data. The interesting thing to note about this graph is that not only does the actuation effect change with incidence with a well defined peak occurring at 1.5°, but also above 8° the direction of the effect changes, in that it goes from producing more lift when active to reducing the lift from the aerofoil when the plasma is energised.

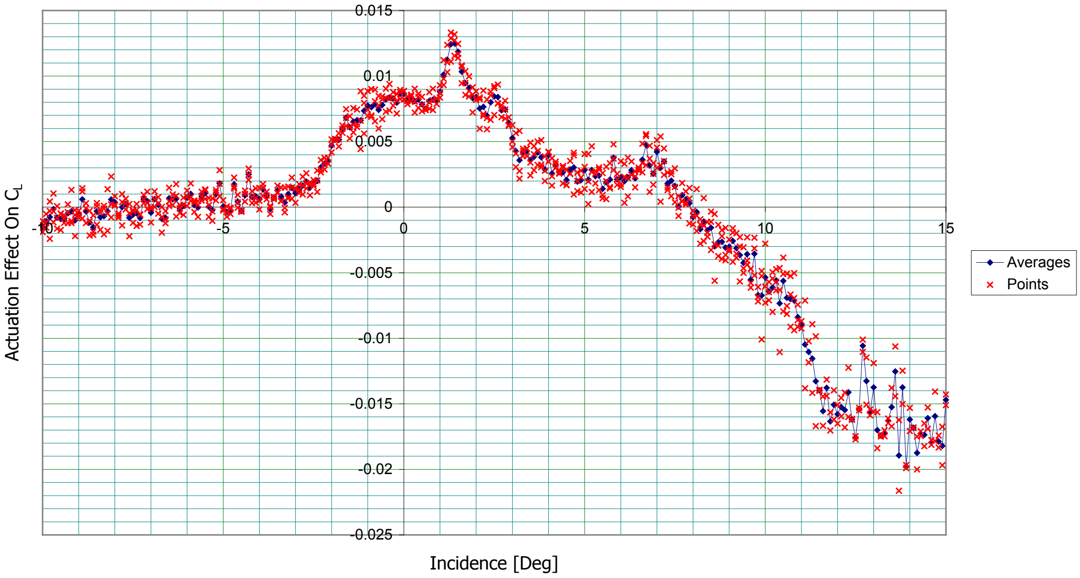

Figure 4.23 Fine Incidence Sweep, (CF 600 Hz, DC 100%, Vel. 20 m.s^{-1})

With the introduction of the 2nd generation HV system came a significant increase in plasma power and, crucially for the behaviour of the actuator, the ability to generate a drive waveform with a much higher carrier frequency. This change in power and carrier frequency has changed the incidence sweep response of the actuator. The analogous graph to Figure 4.23 but compiled with data generated using the 2nd generation HV system is shown in Figure 4.24. The major change shown between the two graphs is the much greater ability to create a negative change in C_L, especially at negative incidence. Interestingly when looking at the range on the data between the peak value of C_L and the value of C_L at 10^o, which is the last common point before the wing stalls, they are very similar: 0.02 on C_L for the lower plasma power 600 Hz actuation against 0.024 on C_L for the higher power 4 kHz carrier wave plasma. This is thought to be due to a resonant interaction with the vortex shedding for the 600 Hz case, with the carrier frequency not being high enough to be considered true continuous forcing (see explanation in Section 4.6.2).

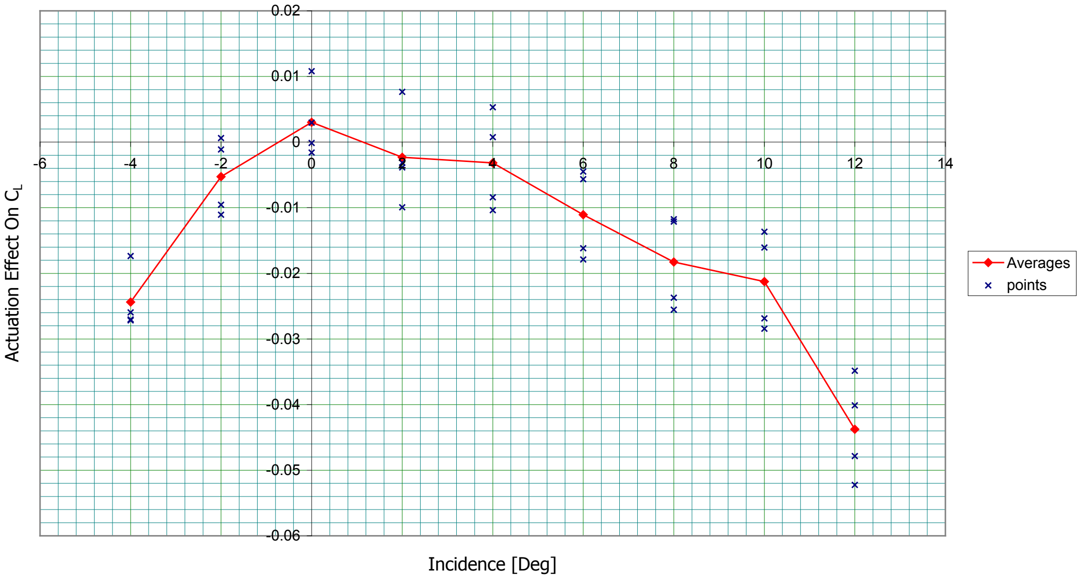

Figure 4.24 Coarse Incidence Sweep, (CF 4 kHz, DV 14 kV, DC 100%, Vel. 20 m.s^{-1})

To test the validity of the result showing an inversion in actuator effect at 0^o, a higher resolution incidence sweep over that section was performed (see Figure 4.25). This confirmed with reasonable probability that the inversion did indeed exist. Unfortunately, due to the need to use the same actuator as had previously been run in the test for Figure 4.24, only a single test run was completed with no repeats before the actuator was destroyed. As a consequence when comparing values for zero crossing point, peak actuation etc. between Figure 4.24 and Figure 4.25 the significant spread on data points seen in the latter needs to be taken into account, as such error bars at $\pm 2\sigma$ have been added where σ is the average standard deviation taken from Figure 4.24, if the spread on the two datasets is comparable, these bars represent the spread in which the true mean of the data will lie with a 95.4% probability.

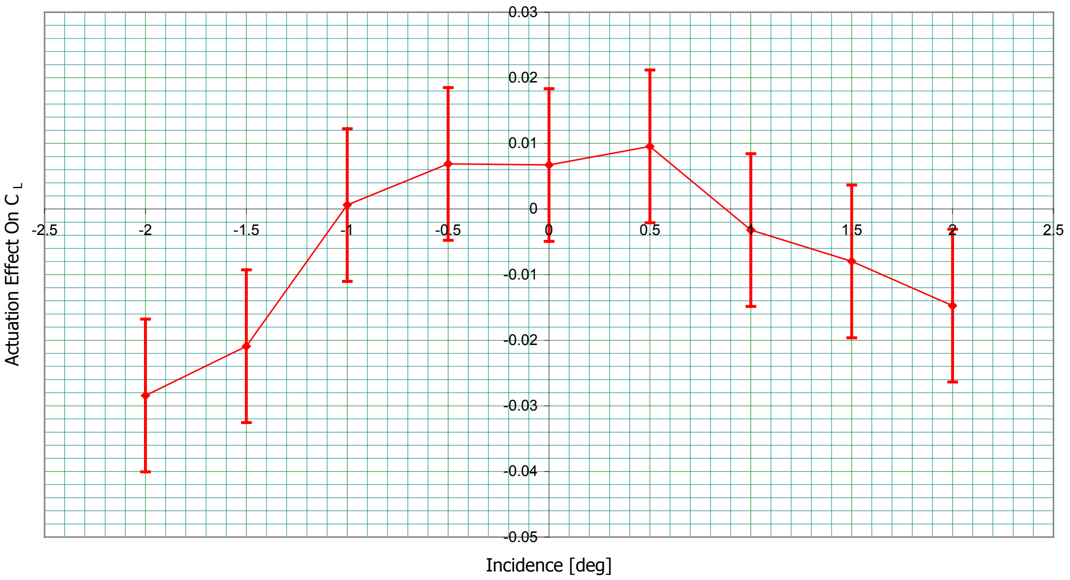

Figure 4.25 Fine Incidence Sweep Over Inversion, Error Bars At ±2σ Based On Data Spread in Figure 4.24, (CF 4 kHz, DC 100%, Vel. 20 m.s^{-1})

Figure 4.26 shows a test done without the wind tunnel running. The plasma was run and the force balance logged, control data points were logged after each active cycle and the difference between the two calculated. In addition to this, pairs of data points were logged with no actuation on during either logging period. Again the difference between the two consecutive readings was calculated; these double 'off' readings should represent the noise floor present on the balance achievable with this logging period. If there was an electromagnetic interference effect between the plasma, or the high voltage electronics powering it, and the balance, then the data would show either an offset in the whole dataset or an increase in the level of noise present when comparing between the two sets of deltas. The experiment was run at varying incidence to ensure that any interaction was not dependent on alignment of any cables or the actuator surfaces that was changing as the incidence was indexed. The results of this test clearly show that the balance is not affected by electrical interference from a continuously driven plasma. In addition, the spread on the data is consistent with the known resolution limits of the balance shown in section 2.4.3.1. It should be noted that as there was no airflow through the wind tunnel lift coefficient is a meaningless quantity for this test, therefore the results are presented as change of force in Newtons. For the purposes of comparison the relationship between the two in the nominal 20 m.s^{-1} tests is a factor of approximately 6.25 N per C_L.

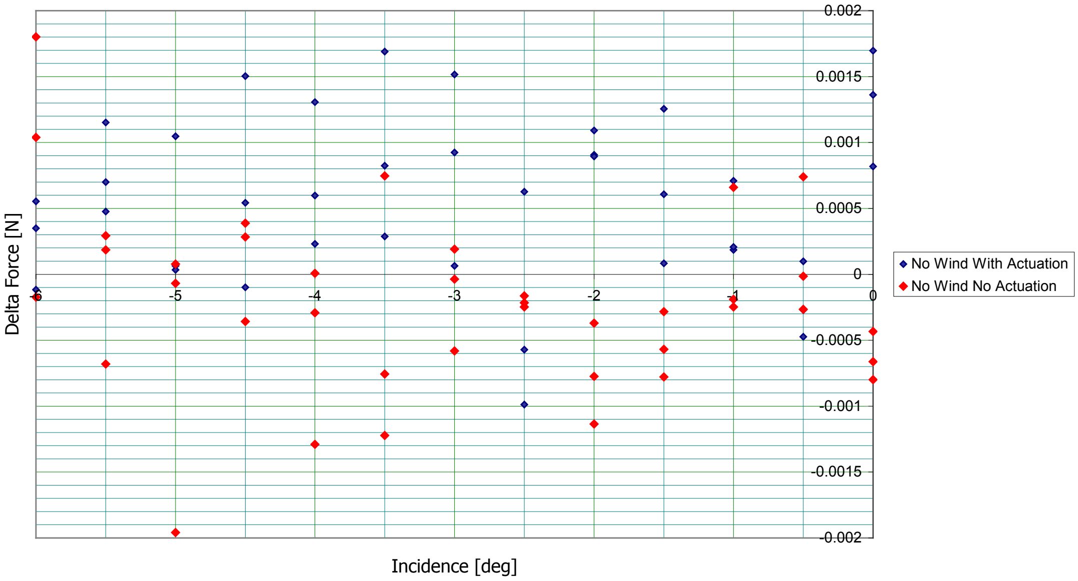

Figure 4.26 Zero Wind Electromagnetic Interaction Test – Incidence Sweep (CF 4 kHz, DC 100%, Vel. 0 m.s^{-1})

Figure 4.27 shows the effect that varying the plasma drive voltage has on the change in C_L due to plasma actuation. The test was conducted at 0 degrees incidence using an uninterrupted plasma and a 3 kHz carrier frequency. The results of this test are in agreement with the flat plate PIV tests shown in Figure 4.3 in that there is almost no actuation present until the plasma ignites at a minimum voltage, and then actuation increases with voltage. The greater number of data points available with the force balance data shows a much clearer representation of the post switch-on relationship. There is a transitional period between 3 and 6 kV, and then from 6 kV peak to peak the actuation becomes proportional to V^2 (Figure 4.28).

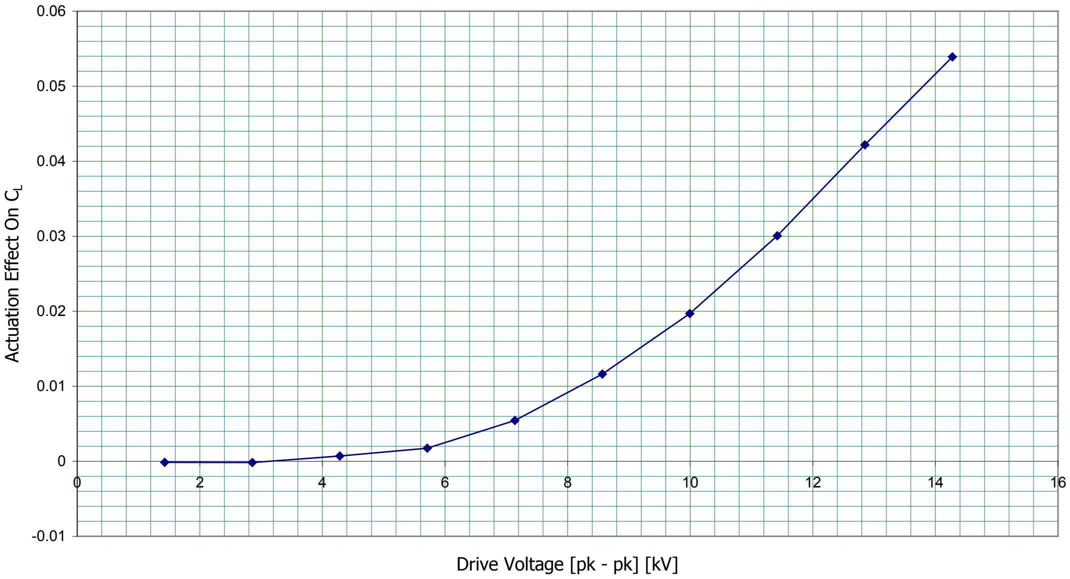

Figure 4.27 Actuation Effect With Voltage Sweep, (CF 3 kHz, DC 100%, Vel. 20 m.s^{-1})

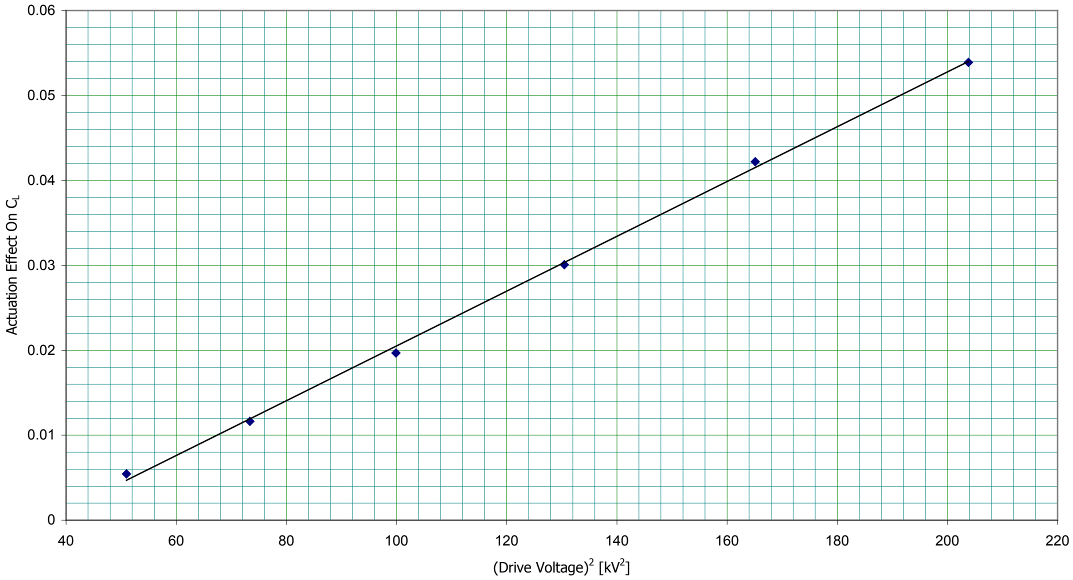

Figure 4.28 Confirmation of V^2 proportionality Post Switch-On

4.4.2 5 Hole Probe Measurements

In contrast to the hot wire measurements, the ceramic 5 hole probe was capable of recording data with the plasma active. Figure 4.29 shows the wake deficit with the plasma active and the same traverse without the plasma; each point is the average of 10 traverses. The 95% confidence interval calculated from the standard deviation between the repeats is shown marked. The main feature of this graph is the minimal change to the wake structure caused by the plasma actuation, although at the locations experiencing the largest shift the difference between the two is still large enough to be statistically significant. The fact that the U_x/U_{ref} does not return to unity outside of the wake has been noted, however as the primary purpose was to asses the difference between actuated and control conditions and as a high degree of statistical confidence had been achieved for this measure, the inaccuracies on the absolute value for the wake deficit were considered insufficiently important to re-run the test. Figure 4.30 shows the vertical component from the same averaged datasets. Again a miniscule but clear difference occurs between the actuated and unactuated traverses.

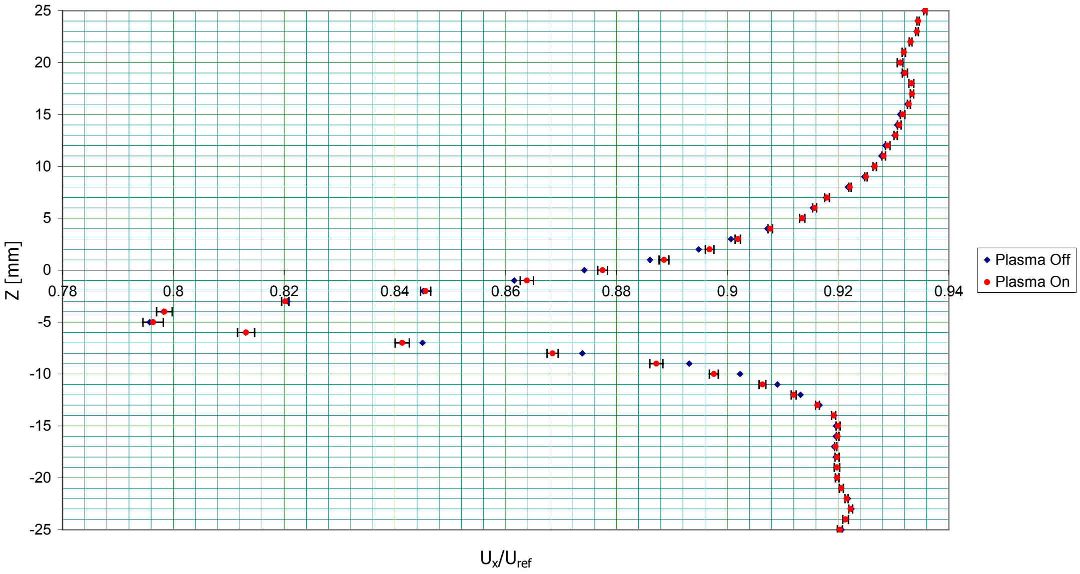

Figure 4.29 5 Hole Probe Actuated And Unactuated Normalised Wake Deficit Measurements With 95% Confidence Interval Error Bars, (CF 600 Hz, DC 100%, Vel. 20 m.s^{-1}, Inc. 0^{o})

To better visualise the change in wake behind the aerofoil, Figure 4.31 and Figure 4.32 show just the difference between the actuated and unactuated runs. Plotted are the individual data points as well as the average to give an idea of spread and to show the increase in variation within the wake. Even though the differences between the two when the traverses are compared directly in Figure 4.29 and Figure 4.30 are not immediately evident, there is a trend evident in both X and Z axis components when the offset is isolated. The physical effect of actuation on the wake that these graphs show is represented schematically in Figure 4.33.

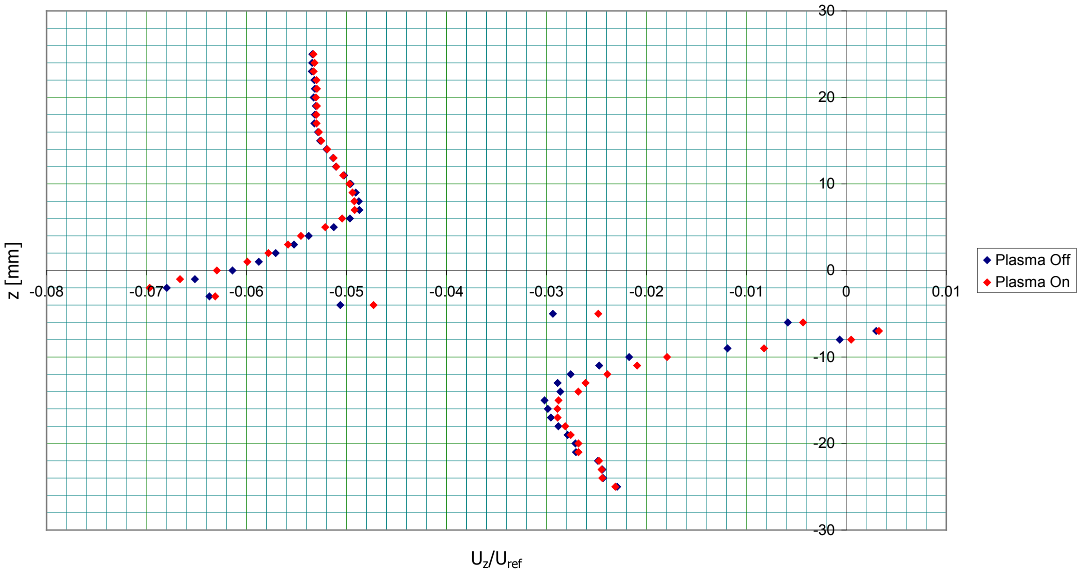

Figure 4.30 Actuated And Unactuated Normalised Z Axis (Vertical) Velocity Component Of Wake, (CF 600 Hz, DC 100%, Vel. 20 m.s^{-1}, Inc. 0^{o})

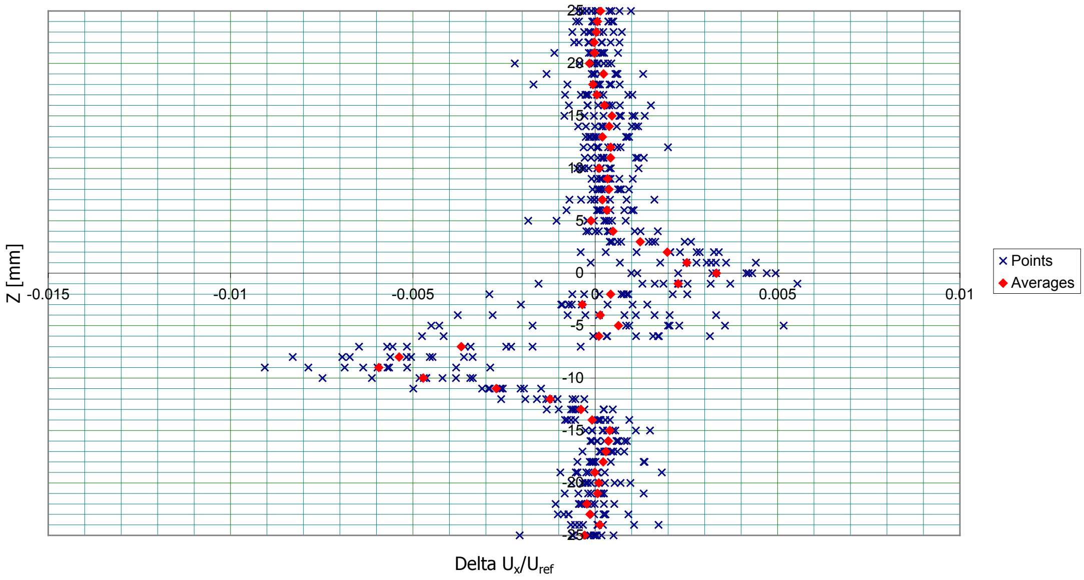

Figure 4.31 Change With Actuation In Normalised X Axis (Axial) Velocity Component, (CF 600 Hz, DC 100%, Vel. 20 m.s^{-1}, Inc. 0^{o})

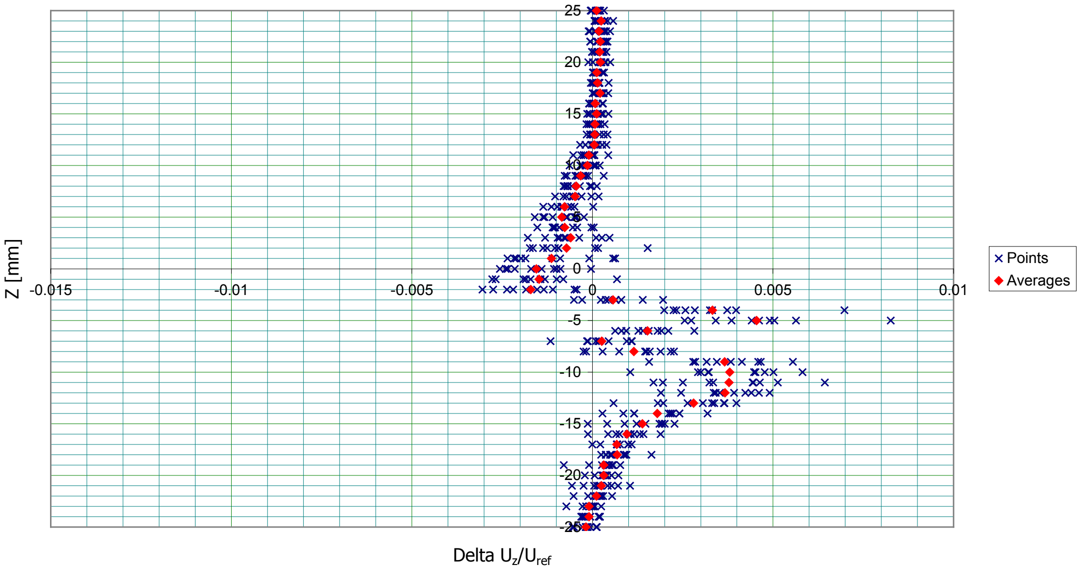

Figure 4.32 Change With Actuation In Normalised Z Axis (Vertical) Velocity Component, (CF 600 Hz, DC 100%, Vel. 20 m.s^{-1}, Inc. 0^{o})

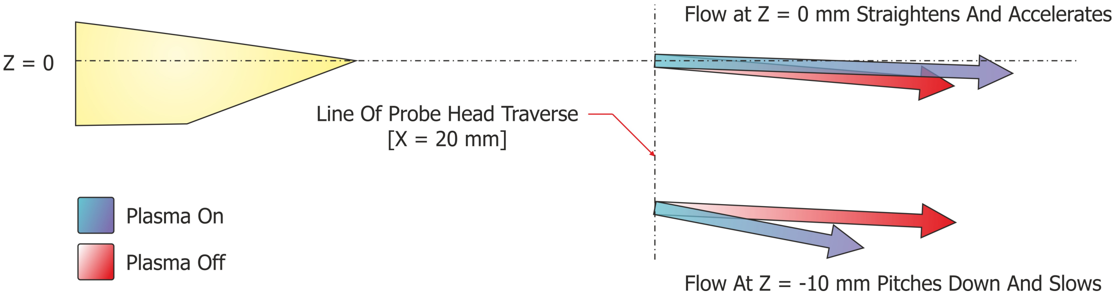

Figure 4.33 5 Hole Probe Data Summary

The previous 5 figures all pertained to the zero incidence case. When the focus shifts to a high incidence case, close to but not in the stall region for the aerofoil, we see that the observable difference between actuated and unactuated cases all but disappears, (see Figure 4.34). When looking at just the differences between the two cases (see Figure 4.35) the averages show the vaguest hint of the same shape that was seen at 0^{o} incidence in Figure 4.31. However, the variation observed on the individual data points almost completely masks the underlying signal. It is important to note that the x-axis (Delta U_x/U_{ref}) scales are identical for both Figure 4.31 (0^{o}) and Figure 4.35 (10^{o}) and thus the vast majority of the decrease in the signal to noise ratio is through an increase in sample variation.

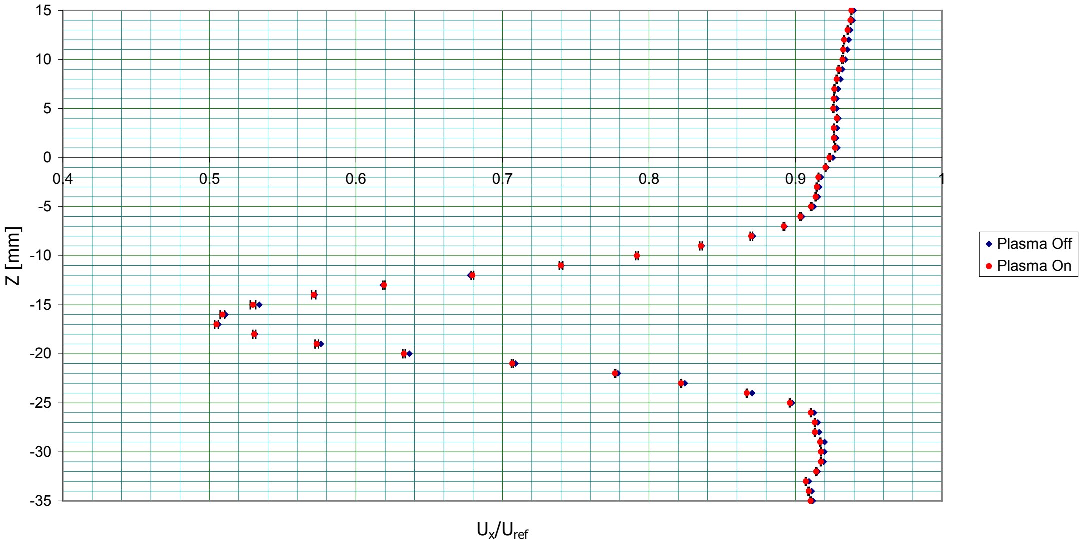

Figure 4.34 5 Hole Probe Actuated And Unactuated Wake Deficit With 95% Confidence Interval Error Bars, (CF 600 Hz, DC 100%, Vel. 20 m.s^{-1}, Inc. 10^{o})

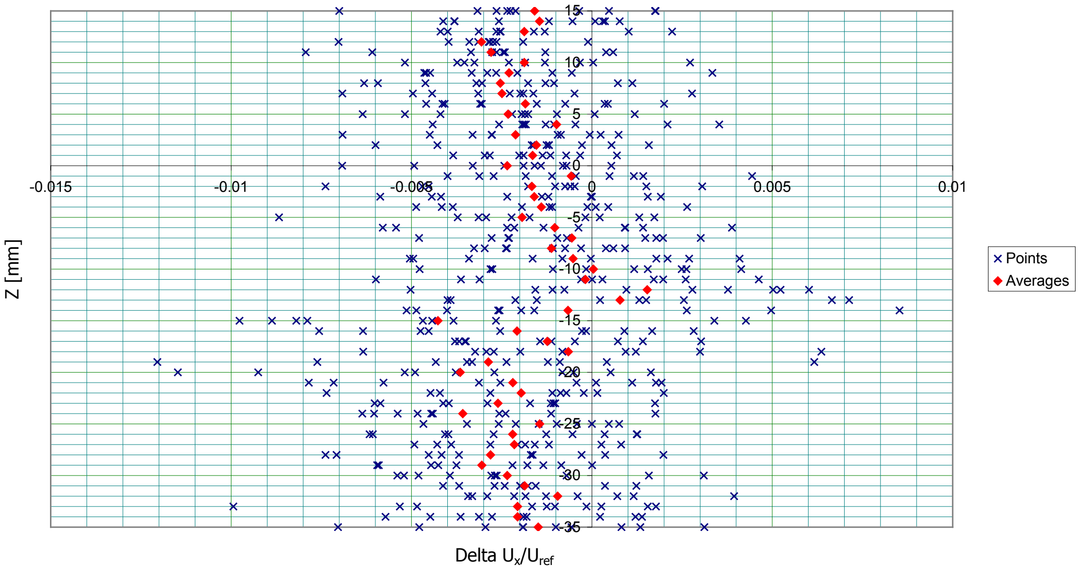

Figure 4.35 Change With Actuation In Normalized X Axis (Axial) Velocity Component, (CF 600 Hz, DC 100%, Vel. 20 m.s^{-1}, Inc. 10^{o})

4.4.3 Continuously Forced PIV Results

Figure 4.36 shows an image of 70% of the aerofoil in both control (unactuated) and uninterrupted (continuously actuated) states. The significantly lower velocity upwash region behind the step when under actuation should be noted. This is consistent with the force results shown in Figure 4.24 where an increase in lift force was seen at zero incidence with a continuously driven plasma.

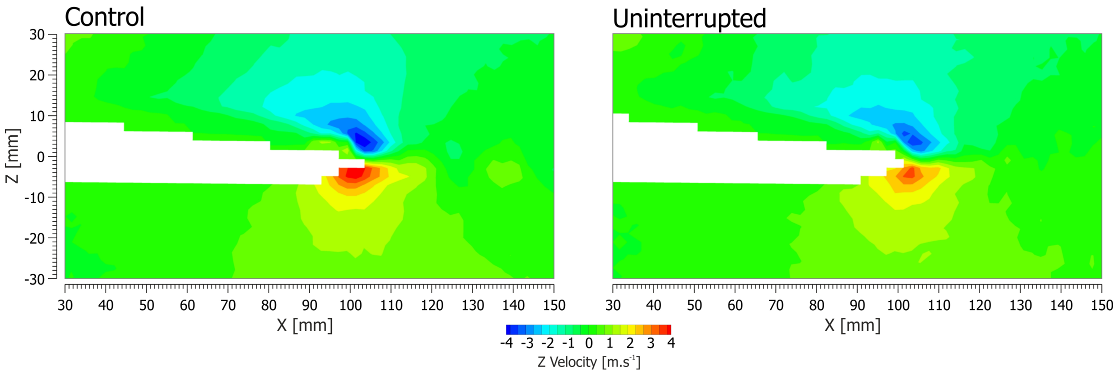

Figure 4.36 Wide Angle Images Of Continuously Actuated Flow Field, (CF 4 kHz, DC 100%, DV 14 kV, Vel. 20 m.s^{-1}), Against Unactuated Control

4.5 Pulsed Actuation Results

4.5.1 Force Balance Data

Figure 4.37 and Figure 4.38 shows the system response to varying interruption frequencies at zero degrees incidence. These two figures allow the direct comparison of the effect of duty cycle at ratios of 0.25 and 0.5. Due to a failure of the dynamic pressure sensor during the test run for the 0.25 duty cycle, data the graph had to be normalised by finding the dynamic pressure for the 0.25 duty cycle dataset which would result in its average C_L value for the unactuated control points equalling the same aggregate from the 0.5 duty cycle dataset. The interesting difference between these two graphs is that whilst both experience a peak in actuation effect at 800 Hz interruption, when forcing with a much shorter pulse as is the case with 0.25 duty cycle ratio the response experiences a second peak at the first sub-harmonic. The explanation for this is laid out in Figure 4.89 in section 4.6.

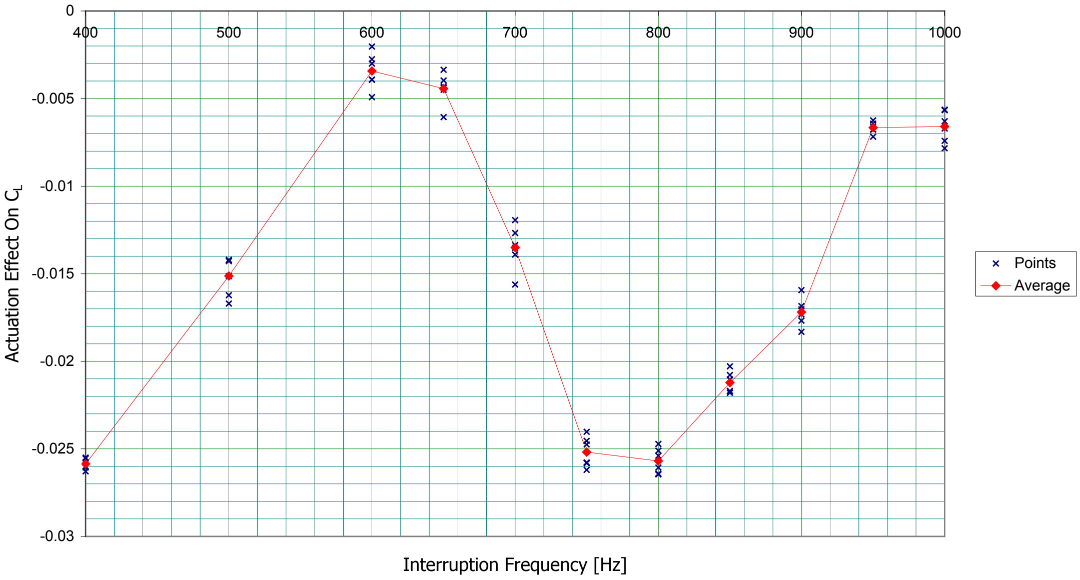

Figure 4.37 Interruption Sweep, (CF 4 kHz, DC 25%, DV 14 kV, Vel. 20 m.s^{-1})

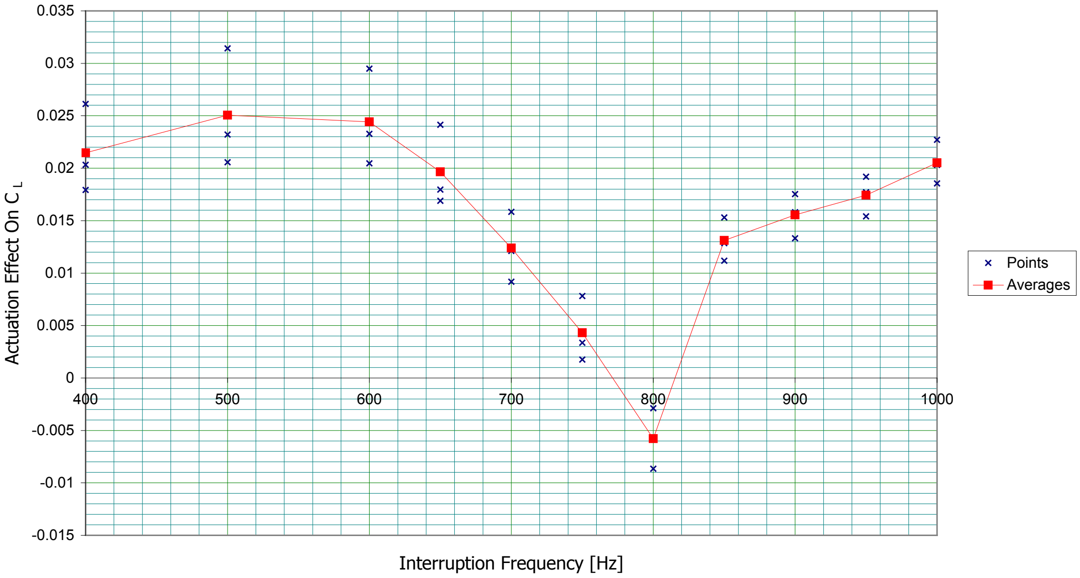

Figure 4.38 Interruption Sweep, (CF 4 kHz, DC 50%, DV 14 kV, Vel. 20 m.s^{-1})

As the parts of the actuators were cut and assembled by hand, even when produced with the utmost diligence and attention to detail, variation between actuators existed. Three nominally identical actuators were prepared and then run through interruption response sweeps. To eliminate atmospheric differences affecting the results, the tests were all run on the same day; each line in Figure 4.39 is the average of 3 repeated test runs for each actuator.

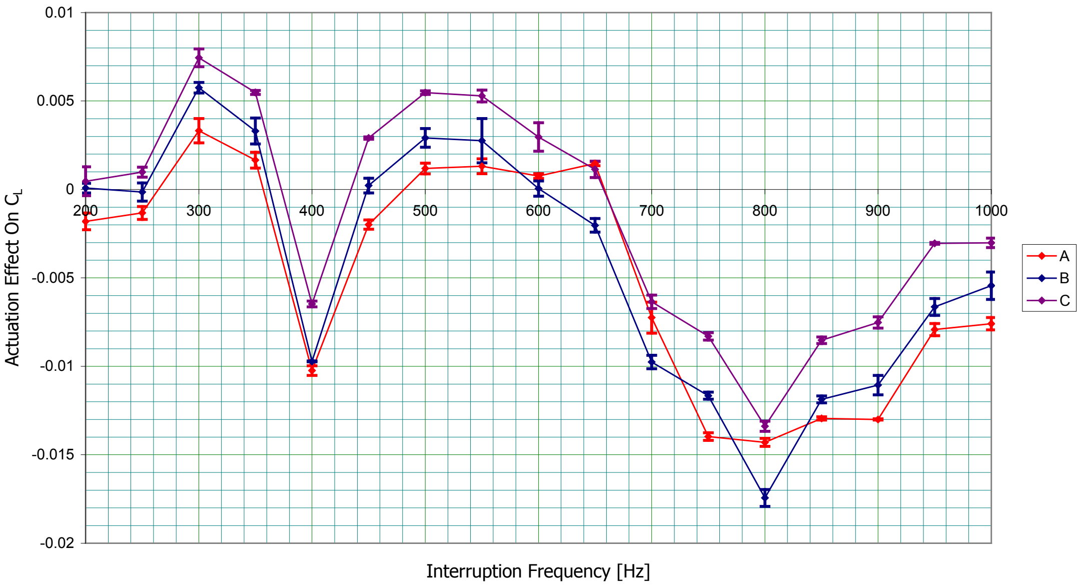

Figure 4.39 Actuator Repeatability Comparison, With 95% CI Error Bars, (CF 4 kHz, DC 25%, DV 14 kV, Vel. 20 m.s^{-1})

In Figure 4.39 at 400 Hz there is an inversion in the observed actuation effect which mostly occurs over a single data point; to confirm this a fine sweep was performed across just this region. The data shown in Figure 4.40 were taken using actuator C (shown purple in Figure 4.39) without removing the wing from the tunnel and therefore eliminating installation variation. The purpose of this graph is to highlight that the inversion appears to be a real, repeatable result. Figure 4.40 also shows that the repeatability of the runs is very high in that the spread on the individual repeat data points is very low and this spread is representative of all three runs included in Figure 4.39. From this we can see that the variation seen between actuators is not caused by insufficiently accurate measurement of the same value and that the variation seen between actuators must be considered a statistically significant variation arising from some part of the actuator manufacture or mounting process. The inversion effect seen arises from a complex relationship between the flow over the aerofoil and the plasma pulsation, this is covered in detail whilst discussing the results in section 4.6 at the end of the chapter, after further supporting data has been presented.

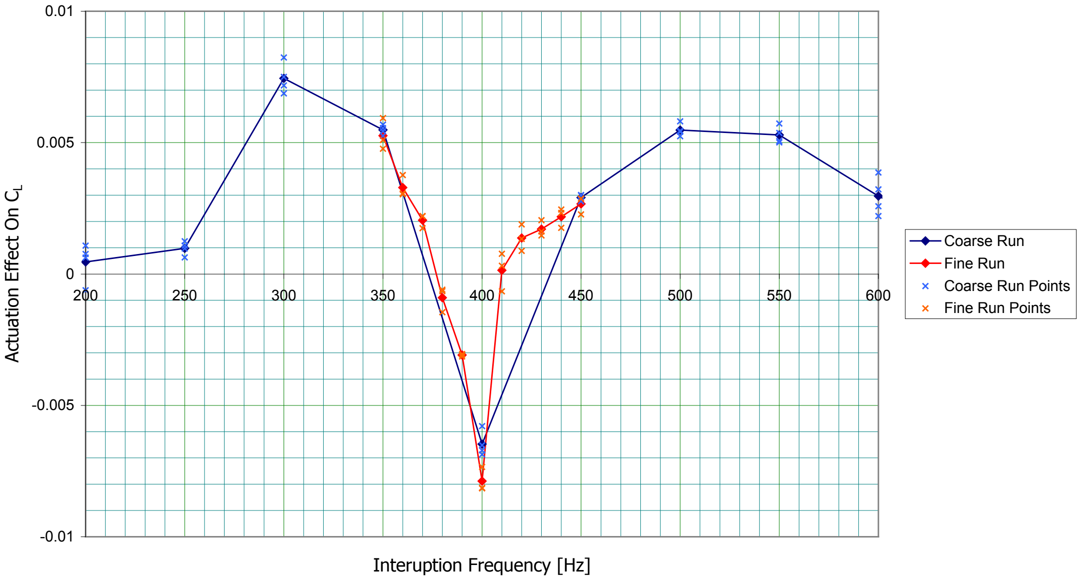

Figure 4.40 Fine Sweep Across Effect Inversion At 400 Hz Interruption, (CF 4 kHz, DC 25%, DV 14 kV, Vel. 20 m.s^{-1})

Figure 4.41 and Figure 4.42 deal with assessing the repeatability of the aerofoil mounting. In the test labelled clamp – reclamp the whole balance assembly complete with wing was taken from the tunnel as it would have been during any actuator change following burnout. The wing and spur were removed from the mounting clamp on the turntable and then the same aerofoil was then reclamped, the balance reinserted and the aerofoil re-levelled in the tunnel before the next dataset was taken. Therefore, as the actuator remains the same, this graph represents any errors introduced in the wing levelling and centring in the tunnel. The graph labelled mount – remount differs in that when collecting this dataset once the wing and spur had been removed from the balance, the actuator section was untaped, and the rear actuator-only section was removed from the back of the aerofoil. It was then reassembled, the joint between the two aerofoil sections was re-taped and replaced in the tunnel. In addition to the errors associated with Figure 4.41 this graph also includes errors introduced by how accurately the wing was able to be reassembled and the two sections taped together. Due to the limited actuator life and the need to complete the test, each run in these two figures comprises a single set of data points. No repeats were taken, but given the exceptional repeatability already seen between runs where the experimental setup remains unchanged this has only a marginal affect on the quality of the data. It should be noted when looking at Figure 4.42 that the deviation from the rest of the results seen in Mount 6 (purple) from 750 Hz interruption and upwards was due to the actuator burning through and failing during this last test run.

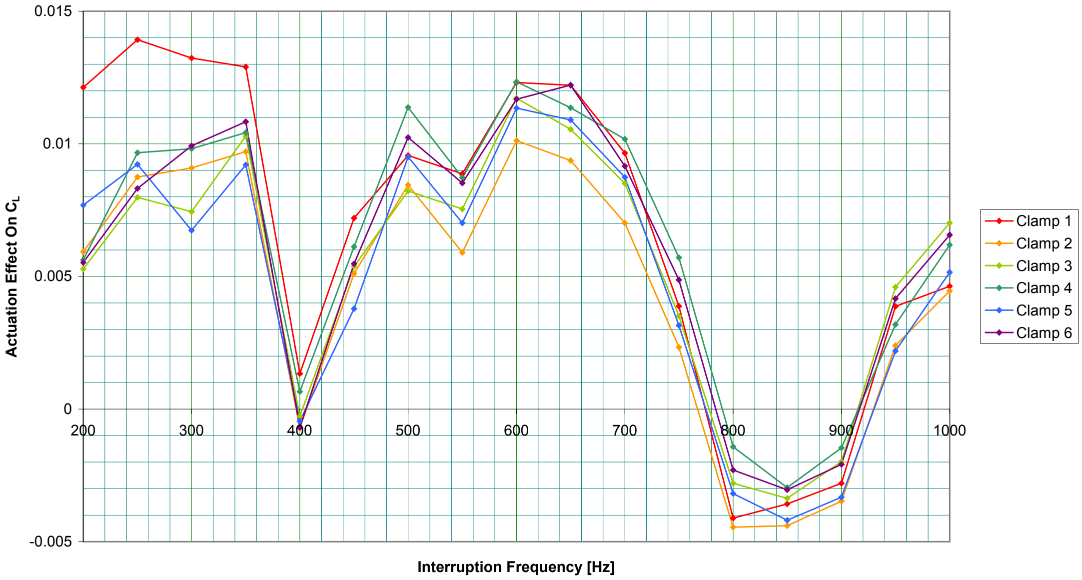

Figure 4.41 Clamp - Reclamp Repeatability, (CF 4 kHz, DC 25%, DV 14 kV, Vel. 20 m.s^{-1})

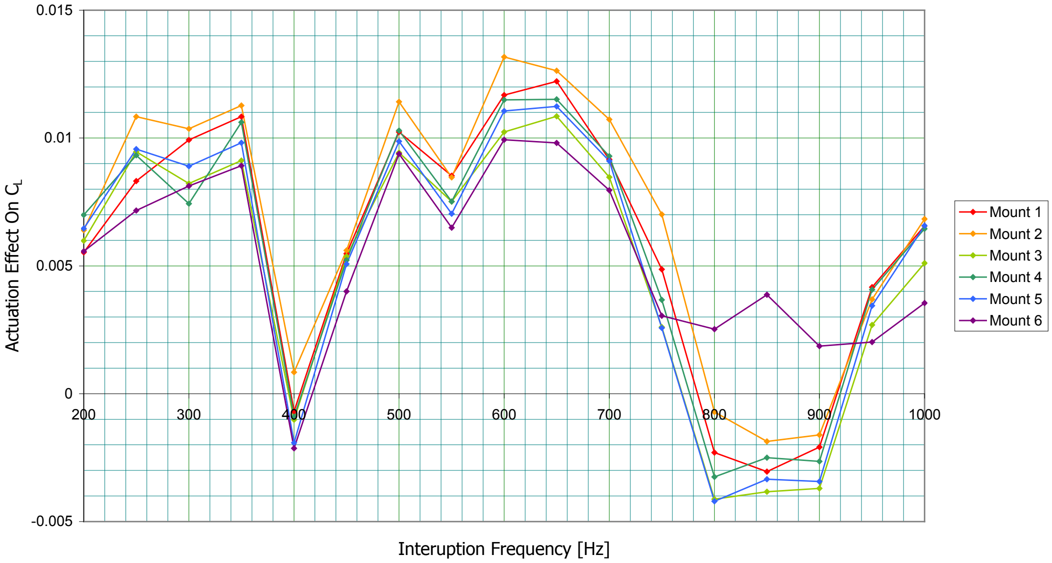

Figure 4.42 Mount - Remount Repeatability, (CF 4 kHz, DC 25%, DV 14 kV, Vel. 20 m.s^{-1})

In a similar vein to the previously discussed Figure 4.26, Figure 4.43 shows the effect of running the plasma without the wind tunnel on. This time the test was run at a variety of interruption frequencies to ensure there were no interference problems associated with chopping the drive waveform. As can be seen there is no offset of shift caused by the activation of the plasma. In addition to this the spread on the data is almost identical to that observed in Figure 4.26. Again we must conclude that electrical interference is not an issue for this data.

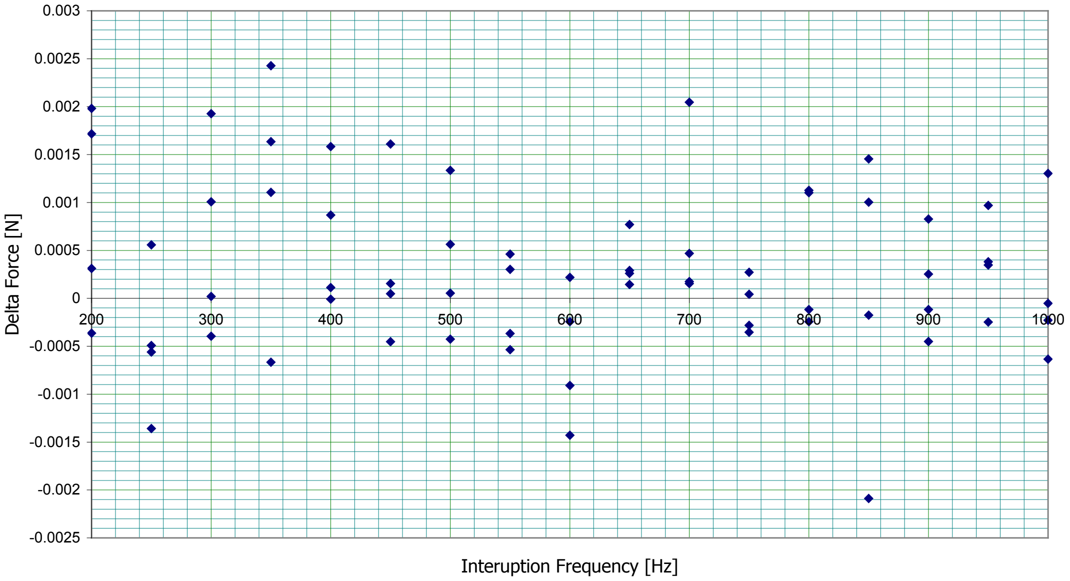

Figure 4.43 Zero Wind Electromagnetic Interaction Test - Interruption Frequency Sweep, (CF 4 kHz, DC 25%, DV 14 kV, Inc. 0°, Vel. 20 m.s^{-1})

Figure 4.44 shows a breakdown of the standard deviations of the data from the four previously discussed tests. With the exception of balance noise the figure represents the standard deviation of all points at a given node averaged over all the nodes in a dataset. The figure for balance noise is slightly artificial; as the test was performed without airflow and represents a non-aerodynamic effect, the changes in force cannot be converted into a C_L value on their own. To allow the data to be presented on the same graph it was normalised using the dynamic pressure from the clamp-reclamp test (but which is nearly identical to the other two as well). In this way it represents the contribution to standard deviation on C_L which would be expected purely from the electrical noise in the load cell, amplifier and power supply system, as part of the other aerodynamic tests. The data point labelled 'balance - tunnel repeatability' is taken from the data presented in experimental method - section 2.5.3.1; it represents the repeatability of the balance in returning the same change in C_L value for a consistent variation in aerodynamic load applied through a repeated change in incidence, (vel. 20 m.s^{-1}). Also included within this measure will be pressure transducer variance for the determination of tunnel velocity. As a whole this figure highlights the individual areas where the variation is arising. As the standard deviation (SD) of the clamping test and mounting test are the same and to remount the actuator it must also be reclamped; this means that the mounting procedure introduces no detectable extra error, with it all coming from the reclamping procedure, most probably in the alignment stage. Comparing the clamping effects to the balance - tunnel repeatability, it is noticeable that the increase in SD from removing and replacing the aerofoil is still fairly small, only increasing the variation by approximately 30%. The actuator repeatability test is almost twice that of clamping and mounting. However by definition this must also include the variation introduced by reclamping and setting up the aerofoil so the extra variation in delta C_L introduced just by changes between actuators is similar to that introduced by the balance – tunnel repeatability, combined with the process of remounting; this does however make it the single largest source of error. Finally, looking at the electrical noise from the balance we can see that this is so small as to be inconsequential when compared to the others.

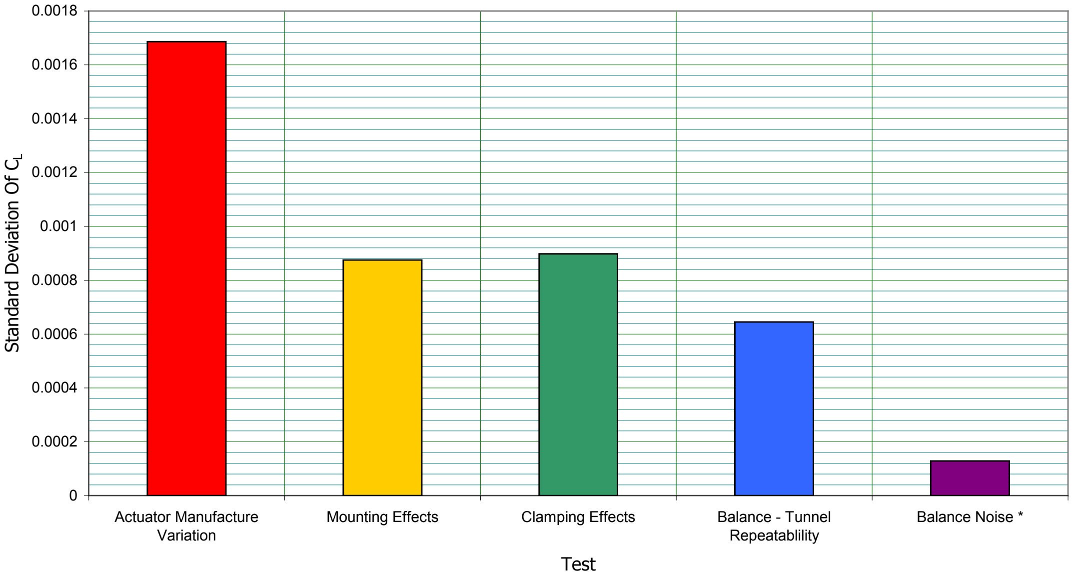

Figure 4.44 Average Standard Deviations Of Repeatability Investigation

Included for completeness in Figure 4.45 are typical pitch and drag coefficient data. It is possible that differentially increasing drag on one wing would be an equally valid form of flight control, especially for flying wing type vehicles where this method is used for yaw control classically implemented with split ailerons. However, as this was not the main focus of the project no repeatability analysis was conducted on the balance in these axes. It is apparent from the shape of the graph that both are influenced by the same aerodynamic mechanism affecting the lift coefficient.

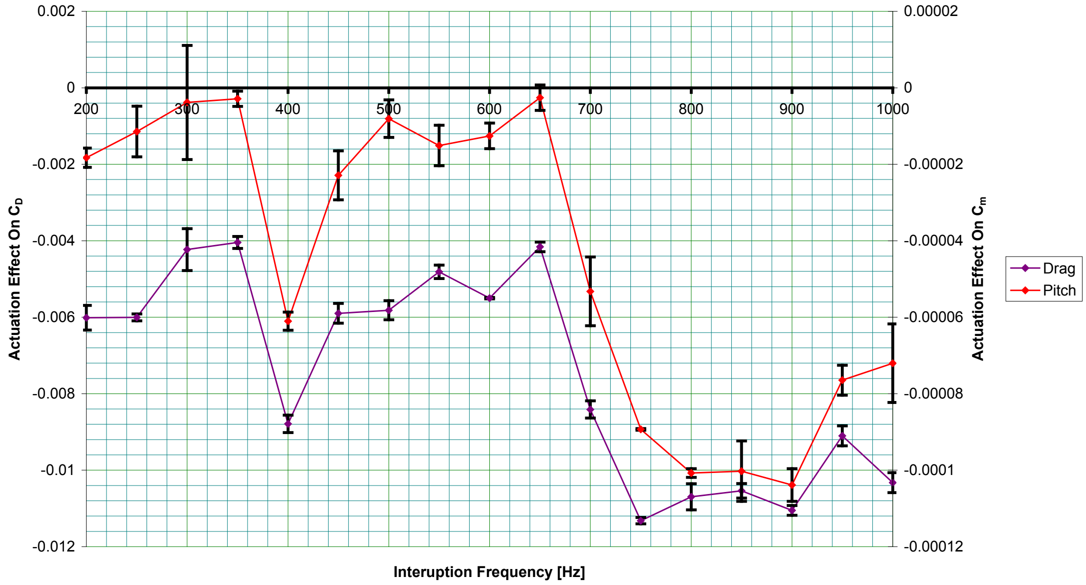

Figure 4.45 Pitch And Drag Coefficient Data With 95% Confidence Intervals

4.5.1.1 Force Balance Data At Non Zero Incidence

Figure 4.46 shows how the interruption response changes at varying incidence. All three traces show a similar response in that there is an optimum forcing frequency and as the interruption moves away from this the effect decays. As the incidence increases, the peak magnitude of change in C_L also increases. Along with this, as incidence increases sensitivity to interruption frequency also increases, i.e. there is a greater difference between maximum and minimum actuation effects. However, whereas the 0^o incidence case has repeatedly shown the ability to produce both positive and negative changes in C_L dependent on forcing frequency, as the maximum delta C_L value increases with incidence it is not being scaled symmetrically about the x-axis. Neither the 4 nor 8 degree data show an inversion, indicating that as incidence increases the method of actuation is going from a bi-stable regime into one where the flow is already fully detached over the step and can only be reattached to a greater or lesser extent by the plasma actuation.

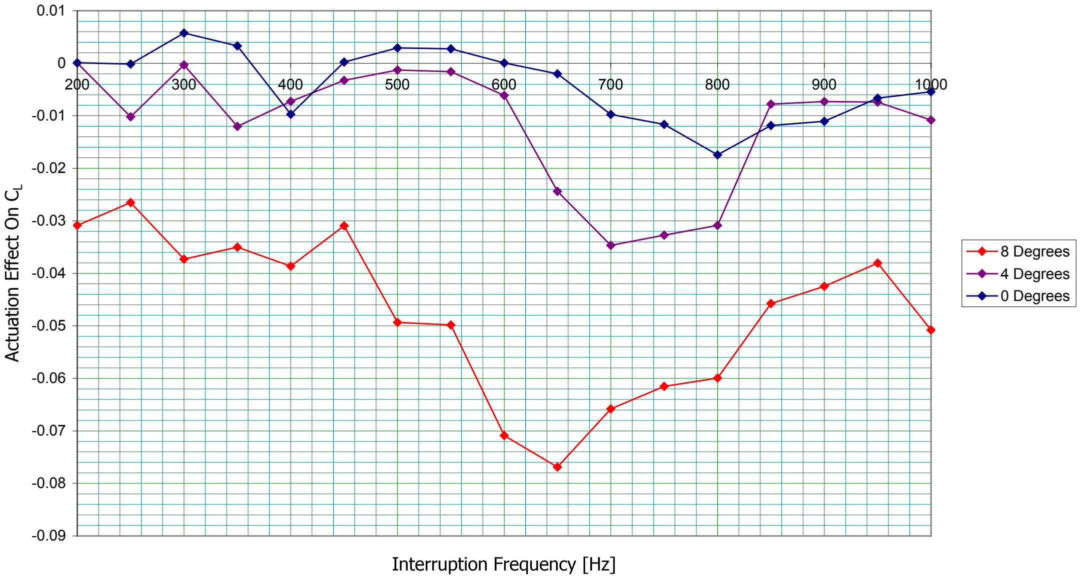

Figure 4.46 Change In Response To Interruption Sweep At Varying Incidence, (CF 4 kHz, DC 25%, DV 14 kV, Vel. 20 m.s^{-1})

With the data for interruption sweeps at 4 and 8 degrees showing a frequency shift in the position of the peak actuation effect (largest absolute magnitude delta C_L), it is interesting to compare this result to the vortex shedding frequencies measured with the hot wire probe. The hot-wire probe data was taken at 5 and 10 degrees rather than the 4 and 8 degree incidences for the full interruption frequency sweep presented in Figure 4.46. To allow a direct comparison, an interruption sweep with increased interruption frequency resolution was conducted over the area where the natural frequencies were expected to occur, at the correct incidences to correspond to the hot-wire data. Figure 4.47 shows the change in lift coefficient data along with the natural shedding frequencies (marked with colour coded vertical lines on the graph). Whilst the peak actuation point at 0^{o} incidence is within 15 Hz of the measured vortex shedding frequency, the 5 and 10 degree traces differ wildly between measured vortex shedding frequency and interruption frequency for peak actuation effect, with 5^{o} incidence experiencing a peak around 730 Hz, more than 80 Hz lower than the measured natural frequency. The 10^{o} data is so far from the measured natural frequency it was not captured within the interruption range covered but must be in excess of 180 Hz away from the measured frequency.

Figure 4.47 Fine Sweep Over Response Peaks From Figure 4.46, (CF 4 kHz, DC 25%, DV 14 kV, Vel. 20 m.s^{-1})

4.5.2 Laser Distance Results

The non-contact laser distance measurement setup was used to track the position of the aerofoil whilst simultaneously logging the force balance to allow the calculation of a lift coefficient, this yielded Figure 4.48. As the lift increases, the fraction of the self-weight of the balance live plate which is supported aerodynamically also increases. As this happens, the load cells must deflect to reduce the mass which they are supporting; this deformation is nominally linearly proportional to the change in force and is what is being tracked by the laser distance sensor. It can be seen that the two traces are clearly in very good agreement as to the overall shape of the actuator response, as the interruption goes into and out of phase with the natural vortex shedding frequency. The most interesting point is that whilst the deflection measurement (blue trace) is always negative (the wing always appeared to moved down) the change on C_L (red trace) goes positive (i.e. lift increased and therefore the wing should have moved upwards) twice, once between 300 – 350 Hz interruption and then again at 600 – 650 Hz.

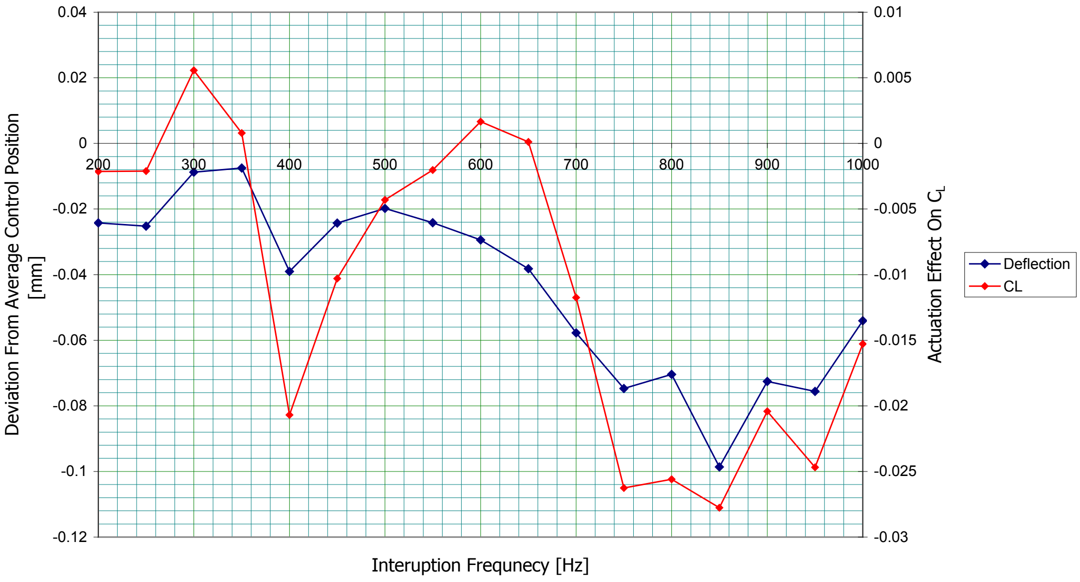

Figure 4.48 Laser Wing Deflection Measurement Compared To Balance C_L, (CF 4 kHz, DC 25%, DV 14 kV, Vel. 20 m.s^{-1})

One hypothesis for the inconsistency seen in the absolute level of the force balance data at different runs (e.g. that seen in Figure 4.39) was that the actuation effect was causing the aerofoil to pivot around the spur, either through relative motion at the wing - spur joint, the clamp or backlash in the turntable, and that this change in incidence was responsible for an interruption invariant force also only present during actuation over which the effect from the change in lift due to the change in flow field was superimposed. The uniform offset seen between different datasets could be explained by mechanical play leading to varying levels of pitch change between mountings but which remained constant over any single run. If any continuous change in pitch was present when the plasma was active this would manifest itself as a constant offset between the front and rear distance signals as they both tracked the motion under the balance. Looking at the figures;

From Figure 4.39 there is a shift on the order of :
0.005 on C_L – at a minimum , sometimes more

From Figure 4.10:
C_L = 0.0826 * Alpha (in degrees) + Const.

Therefore the equivalent change in incidence to equal 0.005 on C_L is:
Alpha = 0.0605°
And from this the approximate offset between sensors this would produce is:
Delta Z, Front - Rear = 102 µm

As is shown in Figure 4.49 there is no evidence of this offset between front and rear traces. Also as the deflection observed is much smaller than the expected magnitude of the offset, if it did exist it would have been clearly visible from this test. From this it can be asserted that the aerofoil translates almost perfectly under its balance mounting with insignificant changes in pitch.

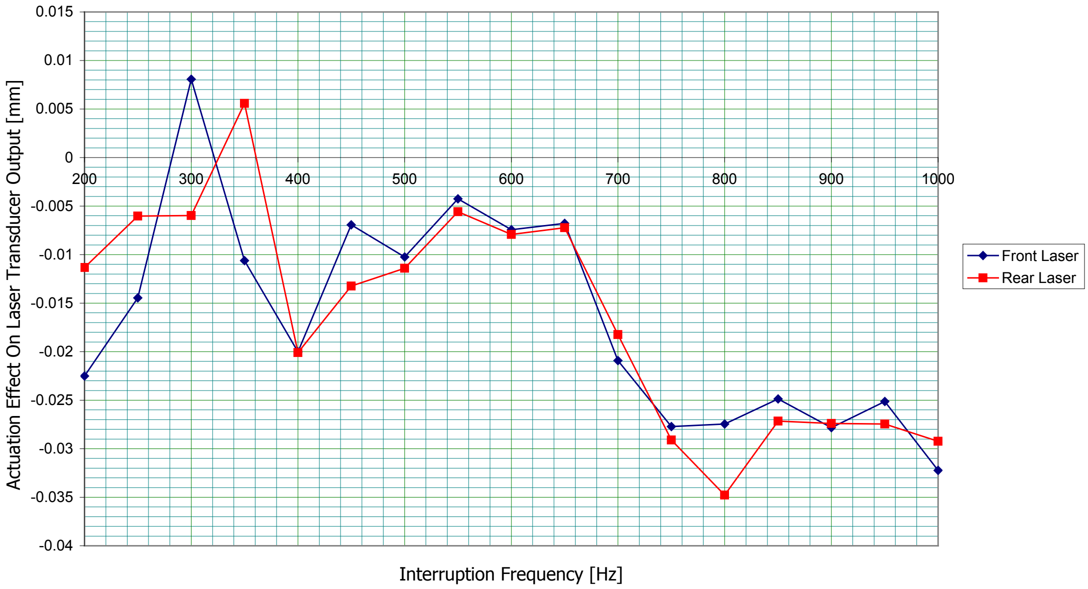

Figure 4.49 Individual Front And Rear Laser Motion Traces, (CF 4 kHz, DC 25%, DV 14 kV, Vel. 20 m.s^{-1})

4.5.3 Particle Image Velocimetry Results For Interrupted Plasma Actuation

4.5.3.1 Averaged PIV Data

Figure 4.50 shows a wide field of view over most of the aerofoil. What can be noticed is a slightly increased level of upwash behind the aerofoil when actuated with an interrupted plasma when compared to the unactuated control; this is in contrast to the data shown previously in Figure 4.36 where the continually actuated data showed a reduction in upwash behind the separation step. The increased upwash seen here is consistent with the force data shown in Figure 4.39 and others which, at 800 Hz interruption, shows a decrease in lift coefficient.

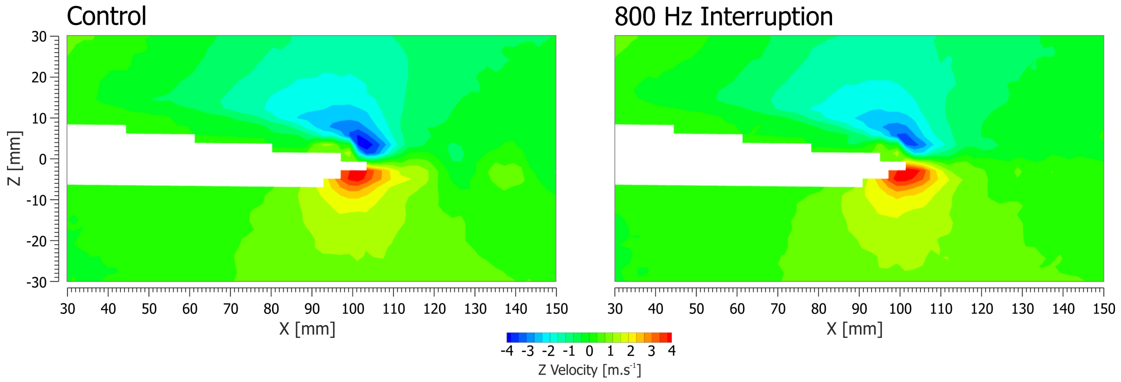

Figure 4.50 Wide Angle Of View Time-Averaged Flow Field, (CF 4 kHz, DC 25%, DV 14 kV, Vel. 20 m.s^{-1})

4.5.3.2 Phase Locked PIV Results

The following results were taken using the phase locked PIV capture technique, a detailed description of which is included in section 2.8.2.3.2. The basic theory of operation was to adjust the interruption frequency, to which the shedding was locked, such that the regular 3 Hz capture rate of the PIV system fell at a different point in the shedding cycle each time an image pair was taken. With sufficient precession in the selection of the plasma drive waveform the 250 image pair PIV run could be made to precisely cover one full shedding cycle. For brevity results are referred to by their nominal interruption frequency. For example, the 398.49075 Hz interruption required to create the correct precession sequence is listed as being 400 Hz. The bulk of the phase locked results can be divided into two main groups; high speed 20 m.s^{-1} data and low speed 3.6 m.s^{-1} data. The range of interruption frequencies that could be generated on top of a 4 kHz carrier at 25% duty cycle whilst maintaining at least one full carrier wave per interruption cycle is limited to 1 kHz or less. This meant that at 20 m.s^{-1} with a shedding frequency of ≈ 825 Hz it was only possible to carry out a full sweep of experimental points with excitation below the natural shedding frequency. This would have left a gap in the data as to the effect of energising the plasma at an interruption frequency above the natural vortex shedding frequency of the aerofoil. To answer this question in the best possible manor with the equipment available, the 3.6 m.s^{-1} data, with a natural shedding frequency of ≈ 149 Hz, allowed data to be collected to in excess of twice the natural shedding frequency. Although both flows existed in the lamina flow regime care should be taken when comparing between datasets due to the differences both in the boundary layer shape and the relative power of the actuator when compared to the freestream. Unfortunately, comparative force balance data for the 3.6 m.s^{-1} data could not be collected due to the 31 times reduction in lift forces compared to the 20 m.s^{-1} test runs which made any change unresolvable. However the greater authority the actuator exhibited over the lower velocity flow allowed some direct observations in the PIV data of the change in flow field under actuation that were not visible in the high speed data.

4.5.3.2.1 High Speed 20 m.s^{-1} Dataset

To assess the degree to which the shedding cycle was locking into the plasma actuation cycle the instantaneous flow field data was processed into pseudo time histories for each point in the field of view. A single point on the periphery of the wake was selected and a sine wave was fitted to the data for the Z-axis (vertical) velocity component by adjusting amplitude and phase of the correct frequency sine wave to minimise the sum of the squared errors. The locations for the selected vector (see Figure 4.51) were different for the low and high speed tests as these points were the ones that provided the cleanest signal and no common point for the two datasets proved as good.

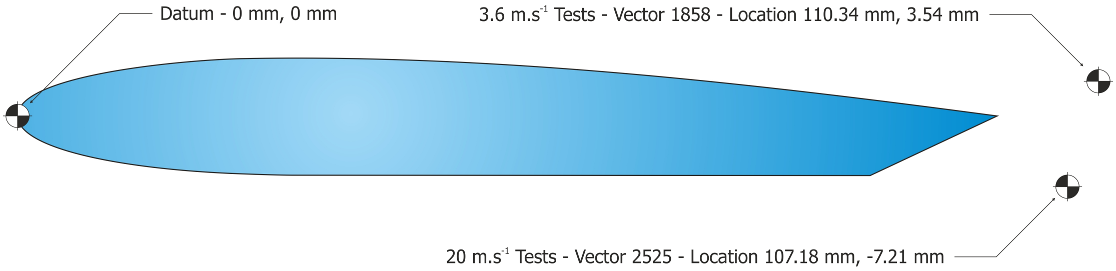

Figure 4.51 Phase Locked Pseudo Time History Locations

There are three sources of variation identifiable in the vertical velocity pseudo time histories. Figure 4.52 annotates these on a dataset; for clarity one of the low speed traces which will be covered later is used as it showed better differentiation. Firstly there are several points residing precisely on the x-axis; these are the result of dropped frames from the PIV capture hardware. Failure of the laser to illuminate the flow field results in totally dark image pairs which are subsequently processed into zeroed vector fields. Normally these would be discarded; however the need to keep the data in sequence meant that they had to remain in place. The second type are those data points where the shedding had broken from its lock-in with the drive plasma and was out of sequence when the vector field images were taken. This can be confirmed by looking at the assembled video of the full vector field plots; the image is of the same quality with respect to noise and clarity of the vortex street. However, it is shifted and appears out of sequence with respect to its neighbouring video frames. Lastly, there is the variation between consecutively sampled vortices; as it is only a 'pseudo' time trace composited together by sampling many different vortices, the data is not the record of a single vortex being convected downstream. Therefore even when the vortex is in the correct position when the PIV images were taken, variation in vortex size and strength results in significant noise on the signal.

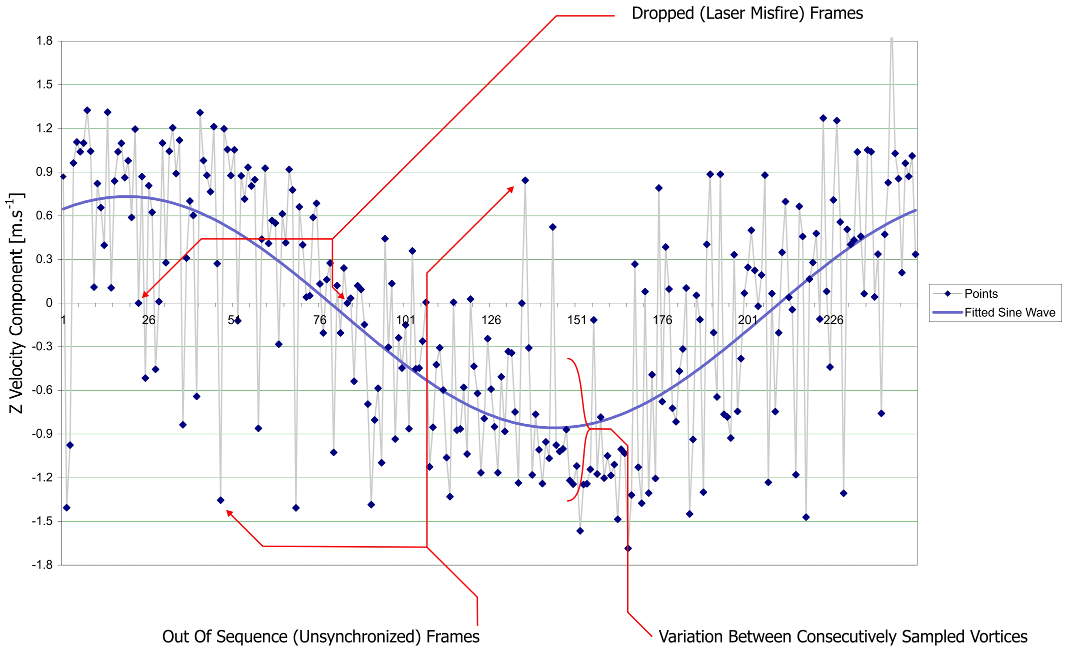

Figure 4.52 Sources Of Noise Within Vertical Velocity Pseudo Time Histories

Figure 4.53 shows the vertical velocity component of the flow at the measured point for different interruption frequencies. To make the data more directly comparable across the range of collected interruption frequencies, the data from the higher interruption frequencies where the dataset spans a shorter time period was repeated to match it to the same total time as the 150 Hz data set. The extent of the unique data in each plot is shown highlighted in red / green with the red section representing the period when the plasma was active. Shown in grey is the best fit sine wave for that data. It is also important to note that while the end points of the velocity scales for each plot are different, the spans are identical and so the relative size of the waves is directly comparable.

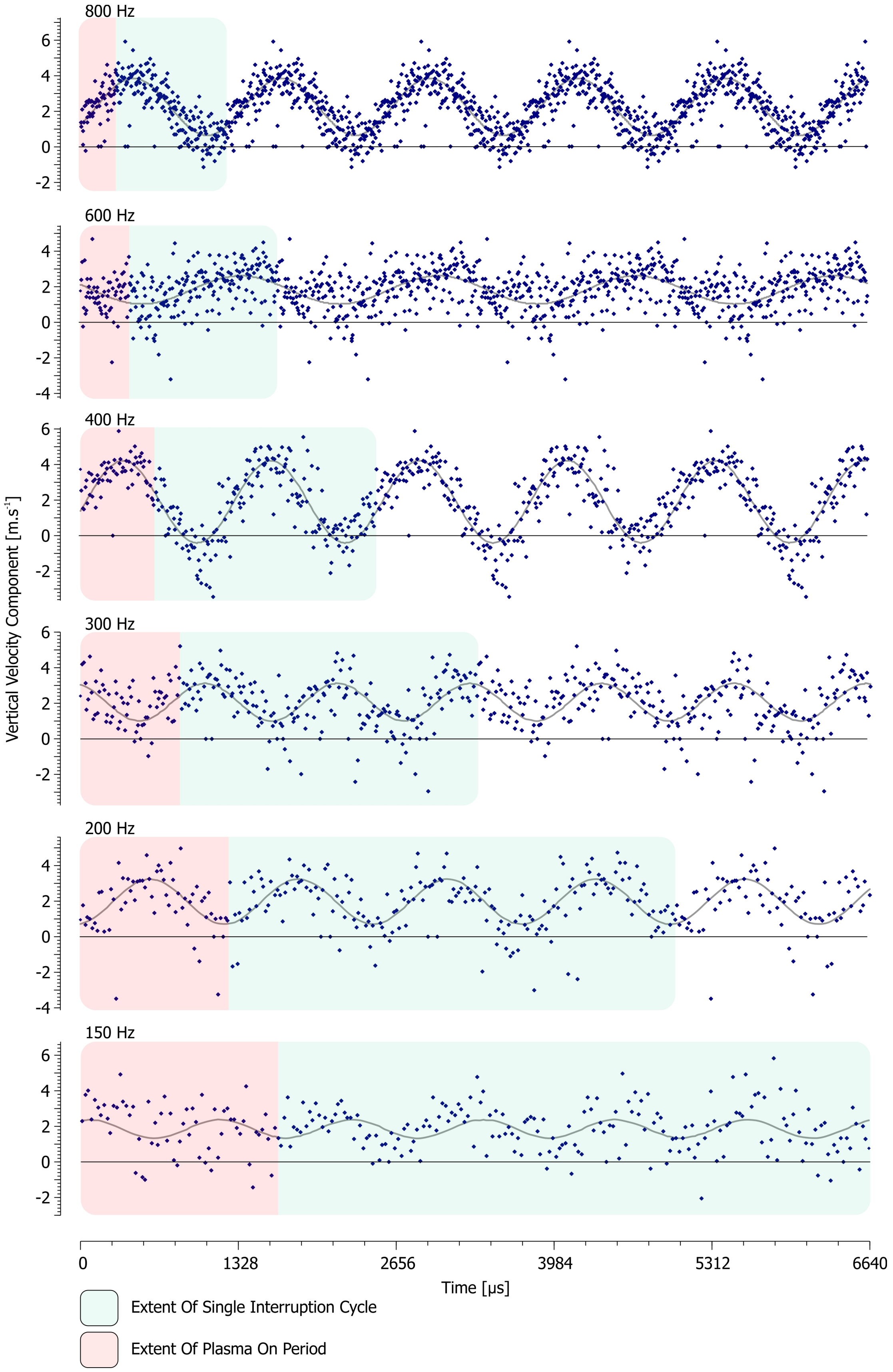

Figure 4.53 20 m.s^{-1} Vertical Velocity Pseudo Time History For Different Interruption Frequencies (CF 4 kHz, DC 25%)

The key points to take from Figure 4.53 are the well defined, high amplitude, locked-in signals at 800 and 400 Hz interruption, compared to the noise-dominated low-amplitude signal present with 600 Hz interruption. This is exactly the pattern we would expect based on the force balance results where the 400 and 800 Hz interruption frequencies both produced lower C_L changes than at 600 Hz. Secondly it is noteworthy that there is a larger amplitude signal from 200 Hz interruption when compared to 300 Hz interruption. At 150 Hz the magnitude of the signal has dropped to the level of the unsynchronised interruption at 600 Hz. It is likely that this remains locked to the capture signal, not through any resonance effect, but through the natural shedding cycle being suppressed whilst the plasma is active. At each interruption cycle it is 'released' to shed naturally, starting from the same point relative to the interruption cycle, and therefore the image capture cycle precesses through as expected.

In Figure 4.53 the sine wave fitted to the data is not that which resulted in the lowest sum of the squared residuals. Figure 4.54 shows the two sine waves considered, periodicity 5 shedding (i.e. 5 vortex shedding cycles per interruption cycle) (shown orange) produces the lowest sum of least squares and it can be seen that in the area of the data showing lowest noise, approximately between frames 50 and 170 the spacing of the peaks appears consistent with this fitting. However it was impossible to reconcile this shedding regimen with the evidence of the full vector field frames assembled into a video. It will be shown later in Figure 4.62 and Figure 4.63 when looking at sequential sections of the flow field images that the only logical fit is the periodicity 6 shedding (shown red in Figure 4.54) and this is the fit used.

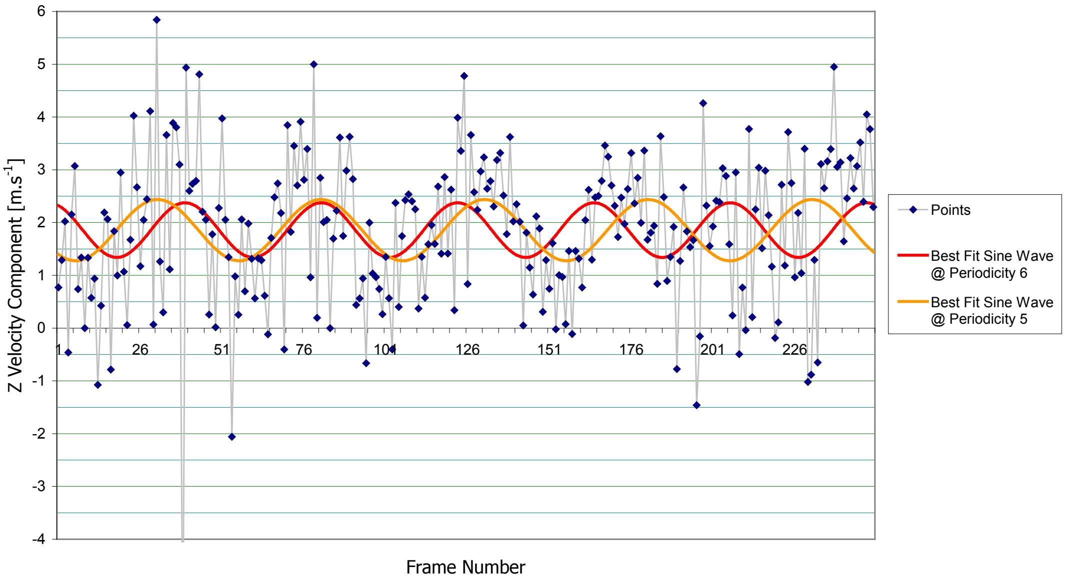

Figure 4.54 Comparison Of 5th & 6th Order Periodicity Shedding (CF 4 kHz, DC 25%, IF 150 Hz, DV 14 kV, Vel. 20 m.s^{-1})

To condense the pseudo time history data down in a quantifiable measure of how well the shedding was locked in, a fit coefficient was developed. This measure expressed how well the data set followed its best fit sine wave (fitted using an iterative least squares method). The fit coefficient was defined as shown in Equation 7. If the data showed no periodicity, the best fit sine wave would be a flat line coincident with the average, the two standard deviations would be the same and fit coefficient would reduce to 0. Conversely, if the data were a perfect sine wave, the standard deviation of the residuals (numerator in the equation) would be zero and therefore the fit coefficient would be 1. As this measure is based on the ratios of two standard deviations it is insensitive to the absolute magnitude of the shedding waveform.

$$\text{Fit Coefficient} = 1 - \frac{\text{Standard Deviation (Instantaneous Data Point - Fitted Sine Wave)}}{\text{Standard Deviation (Instantaneous Data Point)}}$$

Equation 7 – Fit Coefficient Definition

Figure 4.55 shows the fit coefficient for the high speed data dataset. Looking back to Figure 4.53 it can be seen how these figures do tally to the shedding, and also (when inverted) how this will roughly tally to the force data.

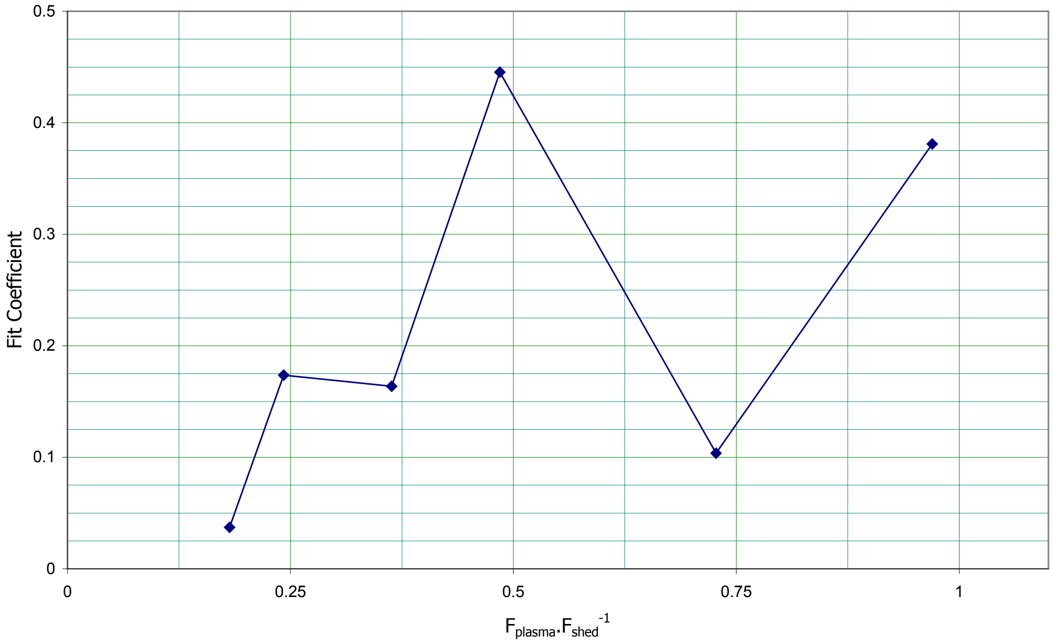

Figure 4.55 Sine Wave Fit Coefficient For 20 m.s^{-1} Data

Streamtraces were extracted from the averaged velocity vector fields using Tecplot 360. At full tunnel velocity the shift in flow field over the aerofoil was so marginal the only noticeable deviation occurs when comparing between maximum and minimum achieved actuation levels. To this end Figure 4.56 shows streamtraces from the two extremes of the interruption sweep and the control. This shows that the 800 Hz interruption is actually managing to better attach the flow to the separation step, whereas the 150 Hz interruption is actually increasing separation, despite the fact that the power into the plasma is identical between the two cases.

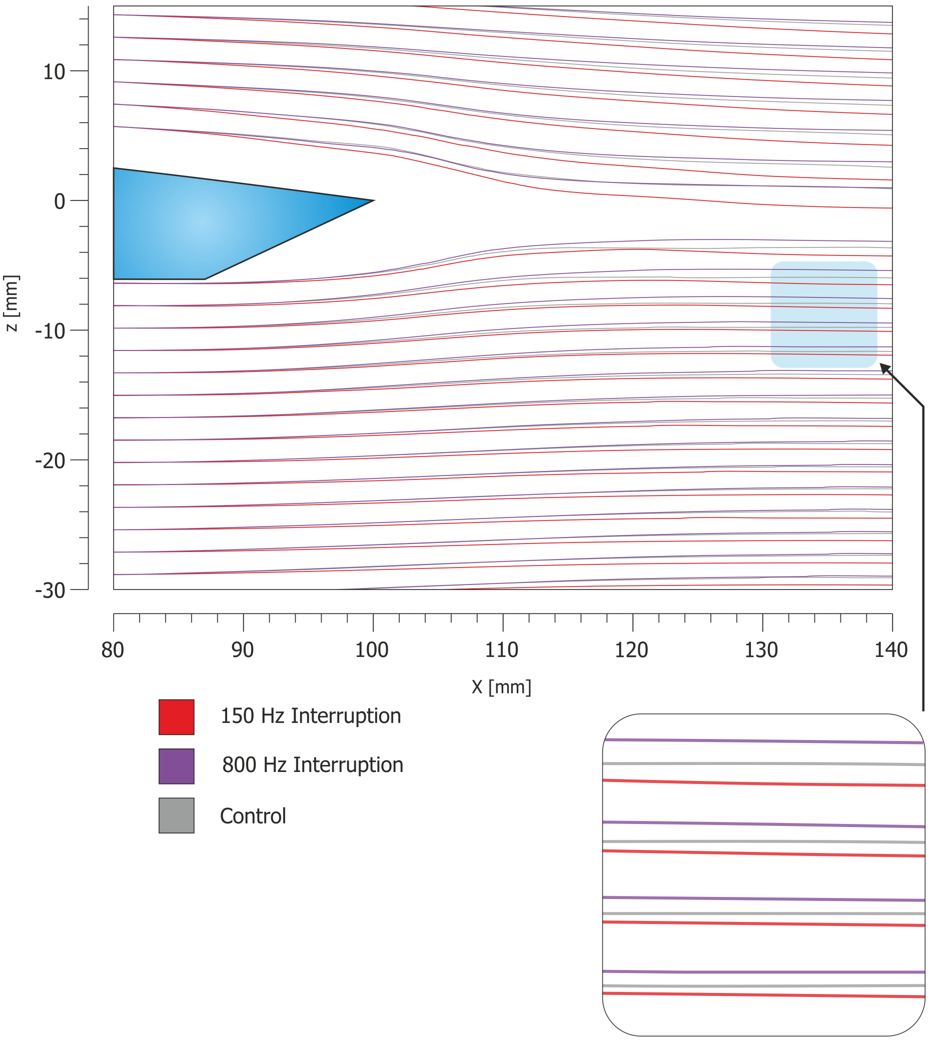

Figure 4.56 Streamtraces At 20 m.s^{-1}

Looking at Figure 4.57 we see a different pair of streamtrace plots, with a high density of streamlines started just downstream of the trailing edge and propagated in both directions the recirculation bubble becomes visible, note the significantly tighter, more compact bubble for the 800 Hz forcing compared to that of the 600 Hz case.

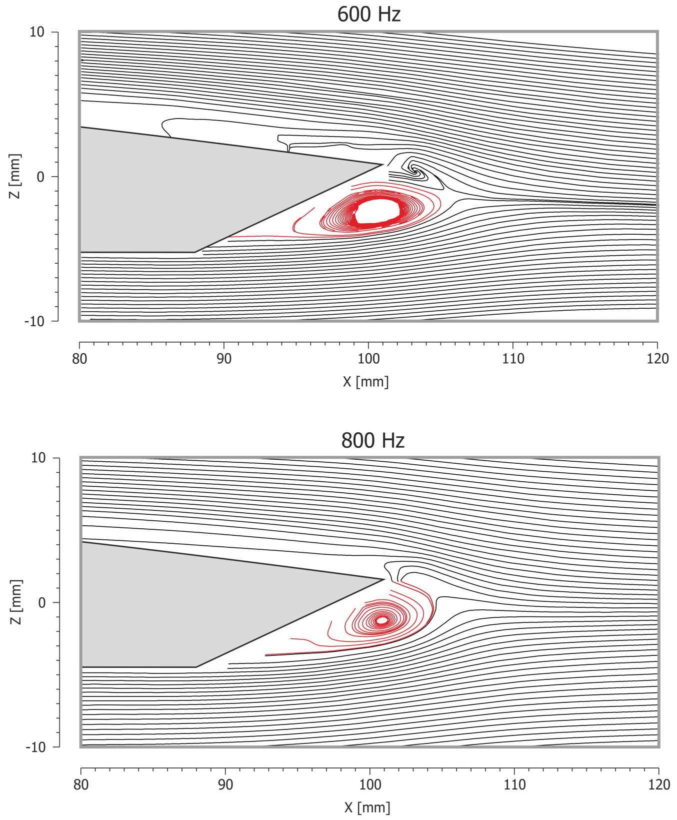

Figure 4.57 High Density Streamtraces Showing Recirculation Bubble

To quantitatively asses the deflection of the wake a section of the vector field was used to give an average flow direction within the wake which could be compared to the average flow direction for an unactuated control; this was again extracted using Tecplot 360. Separate areas were required for analysing runs at high and low speed because, not only was the camera field of view slightly altered between the two, but also the extent of the wake differed in the two cases. The areas averaged at both 3.6 and 20 m.s^{-1} are shown in Figure 4.58.

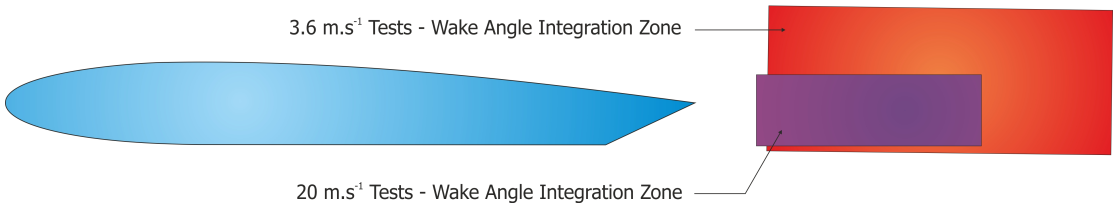

Figure 4.58 Wake Angle Integration Zones

Figure 4.59 shows the results of the integration of the wake behind the aerofoil. The data are presented to give a plot of the change in wake angle relative to the angle of the unactuated control. It can be seen that, as in the stream traces from Figure 4.56, 800 Hz actuation pitches the wake up relative to the control, whereas all other actuation frequencies result in a greater down wash in the wake of the aerofoil. It should be noted how the peaks line up with the harmonic and sub harmonics of the shedding and the troughs line up with the half nodes, indicating this is likely to be areal pattern in the data and not severe noise on a simple upward trend.

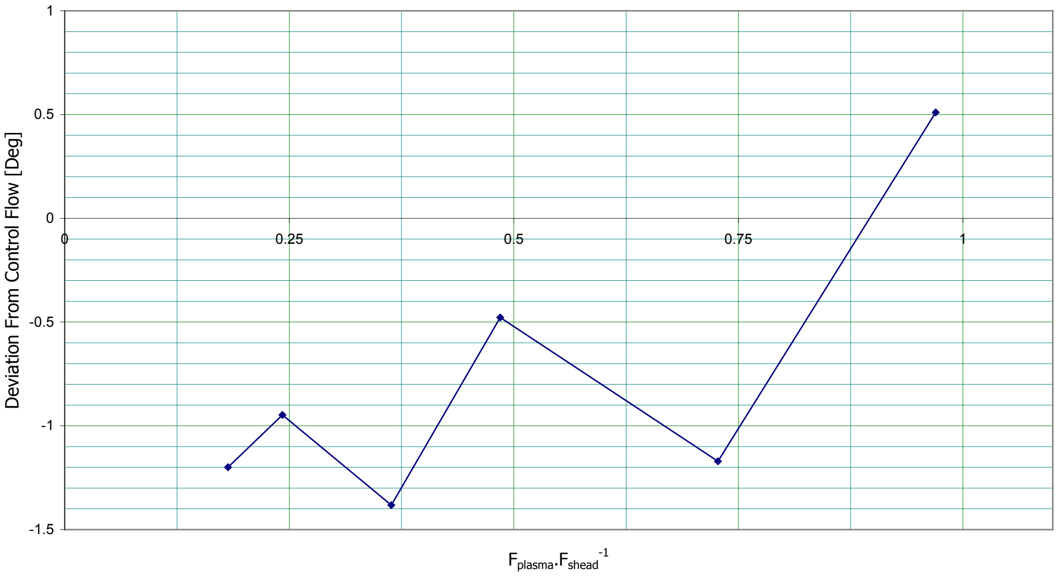

Figure 4.59 Wake Flow Angle Deviation From Control At 20 m.s^{-1}

Figure 4.60 through Figure 4.62 show a subset of images taken from vortex shedding animations assembled from the individual sequenced frames from the PIV data; each vertical column covers the full interruption cycle with equal temporal spacing between each individual image within the column. This layout allows the downwash element of each vortex to be tracked as it is shed from the trailing edge of the wing and progresses downstream. Each vortex is identified with its own uniquely coloured arrow; as the data are periodic, when a vortex reaches the bottom of the column the same vortex (in terms of initiation point relative to plasma cycle) reappears at the top of the column; the dotted lines are included to help the eye keep track of which vortex is which during this and arrow colouring consistency is also maintained.

The first thing to note about these figures is that they, more than any other presented so far, demonstrate the success of the phase-locked PIV capture technique; being able to assemble these images is only possible due to the stability and repeatability of the vortex formation and propagation process. At a more fundamental level these images prove that the vortex shedding locks into the plasma interruption under some conditions. Looking at Figure 4.60, 800 Hz interruption, it can be seen that the image sequence clearly demonstrates a logical progression of the vortices forming at the trailing edge of the aerofoil and being convected downstream. In this particular case the flow demonstrates a single vortex shedding cycle per interruption cycle, as would be expected from both the ratio of interruption to natural shedding frequency and the data shown in the pseudo time histories used to produce Figure 4.53. Looking at the second half of Figure 4.60, the images for 600 Hz interruption, the lack of any cohesive, regular shedding is instantly noticeable. That is not to say that vortices are not being shed, however they are highly disrupted and much weaker than those seen at either 800 Hz interruption or 400 Hz interruption shown in Figure 4.61. From the lack of a locked-in shedding pattern in the images sequence for 600 Hz interruption it can be concluded that the slight sign of a periodic signal at 600 Hz in Figure 4.53 is most probably an anomaly.

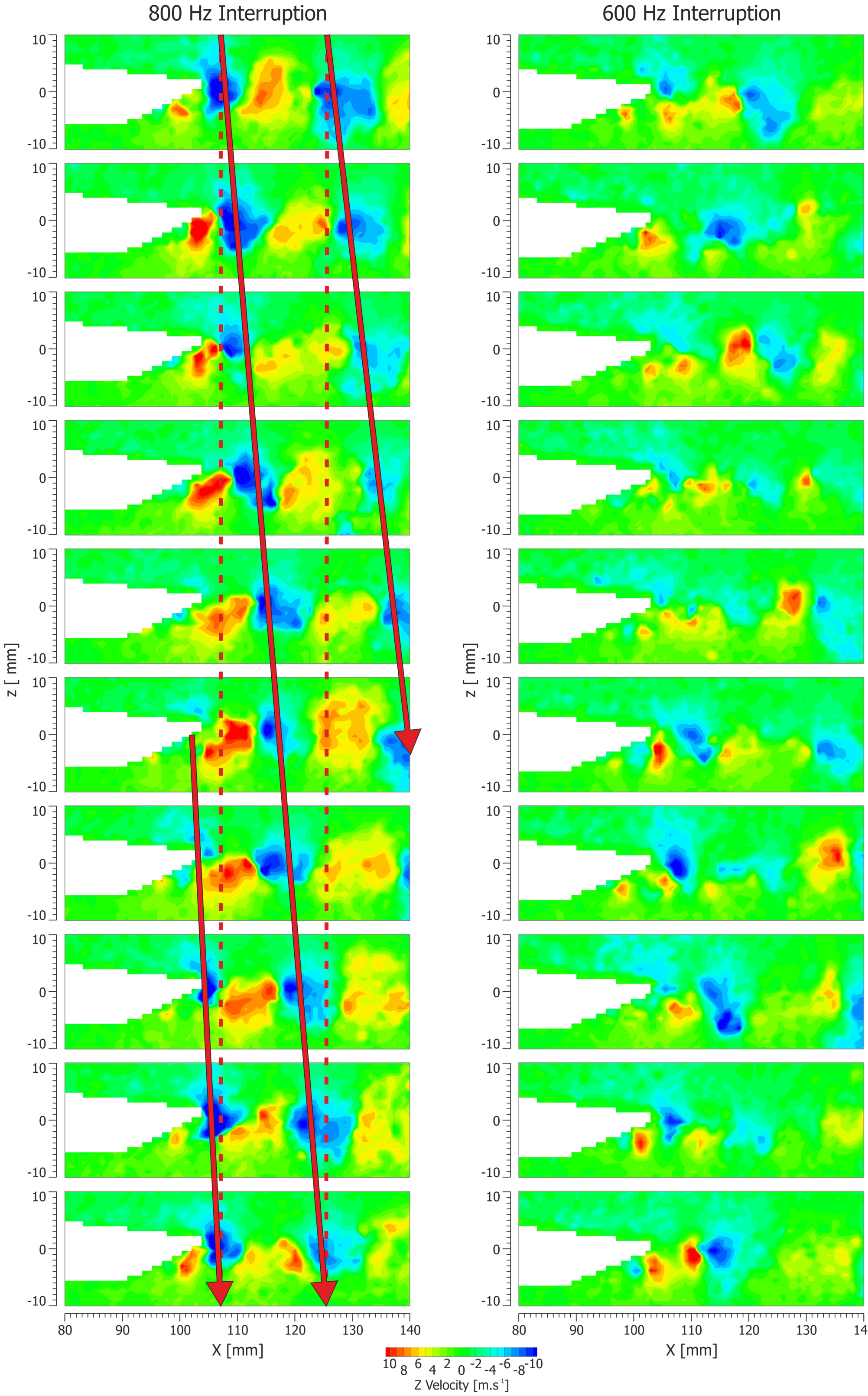

Figure 4.60 Sequential Z Axis (Vertical) Velocity Component Frames At 20 m.s^{-1}, 25% DC, 800 and 600 Hz Interruption Frequency

Looking at the data for 400 Hz interruption in Figure 4.61, the vortex structure shows shedding twice per interruption cycle; again this is the expected result with the shedding trying to maintain a frequency as close to its natural frequency as possible. As the images remain in sequence with the PIV capture rate, the directly actuated upon and the intermediate vortices must both remain locked to the interrupted plasma signal. Observing the 300 Hz interruption sequence, rather than becoming disrupted as is seen at 600 Hz interruption, the shedding remains locked into the plasma drive signal. However, the shedding is forced to occur at 900 Hz, an approximate 9% shift from its natural shedding frequency. Simultaneously, at this interruption frequency with a 25% duty cycle, the plasma active period extends beyond one shedding half cycle; therefore the length of the plasma pulse starts to compromise vortex formation. By comparing 400 to 300 Hz interruption the effect of these two factors can be observed, with the 300 Hz interruption showing a clear reduction in the strength of the vortex street. Also it can be seen that as the time between frames increases, the acceleration of the vortex can be observed as it convects downstream and the tracking arrows have to become gently curved in order to remain aligned.

At this point we can note the correlation between a strong vortex street (800 Hz, 400 Hz interruption frequency) and a local minima in the absolute value of C_L (cf. Figure 4.39) and a week or disrupted vortex street (600 Hz) and a local maxima. This relationship is examined in detail in section 4.6.1.

Lastly, if attention is turned to Figure 4.62 we see the shedding lock-in increasingly become weaker as a greater number of frames fall out of synchronisation. However, both 200 and 150 Hz interruption do still show locked-in behaviour at periodicity 4 and 6 respectively, despite the fact the plasma-on pulse extends up to and beyond a full shedding cycle in these cases. Especially worthy of note is that in the 150 Hz interruption the two worst vortices for having a weak signal and out of place frames are those that occurred during the first 25% of the cycle (indicated with red and yellow arrows). These would have been generated during the plasma active period. This supports the hypothesis presented when discussing Figure 4.53, i.e. at 150 Hz the periodicity at the interruption frequency is produced by releasing the natural shedding response at the same point and then suppressing it again at the start of the next cycle, rather than any lock-in effect.

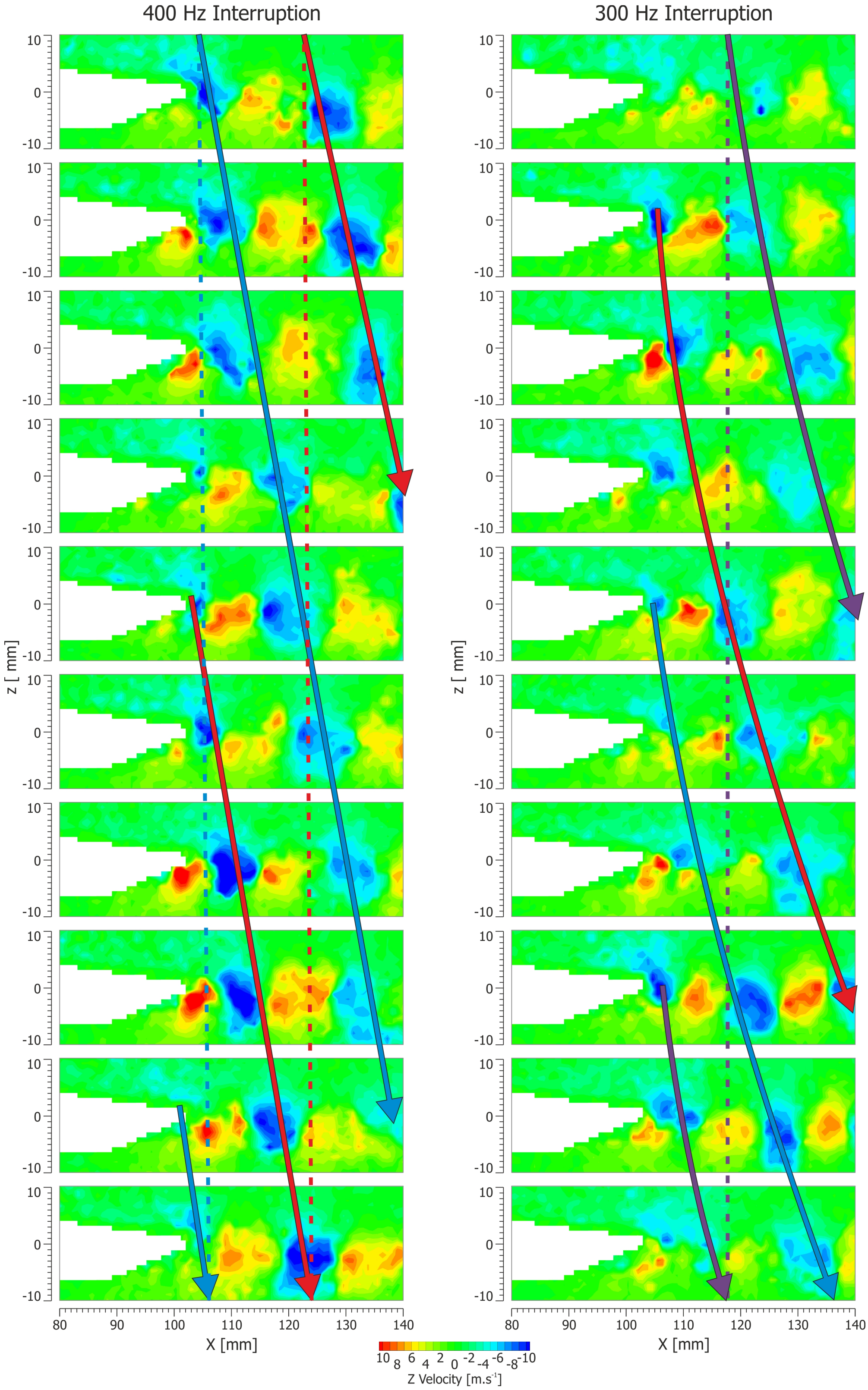

Figure 4.61 Sequential Z Axis (Vertical) Velocity Component Frames At 20 m.s^{-1}, 25% DC, 400 and 300 Hz Interruption Frequency

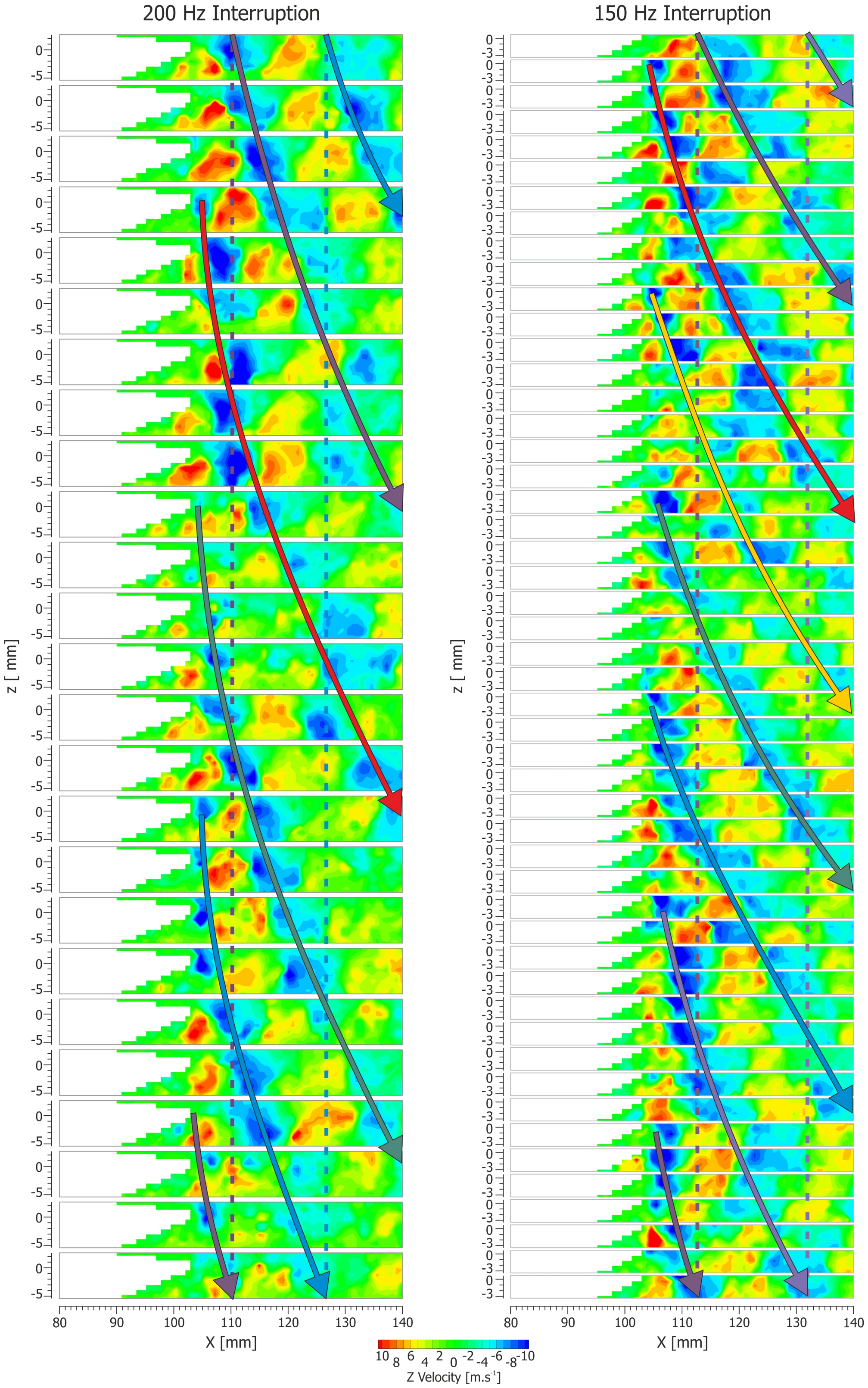

Figure 4.62 Sequential Z Axis (Vertical) Velocity Component Frames At 20 m.s^{-1}, 25% DC, 200 And 150 Hz Interruption Frequency

As was highlighted previously whilst discussing Figure 4.54, when attempting to find the best fit for a sine wave to the 20 $m.s^{-1}$, 150 Hz data there exists a conflict between the shedding behaviour seen in the frame by frame videos and the Z-axis velocity pseudo time history at the point chosen for Figure 4.53. This is complicated by both the fact that this is the noisiest of the phase-locked datasets, and also the high number of shedding cycles per plasma interruption cycle leads to a large degree of motion between frames. It was chosen to classify the flow regime as shedding with periodicity 6 which equates to forced shedding at 900 Hz despite the seemingly better fit for periodicity 5 shedding (5 x 150 = 750 Hz forced shedding) from the time history data. To justify this, firstly when we look at the time period for 1 cycle at 825 Hz this equates to 1212 μs. To fit this into a 750 Hz cycle it must operate with 10% shorter cycle period (121 μs shift), whereas at 900 Hz the cycle period is only 8.3% longer (101 μs shift) so at periodicity 6 the shedding is closer to its natural frequency. Secondly when we look at the individual frames in Figure 4.63 and try to fit both perfect periodicity 5 and periodicity 6 start points to the shedding by tracking the downwash of the vortex (blue) we see that by the 3rd and 4th start points the light blue arrows (periodicity 6) are still tracking the start of a downwash region, and the red arrows have become out of phase and are aligned with upwash regions.

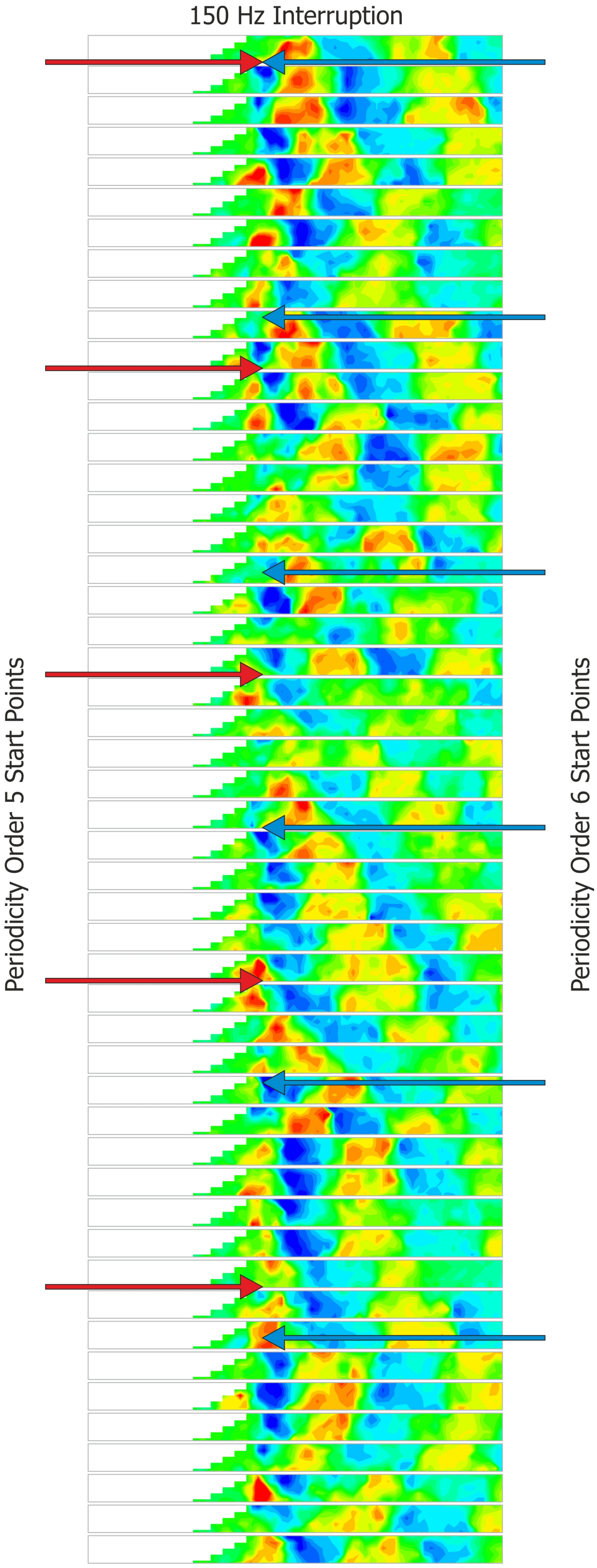

Figure 4.63 150 Hz Interruption Shedding Periodicity Clarification

Figure 4.64 (repeated for clarity, first seen as Figure 4.21) should be compared to the preceding data. It must be carefully noted that this image differs from those before it in that it is not taken from a sequence of data with a rigid unbiased spacing between frames. With the lack of any plasma input to lock the shedding to the PIV capture rate, it had to be assembled by hand from the available unsynchronised frames to form one complete shedding cycle. As such it could look artificially better than the others; however, every possible attempt was made to keep the images representative. Looking back and comparing this to the data in Figure 4.60 through Figure 4.62 we can see that when compared to interruption at 800 and 400 Hz the strength of the vortex street appears similar; however relative to all other interruption frequencies presented Figure 4.64 shows lower levels of vortex disruption and increased strength.

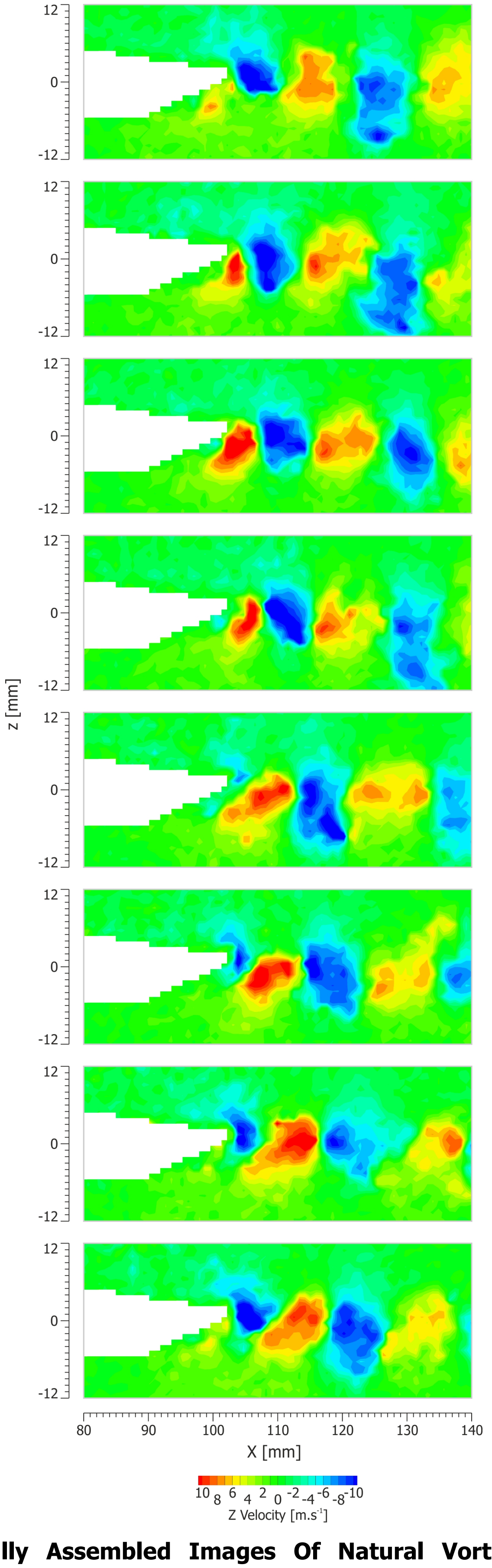

Figure 4.64 Manually Assembled Images Of Natural Vortex Shedding, (Vel. 20 m.s^{-1})

Whilst looking at the dataset for the unactuated natural vortex shedding it would be desirable to fit a sine wave to the vertical velocity data extracted from location (X,Z)=(107.18, -7.21) as was done in the pseudo time histories presented previously in Figure 4.53. Although there is no chance to recover a fit coefficient for the data we can recover the amplitude of the best fit sine wave. To do this, locked in data at 800 and 400 Hz, for which there already existed a best fit sine wave (Figure 4.53), was examined; both the experimental data and the sine wave points were taken and ordered from smallest to largest. Looking at these two plots (shown in the first two panels of Figure 4.65) we see that the experimental data (blue diamonds) contain a significant number of outlying data points; however, the middle 50% of the data (background shaded green) correlates strongly with that of the data from the fitted sine wave (red line). A ½ sine wave (light blue line) is then fitted to the data using the same iterative least squares fit but only taking account of the residuals from the central 50% of the data. The difference between the two fitted sine waves is marked on the figure. It can be seen that fitting the sine wave to the reordered data provides a good approximation of the answer that is obtained by fitting a sine wave to the data in its original order, which arises from the PIV synchronisation to the shedding. Using the same method of fitting a ½ sine wave to the ordered data from the natural shedding case we can predict the size of the sine wave that would have been fitted to the data had it been able to be recorded synchronized to the PIV system. This is shown in the final panel of Figure 4.65.

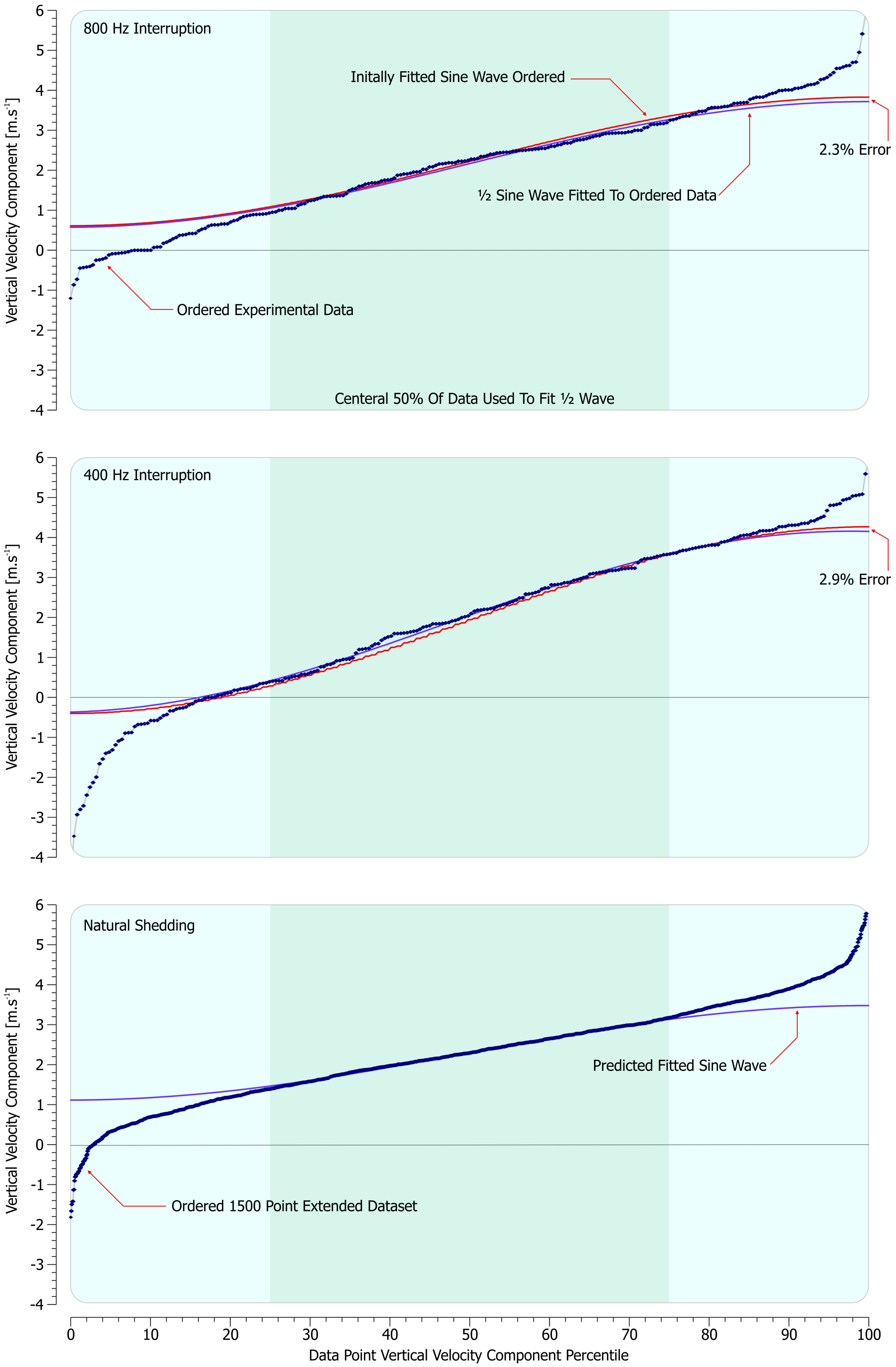

Figure 4.65 Validating The Approach To Fitting Sine Wave To Natural Shedding Data

Figure 4.66 shows the result of plotting the difference between the sine wave amplitudes at each interruption node and the resulting value of sine wave amplitude for the natural shedding data obtained from the process described in Figure 4.65. It is clear that that this measure of merit is not as well linked to the delta C_L behaviour as wake angle. However it does still show peaks in the change in amplitude of the sine wave at the 800 and 400 Hz interruption nodes, which align with the two cases where reinforcement of vortex shedding is either expected or likely to occur, and either no change or a disruption to the shedding pattern for the other cases.

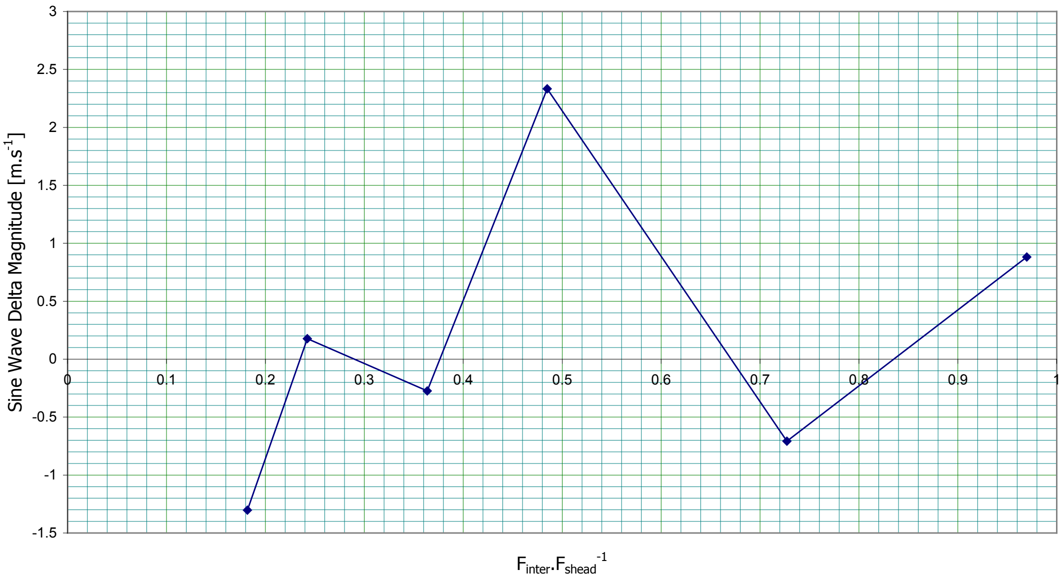

Figure 4.66 Amplitude Of Best Fit Sine Waves At 20 m.s^{-1}

4.5.3.2.2 Low Speed, 3.6 m.s^{-1} Dataset

Figure 4.67 and Figure 4.68 show the pseudo time histories for the low speed datasets. As with the high speed data, the higher frequency interruption traces have been repeated to pad each plot to the same total time. From part 1 (Figure 4.67) the pattern that should be evident is the decay of the sinusoidal signal as the actuation interruption point moves further from the expected natural shedding frequency of 149 Hz. Part 2 (Figure 4.68) shows that once it decays to a near zero vortex shedding point a steady state is reached, and reaching the 1st harmonic of the fundamental does not cause an increase in actuation effect.

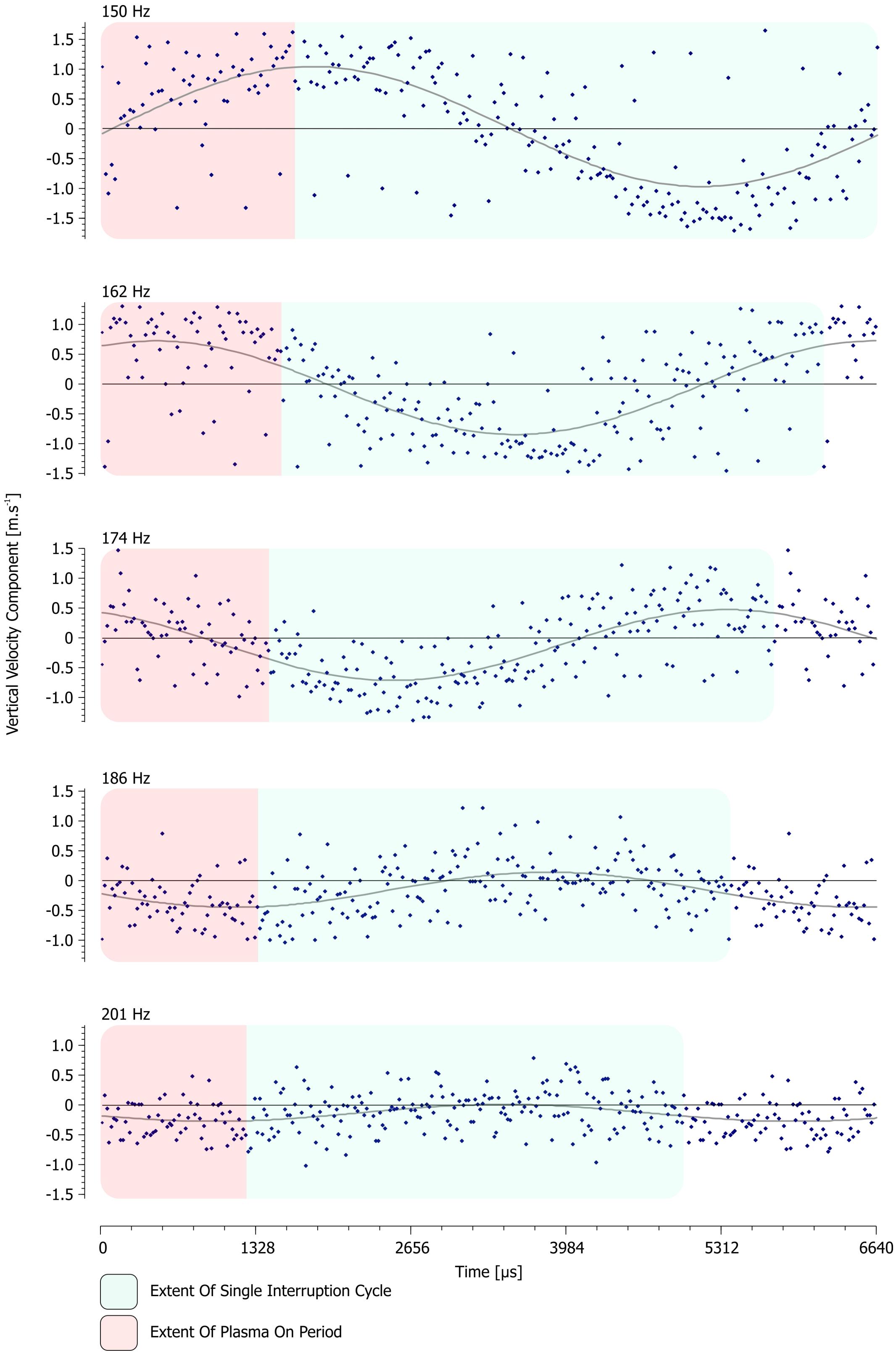

Figure 4.67 3.6 m.s^{-1} Vertical Velocity Pseudo Time History Part 1, (CF 4 kHz, DC 25%)

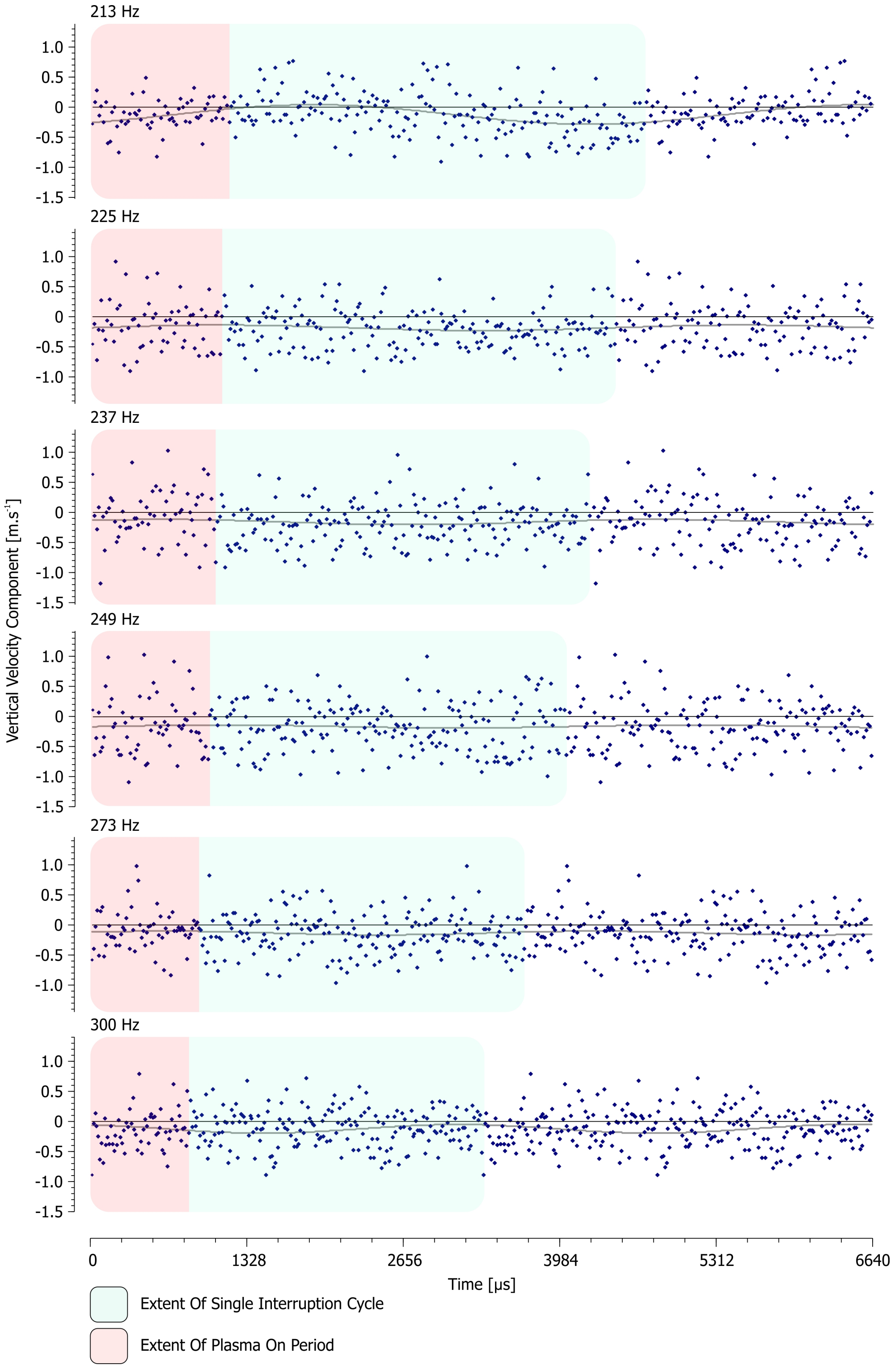

Figure 4.68 3.6 m.s^{-1} Vertical Velocity Pseudo Time History Part 2, (CF 4 kHz, DC 25%)

Taking a look at the fit coefficient for this data, the pattern from the previous two figures is borne out, confirming that from 1.5 times the natural frequency and upwards there is no discernable pattern to the data.

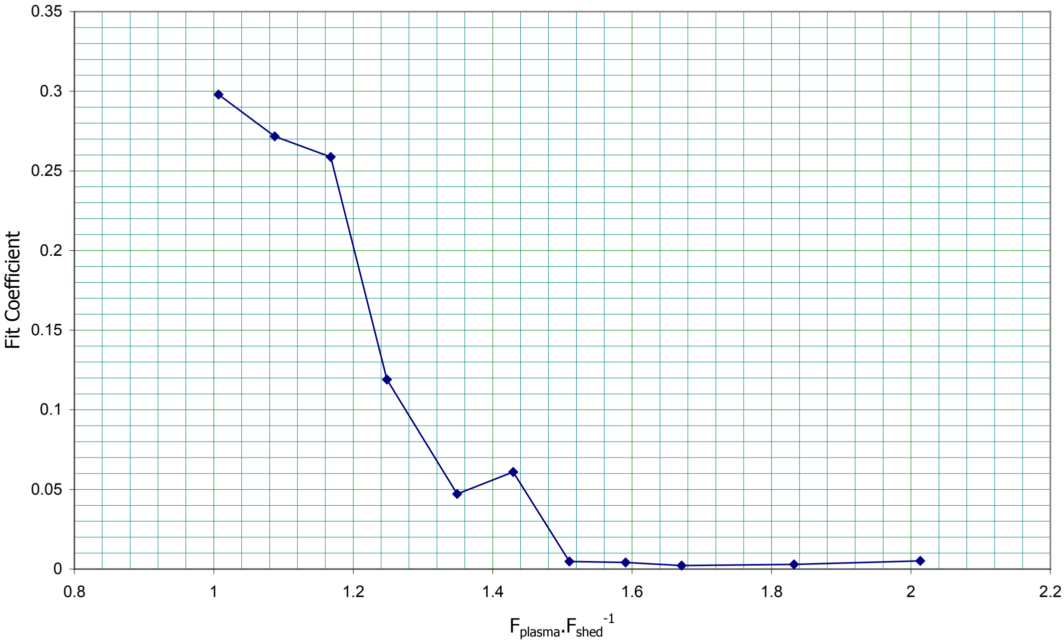

Figure 4.69 Sine Wave Fit Coefficient Data For 3.6 m.s^{-1} Data

Figure 4.70 shows selected streamtraces with isochronal markers from selected points in the low speed dataset. This is unlike the high speed 20 m.s^{-1} dataset, where the changes in the streamtraces were quite small. The increased actuation authority over the lower speed flow allows the progression of the flow from locked-in to not being observed. It is interesting to note the actuation effect of the cases where the flow is not locked-in is not equal to the control, despite showing zero resonant effect. This shows how plasma actuated separation steps, which do not force at the natural frequency or force continuously can still achieve a control effect. It also highlights the significant improvements that can be made by correctly choosing the interruption frequency.

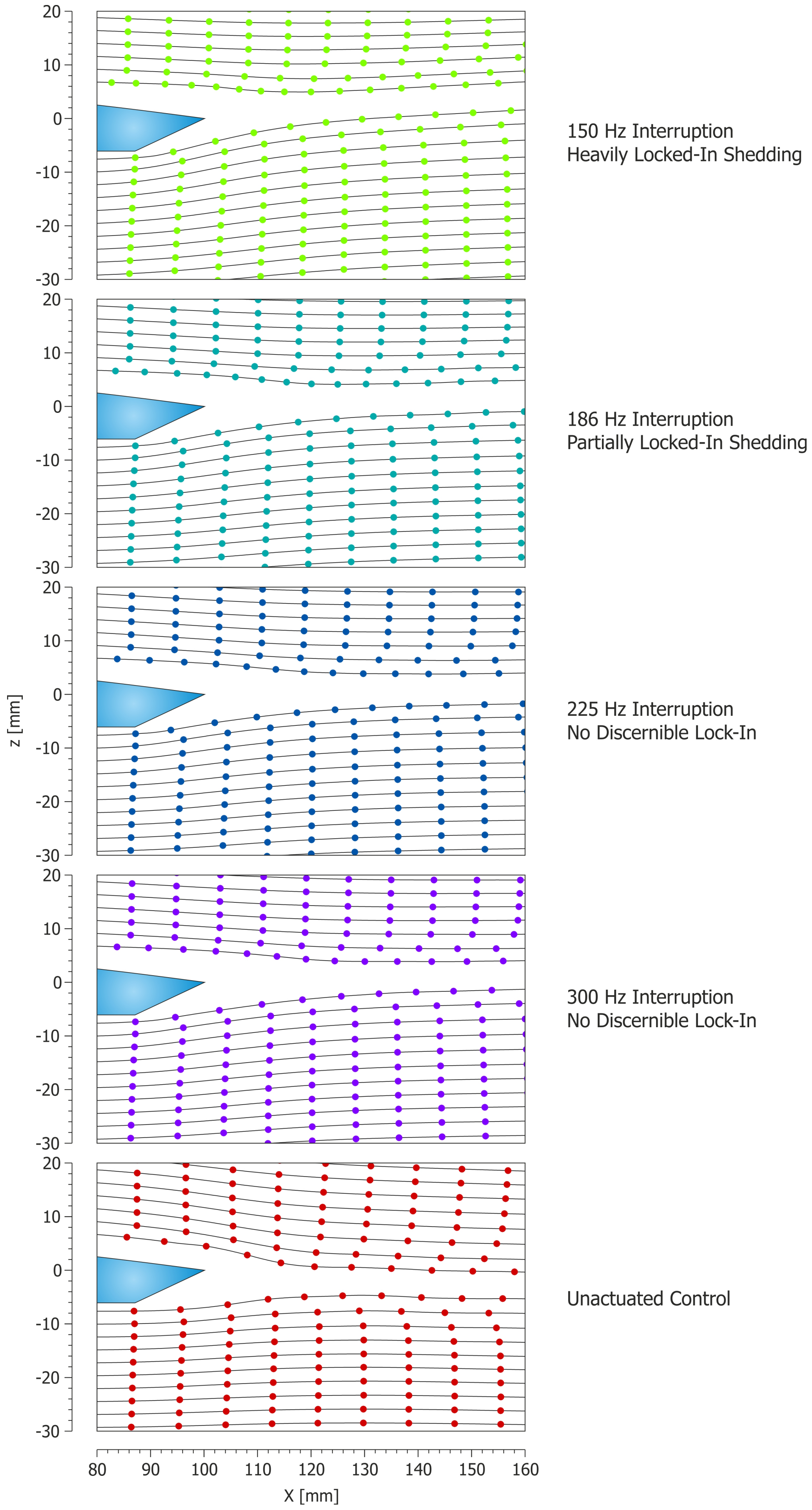

Figure 4.70 Streamtraces At 3.6 m.s^{-1} With Varying Interruption

Figure 4.71 shows quantitatively what can be seen qualitatively in Figure 4.70, again using the integration region illustrated in Figure 4.58. Unlike the 20 m.s^{-1} data where the destruction of the vortex street resulted in the flow separating more effectively at the step compared to the control, the wake angle deviations for the 3.6 m.s^{-1} data all show positive wake angle deviations (i.e. increased upwash). This is probably because the DBD jet velocity is around 10% of the free stream in this case, and this in itself can create significant upwash in the wake even without having to rely on altering the vortex structure to amplify its input into a larger aerodynamic effect.

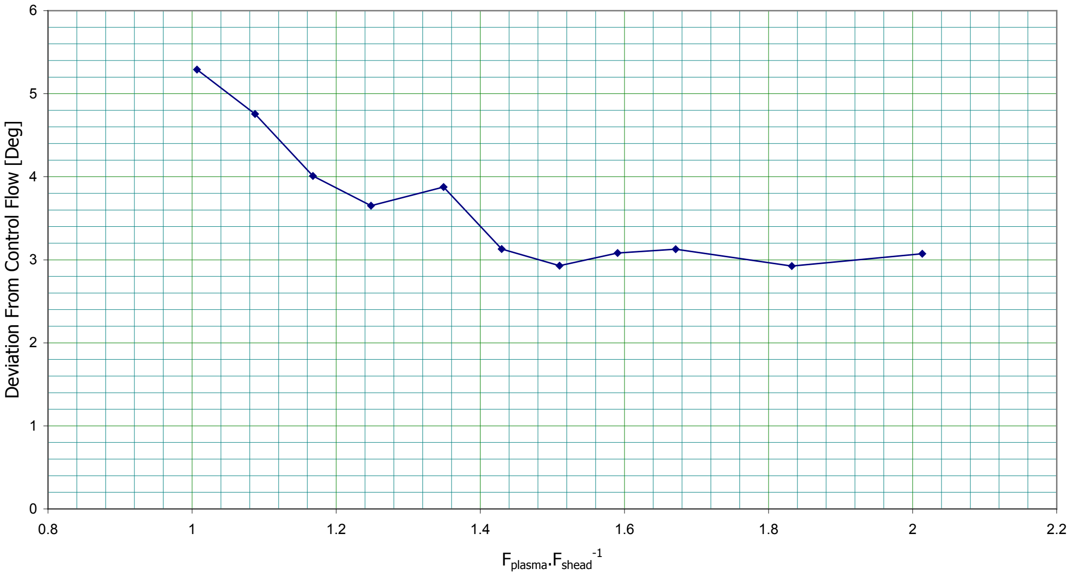

Figure 4.71 Wake Flow Angle Deviations From Control At 3.6 m.s^{-1}

Figure 4.72 backs up the observations seen in Figure 4.71. It shows that while a large difference in the time-averaged flow can be seen between 150 Hz and 300 Hz interruption, with the former having a significantly higher upwash wake structure than the latter, once the vortex street has been disrupted by moving the forcing frequency to around 1.4 times the natural frequency, no further change in the flow is seen as the frequency is increased further. The red dot on the step is an artefact of non-overlapping exclusion zones: this was introduced because the specific PIV software used did not allow storage and recall of a standardised set exclusion zone coordinates. This meant each batch of images had to have the exclusion zone defined by selecting the area manually and therefore it could differ between runs.

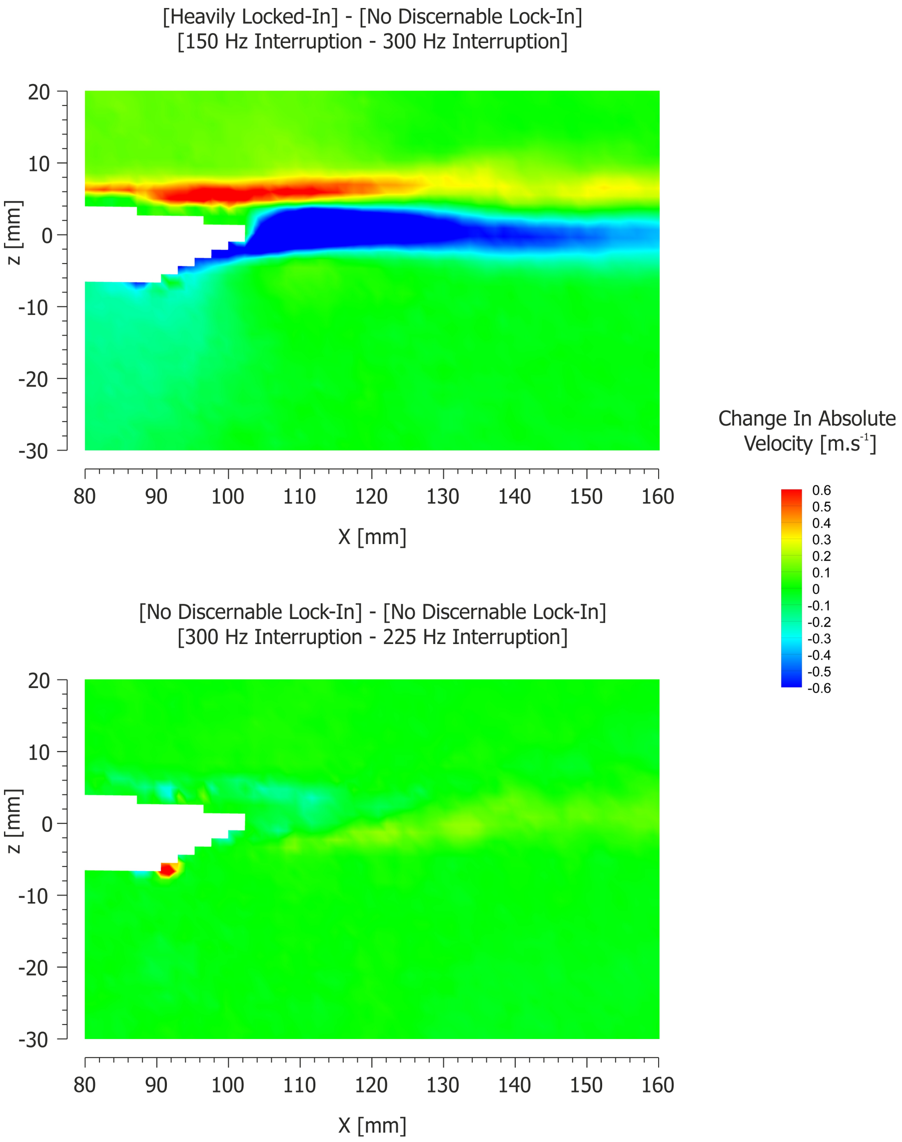

Figure 4.72 Time-Averaged Flow Field Change Between Actuated Cases (CF 4kHz, DC 25%, Vel. 3.6 m.s^{-1})

Figure 4.73 shows the pseudo time evolution of the vortex street rolling off the back of the aerofoil. The key point to note is the clearly defined regular vortex shedding when forced at its natural frequency, and then to compare this to the almost complete destruction of the vortex street by the off-frequency forcing in the 300 Hz interruption scenario. Figure 4.74 plots the same datasets but using the computed variable vorticity around the y-axis, instead of z-axis velocity component; this shows an even clearer picture of the almost total suppression of regular vortex formation under the higher frequency interruption.

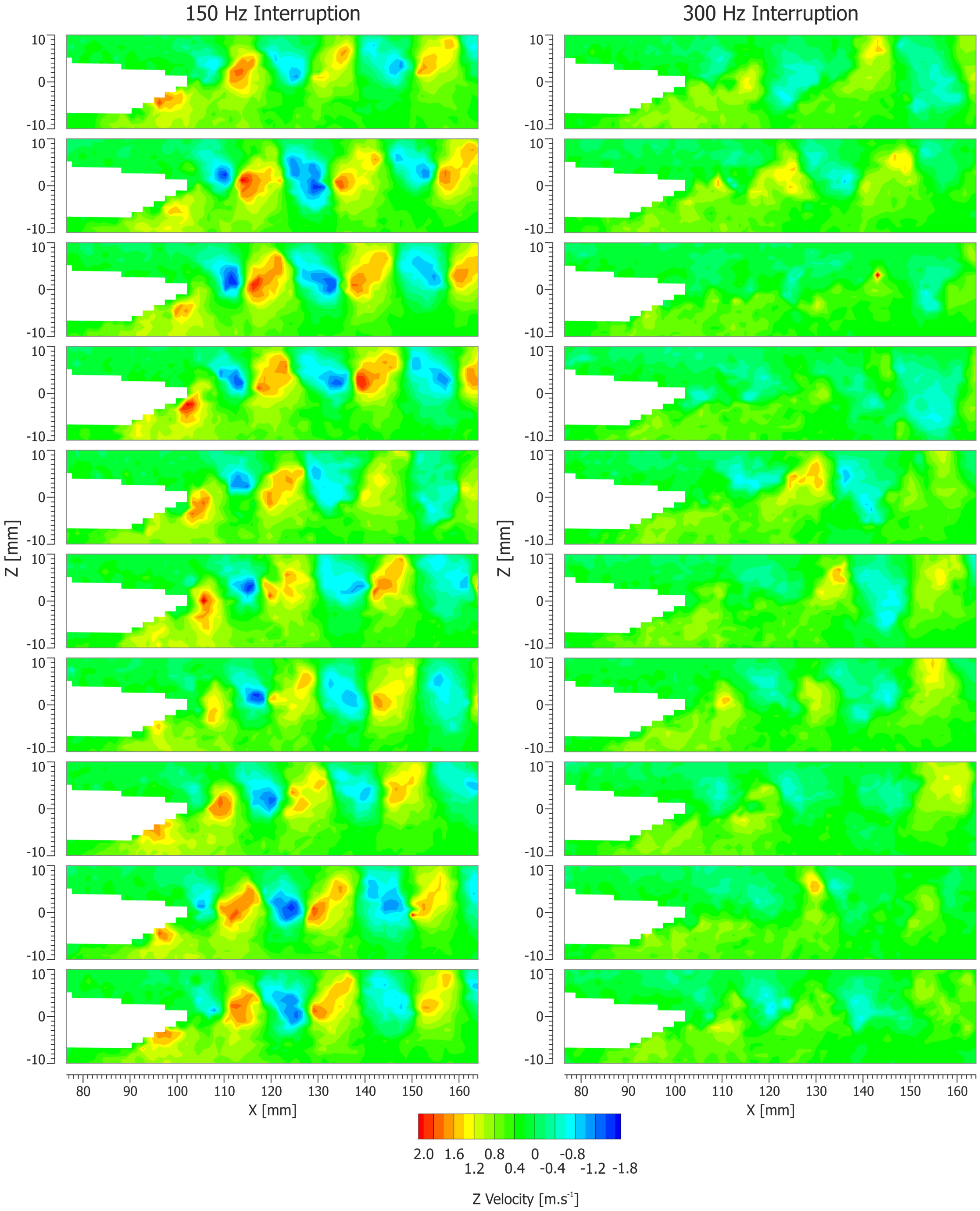

Figure 4.73 Breakdown Of Vortex Shedding By Off Frequency Forcing (Z-Axis Velocity Component) (CF 4kHz, DC 25%, Vel. 3.6 m.s^{-1})

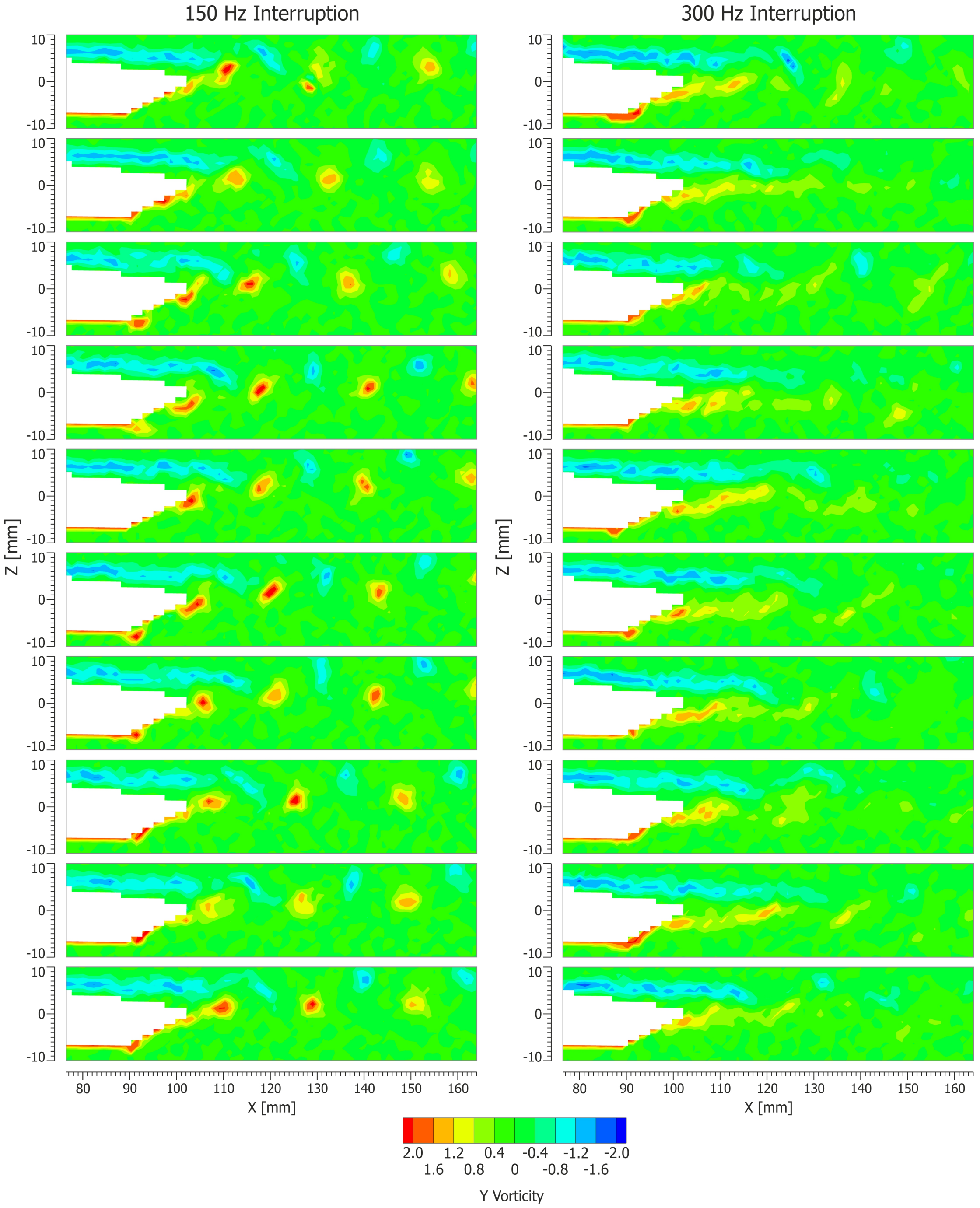

Figure 4.74 Breakdown Of Vortex Shedding By Off Frequency Forcing (Y-Axis Vorticity) (CF 4kHz, DC 25%, Vel. 3.6 m.s^{-1})

To assess both the uniformity of the flow through the wind tunnel and the ability of the PIV system to capture this without distortion, a data set was taken at 3.6 m.s^{-1} without the wing in the tunnel. Without any flow disturbance in the field of view and with the interrogation zone well away from any boundary layer effects caused by the tunnel walls, it could be expected that the returned vector field would be of entirely uniform absolute velocity which contained no component along the z axis. This, however, is not quite the case, as is seen in

Figure 4.75 where both variation in absolute velocity (panel A) and non-zero z axis velocity components (panel B) are seen. These arise from lens distortions, that cannot be corrected for using the simple 4 point calibration that was applied, along with the minor inaccuracies associated with positioning (in the real world) and marking (in software) the centres of the calibration targets; together they give rise to a total error of the order of 0.1 $m.s^{-1}$.

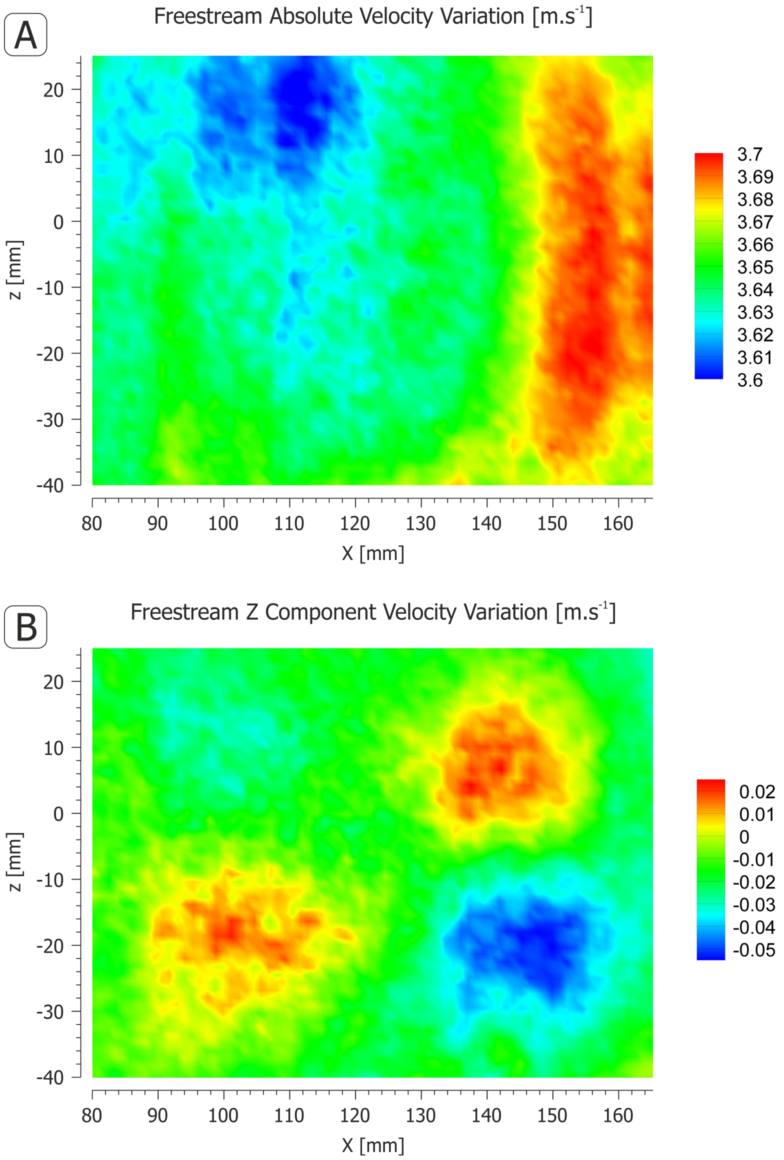

Figure 4.75 Uniformity Of PIV Measurement Across The Flow Field

Figure 4.76 shows the repeatability of a series of three control (unactuated) vector fields each consisting of ≈250 averaged image pairs. Looking at the deltas it can be seen that the general repeatability in the wake is approximately ±0.15 $m.s^{-1}$, and next to the airfoil surface the repeatability is worse due to inaccuracies induced by the edges of the exclusion zones. There is almost complete agreement between control datasets 1 and 3 as the centre image is blanked to an almost uniform green representing zero change. The other 2 images show that there is a slight vortex shedding scheme present in the averaged data from dataset 2. This is possible in the control datasets because the sampling is not locked into the vortex shedding, and as such it is not guaranteed that samples will be taken from an evenly distributed set of points over the shedding cycle and could randomly favour collecting data over a small part of the cycle, and so the vortices will not average out. Figure 4.77 shows the absolute values for Dataset 2; without subtracting the other datasets there is no obvious distortion and it can be seen that the effect of unintentional sample bias is small.

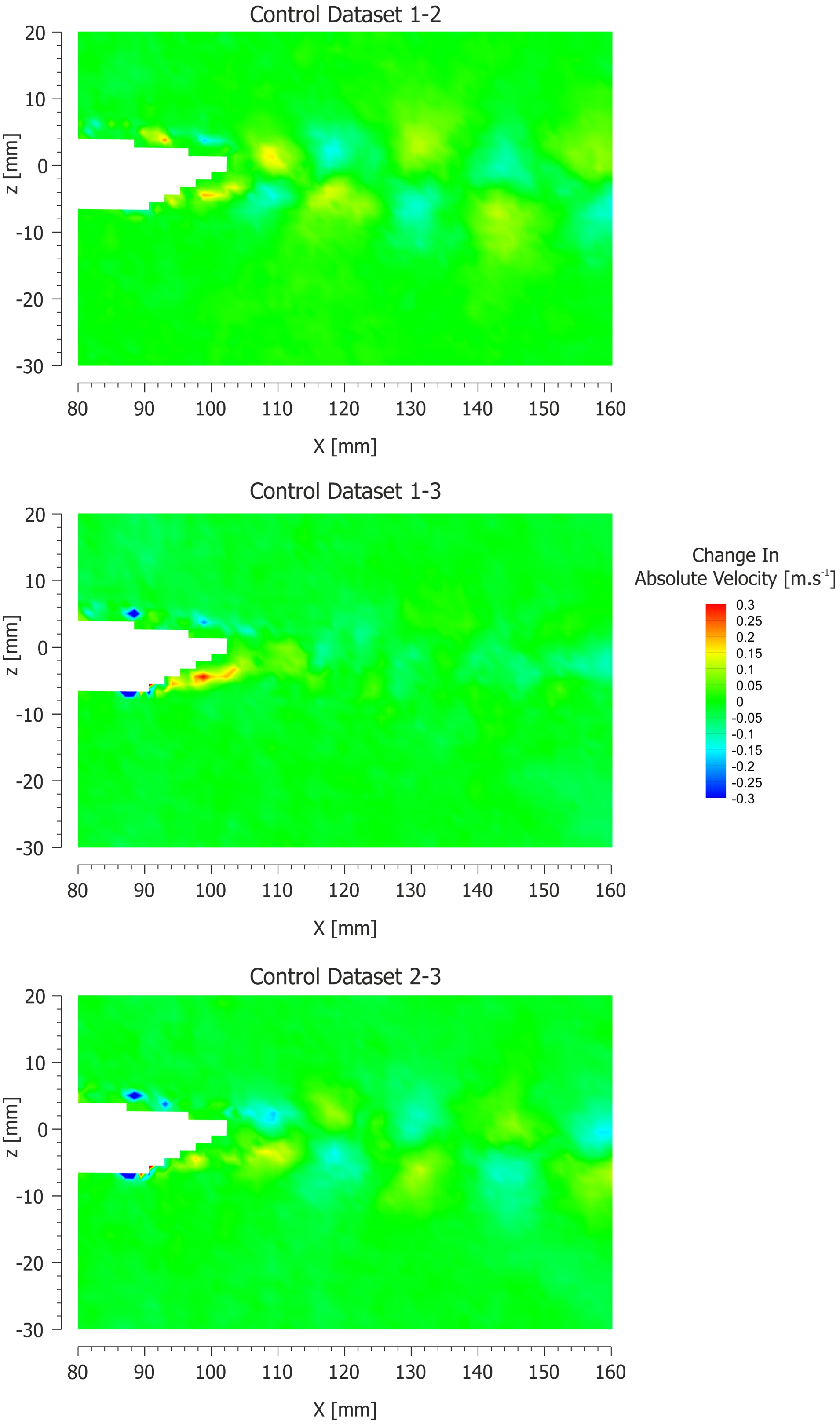

Figure 4.76 Variations Between Control Sets

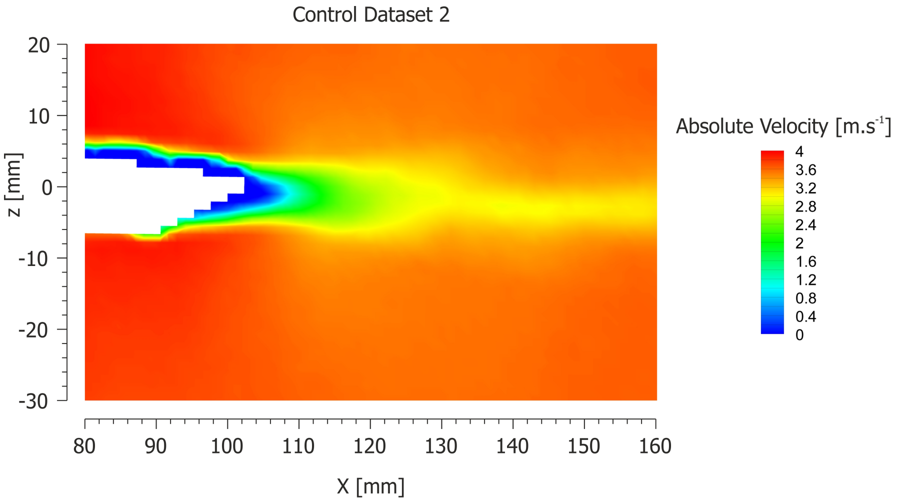

Figure 4.77 Control Data Set Absolute Values

4.5.3.2.3 Synchronised PIV Data At Incidence

Having demonstrated the effect of varying interruption frequency at zero incidence with the main traunch of PIV data, it was appropriate to investigate how the observed behaviour could be modified by varying the flow conditions.

Figure 4.78 and Figure 4.79 show locked-in images of vortex shedding at 4 and 8 degrees incidence. The aim of these images is to show the importance of maintaining the correct interruption frequency based not only on velocity but also on incidence, and to back up the findings in the results shown in the force balance data displayed in Figure 4.46. This figure showed that as the incidence increased, there was a decrease in the interruption frequency which caused the maximum effect on C_L during actuation. The left hand column features images taken with the interruption frequency which corresponds to the maximum delta C_L from the force balance results Figure 4.46 (or the nearest node at which PIV lock in could be achieved), whereas the right hand column contains data which corresponds to 800 Hz interruption, which produces maximum positive reinforcement of the vortex street at zero incidence. Both figures show increased disruption and a degradation in the strength of the vortex street when comparing the results from the interruption frequency which achieved the largest delta C_L in the force measurements to 800 Hz interruption. At 4^o this effect is small, and when looking at the image sequences is probably not immediately obvious; however, at 8^o, where the frequency shift is larger, the effect is much clearer. The general shift in hue is due to the use of the same common colouring scale to aid cross comparison; however, as the incidence angle is increased, this naturally induces greater down wash in the wake. This will bias the image colouring towards the blue end of the spectrum and the up-wash regions of the vortex street will become less prominent; this should be taken into account when comparing across incidences.

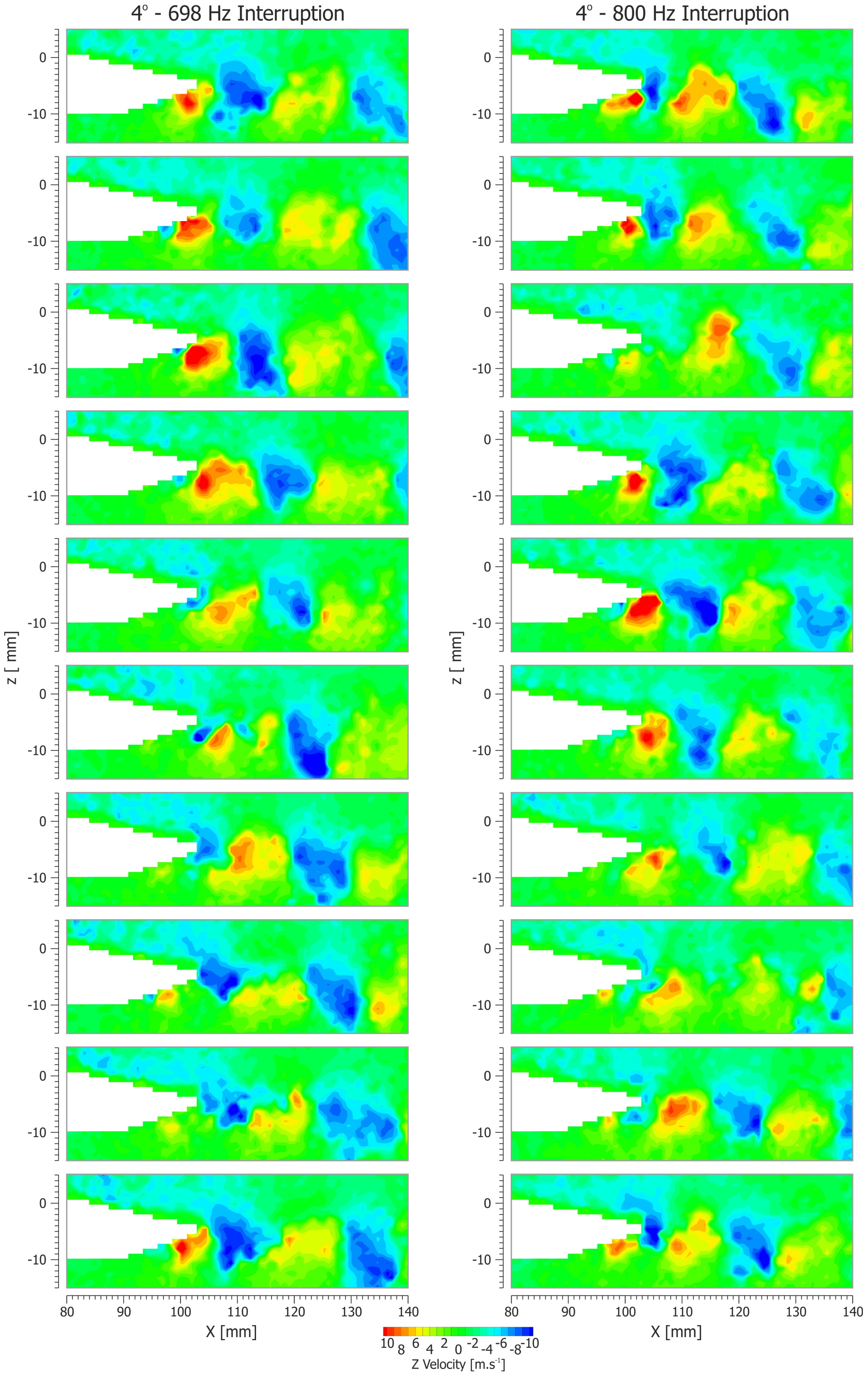

Figure 4.78 Synchronised Sequential Z Axis (Vertical) Velocity Component Frames At 20 m.s^{-1} And 4° Incidence

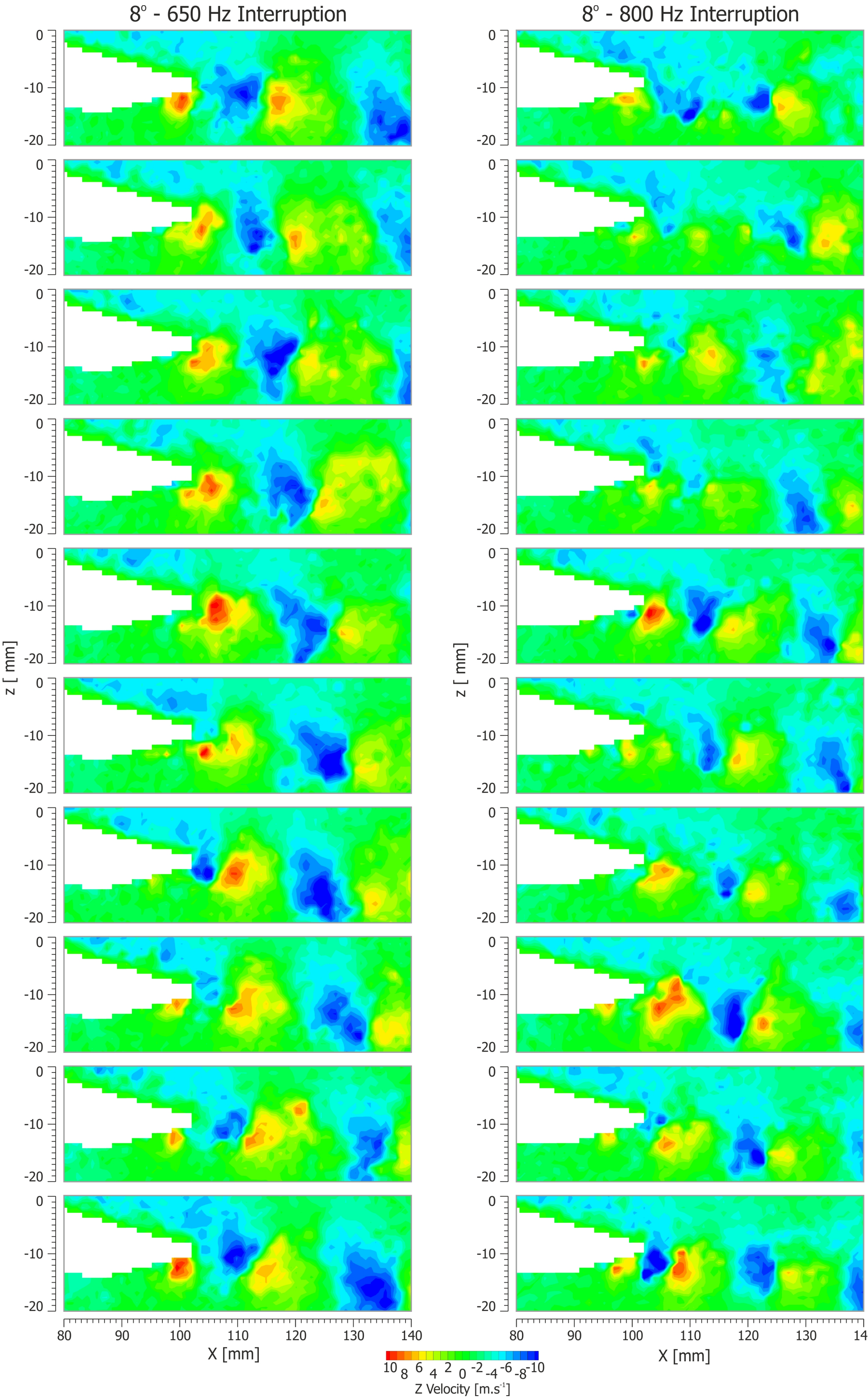

Figure 4.79 Synchronised Sequential Z Axis (Vertical) Velocity Component Frames At 20 m.s^{-1} And 8^{o} Incidence

Figure 4.80 shows the deviation of the wake angle from the control case to the actuated case for the two datasets at 4 and 8 degrees incidence. The red columns represent the 800 Hz forcing and the blue column shows the deviation achieved at the point of maximum C_L actuation. This confirms that, as would be expected from the force data, the flow is turned more when actuated at the point of maximum delta C_L. This also lends weight to the argument that the slight degradation in the vortex street at 4°, 800 Hz is a real effect and not an artefact introduced by the choice of displayed frames distorting the picture through the low number of sample points.

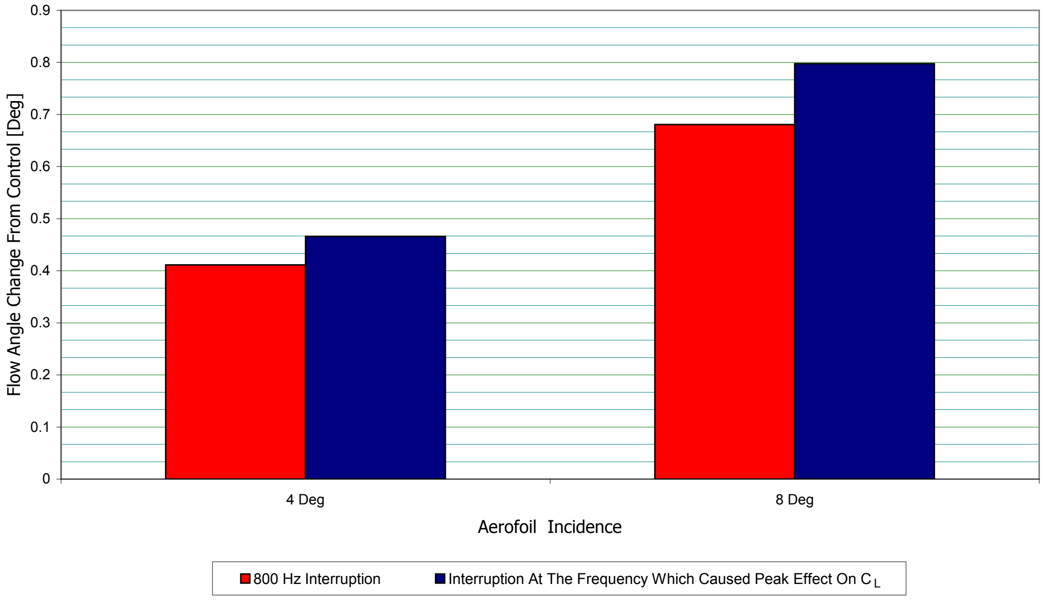

Figure 4.80 Flow Angle Deviations For Incidence Data

4.5.3.2.4 Synchronised Velocity Sweep PIV Data

A velocity sweep was compiled with data collected at 20, 10, 8, 7, and 3.6 $m.s^{-1}$ all with a 4 kHz carrier wave interrupted at 200 Hz with a 25% duty cycle. At these velocities we should see shedding of periodicity 4 and 2 at the 20 and 10 $m.s^{-1}$ points respectively. The next periodicity node change should occur at 5 $m.s^{-1}$; as such it was hoped to see an intermediate transitional behaviour with a broken down vortex street somewhere in the 7-8 $m.s^{-1}$ range. It is notable however that, as can be seen in Figure 4.81, the shedding maintains a low noise well locked-in sinusoid in both these cases, having already transitioned to a one to one shedding to interruption cycle ratio by the time the velocity is reduced to 8 $m.s^{-1}$. As all these datasets were collected at 200 Hz interruption, the time period which they span is the same, and so no padding or repartition was necessary to produce this figure.

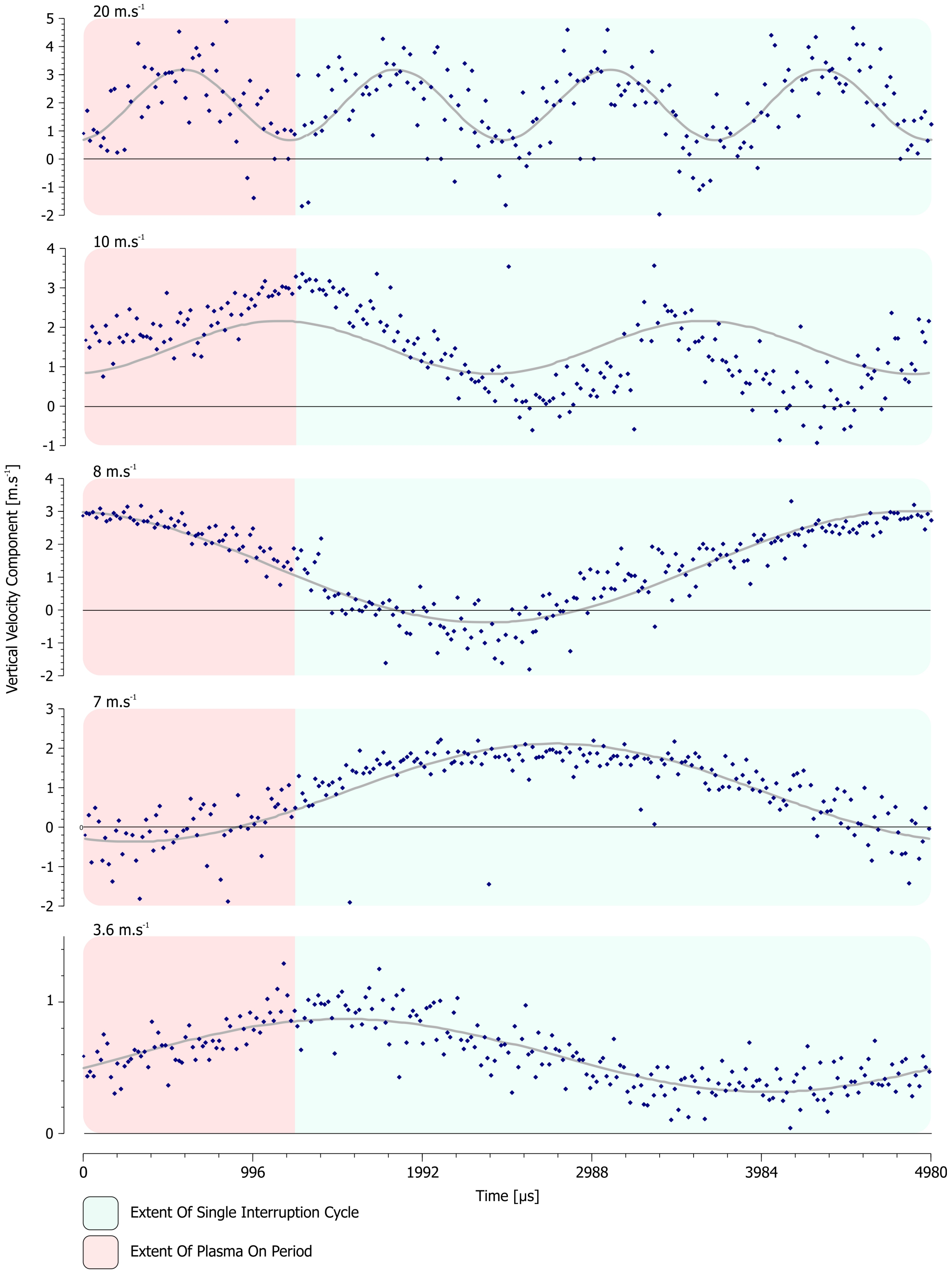

Figure 4.81 Freestream Velocity Sweep Vertical Velocity Pseudo Time History (CF 4 kHz, DC 25%, IF 200 Hz)

One of the most striking features of Figure 4.81 is the exceptionally poor fit for the 10 m.s^{-1} data. Figure 4.82 shows how the first 125 frames almost perfectly fit a single shedding wave over the full interruption cycle (red trace); however, the period of the second half of the data is a good fit for a periodicity three vortex shedding regimen (orange trace). Looking at the sequential PIV frames (Figure 4.85), as would be expected from the natural shedding frequency, the 10 m.s^{-1} flow sheds twice per cycle and shows no signs of varying between two shedding regimen; this is why the periodicity 2 waveform is fitted to the data. Figure 4.83 shows a pseudo time history from a different point in the 10 m.s^{-1} wake which displays sinusoidal periodicity 2 shedding confirming what is seen in the sequential PIV frames. However, this point is not consistent with the other data sets sample location and it would not be good practice to directly substitute it for comparison into Figure 4.81.

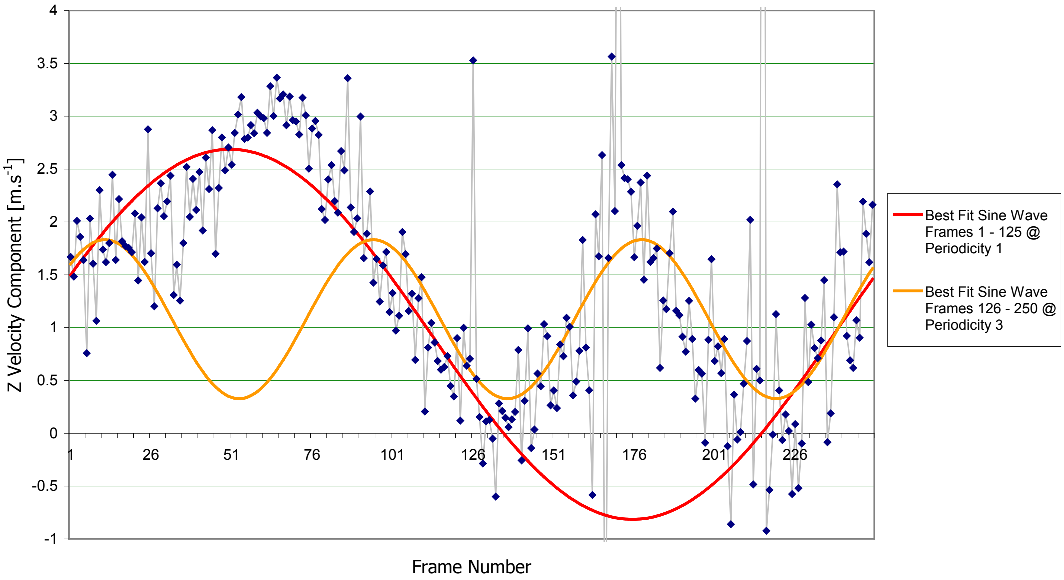

Figure 4.82 Anomalous Behaviour Of The 10 m.s^{-1} Data Point

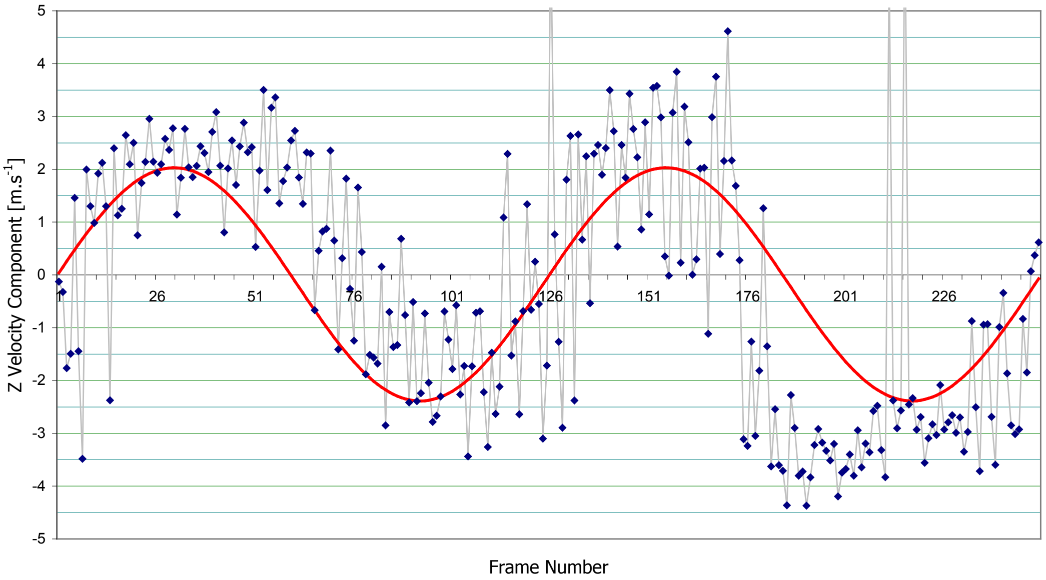

Figure 4.83 Alternative Data Point Within 10 m.s-1 dataset Showing Correct Shedding Sequence at point (X,Z) = (144.16, -0.24) mm

Figure 4.84 and Figure 4.85 show the composited shedding sequences from the velocity sweep data. In order to maintain consistency across this dataset with respect to contour colouring, whilst still maintaining visible vortices at both extremes of test velocity, the z-axis velocity data is normalised by the freestream velocity to give values for $U_z.U_\infty^{-1}$ in the range ±0.5.

Figure 4.84 shows the 7 and 8 m.s^{-1} data, where, as was explained before, the progression from periodicity 2 to periodicity 1 shedding was expected to occur, as the natural vortex shedding frequency decreased with velocity and the interruption frequency remained constant. This figure confirms what was shown previously in Figure 4.81, that the whole flow is strongly locked into a single vortex shedding pattern. There is no sign of a breakup or transition similar to that seen in the 20 m.s^{-1} tests, when the ratio of natural vortex shedding frequency to interruption frequency was altered by changing the plasma interruption frequency to 600 Hz (see Figure 4.60 for reference). Also visible is the increase in speed of downstream convection of the vortices at the higher flow velocity.

Figure 4.85 shows the frames from 10 and 20 m.s^{-1} free stream velocities, the latter of which has already been presented earlier in the chapter. The 10 m.s^{-1} data shows that the flow is definitely shedding with periodicity 2 as was discussed in relation to Figure 4.82. The roughly equally spaced start points for the two vortices show that vortex initiation was not the cause of the anomalous result; however, it can be seen that one of the two vortices formed is far weaker than the other which could have caused the irregularity in the graph. Unfortunately this was the only time this behaviour was witnessed. The explanation offered is that at this tunnel speed the ratio of DBD jet energy to free stream energy has risen by a factor of 4 when compared to the 20 m.s^{-1} case, and as such the flow field should be more susceptible to influence by the actuation. However, the flow is shedding twice per cycle; this means that there is one vortex is being actuated upon by the DBD jet (with much greater actuation authority over the flow than the >1 periodicity results at 20 m.s^{-1}) and one that is not. This is producing the asymmetry by suppressing the downwash of the vortex shed from the step during the plasma active cycle (indicated with the red arrow). At 20 m.s^{-1}, when some of the vortices are being influenced by the actuator and some are not, the difference between the two is not noticeable. This is because the overall effect of the jet on an individual vortex is small at this speed. Equally, this effect is not present in the 3.6 m.s^{-1} data as there is never a vortex which is not being actuated upon.

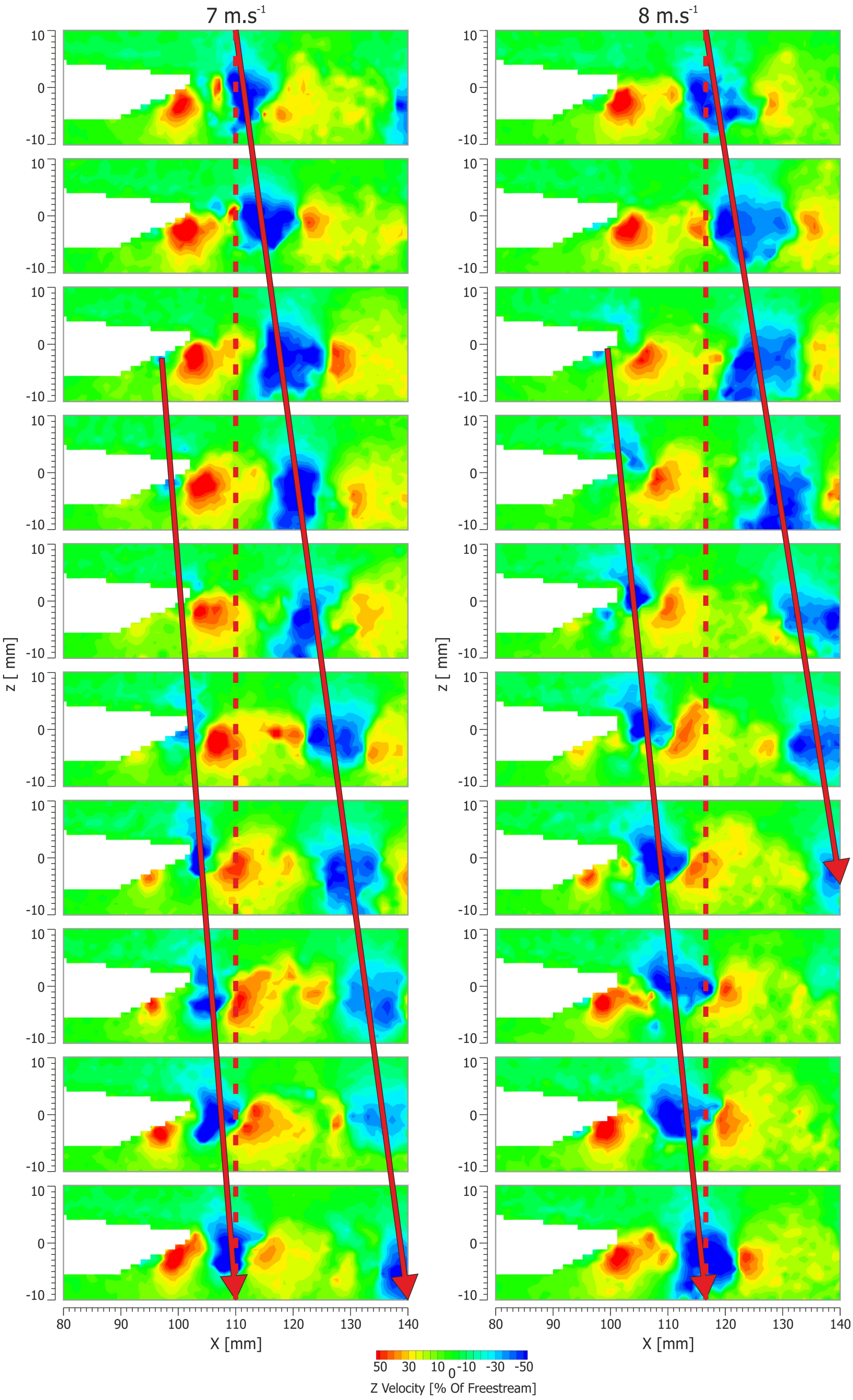

Figure 4.84 Sequential Z Axis (Vertical) Velocity Component Frames At 7 and 8 m.s^{-1} And 200 Hz Interruption Frequency

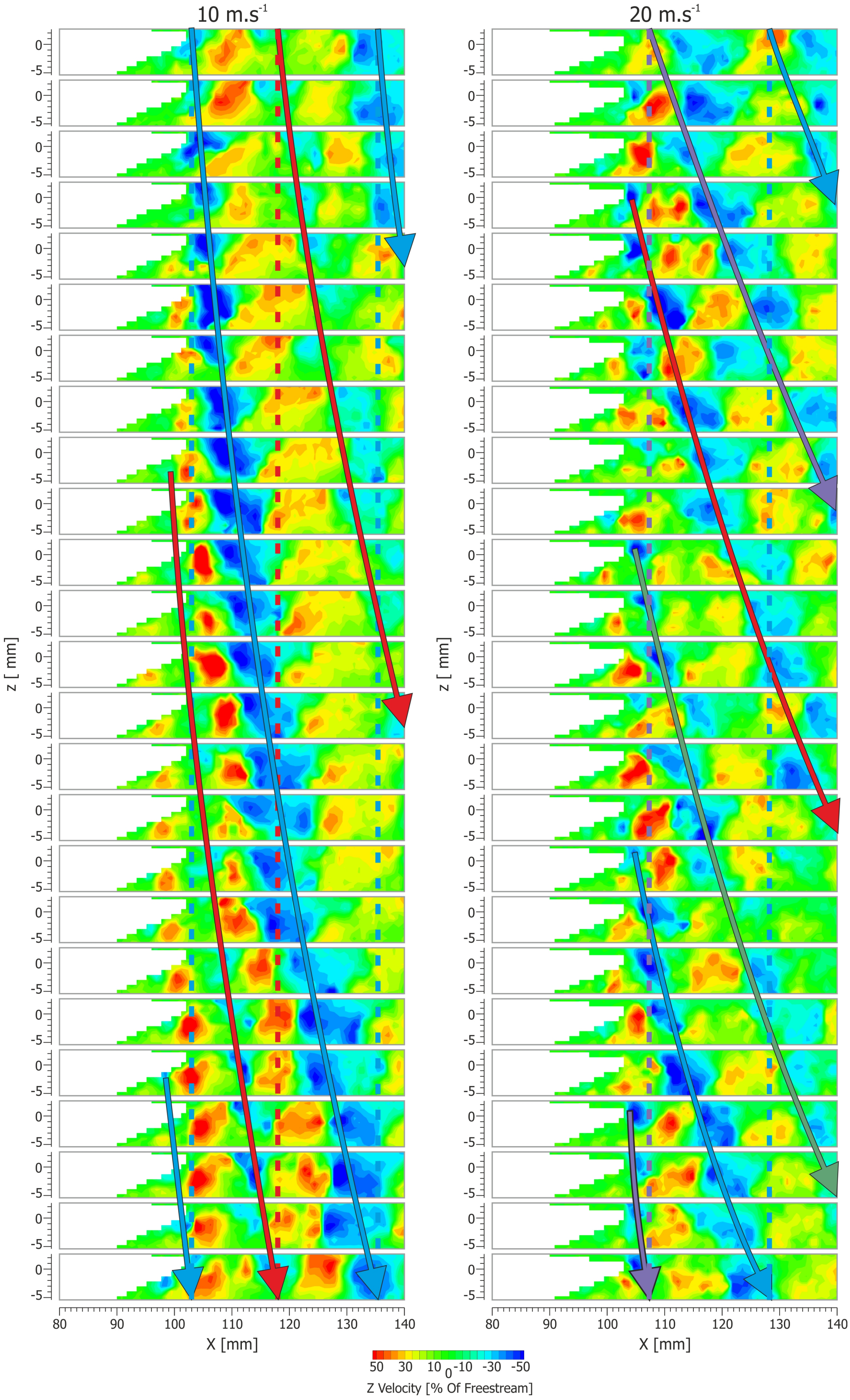

Figure 4.85 Sequential Z Axis (Vertical) Velocity Component Frames At 10 and 20 m.s^{-1} And 200 Hz Interruption Frequency

4.6 Comparisons, Discussion And Overview

4.6.1 Bi-directional Actuation With Interruption Change

Figure 4.86 illustrates the correlations seen between data from the force balance and both time averaged and instantaneous PIV data. This lets us build up a picture of how the actuator is operating. The mechanism appears to be very much tied into modifying the vortex street as is seen in the phase locked PIV data. When exposed to a 20 $m.s^{-1}$, zero incidence airflow and actuated at 800 Hz interruption frequency with a 25% duty cycle, the forcing is close enough to the natural frequency with a sufficiently short pulse length that the excitation actually increases the strength of the vortex street. This is accompanied by a reduction in lift and an increase in the time averaged vertical velocity component in the wake (upwash) this evidenced by both blue and red lines being below the control value at 800 Hz in Figure 4.86.

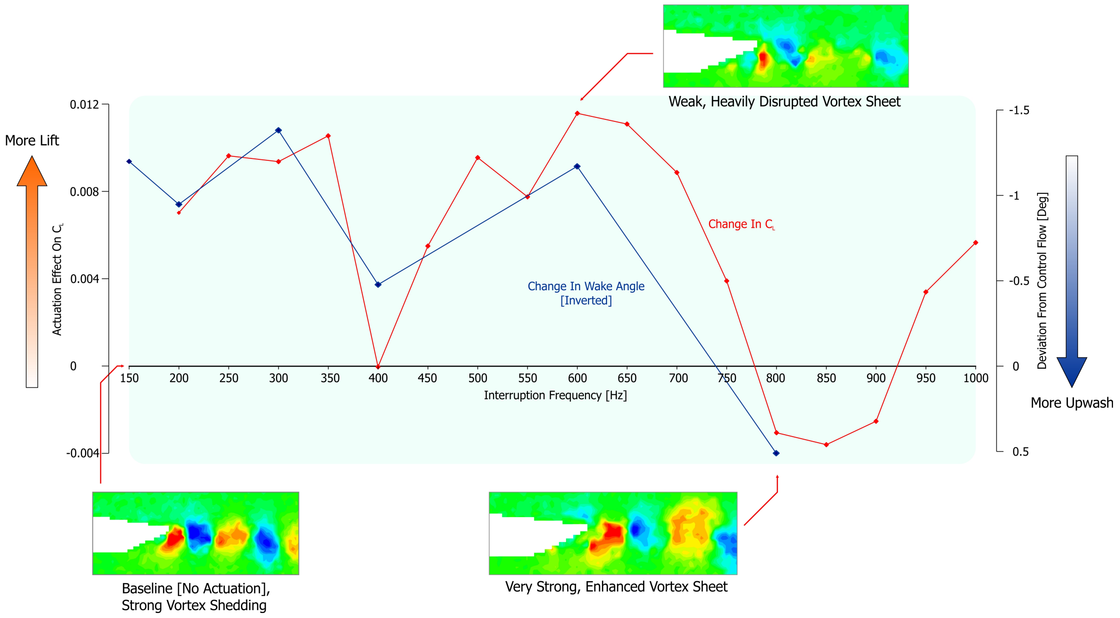

Figure 4.86 Summary Of Correlations Seen Between Datasets

As the interruption frequency is reduced towards 600 Hz the plasma pulses start to hinder the formation of the vortex street by forcing the vortex shedding to occur further and further away from its natural frequency. Once the interruption frequency reaches 600 Hz the pulsing is occurring every 1.5 natural shedding cycles and the shedding can no longer force itself to conform to this regimen. Because of this, the shedding becomes chaotic and the strength of the vortex street is reduced. This reduction modifies the way the flow follows the step; the degree of turning which occurs to the flow as it goes over the step is reduced. This is accompanied by a reduction in lift, evidence of this is seen in the correlation between the wake angle (Figure 4.59) and the force data (Figure 4.39) combined with the phase locked PIV images (Figure 4.60 through Figure 4.62).

Figure 4.87 shows how this change in lift is occurring, firstly in a similar manor to that which Liebeck suggested for the operation of Gurney flaps in [157] it appears that the aerofoil functions with a virtual trailing edge, violating the Kutta condition at the physical trailing edge of the aerofoil and exhibiting off surface pressure recovery. This is supported by the fact that at zero incidence we see positive lift (cf. Figure 4.10) from the aerofoil despite it featuring negative camber, see Figure 4.88, and also in the recirculation bubble and streamlines present in the time averaged PIV results shown in Figure 4.57, sections of these are repeated in Figure 4.87 for clarity.

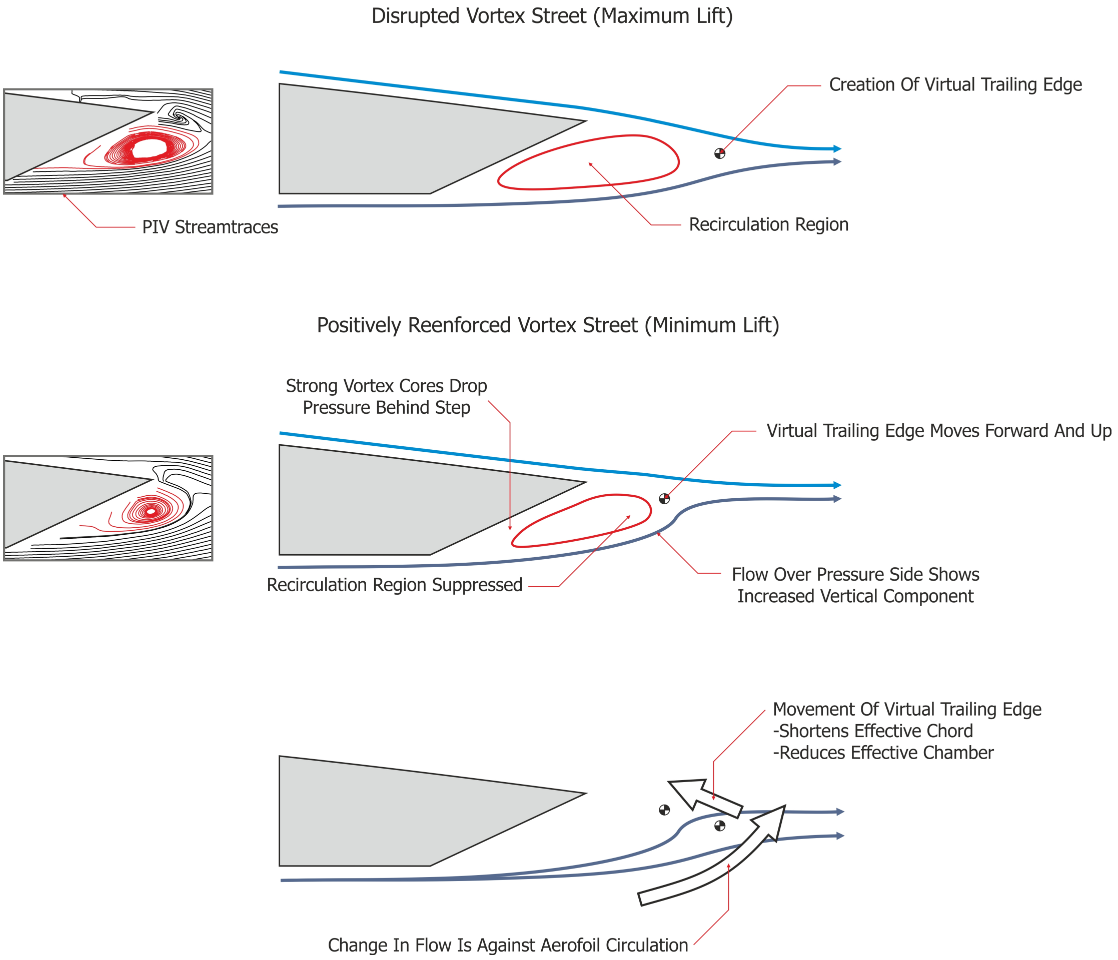

Figure 4.87 Proposed Method Of Operation

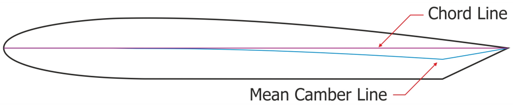

Figure 4.88 Mean Camber Line

Diagrammatically represented alongside the PIV results in Figure 4.57 is the explanation for how this effects the lift in the manor seen. From the discussion on Figure 4.86 when considering the case with a highly disrupted vortex street (600 Hz) we expect increased lit and reduced turning of the flow at the trailing edge, in this case we see a large recirculation bubble with little turning of the pressure side flow and a virtual trailing edge formed significantly below the chord line. Comparing this to the case whit he positively reinforced vortex shedding (800 Hz) we see a reduced bubble with the increased vertically directed turning in the flow on both the pressure and suction side, which is constant with the results shown hereinbefore. The reduction of this bubble by the modification of the vortex street has the consequence that the virtual trailing edge moves forward and up, reducing effective chord and chamber. This modification to the flow when going from a fully disrupted to maximally reinforced vortex street can be described as a change in the flow against the circulation of the aerofoil, leading to a reduction in the generated lift.

When analysing the change in behaviour between 25% duty cycle and 50% duty cycle interruption sweeps (shown in Figure 4.89) the pattern that emerges is consistent with the method of actuation previously described. The main difference between the two data sets is the lack of a second dip in delta C_L at the first sub harmonic in the 50% duty cycle data. This is explained by the relationship between the interruption frequency, duty cycle and the overall actuation pulse length. At 800 Hz interruption, both 25% and 50% duty cycles have a short enough pulse length that the plasma shedding can lock in, so that as the vortex is being shed from the lower edge of the step it is never working against the DBD jet and is being reinforced on every cycle. At 600 Hz both duty cycle ratios perform similarly, the disruption is not primarily due to the length of the pulse, but its timing, the two frequencies (shedding and interruption) can not reconcile to synchronise with each other and so alternate plasma pulses occur out of time with the vortex shedding, hindering the proper vortex formation and leading to the disruption of the vortex street. At 400 Hz interruption the length of the plasma pulse has increased to twice what it was at 800 Hz, in the case of the 25% duty cycle this means that the pulse now covers one half of the shedding cycle and is at the correct frequency to interact with alternate vortices in a positive, reinforcing manner. This alternate vortex lock-in is seen in the PIV data (Figure 4.61). However, at a 50% duty cycle the actuation pulse length is increased to the length of one full shedding cycle. As such, half of the period where the plasma is active occurs during a part of the shedding cycle where it disrupts rather than promotes the vortex shedding. This leads to a disruption to the vortex street which in turn produces an effect on delta C_L which is very similar to that observed at 50% duty cycle, 600 Hz interruption frequency.

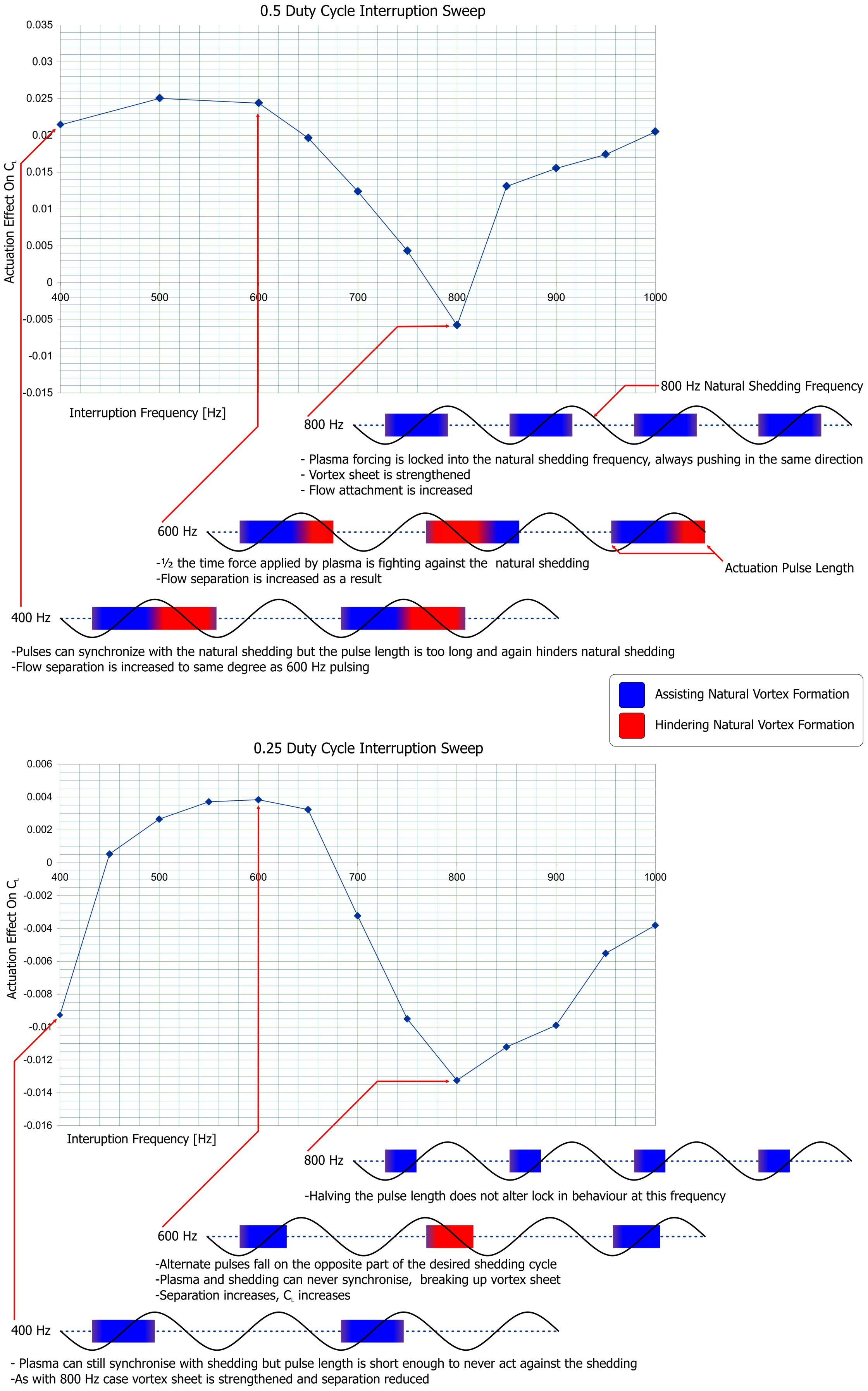

- Plasma forcing is locked into the natural shedding frequency, always pushing in the same direction
- Vortex sheet is strengthened
- Flow attachment is increased

-½ the time force applied by plasma is fighting against the natural shedding
-Flow separation is increased as a result

-Pulses can synchronize with the natural shedding but the pulse length is too long and again hinders natural shedding
-Flow separation is increased to same degree as 600 Hz pulsing

-Halving the pulse length does not alter lock in behaviour at this frequency

-Alternate pulses fall on the opposite part of the desired shedding cycle
-Plasma and shedding can never synchronise, breaking up vortex sheet
-Separation increases, C_L increases

- Plasma can still synchronise with shedding but pulse length is short enough to never act against the shedding
-As with 800 Hz case vortex sheet is strengthened and separation reduced

Figure 4.89 0.25 and 0.5 Duty Cycle Interaction with Shedding

In section 4.5.3.2.1 some effort was spent to extract the amplitude of the sine wave appropriate to the natural shedding data. This figure was subtracted from the data already obtained for the synchronised actuated data and the resultant graph, Figure 4.66, was produced. Although wake angle deviation is a much better metric of how the flow is being affected by the plasma and consequently how the change in lift is produced, the amplitude of the sine wave shows an interesting correlation with the change in lift coefficient. Figure 4.90 shows C_L data from the actuator repeatability study overlaid with the inverted sine wave magnitude trace showing this correlation. This adds further weight behind the theory of operation laid out at the start of this subsection.

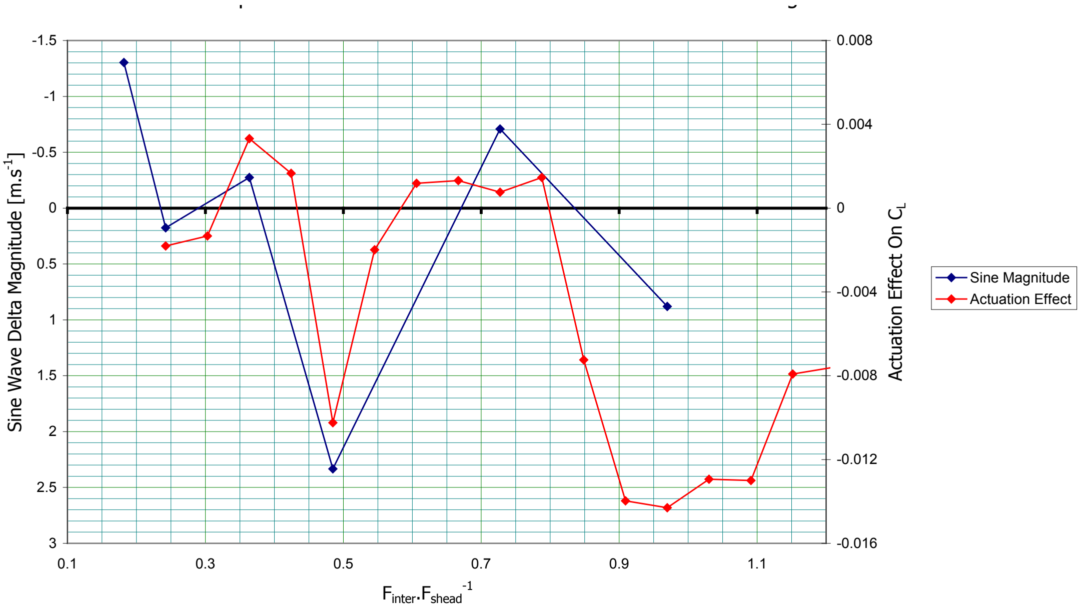

Figure 4.90 Sine Wave Amplitude C_L Overlay

By far the largest irregularity is that of the absolute position of the force balance delta C_L trace (actuated lift compared to unactuated control) with respect to where, or even whether, it crosses the x-axis. Shown in Figure 4.91 are 11 repeats of the same test case taken across the course of the study; all are interruption frequency sweeps taken using the 2nd generation high voltage system at 20 m.s^{-1}, zero degrees incidence and a 25% duty cycle. Which test the data is taken from is noted in the legend; each line represents the average of at least 3 repeated test points at each node, the 12 single run mount-remount and clamp-reclamp tests being grouped into 3s and averaged. As can be seen there is great variation in these results, from the all negative actuation effect of 'actuator repeat 2 remounted' to the almost all positive effect on C_L observed in 'mount 4-6'. All but 3 interruption frequencies have test points on either side of the control level. In addition to this the spread on the test runs is of a similar magnitude to the actuation effect itself. However the similarities between runs are also clear; the same pattern is repeated in every test run. This similarity is highlighted in

Figure 4.92 where the traces have been overlaid on each other along with the overall mean value with the same vertical scaling but independent origins. Considering that the small forces that are involved are at the edge of what the balance can resolve, and the number of variables that had to be maintained between test runs, the level of conformity achieved across those readings in terms of shape of the actuation response is very good.

It is proposed that the cause of the variation was in the construction of the actuator altering the baseline shedding case, and the method proposed for causing the shift in the actuation force is this; minor differences in the construction of the actuator modify the strength of the unactuated vortex street from the back of the aerofoil. This could be as simple as a burr on the back side of the exposed electrode from cutting, or the actuator sitting loose in the clamp during gluing leading to the edge becoming slightly more rounded for this actuator; this affects the amount of upwash in the unactuated flow (see Figure 4.93). As the flow deviation from maximum to minimum effect under actuation is in total less than 2^o, only very minor shifts in baseline separation could cause the variation seen.

Taking the extremes of this hypothesis, for the case where the actuation effect on C_L is for the majority of the tested interruption frequencies a positive shift (i.e. increased lift with actuation), as is seen in the trace for the test marked 'Clamp 1-3' (coloured maroon) in Figure 4.91, according to the theory of operation laid out earlier, the actuator is mostly increasing the size of the recirculation bubble at the step by disrupting the vortex street. This is only possible if the time-averaged flow has a fairly large upwash component naturally. Equally, almost no effect relative to control is seen when forcing at the natural frequency because the flow has not fully separated from the step in order to be reattached by the forcing. This scenario conforms with the idea of the step becoming slightly rounded during gluing (panel A in Figure 4.93). Equally, if we take the other suggestion and introduce a slight burr at the trailing edge on the copper tape of the actuator, it is not inconceivable that the flow would separate more effectively generating a larger natural recirculation bubble. Therefore a flow which naturally had a large recirculation bubble would show little response to the forcing at 600 Hz as disrupting the vortex street further can produce no further increase in aerofoil circulation by inducing a down shift in the wake angle by modifying the bubble, as is seen in the trace from the test marked 'laser' (coloured red) in Figure 4.91. However, with the flow more naturally separated this creates the opportunity for forcing at approximately the natural frequency of 800 Hz to reduce the size of the circulation bubble and introduce greater upwash into the wake reducing circulation and lift (panel B in Figure 4.93).

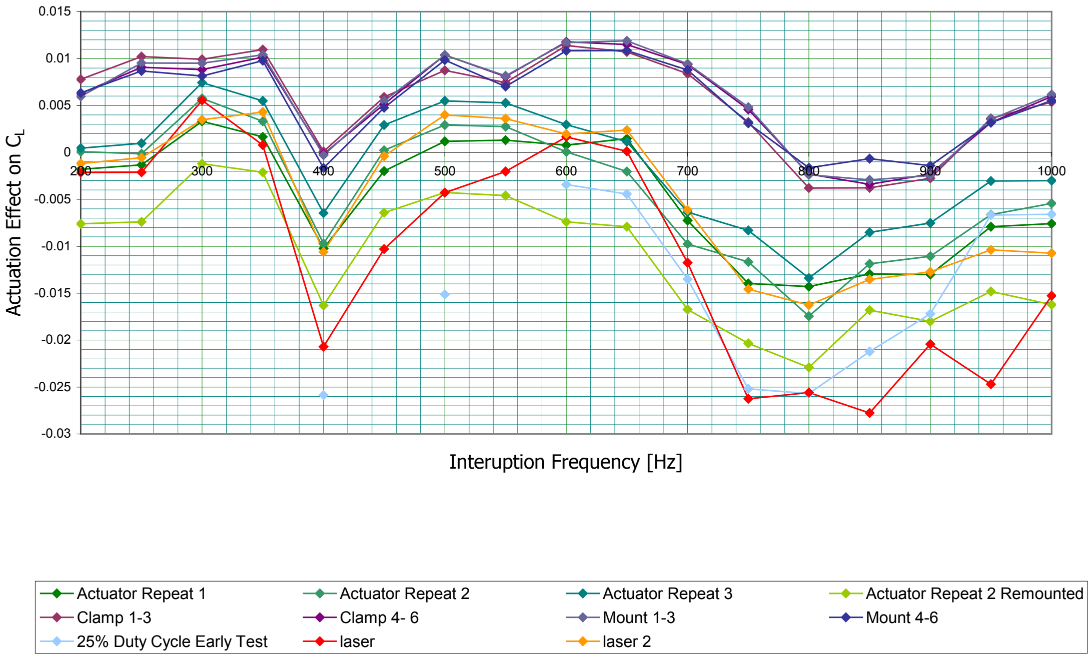

Figure 4.91 All Interruption Sweeps On One Graph

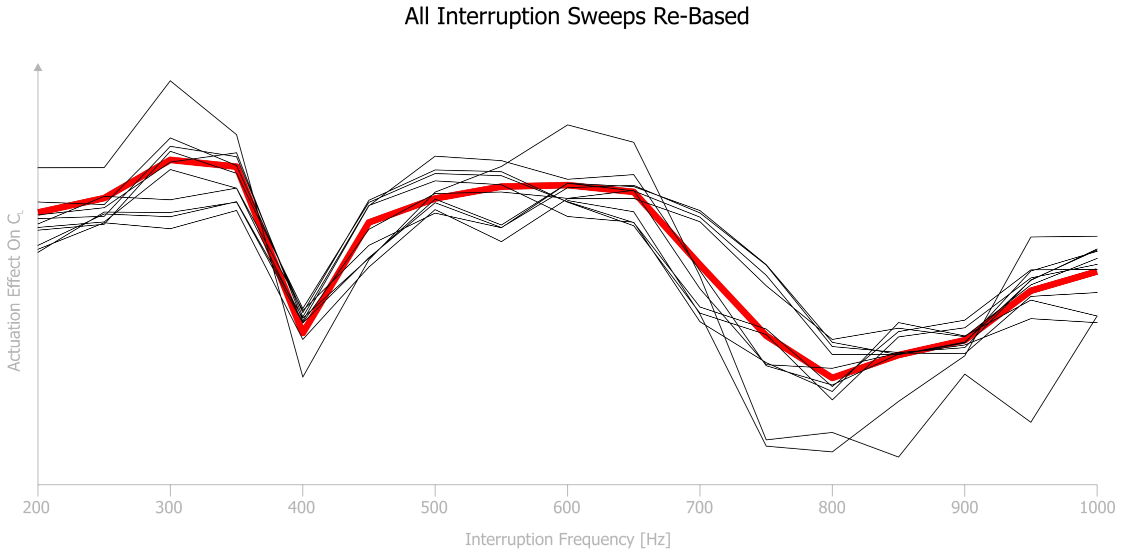

Average shown In Red
Vertical Scales Have Not Been Expanded / Compressed - Only Offset

Figure 4.92 Interruption Sweep Overlay

Although, when looking at the data associated with Figure 4.44, a cause for the shift which was large enough to account for this variability was not evident, it is thought that the actuator repeatability is worse than when it was tested in Figure 4.39 for the following reasons: Firstly, the three actuators for that test were batch produced together, where as most others were made individually. The implication of the batch production of the actuators is that any defects introduced are more likely to have been propagated through the assembly of all three actuators than in those actuators which were produced individually. Secondly with the sample size of three, even if the true population standard deviation due to actuator manufacture differences is high enough to cause the variation seen, there exists a plausible probability that by chance all three measurements would fall within the much smaller clustering seen in the repeatability test. This probability is improved by the fact that the three readings fall in the centre of the spread seen in the population where, if the distribution is assumed Gaussian, the majority of the results would be expected to fall.

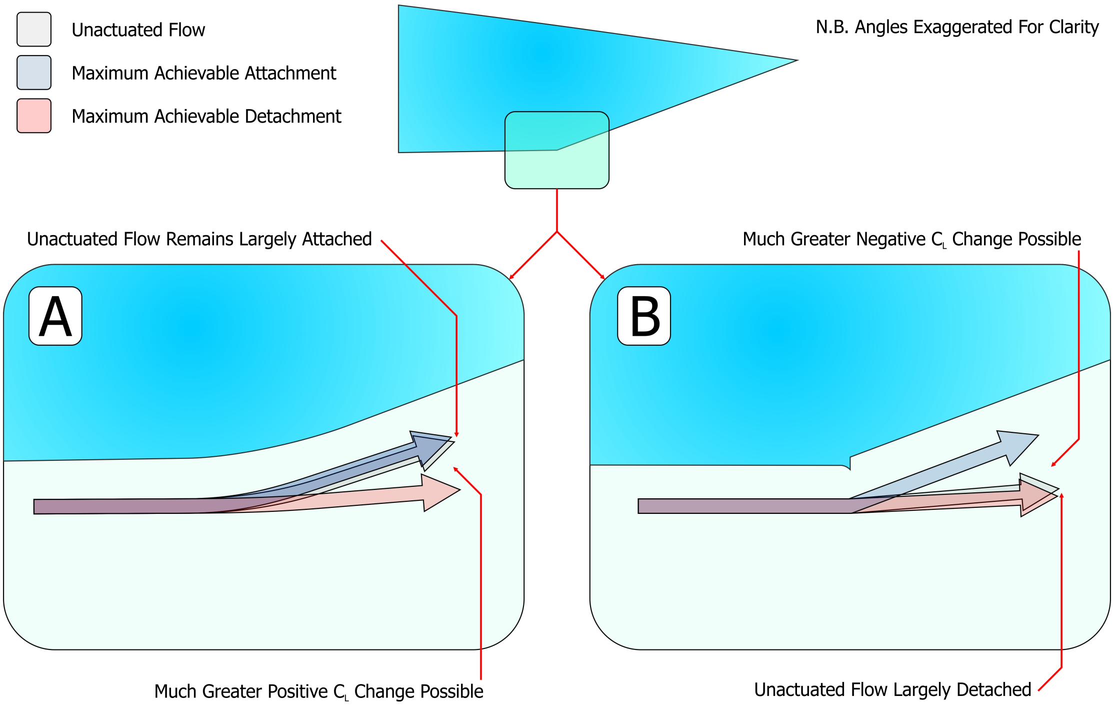

Figure 4.93 Proposed Explanation For Shift In Interruption Response

4.6.2 Low Carrier Wave Frequency Continuous Actuation

To explain the shape of the uninterrupted incidence sweep carried out at 600 Hz (Figure 4.23), it is useful to first look at some electrical measurements. The high voltage trace was measured using a 100:1 reduction high voltage probe, current was measured using a non-contact current sensor, and both were connected to a digital phosphor oscilloscope with a 3 Giga sample per second capability and file export via USB. In Figure 4.94 what can be seen is the typical behaviour previously reported by others and which was detailed in the literature [86]. One thing that is noticeable from this is the relatively short pulse length for the forward stroke; when being driven by a carrier wave of only 600 Hz, this pattern pulses as the plasma repeatedly strikes and extinguishes, and will produce a very similar result to that of the 4 kHz carrier interrupted at 600 Hz. Therefore having shown the importance of forcing frequency in the actuator response when evaluating the interrupted data, even though the data in Figure 4.23 was taken as a continuous plasma actuation dataset, it cannot be considered as such when analysing it; Figure 4.95 shows the analysis of the features of this graph.

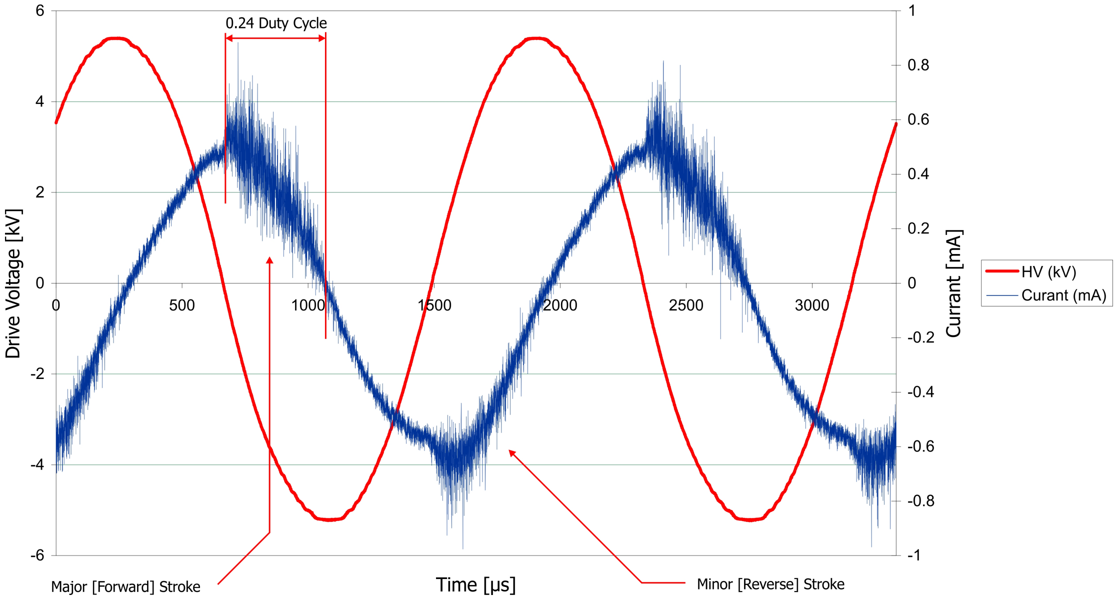

Figure 4.94 Analysis of the 1st Gen HV System Electrical Measurements With Respect To Vortex Street Modification

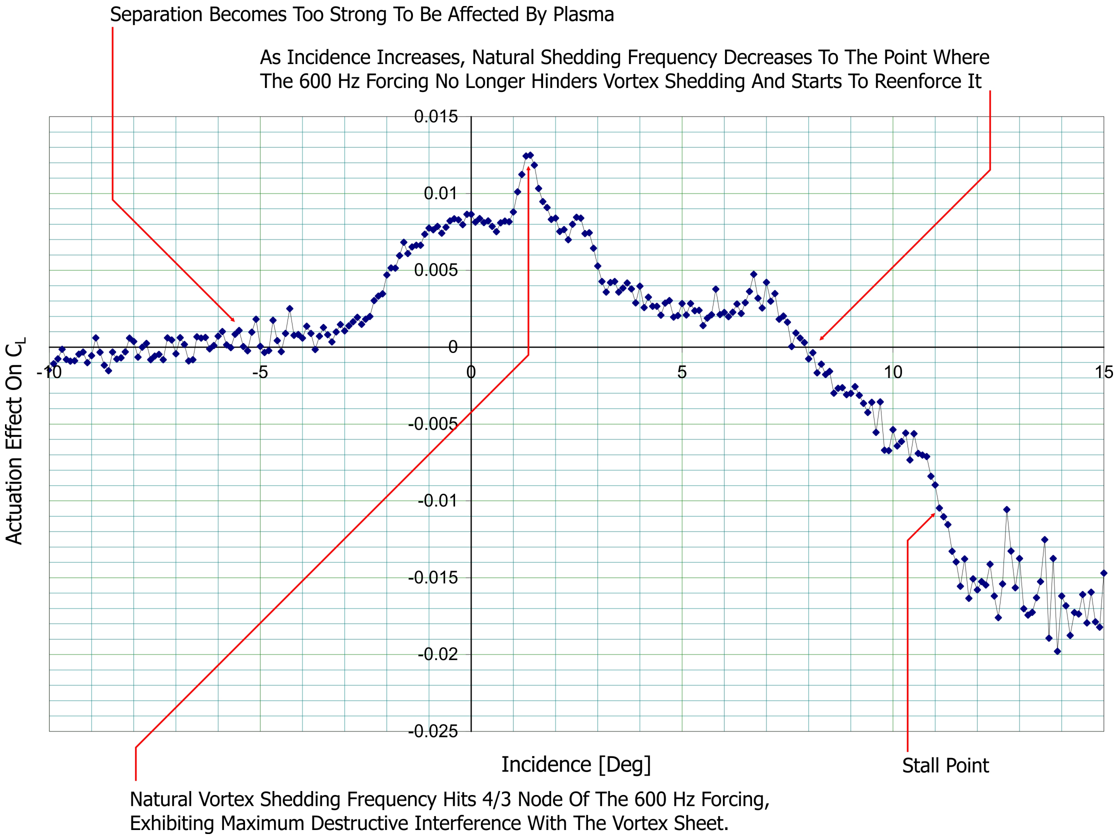

Figure 4.95 Annotated Incidence Sweep Response

4.6.3 Interrupted Actuation Compared To Continuous Actuation

Figure 4.96 shows the considerable increase in actuation authority achievable by using a pulsed plasma over a continuous DBD discharge, and crucially interrupting the plasma at the correct frequency for the flow conditions. The red line in the 3 panes of the figure represents the value with no interruption. It should be noted that dataset from which the continuously actuated data was taken featured unusually large error bars; however the uncertainty is much smaller than the advantage that the interrupted data shows over the continuously forced case. It is also worth noting that the continuously forced data shows approximately the same magnitude of actuation as the interrupted data where the vortex street is being maximally disrupted, i.e. 600 Hz at 0^{o} incidence. However the interrupted plasma is doing the same amount of aerodynamic work with only ¼ of the input power - even before the forcing frequency has been optimised for the flow conditions.

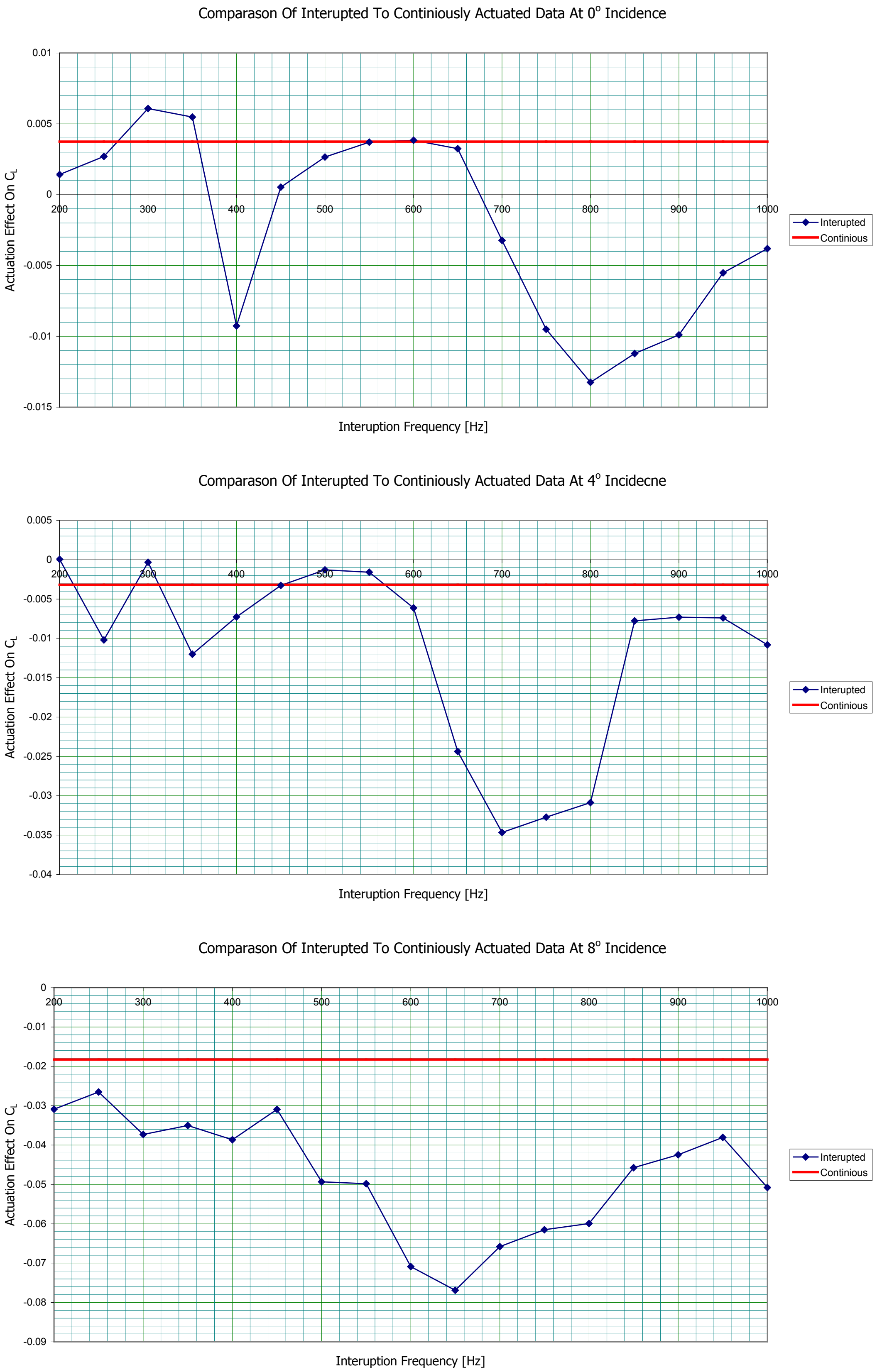

Figure 4.96 Comparison Of Interrupted To Uninterrupted Plasma Actuation. (CF 4kHz, DC 25% or 100% , Vel. 20 m.s^{-1})

4.6.4 Final Observations On System Response To Interruption

Figure 4.97 shows the best approximation of the system to forcing both above and below the natural frequency composited from the 20 and 3.6 m.s^{-1} data; the horizontal axis is the base 2 logarithm of the interruption frequency divided by the natural shedding frequency, and therefore -1 is the first sub-harmonic of the natural frequency and +1 is the first harmonic. As is evidenced by the difference in the wake flow angles between the fully disrupted vortex street at 3.6 m.s^{-1} and greater than 200 Hz and the mostly disrupted vortex street at 20 m.s^{-1} and 600 Hz forcing, the eventual minimum level of wake angle deviation is dependent on the free stream flow speed relative to the actuator power (see Figure 4.59 and Figure 4.71). Therefore it is expected that the position of the x-axis would change with flow velocity and is therefore labelled as arbitrary. This graph also assumes that as the operating point move away form the origin on the x-axis, the value will tend towards the same steady state value. As the actuation pulses move to frequencies which have no frequency based interaction with the vortex street, the forcing becomes more like a continuously operated un-pulsed actuator at ¼ of the time-averaged power.

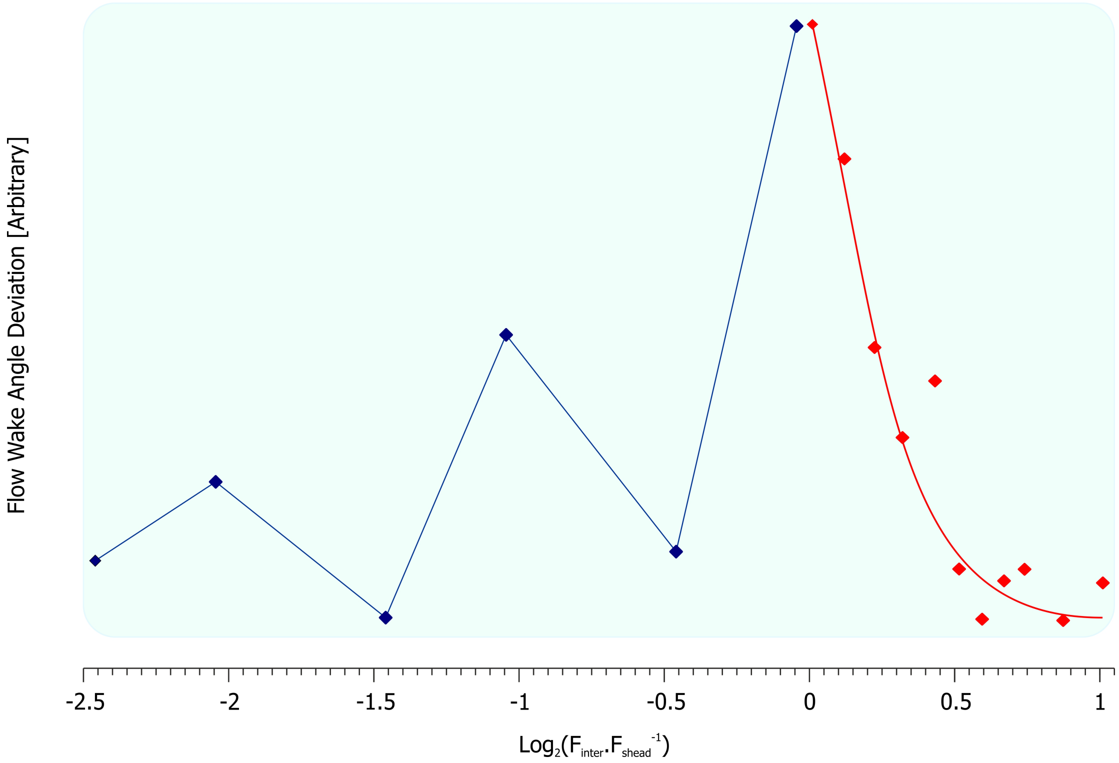

Figure 4.97 Expected Full Range Response Curve

Chapter 5 Conclusions

5.1 Conclusions On Device Construction

5.1.1 Electrode Manufacture

Failure mechanisms for thin film patterned electrodes were investigated, and it was found that low film resistivity and a high melting point are critical to avoid thin films being re-vaporised and ablated during the plasma formation process.

Through the use of evaporated gold on a chromium seed layer a significant increase in the lifetime of the thin film electrodes was achieved in comparison to the initial aluminium devices. However, even the best case gold electrodes experienced degradation after lengthy running. As such it must currently be recommended that macroscopically thick electrodes (tens to hundreds of µm as opposed to evaporated films at hundreds of nm) are maintained for all applications where a runtime in excess of a couple of hours is important.

5.1.2 Dielectric Manufacture

A novel composite laminated dielectric structure was developed which was hardened against the chemical and electrical stresses present in the functioning DBD device. It included a glass fibre reinforced PDMS player for oxygen plasma resistance, and a Kapton® polyimide layer to provide the necessary dielectric strength to resist electrical breakdown. A plasma surface treatment for the PDMS was optimised to sufficiently functionalise the surface to allow the bonding of the two layers of the laminate whilst not distorting or damaging the film. The resulting film showed excellent plasma resistance due to the PDMS layer becoming passivated with a self healing SiO_2 layer upon exposure to the oxygen in the plasma. The film also demonstrated good robustness, a low total laminate thickness of 0.2 mm and excellent flexibility with a minimum bend radius of around 1 to 1.5 mm.

5.2 Conclusions On Experimental Techniques

The results presented in chapter 4 successfully captured the behaviour of a dielectric barrier discharge – separation step system on a modified NACA 0012 aerofoil with respect to its operation at varying interruption frequencies. Overall the achieved changes in C_L were of a magnitude broadly comparable to those achieved in the literature (Peak value at positive incicdence, -0.041 on C_L [3], -0.077 on C_L (this work)) , validating the approach and experimental setup.

Investigations were carried out using a variety of aerodynamic measurement techniques, chief amongst which were lift measurements taken using an in-house force balance with a logging and measurement protocol shown to give a standard deviation of just 0.00065 on C_L when testing at 20 m.s^{-1}, and flow visualisation accomplished with a phase-locked PIV technique based on manipulating the aliasing frequency between the vortex shedding locked to interrupted plasma drive waveform and the PIV capture rate; this successfully delivered sequenced instantaneous images of the vortex shedding pattern.

5.3 Conclusions On Actuator Behaviour And Operation

5.3.1 Pulsed Plasma Actuation Mechanisms

Force balance and hot-wire probe data showed how the aerofoil could experience either an increase in lift or a decrease in lift from the activation of pulsed plasma actuation. Crucially it also showed that the direction of the change in C_L was dependent on the relationship between the natural shedding frequency and the actuation frequency.

Using phase locked PIV measurements it was demonstrated how the pulsed plasma interacts with the vortices being shed from the back of the separation step to produce the bi-directional actuation; specifically, when forcing at the natural shedding frequency or its first sub harmonic (at 25% duty cycle), the vortex street can be reinforced, appearing stronger and reducing the size of the separation bubble at the rear of the aerofoil; this results in a greater upwash in the wake decreasing circulation and therefore lift. Conversely when forcing at the midpoint between these two values the shedding cannot lock into the plasma forcing frequency and the vortex street becomes more broken up and the individual vortices are weaker than the unactuated control; this increases separation from the back of the step, increasing lift.

Comparisons between results where the plasma was interrupted and ones where it was driven continuously showed a significant increase in the maximum achievable effect on delta C_L for the former over the latter; this is in agreement with the literature. This difference in effect is caused by the inability of the continuously forced plasma to interact efficiently with the vortex street formation. As a corollary to this result it is shown that pulsed plasma actuation offers significantly better energy efficiency for the creation of control moments.

5.3.2 Characterisation Of The Effect Of Incidence

Force balance and PIV results taken at positive incidence showed a strong interdependence between the forcing frequency and the change in $C_{L,}$ in a similar manner to those taken at zero incidence. However, once at incidence, the flow over the trailing edge step is no longer naturally in a state where the recirculation bubble can both be increased or decreased in size, and therefore actuation could only decrease the size of the bubble by a greater or lesser extent, thereby always decreasing lift when activated. The forcing frequency at which maximum actuation effect was observed changed with incidence. Previous studies which have used interrupted plasmas across incidence sweeps have not modulated their forcing frequency based on the incidence to achieve maximum effect; it can be concluded from these tests that this factor must be considered when optimising a plasma flight control system.

5.3.3 Characterisation Of The Effect Of Velocity

By comparing data from 20 $m.s^{-1}$ and 3.6 $m.s^{-1}$ test runs, both of which were conducted at nominally constant actuator power (although it should be noted as reported in [111] there is a minor decrease in actuator power with increase in freestream velocity, this was only an ≈ 5% reduction over the tested range), it can also be concluded that the relative energy of the DBD jet compared to the freestream flow is important in determining the behaviour of electro-aerodynamic system. When operating at a freestream velocity of 3.6 $m.s^{-1}$, the energy of the jet is high compared to that of the freestream flow. This causes the actuation effect to always increase the upwash in the wake irrespective of forcing frequency, which is in contrast to the 20 $m.s^{-1}$ case where the jet energy was sufficiently low compared to the freestream that it had to rely on resonant interaction with the vortex street to reattach the flow. Had the balance system been able to resolve the resulting force change at this velocity this would have equated to a reduction in lift and C_L. Instantaneous PIV results still showed that forcing at a frequency away from the natural shedding frequency broke down the vortex street. However, the increased relative power of the actuator was able to overcome this and still force increased attachment over the step. Moreover, the degree of attachment was still further increased when the plasma was interrupted close to the natural shedding frequency.

References

1. Gad-el-Hak, M., *Introduction to Flow Control*, in *Flow Control: Fundamentals and Practices*. 1998, Springer-Verlag. pages. 1-108. ISBN: 3540639365

2. Ben-Hamou, E., E. Arad, and A. Seifert, *Generic Transport Aft Body Drag Reduction.* Flow Turbulence & Combustion, 2007. **78**: p. 365-382.

3. Lopera, J., T.T. Ng, M.P. Patel, S. Vasudevan, E. Santavicca, and T.C. Corke, *Aerodynamic control using windward-surface plasma actuators on a separation ramp.* Journal of Aircraft, 2007. **44**(6): p. 1889-1895.

4. Patel, M., S. Vasudevan, R. Nelson, and T. Corke, *Plasma Aerodynamic Control Effectors For Improved Wind Turbine Performance*, U.S. Department Of Energy, 2008.

5. Patel, M.P., T.T. Ng, S. Vasudevan, T.C. Corke, and C. He, *Plasma actuators for hingeless aerodynamic control of an unmanned air vehicle.* Journal of Aircraft, 2007. **44**(4): p. 1264-1274.

6. Cook, M.V., A. Buonanno, and S.D. Erbsloh, *A circulation control actuator for flapless flight control.* Aeronautical Journal, 2008. **112**(1134): p. 483-489.

7. Zhang, P.F., B. Yan, A.B. Liu, and J.J. Wang, *Numerical Simulation on Plasma Circulation Control Airfoil.* AIAA Journal, 2010. **48**(10): p. 2213-2226.

8. Roskam, J., *Aerofoil Theory*, in *Airplane Design*. 2002, DARcorperation. pages. 83. ISBN: 188488556X

9. Roth, J.R., *Aerodynamic Flow Acceleration Using Paraelectric And Peristaltic Electrohydrodynamic Effects of a One Atmosphere Uniform Glow Discharge.* Physics Of Plasmas, 2003. **10**(5): p. 2117-2126.

10. Sosa, R., G. Artana, E. Moreau, and G. Touchard, *Stall Control at High Angle Of Attack With Plasma Sheet Actuators.* Experimental Fluids, 2006. **42**: p. 143-168.

11. Moreau, E., *Airflow Control By Non-Thermal Plasma Actuators.* Journal Of Physics D: Applied Physics, 2007. **40**: p. 605-636.

12. Duvigneau, R. and M. Visonneau, *Simulation and Optimisation Of Stall Control For An Aerofoil With A Synthetic Jet.* Aerospace Science And Technology, 2006. **10**: p. 279-287.

13. Gross, A. and H.F. Fasel, *Active Flow Control for NACA 6-Series Airfoil at Re=64,200.* AIAA Journal, 2010. **48**(9): p. 1889-1902.

14. Zerihan, J. and X. Zhang, *Aerodynamics of Gurney flaps on a wing in ground effect.* Aiaa Journal, 2001. **39**(5): p. 772-780.

15. Feng, L.-H., T.N. Jukes, K.-S. Choi, and J.-J. Wang, *Flow control over a NACA 0012 airfoil using dielectric-barrier-discharge plasma actuator with a Gurney flap.* Experiments in Fluids, 2012. **52**(6): p. 1533-1546.

16. Little, J., M. Nishihara, I. Adamovich, and M. Samimy, *High-lift airfoil trailing edge separation control using a single dielectric barrier discharge plasma actuator.* Experiments in Fluids, 2010. **48**(3): p. 521-537.

17. Boesch, G., H.D. Vo, B. Savard, C. Wanko-Tchatchouang, and N.W. Mureithi, *Flight Control Using Wing-Tip Plasma Actuation.* Journal of Aircraft, 2010. **47**(6): p. 1836-1846.

18. Houghton, E.L., P.W. Carpenter, S. Collicott, and D. Valentine, *Aerodynamics for Engineering Students*. 2012, Elsevier Science. pages. 299-314. ISBN: 9780080966335

19. Huang, J., T.C. Corke, and F.O. Thomas, *Plasma Actuators For Separation Control of Low-Pressure Turbine Blades.* AIAA Journal, 2006. **44**(1): p. 51-57.

20. Rathnasingham, R. and K. Brewer, *Active Control Of Turbulent Boundary Layers.* Journal Of Fluid Mechanics 2003. **495**: p. 209-233.

21. Endo, T., N. Kasagi, and Y. Suzuki, *Feedback Control Of Wall Turbulence With Wall Deformation.* International Journal Heat and Fluid Flow 2000. **21**: p. 568-575.

22. Rabbeck, H. and K.-S. Choi, *A Wind Tunnel Experiment On Real Time Opposition Control Of Turbulence.* Physics Of Fluids 2006. **18**.

23. Jacobson, S.A. and W.C. Reynolds, *Active control of streamwise vortices and streaks in boundary layers.* Journal of Fluid Mechanics, 1998. **360**: p. 179-211.

24. Suzuki, Y., N. Kasagi, and T. Yoshinto. *R&D Study On Micro Sensors And Actuators For Active Control Of Wall Turbulence*. in *2nd Symposium Smart Control Of Turbulence*. 2001.

25. Bernard, N., J. Jolibois, M. Forte, G. Touchard, and E. Moreau, *Control of an axisymmetric subsonic air jet by plasma actuator.* Experimental Fluids, 2007. **43**: p. 603-616.

26. Ramen, G. and S. Packiarajan, *Jet Thrust Vectoring Using A Miniature Fluidic Oscillator.* The Aeronautics Journal, 2005. **109**(1095): p. 129-138.

27. Labergue, A., E. Moreau, N. Zouzou, and G. Touchard, *Separation Control Using Plasma Actuators: Application To A Free Turbulent Jet.* Journal Of Physics D: Applied Physics, 2007. **40**: p. 674-684.

28. Boeing. *Noise Certification Tests Show MD Explorer, MD 600N, MD 520N As Quietest Helicopters; All Feature NOTAR Anti-Torque System*. 1997 [Accessed Online: 23/09/08]; Available from: http://www.boeing.com/ids/news/mdc/97-21.html.

29. SPG Media. *MD Helicopters MD Explorer Twin-Engined Light Helicopter, USA*. [Accessed Online: 22/09/08]; Available from: http://www.aerospace-technology.com/projects/md_explorer/.

30. Glezer, A. and M. Amitay, *Synthetic Jets.* Annual Review Fluid Mechanics, 2002. **34**: p. 503-634.

31. Deeds, M., D. Gonzales, D. Herman, G. Prybyla, B. Warner, G. Papadopoulos, and C.-Y. Tsai, *Development and Testing of MEMS Control Surfaces For High Speed Projectiles*, in *AIAA Aerospace Sciences Meeting and Exhibit*. 2007, AIAA: Reno Nevada.

32. Deb, D., G. Tao, J.O. Burkholder, and D.R.Smith, *Adaptive Compensation Control Of Synthetic Jet Actuator Arrays For Aerofoil Virtual Shaping* Journal Of Aircraft, 2007. **44**(2): p. 616-626.

33. Bouwmeester, J. and J. Guo, *Survey of worldwide pico- and nanosatellite missions, distributions and subsystem technology.* Acta Astronautica, 2010. **67**(7-8): p. 854-862.

34. Viswamurthy, S.R. and R. Ganguli, *An optimization approach to vibration reduction in helicopter rotors with multiple active trailing edge flaps.* Aerospace Science And Technology, 2004. **8**(3): p. 185-194.

35. Seddon, J. and S. Newman, *Basic Helicopter Aerodynamics: An Account of First Principles in the Fluid Mechanics and Flight Dynamics of the Single Rotor Helicopter*. 1990: American Institution of Aeronautics and Astronautics. ISBN:

36. Aerospaceweb.org. *Helicopter Theory - Flapping Hinges*. [Accessed Online: 25/09/08]; Available from: http://www.aerospaceweb.org/design/helicopter/hinges.shtml.

37. Anderson, W.D., S.R. Patel, and C.L. Black, *Low-speed wind tunnel buffet testing on the F-22.* Journal of Aircraft, 2006. **43**(4): p. 879-885.

38. Kook, H.S., S.R. Shin, and G.D. Ih, *Measurement of the Sunroof Buffeting Noise with an Automatic Deflector-Traversing Device.* International Journal of Precision Engineering and Manufacturing, 2010. **11**(1): p. 5-11.

39. de Jong, A.T., H. Bijl, and F. Scarano, *The aero-acoustic resonance behavior of partially covered slender cavities.* Experiments in Fluids, 2011. **51**: p. 1353-1367.

40. Alex, R., M. Fred, S. Christophe, T. Michel, and K. Kenneth, *Optimal Sunroof Buffeting Predictions with Compressibility and Surface Impedance Effects*, in *11th AIAA/CEAS Aeroacoustics Conference*. 2005, American Institute of Aeronautics and Astronautics. ISBN:

41. Kook, H.-S., S.-R. Shin, and G.-D. Ih, *Measurement of the sunroof buffeting noise with an automatic deflector-traversing device.* International Journal of Precision Engineering and Manufacturing, 2010. **11**(1): p. 5-11.

42. Hemon, P., F. Santi, and X. Amandolese, *On the pressure oscillations inside a deep cavity excited by a grazing airflow.* European Journal of Mechanics B-Fluids, 2004. **23**(4): p. 617-632.

43. CD-adapco. *CFD eliminates unpleasant sunroof noise*. [Accessed Online: 17/07/08]; Available from: http://www.cd-adapco.com/press_room/dynamics/20/saab.html.

44. Ramen, G., S. Raghu, and T.J. Bencic. *Cavity Resonance Suppression Using Miniature Fluidic Oscillators*. in *5th Aeroacoustics Conference*. 1999: American Institute Aeronautics and Astronautics.

45. Glezer, A. and M. Amitay, *Synthetic jets.* Annual Review of Fluid Mechanics, 2002. **34**: p. 503-529.

46. Douglass, M. *Lifetime Estimates And Unique Failure Mechanisms Of The Digital Micromirror Device (DMD)*. in *IEEE Reliability Physics Symposium*. 1998.

47. Douglass, M., *DMD reliability A MEMS Success Story.* Society Of Photo Optical Instrumentation Engineers, 2003. **4980**.

48. Qiao, D.-Y., W.-Z. Yuan, and X.-Y. Li, *A Two Beam Method For extending The Working Range Of Electrostatic Parallel-Plate Micro-Actuators.* Journal Of electrostatics, 2007. **65**: p. 256-262.

49. Pimpin, A., Y. Suzuki, and K. N., *Microelectrostrictive Actuator with Large Out-Of-Plane Deformation For Flow Control Application.* Journal Of Microelectromechanical Systems, 2007. **16**(3): p. 753-764.

50. Dubois, P., S. Rosset, S. Koster, J. Stauffer, S. Mikhailov, M. Dadras, N. Rooji, and H. Shea, *Microactuators based on ion implanted dielectric electroactive polymer membranes.* Sensors And Actuators A Physical, 2006(130): p. 147-154.

51. Shahinpoor, M., *Continuum electromechanics of ionic polymeric gels as artificial muscles for robotic applications.* Smart Materials and Structures, 1994. **3**(3): p. 367.

52. Lee, S.G., H.C. Park, S.D. Pandita, and Y. Yoo, *Performance improvement of IPMC (ionic polymer metal composites) for a flapping actuator.* International Journal of Control Automation and Systems, 2006. **4**(6): p. 748-755.

53. Chen, Z. and X.B. Tan, *MEMS-based Fabrication of Multiple-Degree-of-Freedom Ionic Polymer-Metal Composite Actuators*, in *Electroactive Polymer Actuators and Devices*, Y. BarCohen, Editor. 2010, Spie-Int Soc Optical Engineering: Bellingham. ISBN: 0277-786X
978-0-8194-8057-6

54. Lee, C., G. Hong, Q.P. Ha, and S.G. Mallinson, *A Piezoelectrically Actuated Micro Synthetic Jet Actuator For Active Flow Control.* Sensors and Actuators A Physical, 2003. **108**: p. 168-174.

55. Lu, J., T. Ikehara, Z. Y, R. Maeda, and T. Mihara, *Energy Dissipation Mechanisms In Lead Zirconate Titanate Thin Film Transduced Micro Cantilevers.* Japanese Journal Of Applied Physics, 2006. **45**(11): p. 8795-8800.

56. Warsop, C., M. Hucker, A.J. Press, and P. Dawson, *Pulsed Air Jet Actuators for Flow Separation Control.* Flow Turbulence & Combustion, 2007. **78**: p. 255-281.

57. Rabinovitch, O. and J.R. Vinson, *On The Design of Piezoelectric Smart Fins For Flight Vehicles.* Smart Materials and Structures, 2003. **12**: p. 686-695.

58. Barrett, R. and R. Vos, *Post-buckled precompressed subsonic micro-flight control actuators and surfaces.* Smart Materials & Structures, 2008. **17**(5).

59. Lee, J., K. Kim, and S. Kwon, *Design, fabrication, and testing of MEMS solid propellant thruster array chip on glass wafer.* Sensors and Actuators a-Physical, 2010. **157**(1): p. 126-134.

60. Kohler, J., J. Bejhed, H. Kratz, F. Bruhn, U. Lindberg, K. Hjort, and L. Stenmark, *A hybrid cold gas microthruster system for spacecraft.* Sensors and Actuators a-Physical, 2002. **97-8**: p. 587-598.

61. Werber, A. and H. Zappe, *Thermo-Pneumatically Actuated Membrane Based Micromirror Devices.* Journal of Micromechanics and Microengineering, 2006. **16**(12): p. 2524-2531.

62. Griss, P., H. Andersson, and G. Stemme, *Expandable Microspheres For The Handling Of Liquids.* Lab On A Chip, 2002. **2**(2): p. 117-120.

63. Klintberg, L., M. Karlsson, L. Stenmark, and G. Thornell, *A thermally activated paraffin-based actuator for gas-flow control in a satellite electrical propulsion system.* Sensors and Actuators a-Physical, 2003. **105**(3): p. 237-246.

64. Solano, B. and D. Wood, *Design And Testing Of A Polymeric Microgripper For Cell Manipulation.* Microelectronic Engineering, 2007. **84**: p. 1219-1222.

65. Cao, A., J. Kim, and L. Lin, *Bi-directional Electrothermal Electromagnetic Actuators.* Journal of Micromechanics and Microengineering, 2007. **17**: p. 975-982.

66. Wong, F.C., C.A. Rabbath, N. Hamel, and D. Corriveau, *Shape Memory Alloy Actuated Micro-Flow Effectors For Vortex Manipulation.* Transactions Of The CSME 2007. **31**(1): p. 19-38.

67. Miller, R.A. and Y.-C. Tai, *Micromachined Electromagnetic Scanning Mirrors.* Journal Optical Engineering, 1997. **35**(5): p. 1399-1407.

68. Coe, D., M. Allen, C. Rinehart, and A. Glezer, *Pneumatically Actuated Micromachined Synthetic Jet Modulators.* Sensors And Actuators A Physical, 2006. **132**: p. 689-700.

69. Grosjean, C., G.B. Lee, W. Hong, Y.C. Tai, C.M. Ho, and Ieee, *Micro balloon actuators for aerodynamic control*. Micro Electro Mechanical Systems - Ieee Eleventh Annual International Workshop Proceedings. 1998, New York: Ieee. 166-171. ISBN: 0-7803-4412-X

70. JR, R., D. Sherman, and S. Wilkinson, *Boundary Layer Flow Control Wiht One Atmosphere Uniform Glow Discharge Surface Plasma*, in *36th AIAA Aerospace Sciences Meeting*. 1998: Reno Nevada.

71. Magnier, P., V. Boucinha, B.J. Dong, R. Weber, A. Leroy-Chesneau, and D. Hong, *Experimental Study of the Flow Induced by a Sinusoidal Dielectric Barrier Discharge Actuator and Its Effects on a Flat Plate Natural Boundary Layer.* Journal of Fluids Engineering-Transactions of the Asme, 2009. **131**(1).

72. Forte, M., J. Jolibois, J. Pons, E. Moreau, G. Touchard, and M. Cazalens, *Optimization of a dielectric barrier discharge actuator by stationary and non-stationary measurements of the induced flow velocity: application to airflow control.* Experiments in Fluids, 2007. **43**: p. 917-928.

73. Opaits, D.F., M.N. Shneider, R.B. Miles, A.V. Likhanskii, and S.O. Macheret, *Surface charge in dielectric barrier discharge plasma actuators.* Physics of Plasmas, 2008. **15**(7).

74. Nelson, R.C., T.C. Corke, C. He, H. Othman, T. Matsuno, M.P. Patel, and T. Terry, *Modification of the flow structure over a UAV wing for roll control*, in *45th Aerospace Sciences Meeting*. 2007: Reno Nevada. p. 15.

75. Enloe, C.L., T.E. McLaughlin, G.I. Font, and J.W. Baughn, *Parameterization of temporal structure in the single-dielectric-barrier aerodynamic plasma actuator.* AIAA Journal, 2006. **44**(6): p. 1127-1136.

76. Li, G., Y. Zhang, Y.J. Xu, B. Lin, Y.T. Li, and J.Q. Zhu, *Measurement of Plasma Density Produced in Dielectric Barrier Discharge for Active Aerodynamic Control with Interferometer.* Chinese Physics Letters, 2009. **26**(10).

77. Jolibois, J., M. Forte, and E. Moreau, *Application of an AC barrier discharge actuator to control airflow separation above a NACA 0015 airfoil: Optimization of the actuation location along the chord.* Journal of Electrostatics, 2008. **66**(9-10): p. 496-503.

78. Leonov, S., D. Opaits, R. Miles, and V. Soloviev, *Time-resolved measurements of plasma-induced momentum in air and nitrogen under dielectric barrier discharge actuation.* Physics Of Plasmas, 2010. **17**(11).

79. Enloe, C.L., M.G. McHarg, and T.E. McLaughlin, *Time-correlated force production measurements of the dielectric barrier discharge plasma aerodynamic actuator.* Journal of Applied Physics, 2008. **103**(7).

80. Balcon, N., N. Benard, and E. Moreau, *Formation Process of the Electric Wind Produced by a Plasma Actuator.* IEEE Transactions on Dielectrics and Electrical Insulation, 2009. **16**(2): p. 463-469.

81. Louste, C., M. Daaboul, and H. Romat, *A study of vortex shedding induced by dielectric barrier injection.* Journal of Electrostatics, 2009. **67**(2-3): p. 348-353.

82. Balcon, N., N. Benard, Y. Lagmich, J.P. Boeuf, G. Touchard, and E. Moreau, *Positive and negative sawtooth signals applied to a DBD plasma actuator - influence on the electric wind.* Journal of Electrostatics, 2009. **67**(2-3): p. 140-145.

83. Baird, C., C.L. Enloe, T.E. Mclaughlin, and J.W. Baughn. *Acoustic testing of the dielectric barrier discharge (DBD) plasma actuator*. in *43rd AIAA Aerospace Sciences Meeting and Exhibit*. 2005. Reno, Nevada.

84. Boucinha, V., R. Joussot, P. Magnier, R. Weber, and A. Leroy-Chesneau, *Characterization of the ionic wind produced by a DBD actuator designed to control the laminar-to-turbulent transition*, in *14th Int Symp on Applications of Laser Techniques to Fluid Mechanics*. 2008: Lisbon, Portugal.

85. Enloe, C.L., T.E. Mclaughlin, J.W. Gregory, R.A. Medina, and W.S. Miller. *Surface Potential and Electric Field Structure in the Aerodynamic Plasma Actuator*. in *46th AIAA Aerospace Sciences Meeting and Exhibit*. 2008. Reno, Nevada: AIAA.

86. Enloe, C.L., T.E. McLaughlin, V.D. R., K.K. D., J.E. J., and T.C. Corke, *Mechanisums and Responces of a Single Dielectric Barrier Plasma Actuator: Plasma Morphology.* AIAA Journal, 2004. **42**(3).

87. Enloe, C.L., G.I. Font, T.E. McLaughlin, and D.M. Orlov, *Surface Potential and Longitudinal Electric Field Measurements in the Aerodynamic Plasma Actuator.* AIAA Journal, 2008. **46**(11): p. 2730-2740.

88. Grosch, H., T. Hoder, K.D. Weltmann, and R. Brandenburg, *Spatio-temporal development of microdischarges in a surface barrier discharge arrangement in air at atmospheric pressure.* European Physical Journal D, 2010. **60**(3): p. 547-553.

89. Font, G.I. and W. Lowell-Morgan, *Plasma discharges in atmospheric pressure oxygen for boundary layer separation control*, in *35th AIAA fluid dynamics conference and exhibit* 2005: Toronto, Ontario Caneda. p. 10.

90. Soloviev, V.R. and V.M. Krivtsov, *Surface barrier discharge modelling for aerodynamic applications.* Journal of Physics D-Applied Physics, 2009. **42**(12).

91. Corke, T.C., C.L. Enloe, and S.P. Wilkinson, *Dielectric Barrier Discharge Plasma Actuators for Flow Control.* Annual Review of Fluid Mechanics, 2010. **42**: p. 505-529.

92. Orlov, D.M., G.I. Font, and D. Edelstein, *Characterization of Discharge Modes of Plasma Actuators.* AIAA Journal, 2008. **46**(12): p. 3142-3148.

93. Pancheshnyi, S., *Role of electronegative gas admixtures in streamer start, propagation and branching phenomena.* Plasma Sources Science & Technology, 2005. **14**(4): p. 645-653.

94. Boeuf, J.P. and L.C. Pitchford, *Electrohydrodynamic force and aerodynamic flow acceleration in surface dielectric barrier discharge.* Journal of Applied Physics, 2005. **97**(10).

95. Aleksandrov, N.L. and E.M. Bazelyan, *Ionization processes in spark discharge plasmas.* Plasma Sources Science & Technology, 1999. **8**(2): p. 285-294.

96. Enloe, C.L., M.G. McHarg, G.I. Font, and T.E. McLaughlin. *Plasma-induced force and self-induced drag in the dielectric barrier discharge aerodynamic plasma actuator* in *47th AIAA Aerospace Sciences Meeting Including The New Horizons Forum and Aerospace Exposition*. 2009. Orlando, Florida: AIAA.

97. Font, G.I., C.L. Enloe, and T.E. McLaughlin. *Effect of Volumetic Momentum Addition on the Total Force Production of a Plasma Actuator*. in *39th AIAA Fluid Dynamics Conference*. 2009. San Antonio, Texas: AIAA.

98. Forte, M., L. Leger, J. Pons, E. Moreau, and G. Touchard, *Plasma actuators for airflow control: measurement of the non-stationary induced flow velocity.* Journal of Electrostatics, 2005. **63**(6-10): p. 929-936.

99. Moreau, E., L. Leger, and G. Touchard, *Effect of a DC surface-corona discharge on a flat plate boundary layer for air flow velocity up to 25 m/s.* Journal of Electrostatics, 2006. **64**(3-4): p. 215-225.

100. Sosa, R., H. Kelly, D. Grondona, A. Marquez, V. Lago, and G. Artana, *Electrical and plasma characteristics of a quasi-steady sliding discharge.* Journal of Physics D-Applied Physics, 2008. **41**(3).

101. Louste, C., G. Artana, E. Moreau, and G. Touchard, *Sliding discharge in air at atmospheric pressure: electrical properties.* Journal of Electrostatics, 2005. **63**(6-10): p. 615-620.

102. Benard, N., A. Mizuno, and E. Moreau, *A large-scale multiple dielectric barrier discharge actuator based on an innovative three-electrode design.* Journal of Physics D-Applied Physics, 2009. **42**(23).

103. Benard, N., J. Jolibois, E. Moreau, R. Sosa, G. Artana, and G. Tochard, *Aerodynamic plasma actuators: A directional micro-jet device.* Thin Solid Films, 2008. **516**(19): p. 6660-6667.

104. Santhanakrishnan, A. and J.D. Jacob, *On plasma synthetic jet actuators*, in *44th AIAA Aerospace Sciences Meeting and Exhibit*. 2006: Reno Nevada. p. 19.

105. Schatzman, D.M. and F.O. Thomas, *Turbulent Boundary-Layer Separation Control with Single Dielectric Barrier Discharge Plasma Actuators.* Aiaa Journal, 2010. **48**(8): p. 1620-1634.

106. Huang, X. and X. Zhang, *Streamwise and spanwise plasma actuators for flow-induced cavity noise control.* Physics of Fluids, 2008. **20**(3).

107. Abe, T., Y. Takizawa, S. Sato, and N. Kimura, *Experimental Study for Momentum Transfer in a Dielectric Barrier Discharge Plasma Actuator.* AIAA Journal, 2008. **46**(9): p. 2248-2255.

108. Bernard, N., N. Balcon, and E. Moreau, *Electric Wind Produced by a Surface Dielectric Barrier Discharge Operating Over A Wide Range Of Relative Humidity.*, in *47th AIAA Aerospace Sciences Meeting Including The New Horizons Forum and Aerospace Exposition*. 2009, AIAA: Orlando, Florida.

109. Thomas, F.O., T.C. Corke, M. Iqbal, A. Kozlov, and D. Schatzman, *Optimisation of Dielectric Barrier Discharge Plasma Actuators for Active Flow Control.* AIAA Journal, 2009. **47**(9): p. 2169-2178.

110. Kriegseis, J., S. Grundmann, and C. Tropea, *Airflow influence on the discharge performance of dielectric barrier discharge plasma actuators.* Physics of Plasmas, 2012. **19**(7).

111. Borghi, C.A., M.R. Carraro, A. Cristofolini, and G. Neretti, *Electrohydrodynamic interaction induced by a dielectric barrier discharge.* Journal of Applied Physics, 2008. **103**(6).

112. Versailles, P., V. Gingras-Gosselin, and H.D. Vo, *Impact of Pressure and Temperature on the Performance of Plasma Actuators.* AIAA Journal, 2010. **48**(4): p. 859-863.

113. Erfani, R., H. Zare-Behtash, and K. Kontis, *Plasma actuator: Influence of dielectric surface temperature.* Experimental Thermal and Fluid Science, 2012. **42**: p. 258-264.

114. Kriegseis, J., D. Schroeter, S. Grundmann, and C. Tropea, *Online-characterization of dielectric barrier discharge plasma actuators for optimized efficiency of aerodynamical flow control applications*, in *Proceedings of the 13th International Conference on Electrostatics: Electrostatics 2011*, D.M. Taylor, Editor. 2011. ISBN: 1742-6588

115. United States Environmental Protection Agency. *Waste Water Technology Factsheet.* 1999 [Accessed Online: 12/08/08]; Available from: http://www.epa.gov/owm/mtb/ozon.pdf.

116. United States Enviromental Protection Agency. *Waste Water Technology Factsheet.* 1999 [Accessed Online: 12/08/08]; Available from: http://www.epa.gov/owm/mtb/ozon.pdf.

117. TSO3. *TSO3, Ozone Sterilization - Medical Instrument Sterilizer.* [Accessed Online: 12/08/08]; Available from: http://www.tso3.com/en/index.php

118. purfresh. *Properties Of Ozone.* [Accessed Online: 12/08/08]; Available from: http://www.purfresh.com/tech_ozone.htm

119. National Oceanic and Atmospheric Administration. *How Ozone Is Formed And How It Affects Our Atmosphere* [Accessed Online: 12/8/08]; Available from: http://www.srh.noaa.gov/ohx/ozone/ozone_formation.html

120. World Health Organisation. *Air Quality and Health*. 2008 [Accessed Online: 12/08/08]; Available from: http://www.who.int/mediacentre/factsheets/fs313/en/

121. Environmental Protection UK. *Ozone Pollution*. [Accessed Online: 12/08/08]; Available from: http://www.environmental-protection.org.uk/air-quality-and-climate/air-quality/ozone-pollution/

122. United States Environmental Protection Agency. *Ozone Air Quality Standards - Ground Level Ozone*. 2008 [Accessed Online: 12/08/08]; Available from: http://www.epa.gov/air/ozonepollution/standards.html

123. Health And Safety Executive, *EH 38 Ozone Hazards And Precautionary Measures*. 1986. ISBN: 0118835629

124. Health And Safety Executive, *EH 40/2005 List Of Approved Workplace Exposure Limits* 2005. ISBN: 0717629775

125. Sims-Williams, D.B., PhD Thesis: *Self Excited Unsteadiness Associated With Passenger Cars*, in *School of Engineering*. 2001, University of Durham.

126. NPL. *How can I determine my local values of gravitational acceleration and altitude? (FAQ - Mass & Density)*. 2010 [Accessed Online: 3/12/2011]; Available from: http://www.npl.co.uk/reference/faqs/how-can-i-determine-my-local-values-of-gravitational-acceleration-and-altitude-%28faq-mass-and-density%29.

127. Jorgensen, F.E. *Dantec Dynamics - How To Measure Turbulance With Hot-Wire Anemometers*. 2002 [Accessed Online: 11/04/2012]; Available from: http://www.dantecdynamics.com/Admin/Public/DWSDownload.aspx?File=files%2ffiler%2fsupport_and_download%2fresearch_and_education%2fpracticalguide.pdf.

128. Fraden, J., *Handbook of Modern Sensors: Physics, Designs, and Applications*. 2010: Springer. ISBN: 9781441964656

129. Bruun, H.H., *Hot-Wire Anemometry: Principles and Signal Analysis*. 1995, Oxford University Press. pages. 95-96. ISBN: 9780198563426

130. Dominy, R.G. and H.P. Hodson, *An Investigation of Factors Influencing the Calibration of Five-Hole Probes for Three-Dimensional Flow Measurements.* Journal of Turbomachinery, 1993. **115**(3): p. 513-519.

131. Willert, C.E. and M. Gharib, *DIGITAL PARTICLE IMAGE VELOCIMETRY.* Experiments in Fluids, 1991. **10**(4): p. 181-193.

132. Nobach, H. and M. Honkanen, *Two-dimensional Gaussian regression for sub-pixel displacement estimation in particle image velocimetry or particle position estimation in particle tracking velocimetry.* Experiments in Fluids, 2005. **38**(4): p. 511-515.

133. Lourenco, L. and A. Krothapalli, *ON THE ACCURACY OF VELOCITY AND VORTICITY MEASUREMENTS WITH PIV.* Experiments in Fluids, 1995. **18**(6): p. 421-428.

134. Workshop, E., M. Stanislas, J. Westerweel, and J. Kompenhans, *Particle image velocimetry: recent improvements : proceedings of the EUROPIV 2 Workshop held in Zaragoza, Spain, March 31-April 1, 2003*. 2004: Springer. ISBN: 9783540214236

135. Liu, J.Y. and M. Iskander, *Adaptive cross correlation for imaging displacements in soils.* Journal of Computing in Civil Engineering, 2004. **18**(1): p. 46-57.

136. Piirto, M., H. Eloranta, P. Saarenrinne, and R. Karvinen, *A comparative study of five different PIV interrogation algorithms.* Experiments in Fluids, 2005. **39**(3): p. 571-588.

137. Intelegent Laser Aplications GmbH. *ILA Product Datasheets*. 2010 [Accessed Online: 2/9/2010]; Available from: http://www.ila.de/Products_Mk1.htm.

138. Dupont. *DuPont Kapton Polyimide Film*. 2012 [Accessed Online: 16/3/2012]; Available from: http://www2.dupont.com/Kapton/en_US/assets/downloads/pdf/Gen_Specs.pdf.

139. Schiller, S. and G. Jasch, *DEPOSITION BY ELECTRON-BEAM EVAPORATION WITH RATES OF UP TO 50-MU-MS-1.* Thin Solid Films, 1978. **54**(1): p. 9-21.

140. Madelung, O., H. Landolt, and R. Börnstein, *Technology of Si, Ge and SiC (Numerical Data and Functional Relationships In Science And Technology)*. 1983: Springer. ISBN: 9783540114741

141. Inagaki, M., S. Harada, T. Sato, T. Nakajima, Y. Horino, and K. Morita, *CARBONIZATION OF POLYIMIDE FILM KAPTON.* Carbon, 1989. **27**(2): p. 253-257.

142. Su, J. and A.C. Lua, *Influence of carbonisation parameters on the transport properties of carbon membranes by statistical analysis.* Journal of Membrane Science, 2006. **278**(1-2): p. 335-343.

143. Bhushan, B., *Springer handbook of nanotechnology*. 2006: Springer. ISBN: 9783540298557

144. Drobny, J.G., *Technology Of Fluropolymers*. 2000: CRC Press. ISBN: 0849302463

145. Raghavan, P.S., *Concepts And Problems In Inorganic Chemistry*. 1998: Discovery Publishing House Pvt. Ltd. ISBN: 9788171414185

146. Davidson, T., R.N. Gounder, D.K. Weber, and S.M. Wecker, *Fluropolymers 2: Properties*. 1999: Springer. ISBN: 0306460610

147. DuPont. *DuPont FEP Flurocarbon Film - Information Bulletin*. 1996 [Accessed Online: 16/7/2009]; Available from: http://www2.dupont.com/Teflon_Industrial/en_US/assets/downloads/h55007.pdf.

148. Bhattacharya, S., Y.F. Gao, V. Korampally, M.T. Othman, S.A. Grant, K. Gangopadhyay, and S. Gangopadhyay, *Mechanics of plasma exposed spin-on-glass (SOG) and polydimethyl siloxane (PDMS) surfaces and their impact on bond strength.* Applied Surface Science, 2007. **253**(9): p. 4220-4225.

149. Tserepi, A., G. Cordoyiannis, G.P. Patsis, V. Constantoudis, E. Gogolides, E.S. Valamontes, D. Eon, M.C. Peignon, G. Cartry, C. Cardinaud, and G. Turban, *Etching behavior of Si-*

containing polymers as resist materials for bilayer lithography: The case of poly-dimethyl siloxane. Journal of Vacuum Science & Technology B, 2003. **21**(1): p. 174-182.

150. Dow Corning. *Information about Dow Corning® Brand Silicone Encapsulants*. 2000 [Accessed Online: 17/7/09]; Available from: http://www2.dowcorning.com/DataFiles/090007c88020bcca.pdf.

151. Surface-Tension.de. *Solid surface energy data (SFE) for common polymers* 2007 20/11/07 [Accessed Online: 22/07]; Available from: www.surface-tension.de/solid-surface-energy.htm.

152. Roth, J., V. Albrecht, M. Nitschke, C. Bellmann, F. Simon, S. Zschoche, S. Michel, C. Luhmann, K. Grundke, and B. Voit, *Surface Functionalization of Silicone Rubber for Permanent Adhesion Improvement.* Langmuir, 2008. **24**(21): p. 12603-12611.

153. Kim, J., M.K. Chaudhury, and M.J. Owen, *Hydrophobic recovery of polydimethylsiloxane elastomer exposed to partial electrical discharge.* Journal of Colloid and Interface Science, 2000. **226**(2): p. 231-236.

154. Jacobs, E.N. and A. Sherman, *Airfoil section characteristics as affected by variations of the Reynolds Number - Report 586*. 1937, NACA.

155. Paraschivoiu, I., *Subsonic Aerodynamics*. 2003, Presses internationales Polytechnique. pages. 151-162. ISBN: 9782553011306

156. Gregory, N. and C.L. O'Reilly, *Low-Speed Aerodynamic Charicteristics of NACA 0012 Aerofoil Section, including the Effects of Upper-Surface Roughness Simulating Hoar Frost*, Ministry Of Defence, 1973, Her Majesty's Stationery Office: London.

157. Liebeck, R.H., *Design of Subsonic Airfoils for High Lift.* Journal of Aircraft, 1978. **15**(9): p. 547-561.